Understanding the Formation and Properties of Galaxies from Stellar Kinematics

Felix Schulze

München 2021

Understanding the Formation and Properties of Galaxies from Stellar Kinematics

Felix Schulze

Dissertation
an der Fakultät für Physik
der Ludwig–Maximilians–Universität
München

vorgelegt von
Felix Schulze
aus Isny im Allgäu

München, den 08.03.2021

Erstgutachter: Prof. Dr. Andreas Burkert
Zweitgutachter: Prof. Dr. Eric Emsellem
Tag der mündlichen Prüfung: 10.05.2021

Contents

Zusammenfassung

Obwohl die Entstehung und die Eigenschaften von Galaxien schon seit fast 100 Jahren Gegenstand astrophysikalischer Forschung sind, gibt es grundlegende Aspekte, welche bis heute nicht vollständig verstanden sind. Vor dem Hintergrund der kosmologischen Strukturbildung entwickeln sich Galaxien unter dem Einfluss diverser interner und externer physikalischer Prozesse. Ein komplexes Zusammenspiel dieser Prozesse, welche auf variierenden Zeitskalen agieren, formt die Galaxien die wir heute beobachten. Es ist bekannt, dass dieses Zusammenspiel maßgeblich die orbitale Struktur von Sternen innerhalb von Galaxien beeinflusst und daher Spuren in der Phasenraumverteilung hinterlässt. Die vorliegende Dissertation beschäftigt sich mit der Frage, welche Information aus der stellaren Kinematik extrahiert werden kann, um die Entstehung und Entwicklung von Galaxien umfassender zu verstehen. Im Speziellen untersuchen wir die Geschwindigkeitsverteilung entlang der Blickachse anhand ihrer Momente. Hierfür nutzen wir die hochmoderne hydrodynamische kosmologische *Magneticum* Simulation, in welcher sich auf natürliche und selbstkonsistente Weise eine realistische und statistisch aussagekräftige Galaxienpopulation bildet. Um die kinematische Struktur von Galaxien in größerem Detail zu untersuchen, werden zusätzlich hochaufgelöste idealisierte Simulationen individueller Galaxienverschmelzungen analysiert.

Der erste Teil der Arbeit bezieht sich zunächst auf das Zentrum elliptischer Galaxien. Im Einklang mit Beobachtungen finden wir im Allgemeinen eine bimodale Verteilung aus schnell rotierenden und langsam rotierenden Galaxien, mit konsistenten Häufigkeiten. Die Simulation reproduziert zudem die wichtigsten beobachteten Geschwindigkeitsstrukturen, wie gegenläufig oder entkoppelt rotierende Kerne. Mit Hilfe der dreidimensionalen Information der Simulation zeigen wir, dass es möglich ist, anhand von beobachtbaren Parametern die interne Anisotropie der Sterne abzuleiten. Dies bestätigt die Validität eines theoretischen Modells, welches zur Interpretation von Beobachtungen hinsichtlich der internen Struktur von Galaxien verwendet wird. Diese Resultate zeigen, dass die *Magneticum* Simulation ein exzellentes Laboratorium bereitstellt, um die stellare Kinematik und deren Ursprung zu erforschen. In diesem Zusammenhang finden wir, dass die Population aus langsam rotierenden Galaxien sich graduell seit $z = 2$ aufbaut, und ein signifikanter Anteil dieser nun langsam rotierenden Galaxien ihren Drehimpuls durch eine massive Galaxienverschmelzung verloren hat.

Im zweiten Teil untersuchen wir in einer detaillierten Fallstudie Ursprung, Stabilität und Dynamik eines gegenläufig rotierenden Kerns einer elliptischen Galaxie, die durch einen einzelnen massiven Verschmelzungsprozess zweier Spiralgalaxien in einer idealisierten Simulation entstanden ist. Wir können zeigen, dass solche Kerne aus neu geformten Sternen aufgebaut sind, deren Apoapsis sich innerhalb des Kernradius befindet. Das Rotationssignal verschwindet etwa 3 Gyr nach der Galaxienkollision, ausgelöst durch die gravitative Vermischung der rotierenden Sterne mit Sternen, die den Kern auf stark elliptischen Bahnen intrudieren. Während seiner Lebenszeit vollführt der Kern eine periodische globale Bewegung. Diese Be-

wegung ist ein Indiz für die Konservierung des orbitalen Drehimpulses in der gasförmigen Komponente, welche später durch Sternentstehung den Kern aufbaut.

Im dritten Teil erweitern wir unsere Analyse auf den stellaren Halo der Galaxien. Aufgrund der niedrigen Dichten und damit verbundenen langen Relaxationszeiten dokumentiert der stellare Halo eine Vielfalt an Informationen über Verschmelzungen mit anderen Galaxien. Im Einklang mit Beobachtungen finden wir drei Arten von radialen Rotationsvariationen: stark im Zentrum und schwächer im Halo, kontinuierlich ansteigend mit hoher Amplitude und durchgehend flach mit niedriger Amplitude. Diese Variationen in der Rotation sind Resultat des komplexen Zusammenspiels von interner Sternenstehung und der Akkretion von Sternen. Für die erste Art von Galaxien finden wir starke Indizien, dass der Halo und das Zentrum sich entkoppelt entwickeln. Während das Zentrum einer alten Scheibe entspricht die schon bei $z \sim 2$ existiert und durch interne Sternenstehung wächst, baut sich der Halo durch das anisotrope Akkretieren kleiner Strukturen auf. Dieses Szenario legt nahe, dass eine Verbindung zwischen dem kinematischen Übergang und dem Übergang von insitu geformten zu akkretierten Sternen besteht. Wir demonstrieren, dass eine solche Korrelation existiert, jedoch mit einer gewissen Streuung, die durch einen vermischten Übergangsbereich verursacht wird.

Abschließend wird die Form der Geschwindigkeitsverteilung genauer untersucht, indem wir die Schiefe und Wölbung der Verteilung miteinbeziehen, um die maximale Information aus der Geschwindigkeitsverteilung zu extrahieren. Dies wird erstmals für eine kosmologische Simulation durchgeführt. Wir zeigen, dass Galaxien mit ansteigender stellarer Masse eine zunehmend schmalere Geschwindigkeitsverteilung aufweisen. Diese Veränderung weist auf einen generellen Übergang in der orbitalen Konfiguration hin. Zudem können wir zeigen, dass die globalen wie auch räumlich aufgelösten höheren Momente Rückschlüsse auf die Entstehung von Galaxien zulassen. Galaxien deren lokale Schiefe stark mit der lokalen Rotationsuntestützung korreliert/anti-korreliert, weisen eine erhöhte intrinsische Sternenstehung und ein erhöhtes Reservoir an kaltem Gas auf.

Zusammenfassend zeigt diese Dissertation, dass die stellare Geschwindigkeitsverteilung von Galaxien wertvolle Informationen über die Entstehung und Entwicklung von Galaxien enthält. Unsere Ergebnisse stellen aussagekräftige Interpretationen aktueller Beobachtungen dar und liefern Vorhersagen, die zum Verständnis zukünftiger Beobachtungen maßgeblich beitragen werden.

Abstract

Although the formation and properties of galaxies have been the subject of astrophysical research for almost 100 years, some fundamental aspects are still not fully understood. Against the background of large scale cosmological structure formation, galaxies develop under the influence of various physical processes which interplay in a complex manner to form the galaxies observed today. This includes internal as well as external processes that act on varying temporal and spatial scales. It is known that aspects of this interplay significantly influence the orbital structure of stars within galaxies, and therefore encode in the stellar phase-space distribution. This thesis addresses the question of which information can be extracted from the kinematics of stars in order to further understand the details of the formation and evolution of galaxies. In particular, we study the stellar line-of-sight velocity distribution (LOSVD) based on its moments. For this we use the state-of-the-art hydrodynamic cosmological *Magneticum Pathfinder* simulation, which implements a variety of relevant physical mechanisms in order to build a realistic and statically meaningful galaxy population in a self-consistent manner. In addition, high-resolution idealised simulations of individual galaxy mergers are analysed to examine the kinematic structure of galaxies in greater detail.

The first part of the thesis is constrained to the centre of Early-Type Galaxies. In agreement with observations from integral field spectroscopy surveys, we find a bimodal distribution of fast and slow rotating galaxies with consistent frequencies. Furthermore, the simulation reproduces the most important observed velocity structures, such as counter-rotating or decoupled rotating cores. Exploiting the three-dimensional information provided by the simulation, we demonstrate that it is possible to infer the internal stellar anisotropy from observable parameters. This confirms the validity of a theoretical model, which is generally used to interpret observations regarding the internal kinematic structure of galaxies. These results show that the *Magneticum Pathfinder* simulation provides an excellent laboratory to study the kinematics of galaxies and to explore their origin. In this context we find that the population of slowly rotating galaxies builds up gradually since $z = 2$, and a significant fraction loses its angular momentum due to massive galaxy merger.

Furthermore, we investigate in a detailed case study the origin, stability and dynamics of a counter-rotating kinematically distinct core (KDC) in an elliptical galaxy formed in an isolated galaxy merger simulation. We show, that the KDC consists of stars that have been newly formed during the merger on orbits with an apoapsis within the core radius. The rotation signal disappears approximately 3Gyr after the galaxy merger, triggered by the gravitational mixing of the rotating stars with stars which intrude the KDC on strongly elliptical orbits. During its lifetime, the core performs a periodic global movement comparable to the precession of a gyroscope in a gravitational potential. This global motion originates from the conservation of the progenitor orbital angular momentum in the gaseous component, which later builds up the KDC through star formation.

In the third part we expand the analysis to the stellar halo of galaxies, which encodes a variety of information about interactions with other galaxies for a long period of time due to the low densities and the associated long relaxation timescales in the halo. In agreement with observations we find three characteristic types of radial rotation variations: i) strong in the centre and increasingly weaker in the halo ii) continuously rising with high amplitude iii) continuously flat mostly with low amplitude. These variations in the rotation reflect the complex interplay of internal star formation and external accretion of stars. For the first type of galaxies, we find strong evidence that the halo and the centre are evolving decoupled. While the centre corresponds to an old disk which already exists at $z \sim 2$ and grows through internal star formation, the halo is built up through the anisotropic accretion of small structures which are disrupted in the halo. This scenario suggests a connection between the kinematic transition and the transition from in-situ formed to accreted ex-situ stars. We demonstrate that such a correlation exists, with a certain scatter caused by a transition region where both in-situ and ex-situ stars are strongly mixed. This result represents an important interpretation of recent observations and prediction for future observations which will push the limits of radial coverage of IFS observations.

Finally, to extract the maximum information from the LOSVD, its shape is examined more closely by including higher-order moments measuring the deviations from a Gaussian, i.e. the skewness and kurtosis. This is the first time this analysis is applied to galaxies from a fully cosmological simulation. We show that galaxies with higher stellar masses exhibit a more peaked LOSVD, indicating a transition in the global orbital configuration. Furthermore, we are able to extract information about the formation history of galaxies from the global as well as spatially resolved higher-order moments. Galaxies with a strong anticorrelation/correlation between the local skewness and rotational support exhibit increased insitu star formation and a larger reservoir of cold gas to prolong star formation.

In summary, this thesis shows that the LOSVD of galaxies encodes valuable information about the formation and evolution of galaxies. Our findings represent meaningful interpretations of recent IFS observations and provide predictions that can be probed by future surveys which will be able to reach larger radii and redshifts and to include information about stellar populations.

Chapter 1

Introduction

Many of the recent day research fields in physics are based on few fundamental observations of phenomena in nature that were not explainable at that time paving the way for decades or even centuries of active research. For extragalactic astronomy Edwin Hubble marked the starting point by conclusively proving that the nebulae he observed are not part of the Milky Way, but resemble stellar systems of their own (Hubble, 1925, 1926). Expanding his analysis he furthermore showed in 1929 that the radial velocity of these nebulae correlates roughly linear with its distance, today known as Hubble's Law (Hubble, 1929). This observation provided the first evidence that the Universe we live in is expanding, building the foundation for the research field of observational cosmology. With his work Edwin Hubble fundamentally altered our understanding of the Universe and challenged the natural strive after knowledge inevitable for humankind. Almost hundred years later the origin of these nebula and their varying properties as well as the cosmological evolution of the Universe and their interplay is still explored and is full of puzzles. In the following chapter we will outline the current status of research regarding this topics and provide the foundation for the research conducted in the thesis.

1.1 Galaxies and their Properties in the Present-Day Universe

The first proposal of a galaxy classification was submitted by Edwin Hubble in 1926 (Hubble, 1926). In his study Hubble classified 400 nearby galaxies according to their apparent morphology. This study provided the basis for the well-known Hubble-sequence or Hubble's tuning fork displayed in Fig. 1.1.

In this classification scheme galaxies are broadly separated into *elliptical galaxies* in the left branch and *spiral galaxies* in the two parallel branches on the right. Only 3% of the sample could be assigned to neither of the two types, hence were denoted as *irregulars*. The class of elliptical galaxies feature characteristic elliptical isophotes, merely varying in their apparent elongation. Galaxies of this type do not show any evidence of internal morphological structure, hence a further division according to the elongation was introduced. In the classification diagram the elliptical galaxies become increasingly more elongated from left to right, usually denoted by En with n parameterising the elongation of the galaxy $n = 10 \cdot (1 - b/a)$, where a is the major and b the minor axis of the galaxy. Historically elliptical galaxies are commonly referred to as *Early-type galaxies* (ETG).

Spiral galaxies, however, show distinct internal structure in the form of spiral arms and

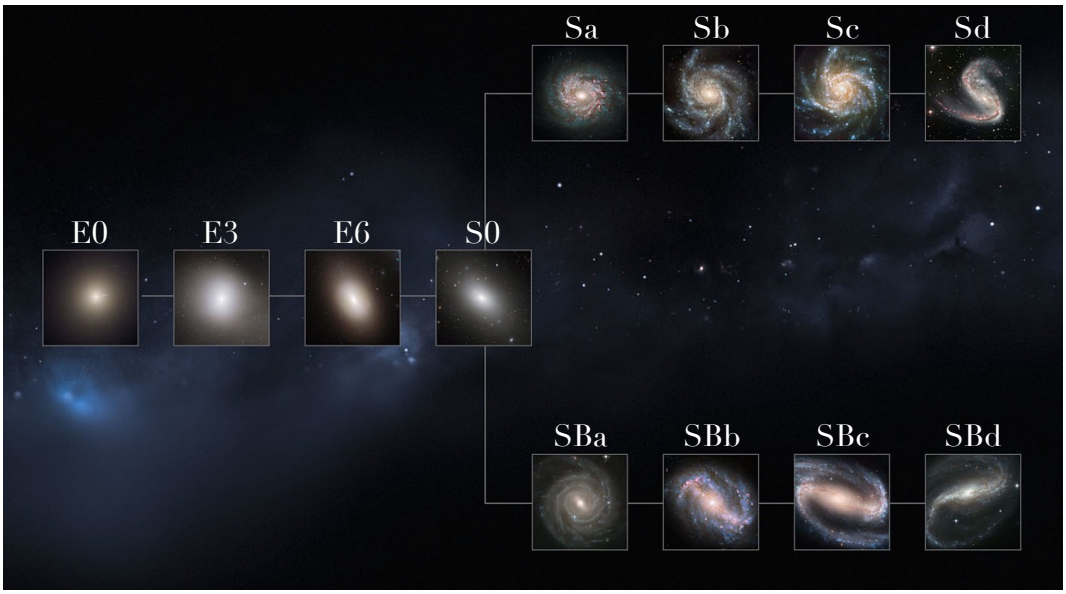

Figure 1.1: Illustration of Hubble's tuning fork proposed by Edwin Hubble in 1936 (Hubble, 1936). While the left branch comprises the elliptical galaxies (E0-E6), the right two parallel branches comprise the spiral galaxies subdivided according to the presence of a bar (S(B)a-S(B)d). Lenticular (S0) galaxies build the merging point between elliptical galaxies and spiral galaxies. Image credit: NASA, ESA, M. Kornmesser.

an apparent central bulge component. Furthermore, some objects of this class exhibit a bar-like structure in the centre connected to the spiral arms. Based on these structural features Hubble introduced a more refined classification for spiral galaxies: The two parallel branches distinguish spiral galaxies according to the presence of a bar in the centre commonly denoted by S (bar-less) in the top branch and SB (bar) in the lower branch. Independent of the existence of a bar, the spiral galaxy branches form a continuous sequence from objects with a prominent bulge and tightly bound arms S(B)a on the left to less prominent bulges with loosely bound arms S(B)d on the right. Historically spiral galaxies are commonly referred to as *Late-Type galaxies* (LTG).

Later on Sandage (1961) firmly established the class of *lenticular* or S0 galaxies at the merging point of elliptical and spiral galaxies. Lenticular galaxies are an intermediate morphological type between the well defined ellipticals and spirals since they share properties with both classes. Similarly to elliptical galaxies, lenticulars typically have a smooth light distribution without a spiral structure. Furthermore, they exhibit a disk and a bulge component similar to spirals galaxies, however typically with a more prominent bulge than spiral galaxies. Together with elliptical galaxies lenticulars form the class of Early-Type galaxies.

The naming convention of LTG and ETG originates from Hubble's interpretation, that the tuning fork represents a temporal sequence. Since the central bulge component of spiral galaxies resembles elliptical galaxies in many properties Hubble believed, that elliptical galaxies evolve into spiral galaxies via the intermediate lenticular state, hence calling elliptical and lenticular galaxies early-type and spiral galaxies late-type. Although it is known today that this sequence is incorrect the historical naming convention is preserved.

This purely morphological classification has already shown to capture several physical properties. In general, ETGs only have little to no gas and therefore are not actively forming

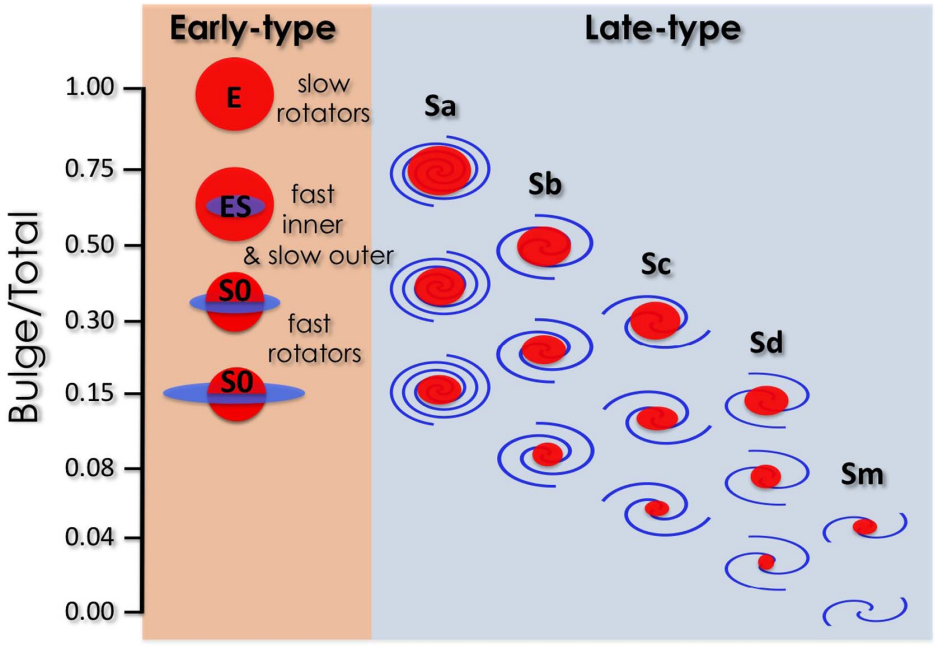

Figure 1.2: Fig. 7 taken from Graham et al. (2016). Ordering of galaxies in a grid of morphological type, according to spiral arms along one axis and the bulge-to-total ratio along the other. It also contains the class of ellicular galaxies as a transition state between elliptical galaxies and S0 galaxies.

stars. Furthermore, ETGs have red photometric colours characteristic of an old stellar population. In contrast, LTGs appear to be bluer, indicative of active star formation mainly in the spiral arms and a young stellar population. In addition ETGs and LTGs show distinct differences in the radial light profile.

With the advancement of observational methods revolutionary parametric measurements of the structure of galaxies became possible. As the first major contribution de Vaucouleurs (1948) showed that the one dimensional light profile of massive ellipticals follow approximately a universal distribution, known as the de Vaucouleurs profile. This was later extended and generalised by Sérsic (1963) who introduced the Sérsic profile which parametrises the profile shape by the Sérsic index n. LTGs typically have $n \sim 1$ corresponding to a exponential profile, while ETGs have $n \sim 4$ equivalent to the de Vaucouleurs profile.

Obviously, morphological classifications such as the Hubble sequence depend on the viewing angle, especially for elliptical galaxies, and therefore only partly reveal the intrinsic morphology. Hence, this classification strongly correlates with inclination rather than with fundamental properties. Due to this drawback the observed ellipticity is often denoted as apparent ellipticity. Based on that issue, Kormendy and Bender (1996) proposed a revision of the Hubble classification. Detailed investigations of the surface brightness of ETG's revealed small deviation of the isophotes from an ellipses. Therefore, they suggested to arrange ETG's depending on the diskyness or boxyness of their isophotal shapes. Claiming that discy ellipticals have significant rotation, little or to no radio and X-ray emission, while boxy ellipticals show less rotation and stronger than average radio and X-ray emission, this classification correlates with fundamental galaxy properties (Bender et al., 1989; Pasquali et al., 2007).

In the further evolution the study of galaxy structure expanded to include the decompo-

sition of galaxies into disk and bulge component (Kormendy, 1977; Capaccioli et al., 1988; Freeman, 1970; Savorgnan and Graham, 2016b). Building on the classification diagram from van den Bergh (1976), Cappellari et al. (2011b) presented a scheme in which S0 galaxies form a parallel sequence to late-type galaxies with varying disk-to-bulge ratios. This is also discussed in Graham et al. (2016) who presented the grid shown in Fig. 1.2, capturing the morphological type according to spiral arms along one axis and the bulge-to-total ratio on the other axis. It also contains the class of ellicular galaxies as a transition state from elliptical galaxies with a intermediate scale disk component to S0 galaxies.

A revolutionary step in studies of galaxy structure and properties was the development of *Integral-Field-Spectroscopy* (IFS) that provides two dimensional spatially resolved spectral information. The earliest IFS observations were conducted by Wilkinson et al. (1986) who moved a long slit across the filed of Centaurus A to map the two dimensional velocity field. Due to significant technological advancements during the past two decades several large IFS surveys, pioneered by the SAURON survey (Bacon et al., 2001), investigated the stellar kinematics of galaxies. Most significantly, these surveys showed that in particular ETGs show a wealth of kinematic substructures that need be considered in any classification scheme and theory of galaxy formation. This topic will be discussed in great detail in main body of this thesis.

1.2 A Canvas for Galaxy Formation

The formation of galaxies in the Universe took place within the paradigm of structure formation on scales much larger than individual galaxies and within an expanding Universe. It is therefore crucial to understand the process of galaxy formation and their evolution in the context of the cosmological evolution of the Universe and the origin of the over-densities in which galaxies formed. The present-day accepted theoretical model describing structure formation in the Universe is the ΛCDM model. In this section an overview over the historical development of the ΛCDM model is given and the most fundamental equations are presented.

1.2.1 Towards a Self-Consistent Model of the Universe

Only since Albert Einstein published his ground breaking theory of General Relativity the theoretical and mathematical background to construct a self-consistent model of the Universe has been established (Einstein, 1915). Based on this theory, the first solutions of Einsteins field equations described an either expanding or collapsing Universe, contrary to Einsteins belief in a static Universe. Assuming the cosmological principles that the Universe is isotropic and homogeneous on large scales, Alexander Friedmann and George Lemaitre independently found solutions that describe a static and an expanding Universe (Friedmann, 1922; Lemaitre, 1927).

Based on the expansion of the Universe George Gamow suggested in the 1940s that the Universe must have developed from a denser and also hotter state at earlier times leading to the Hot Big Bang model. As a consequence he predicted that the residual heat from that epoch should still be detectable in the present day Universe as thermal radiation with a temperature of only a few kelvin. This prediction was confirmed in 1965 by Penzias and Wilson (1965) and Dicke et al. (1965) who measured an isotropic black-body background radiation with a temperature of 3.5K, known as the Cosmic Microwave Background. This discovery firmly established the Hot Big Bang model as the standard model of cosmology.

However, it was realised that this model had some severe shortcomings connected to causality and spatial flatness of the Universe (e.g. Misner, 1968; Dicke and Peebles, 1979). To solve these problems Guth (1981) proposed a scenario in which the early Universe has undergone a phase of rapid exponential expansion driven by a quantum field acting similarly to the cosmological constant. The initial model was later revised by Linde (1982) and Albrecht and Steinhardt (1982) to allow physical processes to establish homogeneity and isotropy as they are observed in the Cosmic Microwave Background. Furthermore, a primordial quantum field of this type is able to provide the density fluctuation, similar to the prediction by Harrison-Zeldóvich, that are consistent with the initial conditions needed to form galaxies (Hawking, 1982; Bardeen et al., 1983).

Parallel to these developments the insight that the visible matter only makes up a small percentage of the total matter content of the Universe and that the majority of the mass is in a unknown dark matter component got validated. The first observational evidence for dark matter was gathered in 1933 by Fritz Zwicky, who studied the velocity of 400 galaxies in the Coma Cluster. He found that the total mass required to stabilise the cluster has to be $\sim$ 400 times larger than the luminous mass in stars. However, only over 40 years later, the existence of dark matter was generally accepted triggered by the results of Ostriker et al. (1974) and Einasto et al. (1974). They extended Zwicky's analysis finding, that massive halos around our Milky Way and other galaxies are required to explain the motion of their satellite galaxies. Furthermore, measurements of rotation curves of spiral galaxies did not show a keplerian decline at large radii, as expected if the visible stars and gas were the only mass component in the system. In contrast the rotation curves plateaued at larger radii suggesting the presence of dark matter (Roberts and Rots, 1973; Rubin et al., 1978, 1980).

In the following several years various candidate particles for dark matter were proposed. The first promising candidate was the electron neutrino detected by Reines et al. (1980). However, it was quickly realised that neutrino dark matter was not consistent with the observed galaxy clustering (White et al., 1983). During that time particle physics provided numerous possible dark matter candidates with much larger masses than the neutrino dark matter. Due to the larger masses these particles initially would have much lower velocities and hence were referred to as warm (WDM) or cold (CDM) dark matter depending on their actual mass. Due to the lower velocities CDM is able to grow significant density perturbations needed to grow the structures observed today. However, measurements of galaxy clustering showed that CDM results in less clustering on large scales causing several alternative models to be postulated (Maddox et al., 1990; Efstathiou et al., 1990). These models converged to a final model assuming CDM and a cosmological constant to assure a flat geometry of the Universe, today known as the ΛCDM model.

Since the early 2000 ΛCDM has proven to be in excellent agreement with the most important cosmological observations. Several experiments measured CMB anisotropies and detected acoustic peaks in the power spectrum in excellent agreement with prediction from ΛCDM (de Bernardis et al., 2000; Hanany et al., 2000; Sievers et al., 2003). In addition, results from the ground breaking COBE, WMAP and Planck missions further strengthened the ΛCDM model and constrained the cosmological parameters to high accuracy (Komatsu et al., 2009; Planck Collaboration et al., 2018). Therefore, ΛCDM is the present-day accepted cosmological model for structure formation in the Universe and sets the basis for the formation and evolution of galaxies.

1.2.2 Expansion in the ΛCDM Universe

The dynamics of the Universe are described by *Einsteins Field Equations*

$$R_{\mu\nu} - \frac{1}{2}Rg_{\mu\nu} + \Lambda g_{\mu\nu} = \frac{8\pi G}{c^4}T_{\mu\nu}, \tag{1.1}$$

where $R_{\mu\nu}$ is the Ricci curvature tensor, R is the scalar curvature, $g_{\mu\nu}$ is the metric tensor, Λ is the cosmological constant, and $T_{\mu\nu}$ is the stress-energy tensor.

The most fundamental assumption of the ΛCDM model is the cosmological principle which states that

- **the Universe is homogeneous** - on large scales the matter is distributed uniformly, independent of an observer's location.
- **the Universe is isotropic** - on large scales the Universe looks the same in all spatial directions, independent of an observer's location.

These assumptions constrain the form of the Friedmann-Robertson-Walker (FRW) metric tensor $g_{\mu\nu}^{FRW}$ and the stress-energy tensor $T_{\mu\nu}$ in Einsteins field equations. The line element in the FRW is given by

$$ds^2 = dt^2 - a(t)^2\left[\frac{dr^2}{1-Kr^2} + r^2\left(d\theta^2 + sin^2\theta d\phi^2\right)\right], \tag{1.2}$$

where (r, θ, ϕ) are the comoving spherical coordinates and t is the proper time. The growth of the cosmic expansion is encoded in the scale factor $a(t)$ and K parametrises the spatial curvature. By definition $a(t_0) \equiv 1$ today. For convenience units that set $c = 1$ are used in the following derivation. Substituting Eq. 1.2 into Eq. 1.1 and using the stress-energy tensor of a perfect fluid yields the *Friedmann Equations*

$$\begin{aligned} \frac{\dot{a}^2}{a^2} + \frac{K}{a^2} &= \frac{8\pi G}{3}\rho + \frac{\Lambda}{3} \\ \frac{\ddot{a}}{a} &= -\frac{4\pi G}{3}(\rho + 3P) + \frac{\Lambda}{3}. \end{aligned} \tag{1.3}$$

Here, ρ denotes the energy density and P the pressure. For the density one distinguishes contributions from a non-relativistic matter component, a radiation component and a vacuum energy component (Λ).

Combining the two equations in Eq. 1.3 yields the evolution equation for the scale factor $a(t)$:

$$\left(\frac{\dot{a}(t)}{a(t)}\right)^2 = H_0^2\left(\frac{\Omega_{\mathrm{r},0}}{a(t)^4} + \frac{\Omega_{\mathrm{m},0}}{a(t)^3} + \frac{\Omega_{\mathrm{k},0}}{a(t)^2} + \Omega_{\Lambda,0}\right), \tag{1.4}$$

where $H_0 = \dot{a}(t_0)/a(t_0)$ is the famous *Hubble Constant*. Furthermore, the $\Omega_{\mathrm{i},0}$ parameters are normalised by the critical density for a flat Universe $\rho_{\mathrm{crit}} = 3H_0^2/8\pi G$ and represent the present day densities of the different component:

- Ω_{r} describes the contribution from radiation. In the early Universe this component was dominant, but is negligible at later times since $\rho_{\mathrm{r}} \propto a^{-2}$.
- $\Omega_{\mathrm{m}} = \Omega_{\mathrm{dm}} + \Omega_{\mathrm{b}}$ combines the contribution from the non-relativistic dark matter and baryonic matter. The corresponding energy density scales with $\rho_{\mathrm{m}} \propto a^{-3}$.

- Ω_Λ describes the dark energy component governed by the cosmological constant Λ and is constant in time $\rho_\Lambda = \Lambda/8\pi G = const.$
- $\Omega_\mathrm{k} = K/(a^2H^2) = 1 - \Omega_\mathrm{m} - \Omega_\mathrm{r} - \Omega_\Lambda$ determines the geometry of the Universe. $\Omega_\mathrm{k} < 0$ describes an open hyperbolic geometry, while $\Omega_\mathrm{k} = 0$ describes a flat geometry and $\Omega_\mathrm{k} > 0$ a spherical and closed geometry.

The cosmological parameters can be constrained from the temperature fluctuations and anisotropies in the CMB as been done by the space probe based COBE, WMAP and Planck missions (Wright et al., 1992; Komatsu et al., 2011; Planck Collaboration et al., 2018). Furthermore, cluster of galaxies and supernova of type Ia as standard candles can be used to determine the cosmological parameters (Perlmutter et al., 1999). In the most recent data release from the Planck Collaboration the parameters are determined to be $H_0 = 66.88 \pm 0.92$, $\Omega_\Lambda = 0.679 \pm 0.013$, $\Omega_{\mathrm{m},0} = 0.321 \pm 0.013$ and $\Omega_{\mathrm{b},0} = 0.049 \pm 0.00049$ (Planck Collaboration et al., 2018).

One fundamental effect induced by the expansion of the Universe is the redshift of photons. It can be observed in the wavelength of a photon, which is emitted at time t_e and absorbed at time t_a. From the FRW metric and the defining property of comoving distances one can derive a relation between $\lambda(t_\mathrm{e})$, $\lambda(t_\mathrm{a})$ and the scale factor $a(t)$:

$$z \equiv \frac{\lambda(t_\mathrm{a}) - \lambda(t_\mathrm{e})}{\lambda(t_\mathrm{e})} = \frac{1}{a(t_e)} - 1. \tag{1.5}$$

This shift of wavelength is parametrised by the so-called redshift z. Hence, every moment in cosmic time is related to a unique redshift.

1.2.3 Structure Formation in the ΛCDM Universe

The modern picture of structure formation assumes that the structures observed today formed from initial density perturbations in the very early Universe. At that time, approximately one Planck time (5.4×10^{-44}s) after the big bang, all matter was concentrated in a very small volume causing extremely high temperatures and pressure. Due to the high temperatures the strong and electroweak force were too weak to bind the particles in nuclei or even atoms. Hence, the Universe was in a plasma state consisting of free charges.

At this early stage the Universe was dominated by photons, scattering with the free charged particles. This process prevented the baryonic matter from forming potential wells, causing density fluctuation to smear out leading to a uniform opaque Universe. However, due to the cosmic expansion, the Universe cooled down allowing the gluons and quarks to form protons and neutrons. Subsequently, due to the further cool down below 3000K, and associated lower velocities of the particles, the electromagnetic force was strong enough to bind protons, neutrons and electrons into neutral atoms. From there on the photons decoupled from the matter and were able to travel freely and the Universe became optically transparent. This global phase transition of the Universe is called *recombination* and occurred about 380000 after the Big Bang. Recombination marks the origin for one of the most important discoveries in observational cosmology, the *Cosmic Microwave Background* (CMB).

The CMB originates from the fact, that in contrast to the baryonic matter, the dark matter was able to grow potential wells caused by quantum fluctuations even before recombination, since it is not influenced by the electromagnetic force. Already before recombination the baryonic matter began to follow the gravitational force of the dark matter and compressed

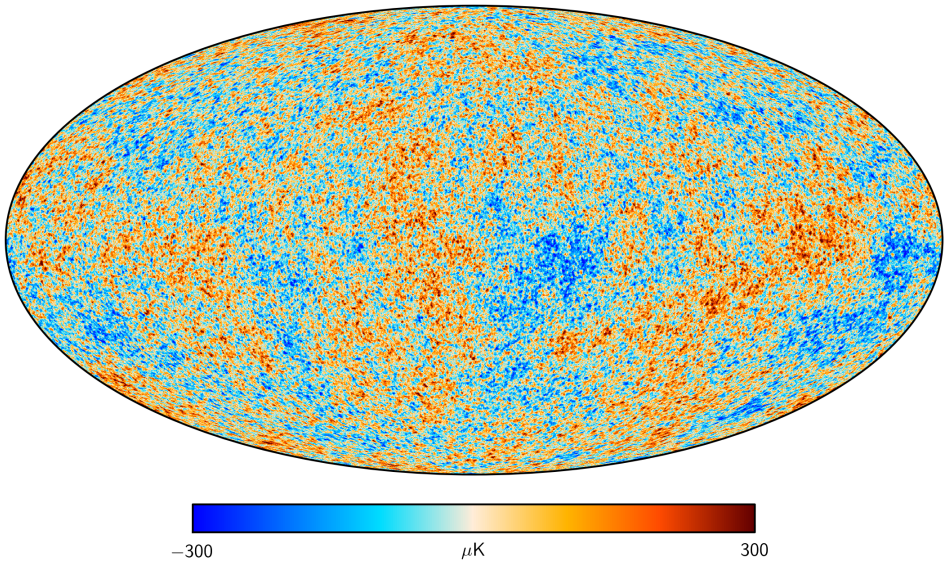

Figure 1.3: Temperature fluctuation map of the cosmic microwave background provided by the Planck mission. Image Credits: NASA/JPL-Caltech/ESA.

until the radiation pressure became strong enough to counteract gravity. This caused the baryons to oscillate between contraction and expansion in the potential wells of the dark matter known as *baryon acoustic oscillations* (BAO). While the temperature of the CMB photons decreased with time due to the cosmic expansion, the imprinted energy distribution from the BAO at the time of recombination is memorised and is observable today. The CMB was first discovered observationally by Penzias and Wilson (1965), who measured a signal distributed isotropically over the complete sky, corresponding to a black-body radiation of temperature 3.5K. However, space-probe based investigations by the COBE, WMAP and recently Planck missions with improved resolution revealed the most striking feature of the CMB: on large scales it is isotropic with a temperature of 2.7K, however on small scales it exhibits minor temperature fluctuations. These fluctuations originate from the BAO right before the recombination epoch and directly map the physical conditions of the Universe at the time of recombination. The observed fluctuations in the CMB imply a scale for the initial density fluctuations in the Universe. A map of the temperature fluctuations observed by Planck is shown in Fig. 1.3. It clearly shows the temperature fluctuations on the order of μK

From the temperature fluctuations it is possible to determine the power spectrum to describe the power of the fluctuation on different spatial scales. Fig. 1.4 shows the power spectrum as observed by the Planck mission (red dots) in comparison to the best fitting ΛCDM model (blue curve). Each peak in the power spectrum represent a different oscillation state of the baryonic matter. The height and the position of the peaks can be used to constrain the cosmological parameters in the evolution equation for the scale factor (Eq. 1.4).

The general growth of density perturbations after decoupling from the radiation field can be modelled with the methods of perturbation theory. The fundamental equations governing

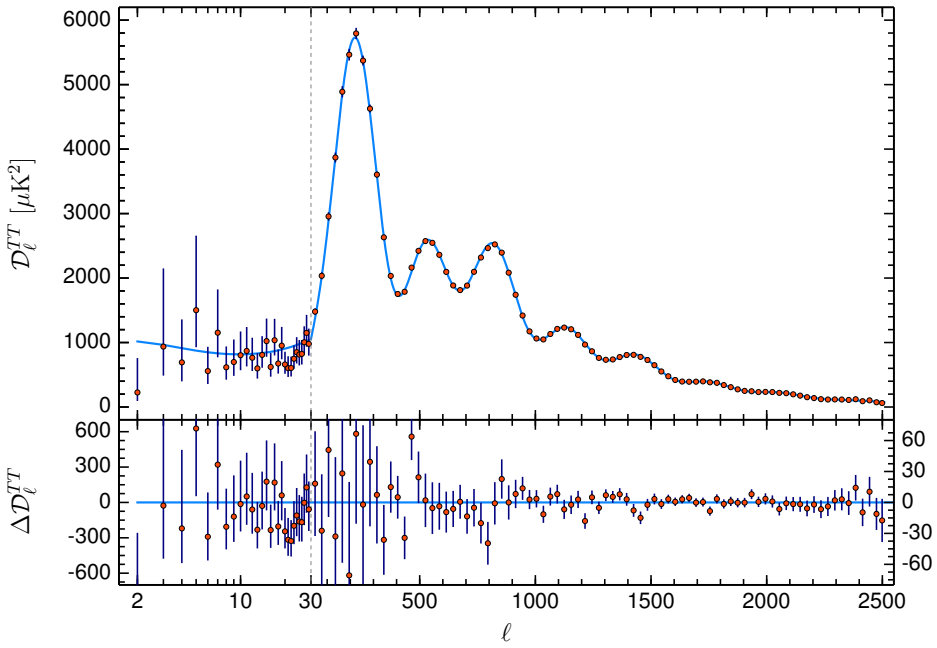

Figure 1.4: The power spectrum as observed by the Planck mission taken from Planck Collaboration et al. (2018). *Upper Panel:* The observed power spectrum (red dots) in comparison to the best fitting ΛCDM model (blue curve). *Lower Panel:* Residuals from the best fitting ΛCDM model with error bars marking the 1σ confidence region.

fluid motions in a self-consistent potential are the *Euler Equation* and the *Poisson Equation*

$$\begin{aligned} \frac{\partial \rho}{\partial t} + \nabla \cdot (\rho \cdot \vec{v}) &= 0 \\ \frac{\partial \vec{v}}{\partial t} + (\vec{v} \cdot \nabla) \cdot \vec{v} + \frac{1}{\rho} \nabla p &= -\nabla \Phi \\ \nabla^2 \Phi &= 4\pi G \rho. \end{aligned} \tag{1.6}$$

The perturbation field is commonly parameterised by the density contrast with respect to the background density of the Universe $\overline{\rho(t)}$

$$\delta(\vec{x}, t) = \frac{\rho(\vec{x}, t) - \overline{\rho(t)}}{\overline{\rho(t)}}. \tag{1.7}$$

One can show that the equation describing the evolution of the density perturbation in the linear regime (small perturbations) is given by

$$\ddot{\delta}(\vec{x}, t) + 2\frac{\dot{a(t)}}{a(t)} \dot{\delta}(\vec{x}, t) = 4\pi G \overline{\rho(t)} \delta(\vec{x}, t). \tag{1.8}$$

In general this equation has a growing and a decaying solution, however for the long term evolution only the growing mode is relevant. From the solution it becomes clear that the expansion of the Universe slows down the otherwise exponential growth of the perturbations.

After some time, when the density contrast approaches unity ($|\delta| \sim 1$), the linear assumption is not valid anymore and the linear framework breaks down. At this point the density

perturbations decouple from the background expansion and over-dense regions will expand slower due to the effect of self-gravity. The further evolution of structure formation is highly non-linear and in general can only be studied numerically.

Within the ΛCDM paradigm the evolution of the baryonic matter on large scales since recombination is at first dominated by the gravitational attraction of the dark matter. However, in contrast to dark matter, gas is able to effectively radiate away energy and redistribute angular momentum (Binney, 1977; Rees and Ostriker, 1977). Therefore, it can cool to the centre of the of the dark matter halos to form the first proto-galaxies (Nilsson et al., 2006). Ongoing gas accretion increases the density in the centre and therefore provides the fuel for star formation. Due to self gravity cold, dens gas clouds fragment to form high-density cores that eventually form stars. The further evolution of the baryonic matter is determined by the complex interplay between several feedback mechanisms. Supernovae explosions and active galactic nuclei can produce enormous amounts of energy which heat the surrounding gas preventing gas from collapsing and forming stars. Furthermore, the growing enrichment of the gas with elements heavier than hydrogen and helium (metals) enables the gas to cool via metal-line cooling, and therefore drastically changes its cooling efficiency. The interplay of these processes significantly influence the star formation properties of the gas and therefore the star formation history of galaxies.

These baryonic processes occur within the background of the hierarchical growth of the dark matter halos to form even larger bound structures by merging, resulting in the 'bottom-up' scenario (White and Rees, 1978). As the progenitor dark matter halos contain galaxies in their centre the galaxies also merge as a result of the violent relaxation process to form a new galaxy. Furthermore, environmental processes during the merging process, as ram-pressure and tidal stripping, strongly influence the properties of the descendant galaxy. These processes are discussed in detail in Sec. 1.3 and 2.2.

1.3 Galaxy Evolution Down to Low Redshift

In the previous section the emergence of structure in the Universe towards the formation of proto-galaxies containing the first population of stars against the background of hierarchical structure growth is described. The present-day properties of galaxies, outlined in Sec. 1.1, however, are determined by a complex interplay between internal processes, such as star formation and regulative feedback, and environmental processes acting on the galaxy during its evolution.

A general two-phase picture of galaxy formation for $z \lesssim 3.5$ has been proposed by Oser et al. (2010) who investigated zoom-in simulations of 39 galaxies in a fully cosmological environment. In a first, rapid phase smooth cold gas gets accreted onto the halo centre through gas flows and clumpy accretion. Since massive galaxies are surrounded by a hot gaseous halo, an efficient mechanism to funnel cold gas to the centre are cold streams which are narrow pipelines of smooth and clumpy cold gas reaching from the cosmic web directly into the galactic centre, providing the fuel for high star formation rates (Dekel et al., 2009). The accretion timescales for this "cold mode" are much shorter than for the "hot mode", in which the gas initially is shock heated to the virial temperature of the surrounding hot halo. Stars that are formed from gas within the galaxy are called "in-situ". However, as the galaxies undergo substantial mass growth driven by internal star formation feedback from black hole growth, stellar winds, and supernovae suppress star formation and heat the surrounding halo,

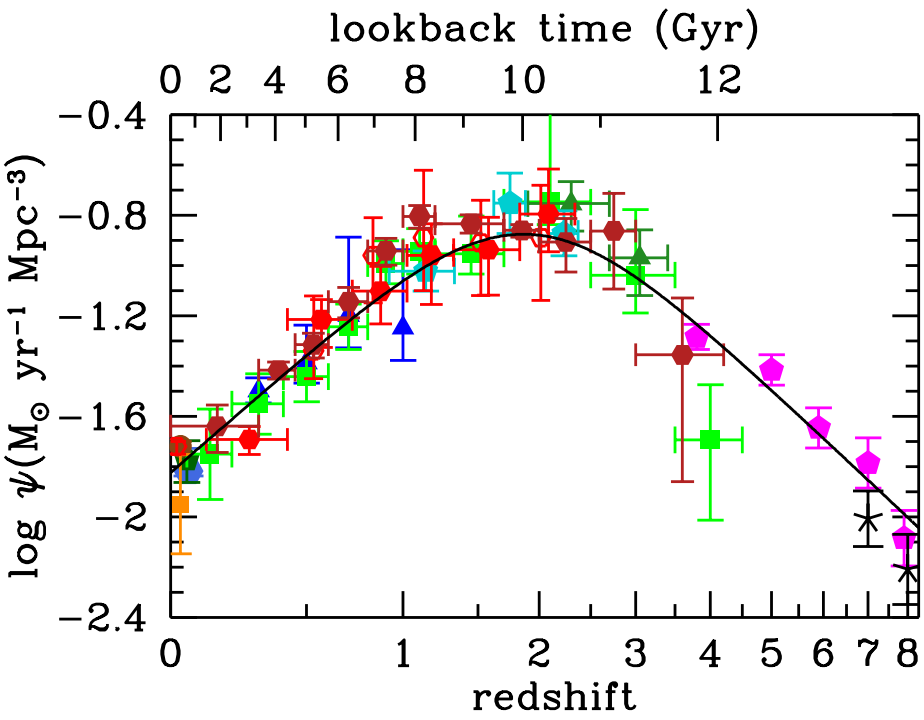

Figure 1.5: Fig. 9 taken from Madau and Dickinson (2014). Evolution of cosmic star formation rate density from FUV+IR rest-frame measurements.

cutting of the gas supply via the cold mode. Therefore, in a second subsequent phase galaxies grow in mass primarily by accretion of stars through merger events. Stars accreted in this manner are called "ex-situ" stars, since they have been formed in a different galaxy and only added to the galaxy later on. As the dominant mechanism driving galaxy formation in this low redshifts phase, galaxy mergers have a major influence on the morphology of galaxies. Especially in the context of ETG formation, various simulations showed that mergers of two late-type galaxies can produce ETGs (Toomre, 1977; Gerhard, 1981; Hernquist, 1992; Barnes and Hernquist, 1996; Burkert and Naab, 2003). However, not only the morphology is affected but also kinematical features such as kinematically distinct or counter-rotating cores can be formed in this manner (e.g. Hoffman et al., 2010; Bois et al., 2011; Tsatsi et al., 2015; Schulze et al., 2017).

The global effect of this two phase picture is directly reflected in the evolution of the cosmic star formation rate density. The evolution of the star formation density measured from different wave bands is shown in Fig. 1.5 indicating an increase of star formation activity until it peaks at $z \sim 2$. At this stage, quiescent galaxies have already formed, however, the majority of galaxies are gas-rich and actively forming stars (Brammer et al., 2011; van de Sande et al., 2013; Marsan et al., 2015). In the range of $0 < z < 2$ the star formation density decreases, building up the class of quiescent galaxies. Hence, in the vicinity of the maximum star formation a physical mechanism is triggered driving galaxies towards the red sequence. In fact, alongside internal feedback it is a complex interplay of various effects which quench the star formation inside galaxies, such as stripping, feedback, strangulation, and merging (Peng et al., 2010, 2012).

While this two-phase picture provides a general framework for the mass growth of galaxies the detailed mechanisms acting on a galaxy during its evolution and how they manifest in the present-day properties of galaxies is not considered in detail. Therefore, in the following an overview over the main physical processes relevant in the $z < 2$ evolution of galaxies is given.

As a result of the hierarchical structure formation process in the Universe, outlined in Sec. 1.2.3, galaxies reside in different environments. The densest environments are *Galaxy Clusters* which typically form at the intersections of cosmic filaments. Clusters can host thousands of galaxies and have typical masses of $M_{\rm tot} > 10^{14} M_{\odot}$ up to *Superclusters* with masses of $10^{17} M_{\odot}$. They generally feature a massive *Brightest-Cluster Galaxy* (BCG) at the centre which has an diffuse and extended outer envelope. Due to the special location within the cluster, BCGs exhibit slightly different properties than non-BCG galaxies, e.g. with regard to scaling relations (e.g. see Kluge et al., 2019). Their visible envelope, or *Intracluster Light* (ICL), is believed to consist of stars that have been stripped from galaxies within the halo (Gallagher and Ostriker, 1972; Merritt, 1983; Murante et al., 2004; Schulze et al., 2020). Another significant component of Clusters is the *Intracluster Medium* (ICM) that permeates the halo. The ICM is detectable by a X-Ray halo emitted by fully ionised gas of temperatures in the range 10^7-10^8K via thermal Bremsstrahlung (Mo et al., 2010, p. 69). The total mass of the hot X-Ray emitting gas in the halo has been found to be considerably larger than the total stellar mass in the halo (Mo et al., 2010, pp. 69-70). In the total halo mass range $10^{13} < M_{\rm tot} < 10^{14} M_{\odot}$ the structure is commonly denoted as a *Galaxy Group*, which consists of at least three galaxies up to a few hundred.

The specific environment a galaxy resides in has substantial impact on its evolution. An observational results that highlights the significance of environmental processes is the *Morphology-Density Relation*. It states that the fraction of ETGs rises significantly with increasing environmental density (Dressler, 1980; Goto et al., 2003). Moreover, denser environments harbour galaxies that are on average more massive, redder, more concentrated, less gas-rich, and less star forming (Kauffmann et al., 2004; Baldry et al., 2006; Weinmann et al., 2006). More recently, several studies have found evidence for a *Kinematics Morphology-Density Relation*, relating the environment to kinematic properties of galaxies (Cappellari et al., 2011b; D'Eugenio et al., 2013; Houghton et al., 2013; Fogarty et al., 2014). They show that the fraction of slow rotating galaxies does not depend strongly on the global environment, however within the clusters this fraction is larger in regions with higher local density. Brough et al. (2017) argues that this relation is driven by mass segregation where slow rotating galaxies form in groups and later on merge with the cluster and sink to the centre due to dynamical friction. Therefore, also the kinematic properties of galaxies are effected by the environment and the related physical processes. In the following a brief overview over the relevant processes acting on galaxies in the cluster and group environment is given. Most of these processes are only relevant for the galaxies in the halo, i.e. not the BCG, which will be refer to as satellites.

One of the most important processes that impacts the dynamics of the satellites is *Dynamical Friction*. This process generally occurs when a massive particle of mass $M_{\rm S}$ moves through a large system of field particles of mass m with $m \ll M_{\rm S}$ under the influence of gravity. The interaction between the massive particle and the field particles causes exchange of energy and momentum with a net tendency for the massive particle to lose energy and momentum. An intuitive way to think about Dynamical Friction is that the massive moving particle perturbs the field particles to form a over-dense wake behind itself and as a result slows down. The drag force on the massive particle has first been estimated by Chandrasekhar (1943) (see also

Mo et al., 2010, pp. 556ff). In a Cluster/Group environment this effect causes satellites to lose energy and momentum and therefore sink to the centre of the potential and eventually to merge with the central galaxy, a process known as *Galactic Cannibalism*. Another effect of Dynamical Friction is the mass segregation of galaxies in the halo. For a simplified model one can estimate the dynamical friction time t_{df}

$$t_{\mathrm{df}} \approx \frac{1.17}{\ln\left(\frac{M_{\mathrm{h}}}{M_{\mathrm{S}}}\right)} \left(\frac{M_{\mathrm{h}}}{M_{\mathrm{S}}}\right) \frac{1}{10H(z)} \tag{1.9}$$

which is the time a satellite of mass M_{S} needs to sink from the edge of the halo of mass M_{h} to the centre due to Dynamical friction. Hence, more massive satellites have lower t_{df} tending to move closer to the halo centre.

The velocities of satellites in a cluster are typically of the order of the velocity dispersion ($\sim$ 1000km/s) of the cluster and hence too high for two galaxies to get captured and subsequently merge. Hence, interactions between member galaxies and substructures are generally high-speed with a low probability of actual merging. The cumulative effect of these high-speed encounters is called *Galaxy Harassment*. During such an encounter orbital energy gets transformed into internal energy heating the galaxy and causing the galaxy to relax into a less bound state after the encounter via the relaxation processes outlined in Sec. 2.2. Thus the galaxy is more susceptible to disruptions and *Tidal Stripping* of its stars in the cluster outskirts, due to the halo potential, forming tidal streams and tails that feed the ICL (Mo et al., 2010, p. 569). Depending on the mass-ratio and the orbit of the interacting systems this can lead to a complete dispersion of the satellite galaxy in the halo. The radial range where the mass of the satellite galaxy gets deposited also strongly depends on the mass-ratio and the orbit (Amorisco, 2017; Karademir et al., 2019). This topic will be discussed in detail in Chap. 6.

Apart from these purely collisionless stellar processes, there are also environmental processes that predominately act on the gaseous component. The most prominent is *Ram-Pressure Stripping*. This process occurs when a satellite is moving within the halo of a cluster/group and the gas associated with the galaxy experiences a ram-pressure from the ICM gas. If the ram-pressure is strong enough to overcome the potential of the satellite it removes the gas from the satellite especially in the less bound outskirts of the satellite. This mechanism has first been discussed by Gunn and Gott (1972). Ram-Pressure Stripping is of special importance for spiral galaxies which contain a large amount of cold gas that is fuelling star formation. The stripping of the cold gas causes the star formation to cease and eventually quench the galaxy (see e.g. Jaffé et al., 2015). Therefore, Ram-Pressure Stripping is often employed to explain the lack of star-forming galaxies in dens environments. A closely related quenching mechanism is *Strangulation*. In a dense environment galaxies can get cut of from their gas supply by the removal of the surrounding gas that fuels star formation either by tides or ram-pressure. In the centre star formation pursues until the internal gas reservoir is depleted (Larson et al., 1980; Kawata and Mulchaey, 2008; Peng et al., 2015). In contrast to Ram-Pressure Stripping, which quenches star formation rather rapidly, this effect decreases the star formation rate gradually.

The most violent and unpredictable interaction between a galaxy and its environment are *mergers* with another galaxy. In the case of low enough orbital energies two encountering galaxies get captured and merge to form a new galaxy. In this process orbital energy of the progenitors gets transferred into internal energy of the descendant. The resulting system will

afterwards relax via violent relaxation and phase mixing (see Sec. 2.2). The properties of the remnant mainly depends on the mass-ratio, morphologies, and the gas-fraction of the progenitors as well as the specific orbital configuration. Merger events are roughly distinguished into wet mergers, involving a large amount of gas, and dry mergers involving only little to no gas. Apart from changing the orbital configuration of the stars within the remnant, mergers can also trigger significant Starbursts and enhanced AGN activity that considerably influences the gaseous component (Barnes and Hernquist, 1991; Mihos and Hernquist, 1996; Lotz et al., 2020). Furthermore, mergers are considered the be the most important effect in the morphological transformation from LTGs to ETGs (Gerhard, 1981; Burkert and Naab, 2003). The effect of merging on the stellar kinematics and how it can be used to constrain the accretion history of galaxies will be discussed in detail in the main body of this thesis.

Alongside the relatively violent environmental processes described in the previous, internal secular processes can also evolve the structure of galaxies. Secular evolution is driven by processes acting on long timescales typically longer than the crossing time of the galaxy. According to Kormendy and Kennicutt (2004) secular evolution requires a driving mechanism such as a bar or a global spiral structure, and therefore is more important for the evolution of LTGs than for ETGs. Secular processes are able to redistribute physical quantities such as matter, angular momentum and energy within the system. One of the most prominent effects of secular evolution is the formation of pseudobulges, also referred to as disc-like bulges or discy pseudobulges. In contrasts to classical bulges pseudobulges are believed to form internally from gas driven to the centre by the bar, typically having a highly flattened geometry and disk-like stellar kinematics (Kormendy and Illingworth, 1982; Kormendy, 1993; Kormendy and Kennicutt, 2004; Fabricius et al., 2012, and references therein). Since state-of-the-art cosmological simulations, as the *Magneticum* simulation used in this study, are not able to properly resolve secular evolution and its impact on the global stellar kinematics a detailed discussion of this topic is omitted here.

Chapter 2

Fundamentals of Stellar Dynamics in Galaxies

2.1 Basic Equations of Stellar Dynamics in Galaxies

Galaxies in the Universe represent large systems typically consisting of $\sim 10^{11}$ stellar particles. Therefore, galaxies are systems that are described by the methods of statistical mechanics. Once decoupled from the hydrodynamics the stellar dynamics are solely determined by the gravitational force between them, the dark matter, the gas and potential external gravitational forces from the environment. The long-range nature of the gravitational force is fundamentally different to the short-range forces acting in other thermodynamic systems, as for example molecules in a box. For systems resembling realistic galaxies the cumulative effect of gravitational two-body interactions between stars is negligible which justifies the assumption of a collisionless system in which the stars move in the potential of a smooth mass distribution, rather than in a collection of individual stars. This is reflected in the relaxation times in galaxies, i.e. the time after which two-body interaction become significant, which are larger than the age of the Universe. In this section the basic equations that govern stellar dynamics in galaxies are derived and it is shown how to adapt them to be applicable to modern observational data, provided by Integral-Field Spectrographs. The derivations in this chapter closely follow Binney and Tremaine (2008) and Mo et al. (2010).

2.1.1 The Collisionless Boltzmann Equation

The theoretical equation describing classical collisionless many body systems in a statistical manner is the *collisionless Boltzmann Equation* (CBE) or Vlasov's equation. Rather than following the orbits of individual stars, it describes the temporal evolution of the distribution function $f(\vec{x}, \vec{v}, t)$ (DF) which is a function in six-dimensional phase-space of positions $\vec{x}$ and velocities $\vec{v}$. Here $f(\vec{x}, \vec{v}, t) d^3\vec{x} d^3\vec{v}$ determines the number of particles occupying the phase-space volume $d^3\vec{x}\ d^3\vec{v}$ around $\vec{x}$ and $\vec{v}$ at time t.

Similar to the conservation of mass in a fluid, which manifests in the continuity equation, $f(\vec{x}, \vec{v}, t)$ is conserved locally leading to the CBE:

$$\frac{\partial f}{\partial t} + \vec{v} \cdot \vec{\nabla} f - \vec{\nabla}\Phi \cdot \frac{\partial f}{\partial \vec{v}} = 0, \tag{2.1}$$

where Φ is the potential of the galaxy and $d\vec{v}/dt = \vec{F}/m = -\vec{\nabla}\Phi$ is used. Solving the partial

differential equation Eq. 2.1 yields the DF, and therefore the statistical temporal behaviour of the system in phase space. The CBE is the fundamental equation of stellar dynamics.

Together with the Poisson-Equation

$$\nabla^2\Phi = 4\pi G\rho = 4\pi G \int f \; d^3\vec{v}, \tag{2.2}$$

which connects the density $\rho(\vec{x})$ and $\Phi(\vec{x})$, Eq. 2.1 represents a complete system that can in principle be solved self-consistently. Under the assumption of a continuous $\rho(\vec{x})$ and therefore $\Phi(\vec{x})$ the only meaningful interpretation of f is that of a probability-density comparable to the wave function in quantum mechanics. In this picture $f(\vec{x},\vec{v},t)$ gives the the probability to find a star at the phase-space position $(\vec{x},\vec{v})$ at time t.

2.1.2 The Jeans Equations

While it is virtually impossible to solve Eq. 2.1 to recover $f(\vec{x},\vec{v},t)$ for realistic astrophysical systems, it is still possible to gain meaningful insights by calculating relations for moments of quantities as for example the velocity moments. Focusing on velocity moments is of high interest, since they can be observed from the spectra of galaxies.

Relations for the velocity moments of f are obtained by multiplying Eq. 2.1 by powers of the velocity and then integrating over all velocities. The general form is given by

$$\int v_i^l v_j^m v_k^n \; \frac{\partial f}{\partial t} \; d^3\vec{v} + \int v_i^l v_j^m v_k^n \; \vec{v}\cdot\vec{\nabla} f \; d^3\vec{v} - \int v_i^l v_j^m v_k^n \; \vec{\nabla}\Phi \cdot \frac{\partial f}{\partial \vec{v}} \; d^3\vec{v} = 0, \tag{2.3}$$

where (l,m,n) are integer exponents and (i,j,k) refer to the three coordinates. Taking the partial derivatives $\partial/\partial t$ and $\partial/\partial x$ in front of the integral and implying the summation convention ($\alpha = 1,2,3$) this is equivalent to

$$\frac{\partial}{\partial t}\int v_i^l v_j^m v_k^n f d^3\vec{v} + \frac{\partial}{\partial x_\alpha}\int v_i^l v_j^m v_k^n v_\alpha f d^3\vec{v} - \frac{\partial\Phi}{\partial x_\alpha}\int v_i^l v_j^m v_k^n \frac{\partial f}{\partial v_\alpha} d^3\vec{v} = 0. \tag{2.4}$$

Let's consider the zeroth moment $(l,m,n) = (0,0,0)$ and recall that $\rho(\vec{x}) = \int f(\vec{x},\vec{v})d^3\vec{v}$ yields

$$\frac{\partial\rho}{\partial t} + \frac{\partial(\rho\overline{v_\alpha})}{\partial x_\alpha} = 0, \tag{2.5}$$

where the divergence theorem is used in the last term and the property that $f \to 0$ for $|v| \to \infty$. Furthermore, the following notation is introduced

$$\overline{v_i} = \overline{v_i(\vec{x},t)} = \int v_i(\vec{x}) f(\vec{x},\vec{v},t) d^3\vec{v}. \tag{2.6}$$

Therefore, $\overline{v_i}$ is the local expectation value of v_i at time t. Eq. 2.5 is the so called *Continuity Equation*.

From the first-order moments $(l,m,n) = (1,0,0)$ and permutations the three *Momentum-Equations* are obtained

$$\frac{\partial(\rho\overline{v_j})}{\partial t} + \frac{\partial(\rho\overline{v_\alpha v_j})}{\partial x_\alpha} + \rho\frac{\partial\Phi}{\partial x_j} = 0 \tag{2.7}$$

for $j = 1, 2, 3$. Subtracting $\overline{v_j}$ times the continuity equation from the *Momentum-Equations* yields the famous set of *Jeans-Equations*

$$\rho \frac{\overline{v_j}}{\partial t} + \rho \overline{v_\alpha} \frac{\partial \overline{v_j}}{\partial x_\alpha} = -\rho \frac{\partial \Phi}{\partial x_j} - \frac{\partial (\rho \sigma_{\alpha j}^2)}{\partial x_\alpha}, \tag{2.8}$$

where the stress-tensor $\sigma_{\alpha j}$ is defined as

$$\sigma_{\alpha j}^2 = \overline{v_\alpha v_j} - \overline{v_\alpha}\ \overline{v_j}. \tag{2.9}$$

Therefore, $\sigma_{\alpha j}^2$ measures the quadratic deviations of the velocities from their expectation value. It is manifestly symmetric ($\sigma_{\alpha j} = \sigma_{j\alpha}$).

Eq. 2.8 was first applied in the context of stellar dynamics by James Jeans in 1915 (Jeans, 1915). In this general form the Jeans-Equations have the 3 streaming motions $\overline{v_j}$ and the 6 components of the stress-tensor as unknowns. Hence, they do not form a closed set of equations, requiring to make further assumption. Considering higher-order moment, and therefore more equations, also increases the number of unknowns and hence does not close the set of equations.

A very important concept in the context of solving the CBE are so-called integrals of motion. An integral of motion is any phase-space function $I[\vec{x}(t), \vec{v}(t)]$ that is constant along any orbit:

$$\frac{dI}{dt} = \frac{\partial I}{\partial \vec{x}} \frac{\partial \vec{x}}{\partial t} + \frac{\partial I}{\partial \vec{v}} \frac{\partial \vec{v}}{\partial t} = \vec{v}\ \vec{\nabla} I - \vec{\nabla}\Phi \frac{\partial I}{\partial \vec{v}} = 0. \tag{2.10}$$

Comparing this condition to Eq. 2.1, it is immediately clear that $I[\vec{x}(t), \vec{v}(t)]$ is a solution of the steady-state CBE ($\partial f / \partial t = 0$). This leads to the two Jeans Theorems (Binney and Tremaine, 2008, pp. 283):

- *Jeans Theorem:* Any steady-state solution of the collisionless Boltzmann equation depends on the phase-space coordinates only through integrals of motion in the given potential, and any function of the integrals yields a steady-state solution of the CBE.
- *Strong Jeans Theorem:* The DF of a steady-state stellar system in which almost all orbits are regular with non-resonant frequencies may be presumed of be a function only of three independent isolating integrals of motion.

From these theorem one obtains first constraints on $f(\vec{x}, \vec{v})$ and on the velocity moments to reduce the number of unknowns in Eq. 2.8. In a axisymmetric potential for example the total energy E and the z-component of the angular momentum L_z are integrals of motion, hence $f = f(E, L_z)$. It is straight forward to show, that in this case $\overline{v_R} = \overline{v_z} = 0$ in cylindrical coordinates (see Binney and Tremaine, 2008, p.287). In realistic systems it is in general necessary to make further assumption to be able to solve Eq. 2.8. See for example Bacon (1985); van de Ven et al. (2003); Cappellari (2008, 2012) on how to model the kinematics of axisymmetric stellar systems based on the Jeans formalism.

2.1.3 The Virial Equations

From the CBE it is possible to derive another fundamental set of equations relating morphological and kinematic quantities of galaxies called the *Virial-Equations* or *Virial Theorem*.

Starting from the Momentum-Equations and multiplying Eq. 2.7 by x_k and integrating over real space yields

$$\frac{\partial}{\partial t}\int \rho x_k \overline{v_j} d^3\vec{x} = -\int x_k \frac{\partial \rho \overline{v_\alpha v_j}}{\partial x_\alpha} d^3\vec{x} - \int \rho x_k \frac{\partial \Phi}{\partial x_j} d^3\vec{x}. \tag{2.11}$$

Using integration by parts on the first term on the right gives

$$\int x_k \frac{\partial \rho \overline{v_\alpha v_j}}{\partial x_\alpha} d^3\vec{x} = -\int \rho \overline{v_k v_j} d^3\vec{x} = -2\mathbf{K}_{kj}, \tag{2.12}$$

where K_{kj} is the *Kinetic Energy Tensor* and it is assumed that $\rho(\vec{x}) \to 0$ for $|\vec{x}| \to \infty$. Physically, this assumptions means that all mass outside the considered system is negligible which lets the surface term go to zero.

It is customary to use the definition of the *Stress Tensor* to split $\mathbf{K}_{kj}$ into contributions from random and ordered motion

$$\mathbf{K}_{kj} = \mathbf{T}_{kj} + \frac{1}{2}\mathbf{\Pi}_{kj} \tag{2.13}$$

with

$$\mathbf{T}_{kj} = \frac{1}{2}\int \rho \overline{v_k}\ \overline{v_j} d^3\vec{x} \qquad\qquad \mathbf{\Pi}_{kj} = \int \rho \sigma_{kj}^2 d^3\vec{x}. \tag{2.14}$$

Furthermore, the Chandrasekhar *Potential Energy Tensor* $\mathbf{W}_{kj}$ and the *Moment of Inertia Tensor* I_{kj} are introduced:

$$\mathbf{W}_{kj} = -\int \rho x_k \frac{\partial \Phi}{\partial x_j} d^3\vec{x} \qquad\qquad \mathbf{I}_{kj} = \int \rho x_k x_j d^3\vec{x}. \tag{2.15}$$

Eq. 2.11 then becomes

$$\frac{1}{2}\frac{d^2\mathbf{I}_{kj}}{dt^2} = 2\mathbf{T}_{kj} + \mathbf{\Pi}_{kj} + \mathbf{W}_{kj}, \tag{2.16}$$

known as the *Tensor Virial Theorem*, relating kinematic and morphological properties of a collisionless gravitating system. The more prevalent *Scalar Virial Theorem* can be obtained by calculating the trace of both sides of Eq. 2.16

$$\frac{1}{2}\frac{d^2 I}{dt^2} = 2K + W, \tag{2.17}$$

where

$$\begin{aligned} I &= tr(I_{kj}) = \int \rho \overline{r^2} d^3\vec{x}, \\ K &= tr(K_{kj}) = \frac{1}{2}\int \rho \overline{v^2} d^3\vec{x}, \\ W &= tr(W_{kj}) = \frac{1}{2}\int \rho \Phi d^3\vec{x}. \end{aligned} \tag{2.18}$$

Here, K is the total kinetic energy of the system and W the total potential energy. Defining the *Total Energy* $E = K + W$ and considering a static system with $d^2I/dt^2 = 0$ the *Scalar Virial Theorem* in its most known form is obtained

$$E = -K = \frac{W}{2}. \tag{2.19}$$

2.1.4 Applying the Tensor Virial Theorem to Observed Data

In the previous sections the theoretical equations describing the connection between global kinematic and morphological quantities are derived. However, direct observations are limited to a certain projection on the sky from which only projected quantities can be extracted. Another observational limitation is the restricted radial extend to where kinematic quantities can be measured due to the decreasing stellar luminosity at larger radii. Therefore, it is necessary to adapt Eq. 2.16 and to make certain assumptions to obtain a relation for observable quantities which are essential to interpret IFS observations. The theoretical framework for that is provided by Binney (2005) which will be followed closely in the following derivation (see also Cappellari et al., 2007).

Observations are able to provide the line-of-sight velocity distribution LOSVD F

$$F(\mathbf{x}_\perp, v_\parallel) = \frac{1}{\Sigma(\mathbf{x}_\perp)} \int dx_\parallel \int f d^2\mathbf{v}_\perp, \tag{2.20}$$

where $\perp$ and $\parallel$ denotes the coordinates perpendicular and parallel to the line-of-sight and

$$\Sigma(\mathbf{x}_\perp) = \int \rho(\vec{x}) dx_\parallel \tag{2.21}$$

is the surface density. In this definition $F(\mathbf{x}_\perp, v_\parallel)$ gives the probability to find a star at the projected phase-space position $(\mathbf{x}_\perp, v_\parallel)$.

Introducing the notation for any function $g(v_\parallel)$

$$\widetilde{g_\parallel}(\mathbf{x}_\perp) = \int g_\parallel F(\mathbf{x}_\perp, v_\parallel) dv_\parallel = \frac{1}{\Sigma(\mathbf{x}_\perp)} \int g_\parallel f(\vec{x}, \vec{v}, t) d^3\vec{v} dx_\parallel \tag{2.22}$$

yields

$$\sigma_\parallel^2(\mathbf{x}_\perp) = \int (v_\parallel - \widetilde{v_\parallel})^2 F(\mathbf{x}_\perp, v_\parallel) dv_\parallel = \widetilde{v_\parallel^2} - \widetilde{v_\parallel}^2. \tag{2.23}$$

Using this relation, the *kinetic energy tensor* $\mathbf{K}$ can be related to the projected observable quantities

$$\int \Sigma(\sigma_\parallel^2 + \widetilde{v_\parallel}^2) d^2\mathbf{x}_\perp = 2\vec{s}\,\mathbf{K}\,\vec{s}, \tag{2.24}$$

where $\vec{s}$ is the unit vector along the line-of-sight. Now consider the case of a axisymmetric static galaxy rotating around its symmetry axis (z-axis) that is observed in the edge-on projection. The x-axis is chosen to be parallel to the line-of-sight. Eq. 2.16 for a static system simplifies considerably under these assumption leaving only two non-trivial equations

$$\begin{aligned} 2K_{xx} + W_{xx} &= 0 \\ 2K_{zz} + W_{zz} &= 0. \end{aligned} \tag{2.25}$$

Together with Eq. 2.24 this gives

$$\frac{W_{xx}}{W_{zz}} = \frac{M\left(\langle\sigma_\parallel^2\rangle + \langle\widetilde{v_\parallel}^2\rangle\right)}{\Pi_{zz}}, \tag{2.26}$$

where M is the mass of the galaxy and the weighted sky-average of an arbitrary function $q(\mathbf{x}_\perp)$ on the sky is introduced

$$\langle q \rangle = \frac{1}{M} \int q \Sigma d^2\mathbf{x}_\perp. \tag{2.27}$$

Defining the global *Anisotropy* parameter δ which measures the degree of deviation from isotropy as

$$\Pi_{zz} = (1-\delta)\Pi_{xx}, \tag{2.28}$$

it is possible to eliminate Π_{zz} from Eq. 2.26 yielding

$$\frac{\langle \widetilde{v}_{\parallel}{}^2 \rangle}{\langle \sigma_{\parallel}^2 \rangle} = \frac{(1-\delta)W_{xx}/W_{zz} - 1}{\alpha(1-\delta)W_{xx}/W_{zz} + 1}. \tag{2.29}$$

Here, α is a dimensionless parameter only depending on the luminosity profile and the shape of the rotation curve, however not on the amplitude of the rotation curve. It measures the amount of shear in the streaming velocity. In general, α is in the range of $0.05 - 0.2$ (Binney, 2005). In practice, Cappellari et al. (2007) adopted a value of $\alpha = 0.15$ to apply this theoretical framework to observed data. The ratio $\langle \widetilde{v}_{\parallel}{}^2 \rangle / \langle \sigma_{\parallel}^2 \rangle$ quantifies the amount of streaming motion to random motion along the line-of-sight. For convenience this quantity will be denoted as (V/σ) in the further course.

In the form of Eq. 2.29 the left side of the TVT contains only quantities that can be observed with integral field spectroscopy, while the right side contains α, δ and the ratio of the components of the *Potential Energy Tensor*. The shape parameter W_{xx}/W_{zz} can, in principle, be determined from photometry under the assumption that the light traces mass sufficiently (e.g. Binney and Strimpel, 1978). Hence, Eq. 2.29 is a powerful tool to study the connection between kinematics, morphology and the orbital structure of observed galaxies.

The main problem arising from Eq. 2.29 is the actual determination of W_{xx}/W_{zz}. This can be simplified considerably by assuming that iso-density surfaces have a constant ellipticity ϵ. Therefore, the model is not applicable to galaxies with morphological twists or radially changing ϵ. However, if the assumption is valid the components of $\mathbf{W}$ depend only on the galaxy's ellipticity (Roberts, 1962; Binney and Tremaine, 2008, p. 95). Using the formulas given in Binney and Tremaine (2008, p. 90) and substituting into Eq. 2.29 gives

$$\delta = 1 - \frac{1 + (V/\sigma)^2}{\left[1 - \alpha\,(V/\sigma)^2\right]\Omega(e)}, \tag{2.30}$$

where

$$\begin{aligned} e &= \sqrt{1-(1-\epsilon)^2} \\ \Omega(e) &= \frac{0.5\left(\arcsin(e) - e\sqrt{1-e^2}\right)}{e\sqrt{1-e^2} - (1-e^2)\arcsin(e)}. \end{aligned} \tag{2.31}$$

The final formulas are taken from Cappellari et al. (2007). Finally, Eq. 2.30 relates the observables ϵ and (V/σ) to the internal anisotropy of the galaxy under the assumption of a static axisymmetric galaxy rotating around its symmetry axis that is observed in the edge-on projection. It implies that a galaxy can be flattened by either rotation or anisotropy. This theoretical framework will be investigated in detail in Chap 4.

2.2 Dynamical Relaxation Processes in Stellar Systems

As described in the introduction, of this section there are periods in the evolution of a galaxy when it is driven out of equilibrium by external disturbances such as galaxy mergers. For an

isolated volume of gas the collisions between the particles can efficiently redistribute momentum and will lead to a Maxwellian velocity distribution. In contrast, for collisionless systems, as dark matter and stars, but also galaxies within clusters, there are different relaxation processed that drive the system towards equilibrium. Since the two-body relaxation times due to gravitational interactions in galaxies are extremely long ($\sim t_{\mathrm{Hubble}}$) this can not be the predominant relaxation process (Mo et al., 2010, p.232).

One of the most fundamental relaxation processes in galaxies is *phase mixing*. It arises from the spreading of neighbouring points in phase space due to differences in their orbital frequency. Lets consider a collection of particles, having approximately the same position and velocity, moving in a stationary potential in two dimensions. In phase space the particles will occupy a well defined volume close to each other. While the energy of individual particles is conserved, due to the small differences in orbital period the occupied phase space volume will deform until it reaches a steady state in phase space. This scenario applies in a more complex way also in three dimensions. For example in a star forming cloud where the newly formed stars are spawned on very similar orbits with only slight differences in their orbit. Due to the effect of phase mixing the stars will be distributed over the galaxy with time. Although phase mixing is a relaxation process it, in principle, is a time-reversible process, hence preserving the information about the initial conditions. However, this only holds as long as the potential is static and no external disturbances occur. Very recent results from the GAIA mission, which provided six dimensional phase-space information for millions of stars in the Milky Way, revealed that the stellar disk of the Milky Way is not in equilibrium. In particular, Antoja et al. (2018) found clear evidence for vertical phase mixing in the galactic disk caused by a perturbation between 300 and 900Myr ago (see also Khoperskov et al., 2019; Laporte et al., 2019; Li and Shen, 2020).

While isolated phase mixing in general conserves the energy of individual particles the effect of *violent relaxation* changes the energy of the particles themselves (Lynden-Bell, 1967). Let's consider a particle moving in a potential $\Phi(\vec{x}, t)$ that also depends on time. The specific energy of the particle is given by $E = \frac{1}{2} \cdot \vec{v}^2 + \Phi(\vec{x}, t)$. The total change of the Energy is then given by

$$\begin{aligned}
\frac{dE}{dt} &= \frac{\partial E}{\partial \vec{v}} \cdot \frac{d\vec{v}}{dt} + \frac{\partial E}{\partial \Phi} \cdot \frac{d\Phi}{dt} \\
&= -\vec{v} \cdot \nabla\Phi + \frac{d\Phi}{dt} \\
&= -\vec{v} \cdot \nabla\Phi + \frac{\partial \Phi}{\partial t} + \frac{\partial \Phi}{\partial \vec{x}} \cdot \frac{d\vec{x}}{dt} \\
&= -\vec{v} \cdot \nabla\Phi + \frac{\partial \Phi}{\partial t} + \vec{v} \cdot \nabla\Phi \\
&= \frac{\partial \Phi(\vec{x}, t)}{\partial t}.
\end{aligned} \tag{2.32}$$

Therefore the time dependence of the potential causes a change of the energy of the particle and hence also a change of its stable orbit. This redistribution of energy drives the system towards an equilibrium state. The exact change of energy depends on the initial position and energy of the particle and can lead to an energy gain or loss. In general, however, it leads to a larger range of accessible energies and therefore phase-space volume. Violent relaxation is a comparably fast relaxation process (Mo et al., 2010, pp. 251).

The described relaxation processes are believed to play an important role in determining the present-day dynamical and kinematic properties of galaxies. The tight scaling relations

obeyed by galaxies, e.g. Tully-Fischer relation for spiral galaxies and Farber-Jackson relation for elliptical galaxies, are directly connected to these relaxation processes. However, it is not yet understood how the initial conditions, in the case of stellar systems given by the properties of the gas from which the stars are formed, impact the relaxation process and the final equilibrium state.

Chapter 3

Numerical Simulations of Galaxy Formation

3.1 Basics of Astrophysical Numerical Simulations

The previous introduction of this thesis showed that the formation of the galaxies we observe today involves many physical processes. While the physical principles of these processes are well established, their complex interplay and the enormous size of the dynamical systems makes it impossible to obtain an exact analytic solution. Due to the development of powerful computers and numerical methods it became possible to simulate structure and galaxy formation, and therefore follow the interplay between gravitational, gas-dynamical, and radiative processes in time. Hence, numerical simulations represent a powerful tool to study galaxy formation in a realistic environment to provide meaningful interpretations and predictions for observations.

In general three types of simulations are employed to study the formation of galaxies:

- **Isolated Merger Simulations:** In this approach the isolated effects of merging, which plays an important role at lower redshift, can be studied in great detail. As one of the first simulations of this kind, Toomre and Toomre (1972) performed simulations of two colliding disk galaxies consisting of only a few hundred particles to investigate the origin of tidal tails and bridges. The initial set-up of such simulations has many free parameters that influence the properties of the remnant galaxy, e.g. is it a binary merger or a sequence of mergers of several galaxies, various orbital parameters like the relative inclination and impact parameter, and internal properties such as mass, angular momentum and gas fractions. In general many combinations of these parameters can occur in reality, defining a extremely large parameter space. Furthermore, setting up stable progenitor galaxies with the desired internal properties is not trivial. A widely used model to set-up binary merger simulations of spiral galaxies is described in Springel et al. (2005a). Due to the described characteristics, isolated merger simulations are most suitable to study specific physical processes that require high resolution and controllable conditions in statistically small samples.

- **Fully Cosmological Simulations:** While isolated merger simulations are a powerful tool to study the effect of merging, they do not account for all effects acting on a galaxy in a cosmological context. Especially further environmental effects are not taken into

account by merger simulations, e.g. tidal and ram-pressure stripping. Fully cosmological simulations, however, simulate large volumes which allow for the self-consistent formation of large-scale structure and galaxies in the realistic environment of groups and clusters. As a trade-off for the large volume, these simulations exhibit lower resolutions than merger simulations constraining the physical processes that can be investigated. Several large simulations have been performed over the past years aiming to understand structure formation and the clustering of dark matter, e.g. Millenium (Springel et al., 2005b), Millenium-II (Boylan-Kolchin et al., 2009), Horizon (Teyssier et al., 2009), and Bolshoi (Klypin et al., 2011). Due to the recent advancement of numerical methods and computational power fully hydrodynamic cosmological simulations including baryons have been conducted with a resolutions that allows to investigate internal properties of galaxies. Some exampled are Illustris (Vogelsberger et al., 2014), Horizon-AGN (Dubois et al., 2014), EAGLE (Schaye et al., 2015), *Magneticum* (used in this work), MUFASA (Davé et al., 2016), and IllustrisTNG (Springel et al., 2018).

- **Cosmological Zoom Simulations:** This method represents a hybrid between isolated simulations and fully cosmological simulations. Starting from a cosmological dark matter only simulation at $z = 0$ a region of interest, typically a large halo, is selected and re-simulated with an increased resolution, self-consistently embedded in a lower resolution large scale cosmological volume. This approach allows to investigate processes that require high resolution while also accounting for the long range gravitational force from surrounding structures, represented by the low-resolution surrounding (e.g. see Tormen et al., 1997). It is also possible to include baryons in the re-simulation to study their physics in high resolution in a cosmological context. For details on the re-simulation technique see Borgani et al. (2006); Springel et al. (2008); Oser et al. (2010); Cui et al. (2018).

The two main components that have to be treated in a astrophysical simulation is the effect of gravity and the hydrodynamics of the gaseous component. For the treatment of the hydrodynamics two competing approaches exist. Eulerian grid-based methods solve the governing equations on a structured or unstructured grid by explicitly calculating the mass, momentum and energy fluxes between grid cells. In contrast, particle based methods follow the motion of individual mass elements in the fluid. In this approach individual particles carry the properties of the fluid, e.g. density, pressure, and temperature, moving with the flow, hence sampling regions of increased density with more particles.

Astrophysical gases in simulations are typically described by an ideal inviscid gas that obeys the following equations in the Lagrangian form

$$\begin{aligned} \frac{d\rho}{dt} + \rho\vec{\nabla}\vec{v} &= 0 \\ \frac{d\vec{v}}{dt} + \frac{\vec{\nabla}P}{\rho} + \vec{\nabla}\Phi &= 0 \\ \frac{du}{dt} + \frac{P}{\rho}\vec{\nabla}\vec{v} + \frac{\Lambda(u,\rho)}{\rho} &= 0, \end{aligned} \tag{3.1}$$

which are the *Continuity Equation*, *Euler Equation*, and *First Law of Thermodynamics*, respectively. Here, $\vec{v}$ is the velocity, P is the pressure, ρ is the density, Φ is the gravitational potential, and u the specific internal energy. In this context the total derivative is

$d/dt = \partial/\partial t + \vec{v} \cdot \nabla$. $\Lambda(u, \rho)$ is the cooling function which accounts for cooling of the gas by radiative processes. Together with the equation of state

$$P = (\gamma - 1)\, \rho u, \tag{3.2}$$

where γ is the adiabatic index, Eq. 3.1 forms a closed set of equations. The aim of the hydrodynamic solver in any astrophysical simulation is to solve this set of equations with numerical methods in an computationally efficient way.

The simulations used in this work utilises the particle based approach of *Smoothed-Particle Hydrodynamics* (SPH) initially developed by Gingold and Monaghan (1977) and Lucy (1977) to solve Eq. 3.1. The basic idea of this method (following Dolag et al., 2008) is to discretise the fluid by mass elements rather than volume elements as in the Eulerian (grid-based) approach. For any field $F(\vec{x})$ one defines the smoothed version

$$\langle F(\vec{x}) \rangle = \int W(\vec{x} - \vec{x'}, h) F(\vec{x'}) d\vec{x'}, \tag{3.3}$$

where the integral runs over the full volume and W is the smoothing kernel that weights the contribution from the environment depending on the distance $(\vec{x} - \vec{x'})$. The kernel has to be normalized, i.e. $\int W(\vec{x}, h) d\vec{x} = 1$, and $W(\vec{x}, h) \to 0$ if $h \to 0$ such that $\langle F(\vec{x}) \rangle \to F(\vec{x})$.

The integral in Eq. 3.3 can be approximated by the summation over particles

$$\langle F(\vec{x_i}) \rangle = \sum_j \frac{m_j}{\rho_j} F_j W(\vec{x_i} - \vec{x_j}, h), \tag{3.4}$$

where the sum runs over all particles and m_j, ρ_j and F_j are the mass, density, and field value of the j^{th} particle. The kernel function W is usually chosen to have compact support, i.e. $W(\vec{x}, h) = 0$ for $|\vec{x}| > h$. Therefore, the sum in Eq. 3.4 runs over a finite number of neighbouring particles in a sphere with radius h. Choosing a adequate functional form of the kernel is crucial to counteract unwanted numerical effects such as to strong smoothing of shocks or the suppression of fluid mixing. Widely used kernel functions in modern simulations are for example the Wendland kernel functions (Dehnen and Aly, 2012). In practice, the density of a fluid element is estimated by

$$\rho_i = \langle \rho(\vec{x_i}) \rangle = \sum_j m_j W(\vec{x_i} - \vec{x_j}, h). \tag{3.5}$$

Estimating the pressure and the derivatives in Eqs. 3.1 in the same way yields the discretised fluid equations of SPH.

In addition to hydrodynamics, also the effect of gravity has to be treated numerically in astrophysical simulations since already the three-body problem can in general not be solved analytically. The simplest approach is to sample the mass distribution by N particles and directly sum up the gravitational forces exerted on a particle from the other particles. However, for such a direct sum approach the number of operations scales with N^2 and is therefore computationally very expensive. Hence, a range of methods have been developed to effectively calculate the gravitational force acting on a particle. The simulations analysed in this work apply a hybrid TreePM method which combines the advantages of the tree and particle-mesh methods (Xu, 1995; Bode et al., 2000; Bagla and Ray, 2003) to efficiently recover the potential from the Poisson equation.

Table 3.1: Overview of the *Magneticum Pathfinder* Simulations

	Size [Mpc/h]	Resolution	N_{Part}	m_{dm} [$\mathrm{M}_\odot$/h]	m_{gas} [$\mathrm{M}_\odot$/h]	$\epsilon_{\mathrm{dm/gas}}$ [kpc/h]	$\epsilon_{\mathrm{stars}}$ [kpc/h]
Box0	2688	mr	2×4536^3	1.3×10^{10}	2.6×10^9	10	5
Box1	896	mr	2×1526^3	1.3×10^{10}	2.6×10^9	10	5
Box2b	640	hr	2×2880^3	6.9×10^8	1.4×10^8	3.75	2
Box2	352	mr	2×594^3	1.3×10^{10}	2.6×10^9	10	5
		hr	2×1584^3	6.9×10^8	1.4×10^8	3.75	2
Box3	128	mr	2×216^3	1.3×10^{10}	2.6×10^9	10	5
		hr	2×576^3	6.9×10^8	1.4×10^8	3.75	2
		uhr	2×1536^3	3.6×10^7	7.3×10^6	1.4	0.7
Box4	48	mr	2×81^3	1.3×10^{10}	2.6×10^9	10	5
		hr	2×216^3	6.9×10^8	1.4×10^8	3.75	2
		uhr	2×576^3	3.6×10^7	7.3×10^6	1.4	0.7
Box5	18	hr	2×81^3	6.9×10^8	1.4×10^8	3.75	2
		uhr	2×216^3	3.6×10^7	7.3×10^6	1.4	0.7
		xhr	2×576^3	1.9×10^6	3.9×10^5	0.45	0.25

3.2 Set up of the Cosmological *Magneticum Pathfinder* Simulations

This section is based on parts of Schulze et al. (2020)

For our analysis we study galaxies extracted from the cosmological hydrodynamic *Magneticum*[1] *Pathfinder* simulations, which are a collection of simulations of various box-sizes and resolutions. Sizes range from 18Mpc/h to 2688Mpc/h box side length, while resolutions cover a particle mass range of $1.9 \times 10^{10} > m_{\mathrm{dm}} > 1.3 \times 10^7 M_\odot/h$ for the dark matter and $2.6 \times 10^9 > m_{\mathrm{gas}} > 3.9 \times 10^5 M_\odot/h$ for gas particles. A summary of the details of the available boxes is given in Tab. 3.1 and is visualised in Fig. 3.1. Therefore, the simulation set covers an enormous dynamical range, implementing key physical processes that allow to study cosmology and cluster physics in the lower resolution boxes as well as intragalactic physics in a cosmological environment in the higher resolution boxes.

Throughout all simulated volumes and resolutions, the simulations employ a standard ΛCDM cosmology with parameters adopted from the seven-year results of the Wilkinson Microwave Anisotropy Probe (WMAP7) (Komatsu et al., 2011), with $\Omega_{\mathrm{b}} = 0.0451$, $\Omega_{\mathrm{M}} = 0.272$ and $\Omega_\Lambda = 0.728$ for baryons, matter and dark energy, respectively. Furthermore, the Hubble parameter is $h = 0.704$ and the normalisation of the fluctuation amplitude at 8Mpc is given by $\sigma_8 = 0.809$.

[1] www.magneticum.org

The simulations were performed with the Tree/SPH code GADGET-3 (**GA**laxies with **D**ark matter and **G**as int**E**rac**T**) which is an extended version of GADGET-2 (Springel, 2005; Springel et al., 2001b), implementing updates in the SPH formulation regarding the treatment of viscosity and the used kernels (Dolag et al., 2005; Beck et al., 2016). The simulation implements state-of-the-art models for a variety of physical processes needed for the self-consistent modelling of galaxy formation. Radiative gas cooling is implemented by the cooling function Λ (see Eq. 3.1), assuming an optically thin gas in (photo-)ionisation equilibrium. The contributions from different chemical species (H, He, C, N, O, Ne, Mg, Si, S, Ca, Fe) are considered under the assumption that three-body cooling processes are negligible (Ferland et al., 1998).

Since star formation happens on spatial scales that are not resolved in the simulation a sub-resolution model for star formation and supernovae (SNe) feedback, following Springel and Hernquist (2003), is used. The model treats the interstellar medium as a two-phase medium where the gas is comprised of condensed clouds in pressure equilibrium with the ambient hot gas, and the clouds providing the material available for star formation. Furthermore, the model includes the effect of SNe feedback that heats the gas depending on the mass of the star.

According to the model by Tornatore et al. (2007) the simulations follows the detailed chemical evolution. Assuming a Chabrier initial mass function (Chabrier, 2003), it considers the energy and metals released by SNe type II, SNe type Ia and asymptotic giant branch (AGB) stars by properly accounting for the lifetimes of stars of different masses. The chemical evolution is directly coupled to the gas cooling, that depends on the metallicity, in a self-consisted manner.

Another important process for galaxy formation is the evolution and feedback from black holes (BHs) which is a key ingredient to prevent over-cooling of the gas. In the simulation this is implemented based on the model presented in Springel et al. (2005a) and Di Matteo et al. (2005), incorporating the same modifications as in Fabjan et al. (2010). According to this model BHs are treated as collisionless sink particles that can grow in mass by gas accretion from the surrounding, limited to the Eddington rate, and merging with other black holes. In addition, BHs release thermal energy to the surrounding medium which is coupled to the gas accretion rate of the BH. The gas accretion rate is estimated according to the Bondi-Hoyle model (Bondi and Hoyle, 1944; Bondi, 1952).

Furthermore, the simulation follows the thermal conduction similar to Dolag et al. (2004), but with 1/20th of the classical Spitzer value (Spitzer, 1962) motivated by full MHD simulations, including an anisotropic treatment of thermal conduction (Arth et al., 2014). For more details on the baryonic physical models we refer to Teklu et al. (2015).

The *Magneticum Pathfinder* simulations have shown to successfully reproduce, and help to interpret, various observational results, such as the pressure profiles of the intra-cluster medium (Planck Collaboration et al., 2013; McDonald et al., 2014), the predicted Zeldovich signal (Dolag et al., 2016), galaxy cluster properties (Remus et al., 2017; Lotz et al., 2019), the properties of the AGN population (Hirschmann et al., 2014; Steinborn et al., 2015, 2016, 2018), the kinematic properties of galaxies (Teklu et al., 2015; Schulze et al., 2018, 2020) and the dynamical properties of early-type galaxies (Remus et al., 2013; Teklu et al., 2017).

The galaxies used in Chaps. 4, 6, and 7 of this work are extracted from Box4, a box with a side length of 48Mpc/h at the uhr resolution level that initially contains 2×576^3 particles (gas and dark matter). The co-moving gravitational softening length for gas particles is $\epsilon_{\mathrm{gas}} = 1.4$kpc/h and $\epsilon_* = 0.7$kpc/h for stellar particles. For dark matter particles the co-moving

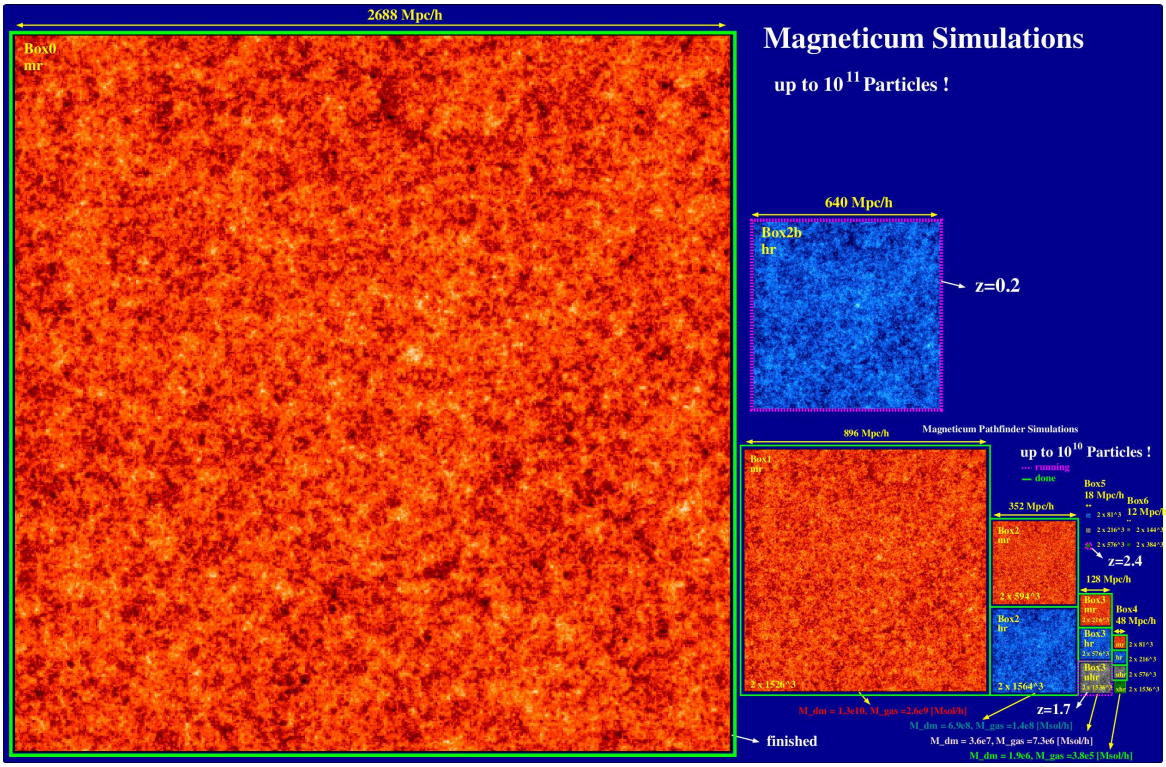

Figure 3.1: Overview over the available box sizes and resolutions in the *Magneticum Pathfinder* simulations. Courtesy of Klaus Dolag.

softening is $\epsilon_{\rm dm} = 1.4 * (1+z)$kpc/h for $z < 2$ and $\epsilon_{\rm dm} = 4.2$kpc/h for $z > 2$. The (initial) particle mass of dark matter and gas are $m_{\rm DM} = 3.6 \times 10^7 M_\odot/h$ and $m_{\rm gas} = 7.3 \times 10^6 M_\odot/h$, respectively. Since a gas particle can spawn up to 4 stellar particles the mass of gas particles is not constant. Furthermore, the mass of stellar particles varies due to stellar wind losses, with an average mass of $M_* \sim 2 \times 10^6 M_\odot/h$. In Chap. 7, also galaxies from Box2 hr are analysed to extend the galaxy sample to higher masses and to include BCGs. The hr resolution has a particle mass resolution of $m_{\rm dm} = 6.9 \times 10^8 M_\odot/h$ and $m_{\rm gas} = 1.4 \times 10^8 M_\odot/h$ for dark matter and gas, respectively, with stars having on average a particle mass of $m_* = 3.5 \times 10^7 M_\odot/h$. The co-moving softening lengths for dark matter is $\epsilon_{\rm dm} = 3.75 * (1+z)$kpc/$h$ for $z < 2$ and $\epsilon_{\rm dm} = 11.25$kpc/h for $z > 2$. The gravitational co-moving softening length for gas particles is $\epsilon_{\rm gas} = 3.75$kpc/h and $\epsilon_* = 2.0$kpc/h for stellar particles.

Halos within the simulation are identified using SUBFIND (Springel et al., 2001a), which utilises a standard Friends-of-Friends algorithm, and is adapted for the treatment of the baryonic component (Dolag et al., 2009), allowing to identify both satellite and central galaxies inside the main halos.

3.2.1 Merger Tree Construction

One of the most powerful features of cosmological simulations is the capability to trace the evolution of individual halos through time in a cosmological environment. This is commonly done using an algorithm that links halos between snapshot resulting in a tree-like structure

that connects halos at $z = 0$ with all its progenitors.

To construct merger trees in *Magneticum* the L-HALOTREE algorithm in the postprocessing is applied, which is outlined in the supplementary information of Springel et al. (2005b). We give a brief overview of the basic concept here: Initially, halo and subhalo structures are identified for all output snapshots by applying a standard Friends-of-Friends algorithm (FOF, Davis et al., 1985), assuming a linking length of 0.16 in combination with an adapted version of the subhalo finder SUBFIND (Dolag et al., 2009; Springel et al., 2001a).

Due to hierarchical merging a halo can have several progenitors, while it in general only has one specific descendant. Therefore, the algorithm determines the descendant of a halo, which implicitly also yields the progenitor information. For a given halo, the appropriate descendant is identified by tracing the unique particle IDs to the subsequent snapshot and finding all halos that contain particles from this halo. The particles are then counted giving higher weights to the particles that are gravitationally more bound, i.e. have a higher binding energy to the halo under consideration. In this manner, the fate of the inner part of the structure is tracked, which is most resistant with regard to stripping processes that occur during the in-fall into a larger structure. After the weighted counting, the halo with the highest count is selected as descendant. A minor side note: In rare cases it is possible that small structures fluctuate below the detection limit in a subsequent snapshot, however appear again in the following snapshot. To deal with these cases the algorithm allows halos to skip snapshots instead of losing track of the structure.

3.3 Set up of the Isolated Merger Simulations used in this Work

This section is based on parts of Schulze et al. (2017)

In Chap. 5 we perform a case study of a single binary merger simulation selected from a sample of 10 high resolution simulations outlined in Schauer et al. (2014). Using the TreeSPH-code GADGET2 (Springel, 2005), all simulations implement various physical processes like star formation, supernova feedback (Springel and Hernquist, 2003) and black hole feedback (Springel et al., 2005a) in a similar way than described in Sec. 3.2. The mass resolution of the different particle types are $m_{\rm star} = m_{\rm gas} = 1.3 \times 10^5 M_\odot/h$ for stars and gas and $m_{\rm dm} = 2.25 \times 10^6 M_\odot/h$ for dark matter. The respective softening length is set to $\epsilon_{\rm stars} = \epsilon_{\rm gas} = 0.02{\rm kpc}/h$ and $\epsilon_{\rm dm} = 0.083{\rm kpc}/h$.

The set of simulations includes five spiral-spiral mergers with a mass ratio for the progenitors of 1:1 and four with a mass ration of 3:1. It also includes one mixed merger that collides a spiral with an elliptical formed in a 3:1 spiral-spiral merger. In all simulations the progenitor spiral galaxies are embedded in a Hernquist dark matter halo with a concentration parameter $c_s = 9$. The progenitor galaxies are initially separated by a pericenter distance $r_{\rm peri} = r_{\rm d,1} + r_{\rm d,2}$, where $r_{\rm d,1}$ and $r_{\rm d,1}$ are the disk-scale radii of the merging spirals. The galaxies approach each other on a parabolic orbit prior to the merging event. Furthermore, the simulations set includes variations of initial properties of the progenitor galaxies and the orbital parameters summarised in Tab. 3.2.

Since we aim to study the formation and evolution of kinematically distinct cores we investigate the simulation set with regard to the existence of a KDC: none of the 3:1 mergers

Table 3.2: Initial properties of binary merger simulations

Model	Ratio	Orbit	$f_{\rm gas}$	Bulge	$V_{\rm vir}$[km/s]
11 NB NG 13	1:1	G13	0.0	No	160
11 NB OBH 13	1:1	G13	0.2	No	160
11 NG 13	1:1	G13	0.0	Yes	160
11 OBH 09	1:1	G09	0.2	Yes	160
11 OBH 13	1:1	G13	0.2	Yes	160
31 ASF 01	3:1	G01	0.2	Yes	160
31 O8BH 13	3:1	G13	0.8	Yes	160
31 OBH 09 320	3:1	G09	0.2	Yes	320
31 OBH 13	3:1	G13	0.2	Yes	160
mix 11 OBH 13	1:1	G13	0.2	Yes	160

show any sign of a KDC, while the presence of a bulge does not seem to influence the existence of a KDC. In fact, the two simulations that exhibit a KDC are identical in all configurations except for the inclusion of a bulge in the progenitor spiral galaxies. Additionally, albeit our sample is small, we also see a coupling between the initial gas fraction f_{gas} and the appearance of a KDC, similar to the results presented by Hoffman et al. (2010). From the different orbital configurations in this sample, only one leads to a KDC. This suggests that the orbital configuration of the initial merger setup is important for the formation of a KD. However, this is not studied in Chap. 5.

For the case study we use the 1:1 spiral-spiral merger that manifests the G13 orbital configuration (11 OBH 13): inclinations $i_1 = -109°$ and $i_2 = 180°$, pericenter arguments $\omega_1 = 60°$ and $\omega_2 = 0°$ according to Toomre and Toomre (1972) (for further information about the simulation, see Johansson et al. (2009b), Johansson et al. (2009a) and Remus et al. (2013)). The meaning of the geometrical parameters is illustrated in Fig. 3.2. The two spiral progenitors are identical clones with an initial gas fraction of 20% hosting a stellar bulge as well as a central black hole. In order to investigate the stability and kinematics of the KDC, we trace several properties such as LOSVD, stellar and gaseous angular momentum, mass, and star formation rates of the KDC in time as well as those of the hosting galaxy. The simulation is run up to 10.2 Gyr. The simulation allows to subdivide the total stellar population into the two subpopulations of initial stars already present in the progenitor galaxies, and stars formed during the simulation runtime.

The selection of this particular merger for this study is based on a visual inspection of the LOSVD at a simulation time of 2.7 Gyr (see Figure 5.1), revealing the presence of a counter rotating kinematically distinct core in the centre. Throughout Chap. 5, LOSVD maps are Voronoi-binned using the method outlined in Cappellari and Copin (2003), ensuring a minimum of 100 particles per cell to reduce the statistical uncertainty of the mean velocity.

The binary merger proceeds as follows: subsequent to the approaching phase lasting until $t = 0.66$ Gyr, a rapid merging phase with two encounters follows. The first encounter takes place at $t_1 = 0.66$ Gyr, while the second and final encounter happens at $t_2 = 1.3$ Gyr. Afterwards, the remnant relaxes under the influence of dynamical friction and violent relaxation (see Sec. 1.3 and Sec. 2.2).

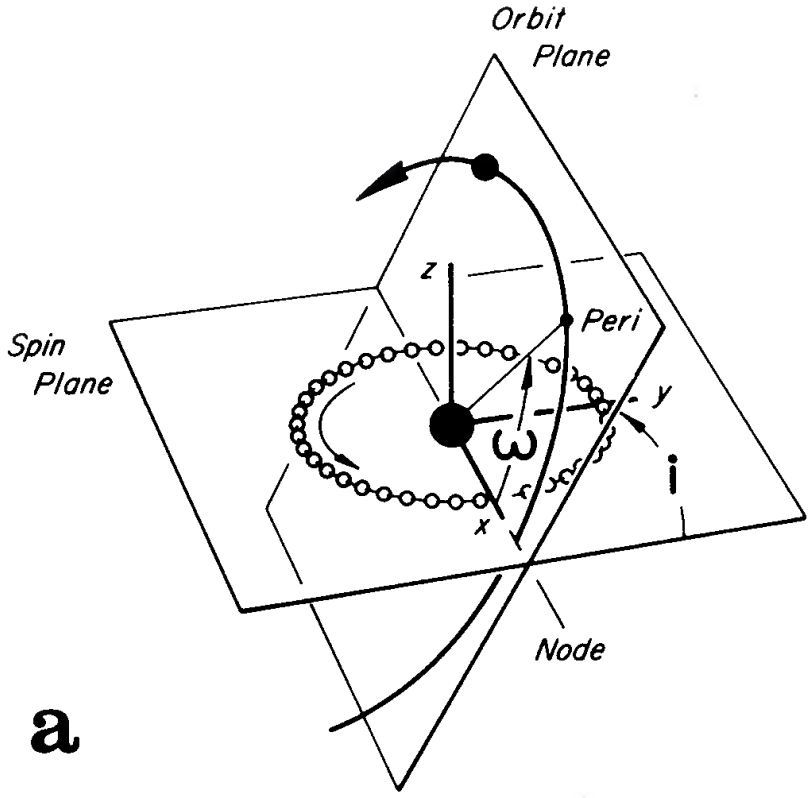

Figure 3.2: Fig. 6. taken from Toomre and Toomre (1972). Visualisation of the geometrical parameters ω and i in a binary merger.

Chapter 4

The Central Kinematics of Early-Type Galaxies

This chapter has been published by Schulze et al. (2018) [1]

Abstract

State-of-the-art integral field surveys like ATLAS^{3D}, SLUGGS, CALIFA, SAMI, and MaNGA provide large data sets of kinematical observations of early-type galaxies (ETGs), yielding constraints on the formation of ETGs. Using the cosmological hydrodynamical *Magneticum Pathfinder* simulations, we investigate the paradigm of fast and slow rotating ETGs in a fully cosmological context. We show that the ETGs within the *Magneticum* simulation are in remarkable agreement with the observations, revealing fast and slow rotators quantified by the angular momentum proxy λ_R and the flattening ϵ with the observed prevalence. Taking full advantage of the three-dimensional data, we demonstrate that the dichotomy between fast and slow rotating galaxies gets enhanced, showing an upper and lower population separated by an underpopulated region in the edge-on $\lambda_{R_{1/2}}$-ϵ plane. We show that the global anisotropy parameter inferred from the $\lambda_{R_{1/2}}$-ϵ edge-on view is a very good predictor of the true anisotropy of the system. This drives a physically-based argument for the location of fast rotators in the observed plane. Following the evolution of the $\lambda_{R_{1/2}}$-ϵ plane through cosmic time, we find that, while the upper population is already in place at $z = 2$, the lower population gets statistically significant below $z = 1$ with a gradual increase. At least 50% of the galaxies transition from fast to slow rotators on a short timescale, in most cases associated to a significant merger event. Furthermore, we connect the M_*-j_* plane, quantified by the b-value, with the $\lambda_{R_{1/2}}$-ϵ plane, revealing a strong correlation between the position of a galaxy in the $\lambda_{R_{1/2}}$-ϵ plane and the b-value. Going one step further, we classify our sample based on features in their velocity map, finding all five common kinematic groups, also including the recently observed group of prolate rotators, populating distinct regions in the $\lambda_{R_{1/2}}$-b plane.

4.1 From Photometry to Kinematics

During the last decade results from cosmological simulations within the ΛCDM framework revealed a two-phase picture of galaxy formation (Oser et al., 2010). Subsequent to the

[1] The section describing the details of the Magneticum simulations is omitted since it is already contained in Chap. 3 of this thesis.

hierarchical merging of dark matter halos, a rapid dissipative phase of smooth gas accretion triggering in-situ star formation proceeds the galaxy assembly. Below $z \approx 1$ the main driver of galaxy growth is minor and major merging of larger structures from outside the halo, hence most new stars are accreted onto the galaxy. Due to the complex interplay of baryonic processes formulating a predictive theory of galaxy formation is still highly debated.

Starting with the famous Hubble-sequence proposed in 1926 (Hubble, 1926) many classification schemes attempted to capture the diversity of galactic structures. Especially within the category of early-type galaxies (ETGs), the improvement of observational techniques revealed a more complex picture of the internal structure. The discovery, that the isophotal shape of ETGs differs from ellipses and can be either 'discy' or 'boxy' as measured by the a_4 parameter led to a revision of the picture of ETGs (Bender et al., 1988). Furthermore, the result that discy ETGs seemed to rotate more rapidly than boxy ETGs and the correlation between the isophotal shape and the central surface density slope led to the proposal of a new classification scheme for ETGs capturing those properties (Kormendy and Bender, 1996; Faber et al., 1997).

Since the discovery and classification of ETGs within the Hubble-sequence the general formation theory has converged to a picture in which, due to the hierarchical assembly of dark matter halos, disc galaxies get morphologically transformed into ETGs in major or multiple minor mergers of disk galaxies (Toomre and Toomre, 1972; Toomre, 1977; Barnes, 1988, 1992; Hernquist, 1992; Mihos and Hernquist, 1996; Naab and Burkert, 2003; Bournaud et al., 2005, 2007). Processes like dynamical friction and violent relaxation during galaxy mergers are capable of drastically modifying the statistical distribution of orbits, while triggered star formation and accretion of fresh gas builds up new cold components (Lynden-Bell, 1967; Thomas et al., 2009; Hoffman et al., 2010). Since the formation of ETGs is predominantly driven by mergers they preserve a richness of information about their assembly encoded in the orbital structure and therefore also in the velocity field.

The emerging picture of ETGs, acquired from photometry, was advanced by the development of integral-field spectroscopy allowing to measure detailed spatial maps of several galaxy properties including stellar kinematics. The SAURON survey was the first project to map the two-dimensional kinematics, ionised gas and stellar population of a statistically significant sample of 48 nearby ETGs (Bacon et al., 2001; de Zeeuw et al., 2002). Already a simple visual investigation of stellar line-of-sight velocity maps within one effective radius revealed two types of kinematics: The class of fast rotators shows a regular rotating velocity pattern consistent with an inclined rotating disc, whereas the class of slow rotators features complex kinematical patterns like kinematically distinct and counter-rotating cores (Davies et al., 2001; Emsellem et al., 2004; Sarzi et al., 2006). These results provoked a paradigm shift towards a kinematically motivated classification scheme closer related to the formation history, since stellar kinematics are believed to encode the detailed accretion history of a galaxy (Cox et al., 2006).

By extending the SAURON sample to 260 ETGs in a volume- and luminosity-limited survey the ATLAS^{3D} project substantiated the dichotomy of fast and slow rotators based on a statistically more meaningful sample (Emsellem et al., 2011). Comprising 86% of the total sample, fast rotators are significantly more frequent and seem to be the dominant kinematical final stage of ETGs. Subsequent to these pioneering studies, Cappellari (2016) combined results from ATLAS^{3D} and the SAMI Pilot survey (Fogarty et al., 2015) to strengthen the existence of the two classes of fast and slow rotators.

Aiming to gain insight into the general formation pathway of these two types of ETGs,

studies were conducted in an attempt to link the cosmological environment of ETGs to their kinematical state, i.e. into a 'kinematic morphology-density relation'. Interestingly, the global fraction of slow rotators within relaxed clusters has proven to be remarkably constant across a large range of clusters with varying galaxy number density (D'Eugenio et al., 2013; Houghton et al., 2013; Scott et al., 2014; Fogarty et al., 2015; Veale et al., 2017a). Only when investigating the local density dependence within the cluster these studies found a rising slow rotator fraction in higher density environments. Interestingly, Veale et al. (2017a) found that for a given absolute K-band magnitude, which is strongly correlated with the stellar mass of a galaxy, the slow rotator fraction is independent of the local and global environment (see also Greene et al. (2018)). This result was confirmed by Lagos et al. (2018a) for the EAGLE hydrodynamic simulations.

Attempting to capture the variety of kinematical features, Krajnović et al. (2011) prior introduced a more refined classification scheme: The velocity map of a galaxy is found to (a) not show any sign of rotation, (b) exhibit a complex velocity pattern without any specific feature, (c) feature a kinematically distinct core (KDC, including counter-rotating cores CRCs), (d) show a double peak in the dispersion map or (e) show a regular rotation pattern. Classifying those groups into fast and slow rotators revealed that group (a)-(d) are in general slow rotating, while members of group (e) are fast rotating (Emsellem et al., 2011).Observational results from McDermid et al. (2006a) revealed that young and very compact KDCs can also be found in fast rotating ETGs. Furthermore, Schulze et al. (2017) showed that KDCs can dissolve on a timescale of 1.5Gyr and feature a complex global motion with respect to the surrounding galaxy.

To depict the different formation pathways responsible for the dichotomy of fast and slow rotators in ETGs, several hydrodynamic simulations using isolated galaxy mergers have been performed. Since this kind of simulations allows to follow the evolution of galaxy properties through time they represent a diagnostically conclusive method to probe the formation of fast and slow rotators, and even more detailed kinematical features, depending on the respective merger configuration. These studies confirmed the notion that galaxy mergers are capable of transforming kinematically cold disks into spheroidal hot objects, resembling the kinematics of fast and slow rotators (Jesseit et al., 2009; Bois et al., 2010, 2011; Moody et al., 2014). The kinematical properties of the remnants crucially depends on the orbital parameters of the merger, the detailed merger sequence (binary or multiple mergers) and the intrinsic properties of the progenitors like mass-ratio and gas content.

Although idealised disk merger simulations had major success in resembling kinematic and photometric properties of galaxies, this method is limited to artificially determined initial conditions and hence does not represent a natural formation pathway in a fully cosmological environment. Due to a significant improvement of computational and numerical techniques, recent state-of-the-art hydrodynamic cosmological simulations reach resolutions that allow to investigate the kinematic properties of ETGs in a statistical meaningful manner. Recent studies using cosmological zoom-in simulations showed that fast and slow rotators can be formed in various scenarios through minor and major mergers (Naab et al., 2014; Choi and Yi, 2017a). However, investigating the influence of different physical processes on the spin evolution, Choi and Yi (2017a) found that, in contrast to the general expectation, the combined impact of effects other than mergers like extremely minor mergers (of ratios smaller than 1/50), secular evolution, fly-by encounters, harassment and dynamical friction is dominating the spin evolution. Therefore, the simple picture of relating the kinematic evolution of ETGs solely to mergers seems to be insufficient. In a first attempt to comprehend the formation

of fast and slow rotators in a fully cosmological context Penoyre et al. (2017) followed the evolution of ETGs in the Illustris simulation. They find that at $z = 1$ the respective progenitors of fast and slow rotators are indistinguishable. At lower redshift they find major mergers to be the driving mechanism engendering the kinematical dichotomy. As a key difference in the evolution of fast and slow rotators they conclude that fast rotators, in contrast to slow rotators, get spun up by accretion of fresh gas and stars from the cosmic environment. In line with these results Lagos et al. (2018b) show that, within the EAGLE simulation, gas-rich mergers can significantly increase the angular momentum content of galaxies.

The aim of the following chapter is to study the kinematic properties of ETGs in a statistical manner using the cosmological hydrodynamic *Magneticum Pathfinder* simulations. Rather than focusing on individual formation pathways we follow the formation of fast and slow rotators as populations and relate their intrinsic kinematics to global and morphological properties. We describe the sample selection as well as the methodology of the galaxy analysis in Sec. 4.2. In Sec. 4.3, we extensively investigate the λ_R-ϵ plane with regard to state-of-the-art observations, the physical meaning of fast and slow rotation, and the implications of its temporal evolution on the formation pathways of the populations of fast and slow rotators. In Sec. 4.4, we connect the kinematics of our sample to the position in the M_*-j_* plane and the stellar density profile quantified by the b-value and the Sérsic-Index. In a second step we apply a refined classification based on kinematical features in the velocity maps similar to Krajnović et al. (2011) and (Emsellem et al., 2011), including the recently observed prolate rotators (Ebrová and Łokas, 2017; Tsatsi et al., 2017), to further disentangle the kinematical variety of ETGs presented in Sec. 4.5. Sec. 4.6 summarises our results and conclusions.

4.2 Sample Selection and Analysis

4.2.1 Sample Selection

Since we aim to conduct a statistical comparison to results which are based on various observational samples, the galaxy selection should ensure a meaningful comparability. The observational classification scheme which essentially all authors converged on is purely based on the morphological properties of a galaxy (de Vaucouleurs, 1959, 1963; Sandage, 1961). Adopting the separation criterion between late-type galaxies (LTGs) and ETGs outlined by Sandage (1961), they select ETGs from their complete sample by visually inspecting multi-colour images. Therefore, the separation between LTGs and ETGs is strongly based on the presence of spiral arms, while other galaxy characteristics, which vary with morphology, are neglected (Sandage, 1975). This classification scheme was adopted to create the frequently used RC2 and RC2 galaxy catalogue (de Vaucouleurs et al., 1976, 1991).

Due to the potentially large sample size and the challenging task of generating realistic multi-colour images from simulated data, a visual inspection is not convenient for our study. Therefore, we first select all main- and subhalos identified by SUBFIND with a total stellar mass $M_* > 2 \cdot 10^{10} M_\odot$ to ensure a proper mass-resolution (i.e. number of stellar particles). In comparison to the ATLAS^{3D} observations, which represents the largest comparison sample, this lower mass limit introduces a minor bias since they comprise ETGs down to $M_* \gtrsim 6 \cdot 10^9 M_\odot$ in their sample. In total, we find 1147 galaxies satisfying this condition in *Magneticum* Box4.

In order to assure an adequate spatial resolution the selection proceeds by constraining

Table 4.1: Characteristics of the *Magneticum* ETGs at $z = 0$

Total number of ETG's:	900
Total halo masses:	$2.7 \cdot 10^{10} - 1.2 \cdot 10^{14}\ M_\odot$
Galaxy stellar masses:	$2 \cdot 10^{10} - 1.6 \cdot 10^{12}\ M_\odot$
Galaxy cold gas fractions:	$1 \cdot 10^{-4} - 0.099$
Galaxy half-mass radii:	$2.0 - 30.5$ kpc

the stellar half-mass radius to be larger than twice the stellar softening length:

$$R_{1/2} > \frac{1.4 \text{ kpc}}{h\ (z+1)}. \tag{4.1}$$

Since the softening length is defined to be constant in comoving coordinates, the threshold involves a redshift dependence in physical units. The half-mass radius is determined to be the radius of a three dimensional sphere containing half of the total stellar mass M_*.

Due to the star-forming nature of spiral arms their presence is tightly coupled to the amount of cold gas available in the galaxy. Therefore, we impose a upper limit on the cold-gas fraction f_{gas} rather than visually identifying the absence of spiral arms to select a galaxy to be an ETG:

$$f_{\text{gas}} = \frac{M_{\text{coldgas}}}{M_*} \leq 0.1. \tag{4.2}$$

Here, M_{coldgas} is the total mass of all gas particles possessing a temperature below $10^5 K$ within $3R_{1/2}$. Serra et al. (2014) investigated the M_{HI}/M_*-fractions for a subsample of the ATLAS^{3D} ETGs, observing values ranging from 0.04% to 10%. To ensure a proper comparability we checked the maximum M_{HI}/M_*-fractions within our selected ETG sample, yielding a value of 5%. Hence, a gas fraction of 10% imposes a conservative limit on the M_{HI}/M_*-fractions of our selected ETGs in comparison to the observations.

Our final sample of ETGs at $z = 0$ includes 900 galaxies, which we will refer to as *Magneticum* ETGs in the following. Some basic characteristics of our sample are summarised in Tab. 4.1.

To select our sample at higher redshifts we maintain the lower mass cut and the gas fraction threshold, whereas the lower limit for $R_{1/2}$ is adapted according to Eq. 4.1. This leaves us with a sample size of 161, 767 and 894 at $z = 2$, $z = 1$ and $z = 0.5$, respectively. Therefore already at $z = 2$ we find a significant number of ETGs with a low fraction of cold gas and stellar masses above $2 \cdot 10^{10} M_\odot$.

4.2.2 Mass-Size Relation

Fig. 4.1 shows the mass-size relation for all galaxies in the simulation satisfying the resolution criteria, separated into selected (left column, black circles) and rejected (right column, grey circles). In each panel the horizontal dashed lines correspond to the resolution limit (Eq. 4.1). We include observational results from the GAMA (Baldry et al., 2012; Lange et al., 2015), CALIFA, SLUGGS (Forbes et al., 2017) and ATLAS^{3D} (Cappellari et al., 2013a) surveys as given in the legend.

The green and blue solid lines depict the most recent GAMA results by Lange et al. (2015) representing the statistically most significant observational sample in our comparison. From the various relations presented in Lange et al. (2015) we adopt the relations obtained by fitting

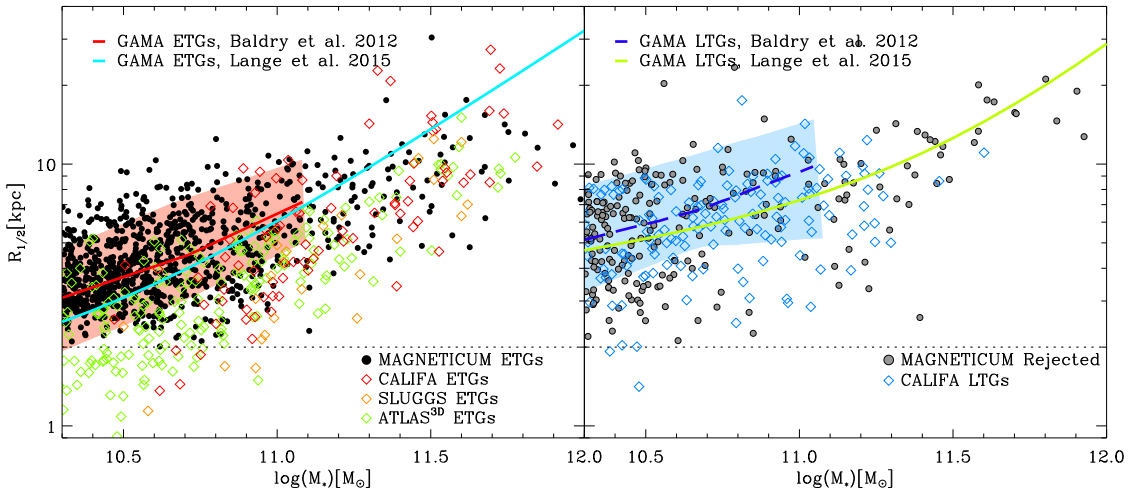

Figure 4.1: The mass-size relation at $z = 0$ for the *Magneticum Pathfinder* simulation in direct comparison to recent observations. *Left panel:* Black circles show the distribution for *Magneticum* ETGs. Diamonds correspond to observations by the ATLAS^{3D}, SLUGGS and CALIFA survey with colours as given in the legend. The red and blue solid lines represent observations for ETGs from the GAMA survey. *Right panel: Magneticum* galaxies which are selected to not resemble ETGs in grey, while blue diamonds show observations by the CALIFA survey. The blue dashed line marks observations for LTGs from the GAMA survey (Baldry et al., 2012). In both panels the 1σ range for the GAMA observations are marked by the shaded areas.

a double power-law function to the visually identified ETGs and LTGs. It is important to note that Lange et al. (2015) uses actual major-axis effective radii taking the elliptical shape of the isophotes into account (Kelvin et al., 2012). Hence, especially for highly elongated galaxies, this can lead to a bias towards larger radii with respect to the half-mass radii determined for the *Magneticum* sample.

An interesting general feature among the observational samples is the considerable scatter between them. For a given mass, the SLUGGS, CALIFA and ATLAS^{3D} ETGs seem to be systematically more compact than the GAMA galaxies. Since the half-light radii of those samples are obtained by different methods, this suggests a significant impact of the observational approach on the result (Cappellari et al., 2013b).

At the stellar mass range of $2 \cdot 10^{10} M_\odot < M_* < 10^{11} M_\odot$ the observations show that LTGs have larger effective radii at a given mass than the ETGs. This difference is also present between the *Magneticum* ETGs and rejected galaxies, albeit with a significant overlap, similar to the results from CALIFA and GAMA. However, the rejected galaxies in the right panel of Fig. 4.1 include disc-like galaxies as well as peculiar galaxies, potentially influenced by interactions. Hence, a rigorous comparison to observations is not reasonable due to the contamination by disturbed objects.

The *Magneticum* ETGs are in substantial agreement with GAMA observations by Baldry et al. (2012) showing a clustering in the vicinity of the red curve with a weak trend towards larger radii (see left panel of Fig. 4.1). The more recent results by Lange et al. (2015) exhibit slightly smaller radii in the considered mass range up to $10^{11} M_\odot$, however still larger than those found for the ATLAS^{3D} galaxies. For galaxies more massive than $10^{11} M_\odot$, the *Magneticum* ETGs follow the almost linear trend found for the GAMA ETGs, albeit tending towards slightly smaller radii. It is important to note that, due to the limited size of the simulated box, the high-mass end of the *Magneticum* ETGs is underpopulated and therefore

statistically unreliable.

Overall, the mass-size relation found for the *Magneticum* ETGs is consistent with the observed trend. Furthermore, the galaxies considered in this study are in agreement with present day scaling relations since they represent an extension of the sample investigated in Remus and Dolag (2016) and Remus et al. (2017).

4.2.3 Angular Momentum Proxy: λ_R

For many years the V/σ parameter has been used to quantify the relative amount of stellar rotation in a system, where V and σ denote the projected stellar velocity and velocity dispersion, respectively. This parameter is a useful tool to investigate the dynamical state of ETGs. However, it fails to distinguish between small-scale rotation (like kinematically distinct cores) and large-scale rotation (Emsellem et al., 2007). Therefore, a new parameter was introduced by Emsellem et al. (2007) within the SAURON project, which takes the global velocity structure into account and in addition maintains the information about the dynamical state, i.e. ordered vs. random motion.

For observed two-dimensional velocity and dispersion maps it is defined as

$$\lambda_R = \frac{\langle R\ |V| \rangle}{\langle R\ \sqrt{V^2 + \sigma^2} \rangle}, \tag{4.3}$$

where R is the projected radius, V the line-of-sight velocity and σ the projected velocity dispersion. $\langle \cdot \rangle$ denotes the luminosity-weighted average over the full two-dimensional kinematic field. Inserting the velocity weighting it reads

$$\lambda_R = \frac{\sum_{i=1}^{N_p} F_i\ R_i\ |\overline{V}_i|}{\sum_{i=1}^{N_p} F_i\ R_i\ \sqrt{\overline{V}_i^2 + \sigma_i^2}}, \tag{4.4}$$

with the sum running over all pixels in the considered field of view. F_i, R_i, $\left|\overline{V}_i\right|$ and σ_i are the flux, projected distance to the galaxy centre, mean stellar velocity and velocity dispersion of the i$^{\text{th}}$ photometric bin, respectively.

For a purely rotational supported system, λ_{R} tends to unity. The lower limit of $\lambda_{\mathrm{R}} \to 0$ corresponds to either a purely dispersion-dominated system with no ordered rotation, or a rotating system where the total angular momentum vector is along the line of sight. The usage of $\langle R\,|V| \rangle$ as a surrogate for the angular momentum ensures the distinction between large-scale or small-scale rotation. Investigating remnants of simulated binary disc mergers, Jesseit et al. (2009) found that λ_{R} is a robust indicator of the true intrinsic angular momentum content of these objects. It is important to mention that λ_{R} obviously depends on the spatial size, over which the sum in Eq. 4.4 is taken. Moreover, it is sensitive to the tessellation method used for the velocity and dispersion maps. λ_{R} is specifically customised to fit the needs and constraints of the current observational methods. It solely uses projected quantities and fluxes, which can be observed by multi-wavelength surveys.

For simulations the fluxes are replaced by stellar masses, assuming a constant mass-to-light ratio within each galaxy. Following previous theoretical studies (Jesseit et al., 2009; Bois et al., 2011; Naab et al., 2014; Wu et al., 2014), the expression for λ_{R} is transformed into

$$\lambda_R = \frac{\sum_{i=1}^{N_p} M_i\ R_i\ |\overline{V}_i|}{\sum_{i=1}^{N_p} M_i\ R_i\ \sqrt{\overline{V}_i^2 + \sigma_i^2}}. \tag{4.5}$$

Eq. 4.5 is the final formula we will use in this study to calculate λ_{R} from the kinematical maps.

In order to calculate λ_{R} given in Eq. 4.5, we need to generate two types of kinematical maps. The mean projected velocity $\overline{V}_i$ within a pixel is given by

$$\overline{V}_i = \frac{\sum_{j=1}^{N_c} V_j}{N_c}, \tag{4.6}$$

where V_j is the particle velocity, and the sum runs over all N_c particles within a cell. Similarly, the projected velocity dispersion is defined as

$$\sigma_i = \sqrt{\frac{\sum_{j=1}^{N_c} V_j^2}{N_c} - \left(\frac{\sum_{j=1}^{N_c} V_j}{N_c}\right)^2}. \tag{4.7}$$

To be comparable to observations we have to use calculation methods which take the properties of numerical simulations into account. For example, the limited mass resolution in SPH leads to low particle numbers when assigning particles onto a grid, which causes statistical errors. Another issue is the limited spatial resolution which makes the maps sensitive to numerical small-scale fluctuations. For a detailed resolution study on this subject see Bois et al. (2010). In order to avoid artificial statistical noise we adopt the following approach for each galaxy: The stellar particles within the considered spatial domain and projection are sampled onto a rectangular grid with a spatial resolution comparable to state-of-the-art IFU surveys. Subsequently, a Centroidal Voronoi Tessellation (CVT) is performed, which combines pixels into cells containing a minimum of 100 particles, while preserving a proper spatial resolution (Cappellari and Copin, 2003). To determine λ_{R} we then calculate the line-of-sight mean velocity, velocity dispersion and the radius of the centre of mass within each CVT cell.

The calculation of λ_{R} proceeds by determining the spatial area over which the sum in Eq. 4.5 is taken. Given the ellipticity of the galaxy the calculation domain is specified to be an ellipse with the corresponding ellipticity enclosing an area of $A_{\mathrm{ellipse}} = \pi R_{1/2}^2$. We indicate this by assigning a subscript '1/2' to the parameter name $\lambda_{\mathrm{R}_{1/2}}$. This procedure of calculating $\lambda_{\mathrm{R}_{1/2}}$ ensures maximal comparability to observational results.

It is crucial to emphasise that the smallest values obtained from this procedure have to be interpreted with caution due to the functional definition of $\lambda_{\mathrm{R}_{1/2}}$. As $\lambda_{\mathrm{R}_{1/2}}$ is a cumulative parameter of absolute values, the statistical noise of Voronoi cells with nearly zero velocity adds up, creating a lower limit for $\lambda_{\mathrm{R}_{1/2}}$ (Bois et al., 2010; Naab et al., 2014). We verify this notion by calculating $\lambda_{\mathrm{R}_{1/2}}$ for all galaxies assuming zero velocity, only considering the statistical noise. It reveals a mean value of 0.07, which corresponds to the lowest values found for the simulated *Magneticum* galaxies.

4.2.4 Morphological Parameters: Ellipticity and Sérsic-Index

During the course of this paper we make use of the ellipticity or flattening ϵ of galaxies. In general ϵ is given by $\epsilon = 1 - b/a$, where b and a are the semi-minor and semi-major axis, respectively. Following Cappellari et al. (2007) ϵ can be determined by diagonalising the moments of inertia tensor within a given aperture. In order to calculate ϵ for a given projection of a simulated galaxy we iteratively approximate an iso-density contour: Starting with a circular aperture of radius $1.5R_{1/2}$, ϵ is calculated by diagonalising the inertia tensor. In

the following step we use an elliptical aperture with the previously determined ϵ containing the same amount of stellar mass as the initial circle. Reiterating this procedure until ϵ converges gives an estimate of the average global ellipticity mostly independent of central substructures.

Since the Sérsic-index describes the curvature of the Sérsic-profile fitted to the stellar radial surface density distribution, it is a purely morphological parameter. The Sérsic-profile is given by

$$\Sigma(R) = \Sigma_e \exp\left(-b_n\left[\left(\frac{R}{R_e}\right)^{\frac{1}{n}} - 1\right]\right) \tag{4.8}$$

(Sérsic, 1963), where R_e is the effective radius, Σ_e is the surface density at the effective radius, and n is the Sérsic-index. The dimensionless parameter b_n is defined according to the definition of the effective radius. There is no analytic solution to the defining equation for b_n. Hence, we use a numeric approximation given in Ciotti and Bertin (1999).

The Sérsic fits are performed on the edge-on projection of the stellar component which is subdivided into elliptical annuli of fixed ellipticity and position angle. Hence we neglect effects of isophotal twists or variations of ϵ with radius. The border of the annuli are determined by demanding a constant particle number of 200, ensuring a proper weighting of all data points. Excluding one effective radius in the centre the moving window approach is extended out to 5 R_e. In this manner we exclude the influence of central subcomponents like cusps or cores on the fit.

4.3 The λ_R-ϵ Plane

Based on a sample of 48 ETG's, Emsellem et al. (2007) used λ_{R_e} to separate ETG's into fast and slow rotating objects, depending on whether the galaxy exhibits a λ_{R_e} larger or smaller than 0.1.

Having access to a statistically more complete sample ATLAS^{3D} redefined the criterion to disentangle fast and slow rotators based on 260 ETGs, including the galaxies' shapes:

$$\begin{aligned} \lambda_{R_e} &> 0.31 \cdot \sqrt{\epsilon_{R_e}} \rightarrow \text{fast rotator} \\ \lambda_{R_e} &\leq 0.31 \cdot \sqrt{\epsilon_{R_e}} \rightarrow \text{slow rotator} \end{aligned} \tag{4.9}$$

It is based on qualitative theoretical considerations and has proven to properly distinguish the two kinematical families (Emsellem et al., 2011). For our simulated sample of galaxies, we will use an analogue, approximating λ_{R_e} by $\lambda_{R_{1/2}}$ and ϵ_{R_e} by $\epsilon_{R_{1/2}}$

4.3.1 Statistical Comparison to IFU Observations

We want to test if our simulated sample of ETG's reproduces the observed distribution in the $\lambda_{R_{1/2}}$-ϵ plane. The comparison sample combines observations from the ATLAS^{3D}, CALIFA, SAMI and SLUGGS survey extracted from Emsellem et al. (2011), Querejeta et al. (2015), van de Sande et al. (2017b) and Arnold et al. (2014), respectively. Since the observations are limited to one random projection for each galaxy, we choose an arbitrary viewing angle for each simulated galaxy to determine $\lambda_{R_{1/2}}$ and ϵ.

Fig. 4.2 shows the $\lambda_{R_{1/2}}$-ϵ plane for the simulated sample (red circles) in direct comparison to the IFU observations (blue and grey symbols). The threshold between fast and slow rotators given in Eq. 4.9 is shown as solid green line. Furthermore, Fig. 4.2 comprises cumulative

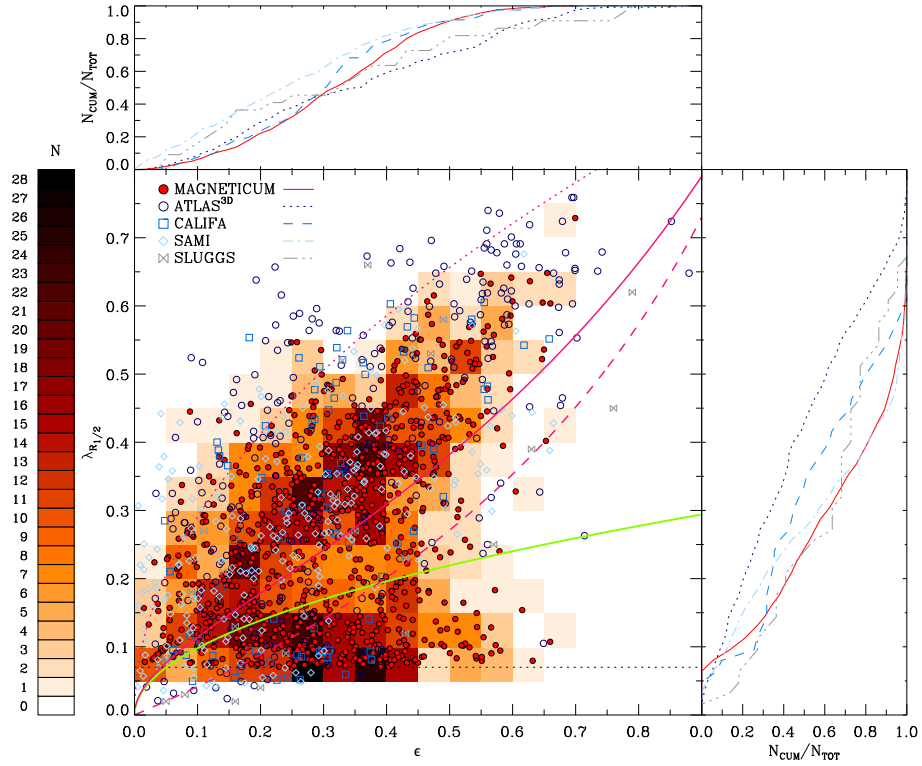

Figure 4.2: Comparison of the *Magneticum* ETGs with ATLAS^{3D}, CALIFA, SLUGGS, and SAMI observations in the $\lambda_{R_{1/2}}$-ϵ plane. *Main panel*: Filled circles indicate the *Magneticum* ETGs, whereas the open blue and grey symbols mark the observations as indicated in the legend. The green line defines the threshold between fast and slow rotators. The magenta line shows the theoretical position of edge-on viewed ellipsoidal galaxies with an anisotropy parameter $\delta = 0.7 \times \epsilon_{intr}$, while the magenta dashed line corresponds to a factor of 0.8 (for further details see Cappellari et al. (2007)). Accordingly the dotted magenta line represents the theoretical position for edge-on projected isotropic galaxies with $\delta = 0$. The number density in the plane is illustrated by the red squares. *Upper and right panel*: Cumulative number of galaxies (N_{CUM}) normalised by the total number of galaxies (N_{TOT}) of the respective sample for $\lambda_{R_{1/2}}$ and ϵ, respectively.

distributions for $\lambda_{R_{1/2}}$ on the right and for ϵ on top of the main panel each split up into the various samples.

The *Magneticum* simulation reproduces both, fast and slow rotating ETG's with $\lambda_{R_{1/2}}$ and ϵ in the range $0.069 < \lambda_{R_{1/2}} < 0.72$ and $0.014 < \epsilon < 0.69$, respectively. With 70% (629/900) the vast majority is classified as fast rotators, accordingly only 30% (271/900) are slowly rotating. This is in good agreement with the results from the ATLAS^{3D} survey, where 86% (224/260) of the ETGs are fast rotators and 14% (36/260) are slow rotators (Emsellem et al., 2011). Due to the lower mass cut for the simulation, the lower percentage of fast rotators in the *Magneticum* sample is an expected behaviour as the fast rotating regime is preferentially occupied by low-mass galaxies. The frequencies of slow and fast rotators in the SAMI sample are with 15% slow rotators and 85% fast rotators very similar to ATLAS^{3D}. Within the CALIFA and SLUGGS sample the frequencies differ significantly from ATLAS^{3D}: 28% of the CALIFA sample are slow rotating, while 72% are fast rotating. Similarly, 27% of the SLUGGS sample are slow rotators and 73% are fast rotators. The discrepancies among the observational samples are most probably due to the underlying galaxy selection and the associated environmental bias. Although the SLUGGS sample covers the full range of

environments it only contains 22 ETGs. Even the volume-limited ATLAS^{3D} sample, which covers a volume of 42Mpc, is not representative for the total ETG population in the Universe. ATLAS^{3D}, however is a volume- and magnitude-limited sample aiming to be representative of the low redshift galaxy population. Hence, for a abundance comparison of fast and slow rotators the ATLAS^{3D} sample is the most sensible choice.

The fast rotating regime is in excellent agreement with the different observational samples. Similar to the observations, we see a well-defined upper envelope: as ϵ increases, the maximum $\lambda_{R_{1/2}}$ increases accordingly. However, the ATLAS^{3D} sample reveals an envelope reaching higher $\lambda_{R_{1/2}}$ values for a given ϵ. This can be explained by the applied mass selection criterion, an issue that was already reported in several former studies using isolated merger simulations (Jesseit et al., 2009; Bois et al., 2011) as well as in cosmological zoom-in simulations (Naab et al., 2014; Wu et al., 2014). A similar behaviour is visible when comparing ATLAS^{3D} to the remaining observations, where only one ETG exhibits a $\lambda_{R_{1/2}}$ larger than 0.65. Therefore, the discrepancies in the extremely fast rotating range might be due to the different definitions of an ETG applied to classify the galaxies within the different samples, or driven by the different environments included in these studies.

In the slow rotating regime we clearly see the aforementioned resolution limit of $\lambda_{R_{1/2}} > 0.07$, as the simulation does not reach values lower than 0.07. We find a significant fraction of slow rotators with $\epsilon > 0.4$ which is not present in the observations. Although there are three galaxies observed in this regime, we find a distinctly larger fraction of 8.5% of the total sample in the simulation. This tension with observations was already reported by Naab et al. (2014) based on a sample of 44 zoom-in simulations of individual galaxies (Oser et al., 2010). In addition, high-resolution isolated galaxy merger simulations by Bois et al. (2011) and Moody et al. (2014) also produced highly elongated slow rotators, albeit their higher resolution in the simulations, and the different implementation of physics as well as the very different nature of such isolated merger simulations. Thus, the origin of these elongated slow rotators remains to be explored in future work.

4.3.2 Edge-on Projections and Environmental Dependence

For galaxies that rotate around their minor axis, $\lambda_{R_{1/2}}$ is largest if the galaxy is seen edge-on. The edge-on projection is the plane spanned by the minor and major axis of the stellar distribution. Therefore, also the maximum ellipticity should be obtained under this projection.

We rotate all our galaxies[2] into edge-on projections, and the result is shown in Fig. 4.3. The grey circles mark the galaxies that satisfy the resolution criteria but are rejected from the ETG sample by Eq. 4.2, while the other colours comprise the *Magneticum* ETGs.

As expected, we find that the non-ETGs are much more common at the high-λ_R end than the ETGs, and that flat ellipticities are also much more frequent for the non-ETGs than for the ETGs. However, we also clearly see that the population of non-ETGs is contaminated by objects currently influenced by interactions: A certain portion of these galaxies do not follow the expected behaviour of high $\lambda_{R_{1/2}}$ and ϵ_e values characteristic for late-type galaxies (Bois et al., 2011; Cappellari, 2016). In addition, recent observations revealed that early-type galaxies can posses a significant amount of cold gas, with f_{gas} distinctly larger than 0.1 (Davis et al., 2015), and hence these ETGs would be included in the non-ETG population by our selection criterion. Therefore, the non-ETGs cover the full range of $0.07 \leq \lambda_{R_{1/2}} \leq 0.82$ and

[2]All galaxies that satisfy the resolution criterion are treated like this, independent of further classifications

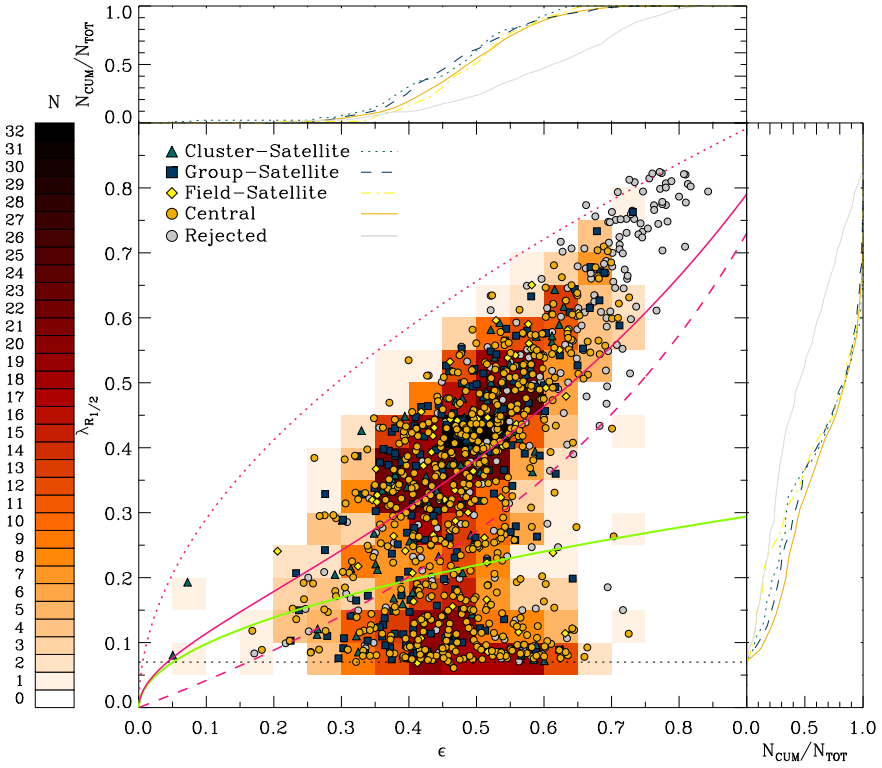

Figure 4.3: *Main Panel*: $\lambda_{R_{1/2}}$-ϵ plane for *Magneticum* galaxies with $M_* > 2{\cdot}10^{10} M_\odot$ in the edge-on projection. The grey symbols represent the rejected galaxies according to Sec. 4.2.1, while the other colours comprise the *Magneticum* ETGs. The *Magneticum* ETGs are furthermore split up according to their large-scale environment into cluster satellites (turquoise triangles), group satellites (blue squares), field satellites (yellow diamonds), and centrals (orange circles). The green line defines the threshold between fast and slow rotators given in Eq. 4.9. The magenta lines are equivalent to Fig. 4.2. The number density in the plane is illustrated by the red squares. *Side panels* show the cumulative number of galaxies (N_{CUM}) normalised by the total number of galaxies (N_{TOT}) of the respective sample split up into different environments.

$0.17 \leq \epsilon \leq 0.84$. For very low λ_R, nevertheless, the non-ETGs become rare. This is in good agreement with expectations, as the very round and slow-rotating galaxies do usually not have that much cold gas. Nevertheless, a substantial amount of the non-ETGs populate the extremely high $\lambda_{R_{1/2}}/\epsilon$ domain, showing the expected trend for late-type galaxies, which can be seen even better in the sideways cumulative distributions of Fig. 4.3.

Additionally, we separate the *Magneticum* ETGs into centrals (i.e. galaxies that reside at the centre of the potential, filled orange circles in Fig. 4.3) and subhalos (i.e. galaxies that are satellite galaxies within the halo of another galaxy). Furthermore, we split the subhalo ETGs according to the environment they are living in, into cluster satellites (filled green triangles), group satellites (filled blue squares), and field satellites (filled yellow diamonds).

We do not find any difference between the ETGs residing in different environments, and only a slight difference between centrals and satellite ETGs, with a tendency for the extremely slow rotating galaxies to be preferentially central galaxies and not satellites. This is in good agreement with recent studies of environmental dependencies of $\lambda_{R_{1/2}}$, which also could not find any substantial influence of the large-scale environment on the kinematical properties of ETGs, as discussed above.

The shaded red areas in Fig. 4.3 illustrate the number density of the *Magneticum* ETGs in the $\lambda_{R_{1/2}}$-ϵ plane. They reveal two distinct populations of ETGs, fairly well separated by the magenta line and the observational fast-slow rotator threshold, with only very few galaxies in the transition region.

The population of slow rotators is clearly separated from the upper population, indicating that the different behaviour of slow- and fast rotators in the $\lambda_{R_{1/2}}$-ϵ plane is not just a line drawn visually but actually contains physical meaning. The clustering of galaxies in the vicinity of the black dashed line is caused by the resolution limit[3] described in Sec. 4.2.3 and thus does not contain physical meaning other than that the global kinematic properties of these ETGs are slowly- or even non-rotating.

The fast rotator population splits up into the galaxies in the transition region and a well defined upper population, with the majority of the fast rotators being above the dashed magenta line. Most of these 'real' fast rotators are actually residing within the isotropic line and the magenta dashed line shown in Fig. 4.3, with no ETGs above the isotropic line. The nature of these curves will be discussed in detail in the following subsection.

This observed segmentation suggest a fundamental difference between the slow- and the fast rotating population of ETGs, with only few ETGs in a transition state between them. Thus, it supports the idea that there are distinct formation histories for the fast- and slow rotating populations, and not a slow, continuous transformation from one population to the other.

4.3.3 Global Anisotropy

The theoretical framework provided by Binney (2005) from first principles, i.e. the tensor virial theorem, allows us to write a direct relation between V/σ and the intrinsic ellipticity $\epsilon_{\rm intr}$, under the assumption of a flattened, axisymmetric galaxy in the edge-on projection with a given anisotropy. Following on the tight correlation between $\lambda_{R_{1/2}}$ and V/σ emphasised by Emsellem et al. (2011), and notations as in Cappellari et al. (2007), we can thus predict the location of such systems within the $\lambda_{R_{1/2}}$-ϵ plane (see also sec. 2.1.4).

Parameterising the anisotropy δ as

$$\delta = 1 - \frac{\Pi_{zz}}{\Pi_{xx}} = 1 - \frac{\sum_{i=1}^{N} M_i \ \sigma_{z,i}^2}{\sum_{i=1}^{N} M_i \ \sigma_{x,i}^2} \tag{4.10}$$

and using the dimensionless parameter α defined in Binney (2005), we can write:

$$(V/\sigma)^2 \approx \frac{(1-\delta)\ \Omega(\epsilon_{\rm intr}) - 1}{\alpha\ (1-\delta)\ \Omega(\epsilon_{\rm intr}) + 1}, \tag{4.11}$$

with

$$\Omega(\epsilon_{\rm intr}) = \frac{0.5\ (\arcsin(e) - e\ \sqrt{1-e^2})}{e\ \sqrt{1-e^2} - (1-e^2)\ \arcsin(e)}, \tag{4.12}$$

and

$$e = \sqrt{1 - (1-\epsilon_{\rm intr})^2} \tag{4.13}$$

[3]Estimating the effect of an increased mass resolution is not trivial: In general an increase in resolution reduces the statistical noise allowing to reach lower $\lambda_{R_{1/2}}$ values. It is however not possible to predict the impact of a more resolved velocity distribution on $\lambda_{R_{1/2}}$ due to the increased number of particles, which could for example reveal small kinematical distinct cores in the centres which would lead to larger measured $\lambda_{R_{1/2}}$ values.

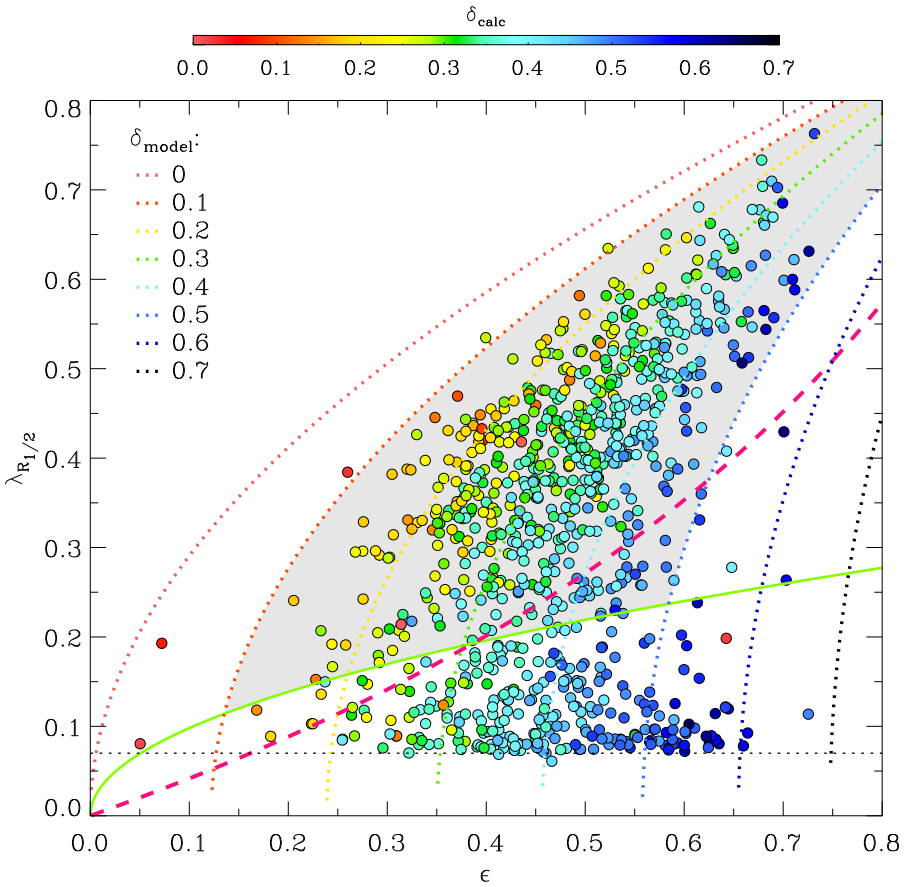

Figure 4.4: $\lambda_{R_{1/2}}$-ϵ plane colour coded according to δ_{calc}. The coloured dashed lines show the result for the theoretical model assuming different δ_{model} as given in the legend. The magenta dashed line corresponds to the model prediction for edge-on viewed ellipsoidal galaxies with an anisotropy parameter $\delta = 0.8 \times \epsilon_{intr}$. The threshold between fast and slow rotators is marked by the green curve.

which is finally linked to $\lambda_{R_{1/2}}$, via:

$$\lambda_{R_{1/2}} \approx \frac{k\ (V/\sigma)}{\sqrt{1 + k^2\ (V/\sigma)^2}} \tag{4.14}$$

where k is estimated to be ≈ 1.1.

Following the model, each point in the $\lambda_{R_{1/2}}$-ϵ plane can be assigned a model anisotropy $\delta_{\rm model}$ based on such assumptions, to be compared with the actual anisotropy of the system, $\delta_{\rm calc}$, which is directly calculated from the particle distribution for each ETG. The solid magenta line in Fig. 4.2 and Fig. 4.3 illustrate the model under the assumption of a linear connection between δ and $\epsilon_{\rm intr}$ with a factor of 0.7, while the dashed magenta line corresponds to a factor of 0.8. The dotted magenta line in Fig. 4.2 and Fig. 4.3 shows the theoretical prediction for an isotropic ($\delta = 0$) galaxy.

Remarkably, we find a linear, almost 1:1 relation between $\delta_{\rm model}$ and $\delta_{\rm calc}$ (with a scatter of $(0.016, -0.089)$), with only a slight trend for $\delta_{\rm calc}$ to be larger than $\delta_{\rm model}$ (see Fig. 4.19 in App. 4.A). This is nicely illustrated in Fig. 4.4 where we show the $\lambda_{R_{1/2}}$-ϵ plane for the *Magneticum* ETGs, with symbols coloured according to their anisotropy $\delta_{\rm calc}$, together with

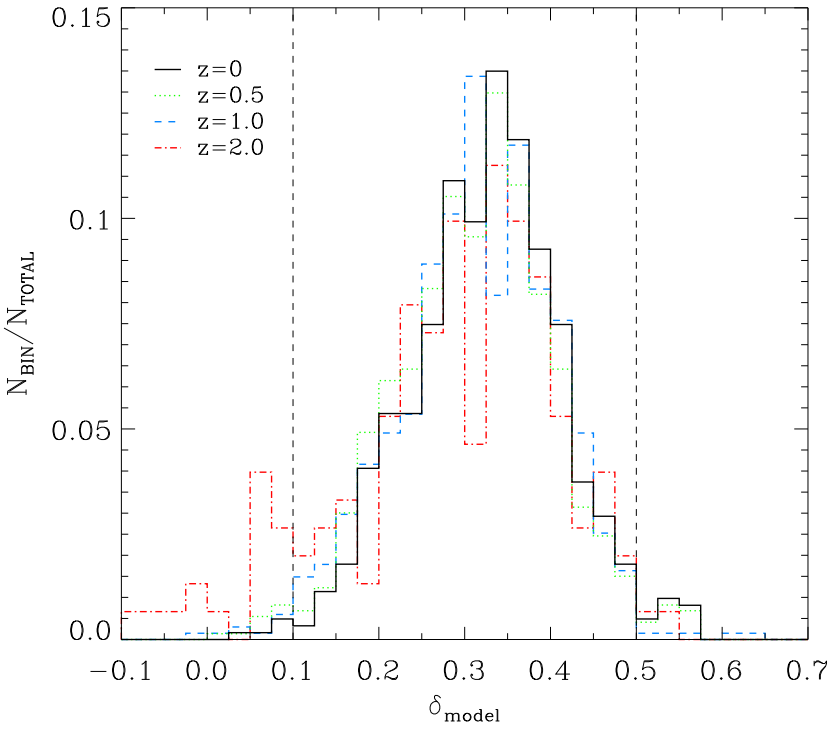

Figure 4.5: Anisotropy distribution of fast rotators at different redshifts as indicated in the left upper corner.

the predicted lines for edge-on systems with constant values of the anisotropy δ, from 0 (isotropy) to 0.7 (strongly anisotropic). We therefore conclude that the edge-on view of the $\lambda_{R_{1/2}}$-ϵ plane provides an excellent proxy for the determination of anisotropy. It further means that, given the inclination of a fast rotator, we could constrain its actual anisotropy from projected quantities alone.

We can take this further by looking at the overall distribution of fast rotators in the $\lambda_{R_{1/2}}$-ϵ plane. The vast majority of fast rotators are contained within the two limiting curves defined by $\delta = 0.1$ and 0.5 (see also the black histogram in Fig. 4.5). These two limits, plus the empirical fast-slow rotator separation line ($\lambda_{R_{1/2}} = 0.31\sqrt{\epsilon}$), provide a simple way of defining the main regions where fast rotators concentrate. Another interesting reference line is given by the demand $(V/\sigma)^2 \geq 0$ in Eq. 4.11. Following Cappellari et al. (2007), it further gives a natural upper limit for δ for a given $\epsilon_{\rm intr}$:

$$\delta \leq 1 - \frac{1}{\Omega(\epsilon_{\rm intr})} \approx 0.8\epsilon_{\rm intr} + 0.15\epsilon_{\rm intr}^2 + 0.04\epsilon_{\rm intr}^3 + ... \tag{4.15}$$

As emphasised by Cappellari et al. (2007), $\delta = 0.8\epsilon_{\rm intr}$ corresponds to the steepest allowed linear relation within this framework. The dashed magenta line in Fig. 4.4 shows the model prediction for $\delta = 0.8\epsilon_{\rm intr}$, nicely complementing the edge-on view of the $\lambda_{R_{1/2}}$-ϵ plane with most of the *Magneticum* fast rotating ETGs on its left side (see also the discussion in Cappellari (2016)).

Interestingly, we cannot find a significant change in the anisotropy distribution of the ETGs with redshift, as demonstrated for the fast rotator population in Fig. 4.5. Only at $z = 2$, there is a peak for low anisotropies which is not present for the other redshift, albeit

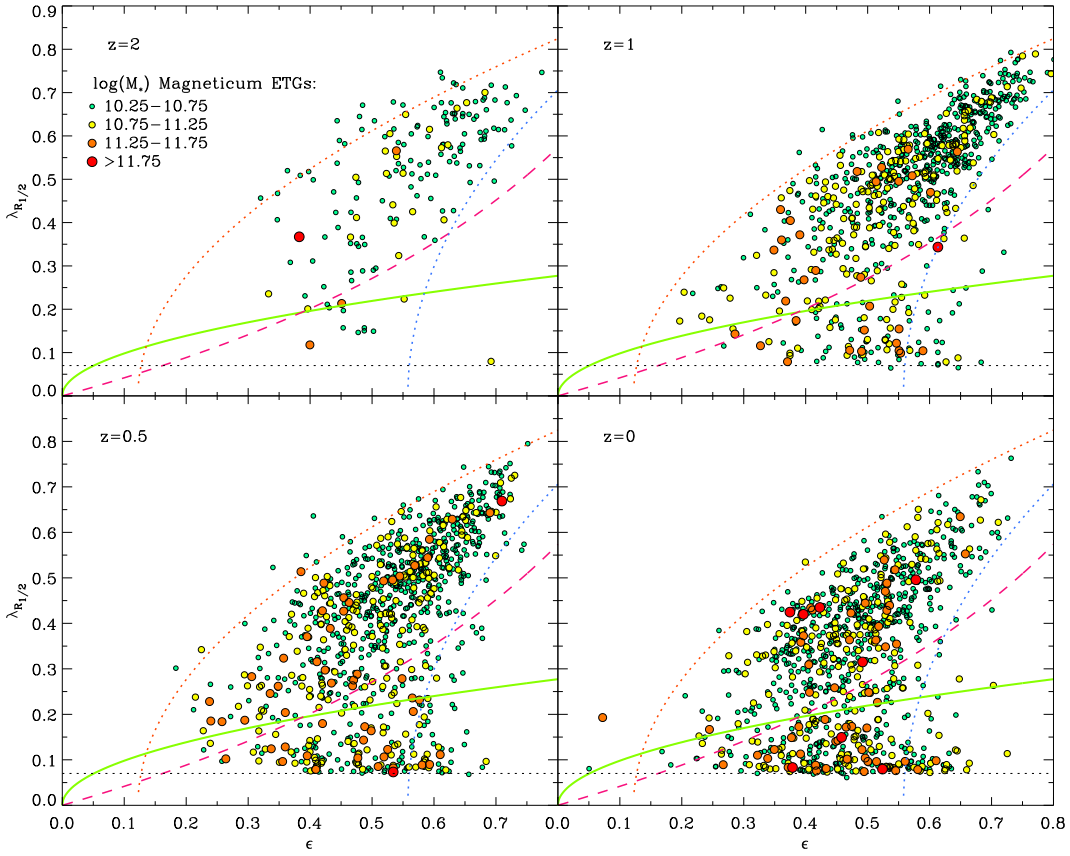

Figure 4.6: Redshift evolution of the *Magneticum* ETGs in the $\lambda_{R_{1/2}}$-ϵ plane from $z = 2$ (upper left panel) to $z = 0$ (right lower panel). The magenta and green lines are as in Fig. 4.4. The dashed orange and blue lines show the model prediction for $\delta_{model} = 0.1$ and $\delta_{model} = 0.5$, respectively. The colour and size of the symbols is according to the stellar mass as indicated in the left upper panel.

that is also the smallest sample of ETGs and this might thus only be a statistical effect. This is discussed further in the next section.

4.3.4 Redshift evolution

While we do not see strong evolution trends with redshift in the anisotropy of our ETGs, we find a clear evolution of the $\lambda_{R_{1/2}}$-ϵ plane with redshift. Fig. 4.6 shows the $\lambda_{R_{1/2}}$-ϵ plane for redshifts from $z = 2$ to $z = 0$.

The significant decrease in the total number of ETGs towards higher redshifts confirms that most galaxies are still gas-rich at $z = 2$, and quenching mechanism have a substantial impact below this redshift. At $z = 2$, most of the galaxies are in the vicinity or above the magenta relation, while only a very small fraction is classified as slow rotators. Already at this stage of the evolution, only a small fraction of ETGs exceed the isotropic relation. Therefore, the fast rotating population is already in place at $z = 2$, while the slow rotating population only begins to form. All of the subsequent redshifts show a well-defined fast rotating population.

As the redshift decreases, the slow rotator population becomes statistically more signifi-

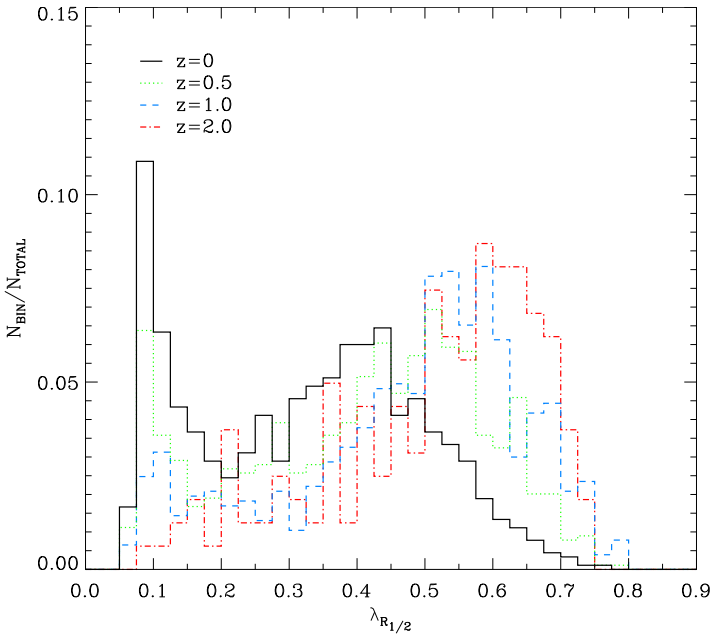

Figure 4.7: Statistical distribution of $\lambda_{R_{1/2}}$ presented as histograms of the relative frequency. The colour distinguishes four redshift as given in the legend.

cant. Therefore, we conclude that the mechanism which leads to the formation of the slow rotators, starts to take effect below $z = 2$. This is consistent with the results from Naab et al. (2014) who found that particularly (multiple minor) merger events after $z = 2$ drive the formation of slow rotating ETGs.

The detailed evolution of $\lambda_{R_{1/2}}$ with redshift can be seen in Fig. 4.7, which shows the histograms of $\lambda_{R_{1/2}}$ for the four considered redshifts. It clearly confirms that the slow rotating population only begins to build up at $z = 2$, and gets more prominent towards $z = 0$: At $z = 2$, the distribution exhibits a clear peak in the range $0.5 < \lambda_{R_{1/2}} < 0.7$, with a decreasing tail towards lower values. Subsequently, at $z = 1$ a peak at $\lambda_{R_{1/2}} \approx 0.1$ close to the resolution limit emerges. In the further evolution, more galaxies drop to the slow-rotator regime, enhancing this peak at the resolution limit value.

In the high-$\lambda_{R_{1/2}}$ regime, we observe a continuous shift of the peak towards lower $\lambda_{R_{1/2}}$, implying a general spin-down of the complete fast rotating population with decreasing redshift. Due to a simultaneous decrease of ϵ, as seen in Fig. 4.6, the complete fast rotating population shifts approximately within the region constrained by the magenta curves. Therefore, the most dominant effect in the evolution of the upper population decreases both $\lambda_{R_{1/2}}$ and ϵ gradually, while the anisotropies do not change, indicating that this mechanism leads to an enhancement of the velocity dispersion while simultaneously shaping the ETGs to be more spherical. The most likely mechanism to be responsible are multiple merger events, again supporting the previously discussed growth mechanisms for ETGs.

Interestingly, the transition region between the fast and slow rotator branch, found in Fig. 4.3, is present at all redshift. This suggests that ETGs, which change their kinematical flavour from 'real' fast rotation to slow rotation, pass through this transition region rapidly. In order to investigate this in more detail we followed the evolution of $\lambda_{R_{1/2}}$ for all slow

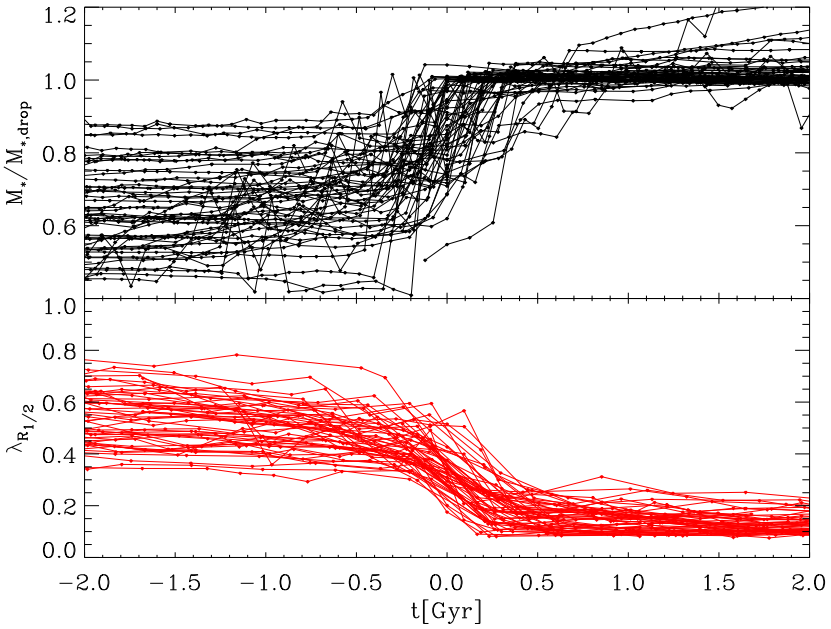

Figure 4.8: *Upper panel:* Temporal evolution of the stellar mass M_* for individual slow rotators which show a rapid decline in $\lambda_{R_{1/2}}$ associated with a merger event in the range between 1:5 and 1:1 representing 30% of all slow rotators. M_* is normalised to the average stellar mass after the drop in $\lambda_{R_{1/2}}$ ($M_{*,drop}$). The time axis is fixed such that the zero point represents the time of the drop. *Lower panel:* Temporal evolution of $\lambda_{R_{1/2}}$ demonstrating the rapid decline.

rotators individually. We find that more than 50% of all slow rotators are formed in a quite short and distinguishable transition from fast to slow rotators. A closer inspections shows, that at least 30% of all slow rotators at $z = 0$ unambiguously underwent this transition on a timescale of less than 0.5Gyr, and exclusively are associated with a significant merger with a mass fraction in the range between 1:5 and 1:1, as shown Fig. 4.8.

On a final side note: Due to several quenching mechanisms and galactic merger events, galaxies can change their morphologies between the considered redshifts from discy to spheroidal. Furthermore, it is theoretically possible for galaxies to re-accrete fresh cold gas and hence become discy again. To ensure that the evolution trends found with redshift are not driven by the underlying classification criteria used at the different redshifts, we show the $\lambda_{R_{1/2}}$-ϵ evolution with redshift for all galaxies in the *Magneticum* simulation in App. 4.C. As can be seen from Fig. 4.21, all reported redshift trends are physical and do not depend on the selection criteria, and are similarly present also for disk-like galaxies.

4.4 Connecting Morphology and Kinematics

4.4.1 The $\lambda_{R_{1/2}}$-ϵ and the M_*-j_* Plane

We want to connect the results deduced in the previous section to the fundamental classification introduced by Fall (1983) and reviewed in Romanowsky and Fall (2012). When investigating a plane spanned by the stellar specific angular momentum $\log_{10}(j_*)$ and the total stellar mass $\log_{10}(M_*)$, they found a continuous linear sequence of morphological types.

Furthermore, they found that LTGs and ETGs follow a parallel sequence with a slope of approximately 2/3, implying a power law relation in the non-log plane. This result was confirmed for a larger sample of galaxies within one effective radius by Cortese et al. (2016). Furthermore these findings are in agreement with recent predictions from cosmological simulations (Genel et al., 2015; Pedrosa and Tissera, 2015; Teklu et al., 2015). Especially Teklu et al. (2015) performed a rigorous investigation of the M_*-j_* plane, considering the same simulated box as this study, introducing the so-called "b-value" defined as

$$b = \log_{10}\left(\frac{j_*}{\text{kpc km/s}}\right) - \frac{2}{3}\log_{10}\left(\frac{M_*}{M_\odot}\right) \tag{4.16}$$

to effectively parametrise the position of a galaxy in the plane, with j_* given by

$$j_* = \frac{|\sum_{j=1}^{N} m_i \ \vec{r}_i \times \vec{v}_i|}{\sum_{j=1}^{N} m_i}. \tag{4.17}$$

This b-value is by definition the y-intercept of a linear function with slope 2/3 in the $\log_{10}(M_*)$-$\log_{10}(j_*)$ plane. As shown by Romanowsky and Fall (2012) and Teklu et al. (2015), at $z = 0$ objects with $b \approx -4$ are disc-like galaxies, followed by a smooth transition to lenticular and elliptical galaxies with decreasing b-value. Therefore, this parameter represents a fundamental connection between three parameters describing a significant part of galaxy formation: the total stellar angular momentum j_*, the total stellar mass M_*, and the present-day morphology. The striking implication of the slope of 2/3 is that, for a given specific angular momentum, which is per definition normalised by the total stellar mass, all different morphologies are possible. We use the b-value as a tracer for the morphology within the *Magneticum* ETGs.

Fig. 4.9 shows the edge-on $\lambda_{R_{1/2}}$-ϵ plane coloured according to b-value. For the calculation of M_* and j_* we used all stellar particles within a sphere of radius $3R_{1/2}$ centred on the galaxy's centre of mass. The mean value for b for the fast rotators is $\overline{b} = -4.7$, while for the slow rotators $\overline{b} = -5.3$, clearly showing that the lower population is dominated by classical spheroidal galaxies. This confirms the evolution towards less disc-like galaxies with decreasing $\lambda_{R_{1/2}}$, as already found in observations and for the progenitors of isolated merger simulation (Bois et al., 2011; Krajnović et al., 2013; Falcón-Barroso et al., 2015).

For the upper population there is a clear trend for the b-value to increase with raising $\lambda_{R_{1/2}}$ and ϵ. The colour gradient seems to evolve continuously along a linear relation indicating a transition from more elliptical-like galaxies towards disc-like morphologies with increasing $\lambda_{R_{1/2}}$ and ϵ. This behaviour also suggests a continuous sequence of accretion histories along the gradient in b, assuming galaxies to usually have high j_* and a disk-like morphology at high redshift. In general, mergers diminish the angular momentum in a moderate fashion while enhancing the stellar mass (Lagos et al., 2017a), leading to a simultaneous decrease of b and $\lambda_{R_{1/2}}$, creating the vertical evolution visible in Fig. 4.9 (see also Choi and Yi (2017a)). Such an effect of merging was already suggested by Romanowsky and Fall (2012) to move within the M_*-j_* Plane. Furthermore, mergers lead to higher dispersions, resulting in a puffed-up galaxy with smaller ellipticity responsible for the horizontal evolution. Therefore, within this scenario, the evolution in b is driven by the amount of merging a galaxy has undergone during its recent assembly. Of course, the path of a galaxy in the parameter space spanned by $\lambda_{R_{1/2}}$, b and $\epsilon_{1/2}$ strongly depends on the configurations of the mergers involved in the formation.

A similar behaviour, however much weaker, is visible for slow rotators: galaxies with the smallest and therefore most elliptical-like b are located in the vicinity of the resolution limit.

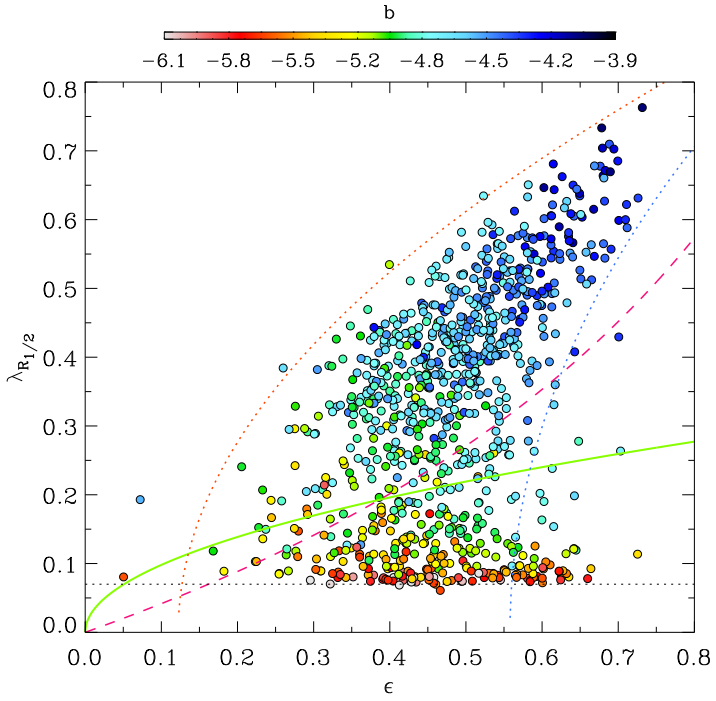

Figure 4.9: Edge-on $\lambda_{R_{1/2}}$-ϵ plane for the *Magneticum* sample with colours indicating the b-value as indicated in the colourbar. The lines are identical to the ones in Fig. 4.6.

To investigate the connection between $\lambda_{R_{1/2}}$ and b in more detail, Fig. 4.10 displays their direct correlation colour (coded by the half-mass radius). It elucidates the conclusion that $\lambda_{R_{1/2}}$ and b are directly correlated. The distribution is well confined by an upper and lower envelope. For $\lambda_{R_{1/2}} \gtrsim 0.3$, the correlation follows a almost linear relationship with a certain scatter. Below $\lambda_{R_{1/2}} \lesssim 0.3$ the dependency gets flatter until resolution effects get significant. Interestingly, this is approximately the threshold between the upper population and the transition population.

Investigating the distribution of $R_{1/2}$ we find that galaxies exhibiting the same $R_{1/2}$ lie on separated relations parallel shifted to the residual $R_{1/2}$ with a continuous transition from lower $R_{1/2}$ at lower b to larger $R_{1/2}$ at higher b. Therefore for a fixed b galaxies exhibiting a higher $\lambda_{R_{1/2}}$ have smaller $R_{1/2}$. This correlation is especially prominent for fast rotating ETGs with $\lambda_{R_{1/2}} > 0.2$, while in the slow rotating regime the correlation is not present. Therefore, the mechanism driving this correlation is only effective for fast rotating ETGs indicating a different formation pathway for fast and slow rotators.

To further explore the functional form of the relation we use a simplified toy model. The model is based on the following assumptions:

- The stellar density follows a Hernquist profile (Hernquist, 1990) given by

$$\rho(r) = \frac{\rho_0}{\frac{r}{r_s}\left(1+\frac{r}{r_s}\right)^3}. \tag{4.18}$$

- The velocity and position vector of the stellar particles are perpendicular to each other

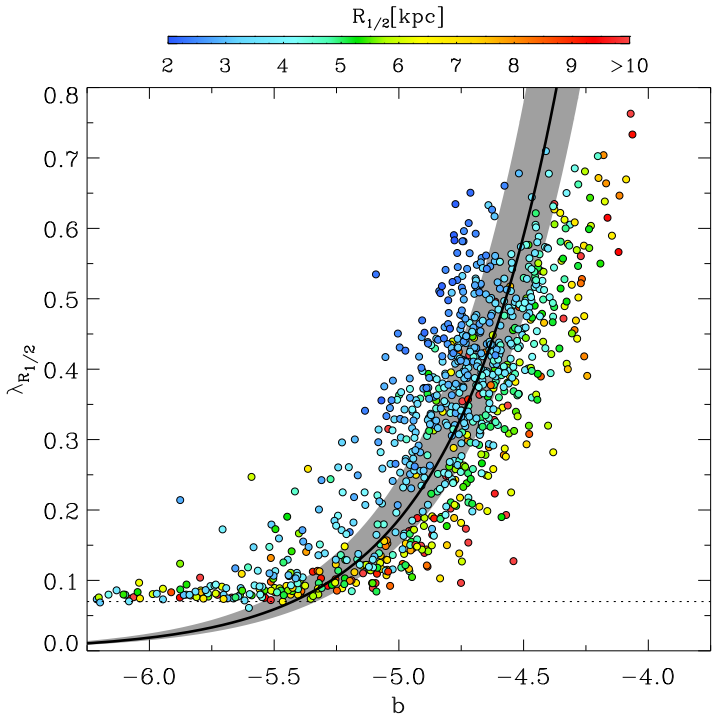

Figure 4.10: Relation between $\lambda_{R_{1/2}}$ and b. The colour corresponds to the half-mass radius as given in the colourbar. The black curve represents the theoretical prediction of the model outlined in Sec. 4.4.1 for a galaxy with $M_* = 5 \cdot 10^{10} M_\odot$. The grey-shaded area indicates the 1σ error adopted from the scatter in the mass-size relation. The dashed black line marks the resolution limit for $\lambda_{R_{1/2}}$.

$\vec{v} \perp \vec{r}$. This conditions constrains the particles to be on circular orbits, however, the planes of rotation can be tilted with respect to each other.

- The rotational velocity v_{rot} and the velocity dispersion σ are spatially constant and are connected by:

$$V_{vir} = \sqrt{v_{rot}^2 + \sigma^2}. \tag{4.19}$$

  This equation states that the total energy in the system obtained from the virial theorem is distributed between ordered and random motion. This relation, however, only holds for systems in virial equilibrium.

- We neglect the projection effects on v_{rot}, σ and $\rho(r)$ occurring in the calculation of $\lambda_{R_{1/2}}$. This is probably the most error-prone assumption.

- We use the mass-size relation determined for the *Magneticum* ETGs in Sec. 4.2.2.

Applying these assumptions, $\lambda_{R_{1/2}}$ simplifies considerably

$$\lambda_{R_{1/2}} = \frac{\int_{\partial A} \rho_p(r) r_p |v_{rot,p}| dA}{\int_{\partial A} \rho_p(r) r_p \sqrt{v_{rot,p}^2 + \sigma_p^2} dA} \approx \frac{|v_{rot}|}{\sqrt{v_{rot}^2 + \sigma^2}}, \tag{4.20}$$

where the subscript p indicates the projected quantities. To calculate b, it is necessary to integrate the stellar angular momentum and the density over the considered volume

$$b = \log_{10}\left(\int_{\partial V} \rho(r)|\vec{r}\times\vec{v}|dV\right) - \frac{2}{3}\log_{10}\left(\int_{\partial V}\rho(r)dV\right). \tag{4.21}$$

The only free parameters we have to feed into the model are M_* and v_{rot}. The result for $M_* = 5\cdot 10^{10} M_\odot$ with varying v_{rot} in the range $[0, V_{vir}]$, and therefore from a completely dispersion dominated system to a purely rotational supported system, is shown as a black curve in Fig. 4.10. The grey-shaded area marks the 1σ scatter adopted from the mass-size relation. The impact of this error suggests that the trend for the scatter with radius is a translation of the scatter in the mass-size relation into this correlation. It is remarkable that this extremely simplified model can already reproduce the generic functional form visible in Fig. 4.10. Down to the resolution limit the black curve resembles the lower and upper envelope for the total distribution seen from *Magneticum* as well as the intrinsic shape for a given $R_{1/2}$.

To investigate whether the correlation found in Fig. 4.10 is already established at higher redshifts, Fig. 4.11 displays its evolution with redshift.

The correlation between $\lambda_{R_{1/2}}$ and b is already present at $z = 2$, however the tail towards lower b is not established yet. At $z = 1$, the tail region starts to be populated, and becomes more prominent at the subsequent redshifts. Generally, we find a clear trend that the low b-values are established parallel to the appearance of the slow-rotator population in ETGs, in line with the results presented in Fig. 4.6 & 4.7. In the fast rotator regime the spin-down in $\lambda_{R_{1/2}}$ is visible, while also a shift towards higher b is present. The shift in b with redshift for disc galaxies was also found by Teklu et al. (2016) in the *Magneticum* simulation, showing the agreement with the theoretical model presented in Obreschkow et al. (2015).

In the lower right panel of Fig. 4.11 we include observations by the SAMI survey (filled diamonds, Cortese et al. (2016)) and a cross-match of ATLAS^{3D} data ($\lambda_{R_{1/2}}$) and data obtained from Romanowsky and Fall (2012) (R12, b-values) shown as open diamonds. In order to obtain the b-values for the SAMI data we extracted stellar masses and the inclination corrected stellar specific angular momentum for the elliptical and S0 galaxies from Fig. 2 in Cortese et al. (2016), while $\lambda_{R_{1/2}}$ is extracted from Fig. 7. The SAMI data is in excellent agreement with the *Magneticum* ETGs as well as with our theoretical toy model. The slight disagreement found in both data sets is most probably caused by inclination effects, since only the stellar angular momentum for the SAMI data is inclination corrected.

At $z = 2$ the ETGs are very compact, as minor mergers as the main driver for an increase of $R_{1/2}$ get more prominent at lower redshifts. This is reflected by the occurrence of more extended ETGs in the further evolution down to $z = 0$. The growth of $R_{1/2}$ with decreasing redshift is in agreement with the observational findings by Huertas-Company et al. (2013). From the evolution of the colour gradient and the width of the distribution we can furthermore conclude that the scatter increases significantly between $2 < z < 1$, followed by a modest increase with decreasing redshift. We checked the evolution of the mass-size relation with redshift and found the same trend in the scatter (see also Remus et al. (2017) for the redshift evolution of the mass-size relation for ETGs in *Magneticum*). This supports the idea that the scatter in the $\lambda_{R_{1/2}}$-b correlation is a reflection of the scatter in the mass-size relation.

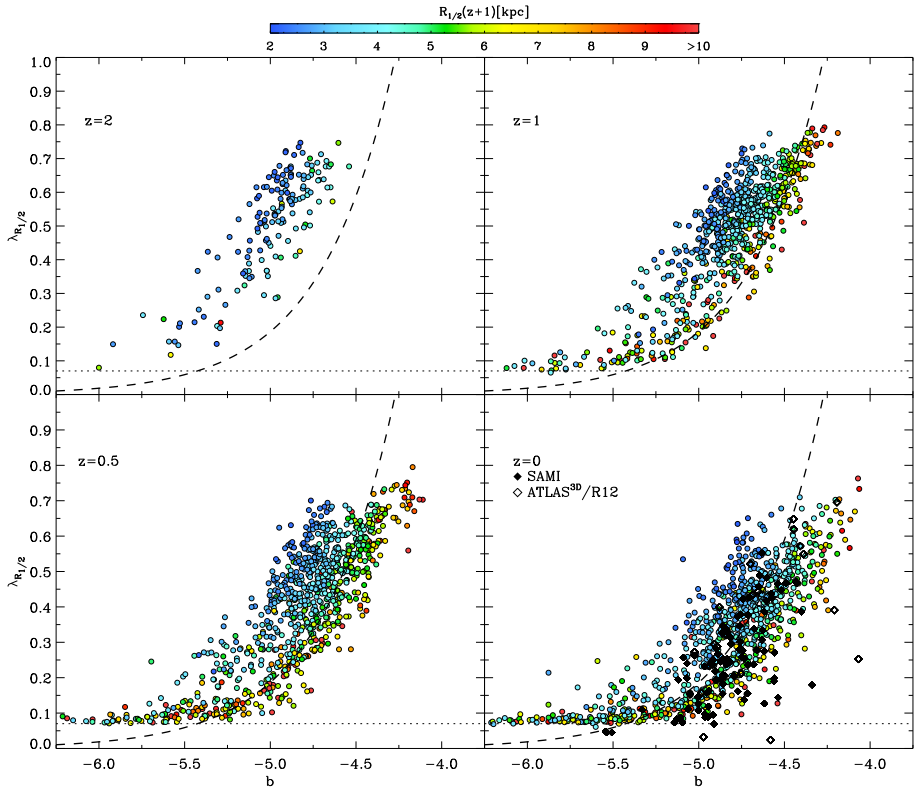

Figure 4.11: The redshift evolution of the correlation between $\lambda_{R_{1/2}}$ and b. Each panel corresponds to one redshift as indicated in the left-upper corner. The colour of the symbols marks the half-mass radius of each galaxy in comoving coordinates as given in the colourbar. In the lower right panel the black diamonds show observations from the SAMI survey (filled diamonds, Cortese et al. (2016)) and a combination of ATLAS^{3D} data ($\lambda_{R_{1/2}}$) and data obtained from Romanowsky and Fall (2012) (R12, b-values) shown as open diamonds. The black dashed line in each panel represents the resolution limit for $\lambda_{R_{1/2}}$, while the thick dashed line shows the relations obtained from our toy model.

4.4.2 Connecting Morphological and Kinematic Properties

Another tracer of a galaxies's morphology is the Sérsic-Index n, since it describes the curvature of the Sérsic-profile fitted to the radial light distribution. The details of the fitting procedure are outlined in Sec. 4.2.4. We investigate the correlation between the Sérsic-Index and the two parameters $\lambda_{R_{1/2}}$ and b.

Fig. 4.12 shows the direct correlation between $\lambda_{R_{1/2}}$ and the Sérsic-Index, while the colour encodes b. We find no clear correlation between n and $\lambda_{R_{1/2}}$, in agreement with observational results found for the ATLAS^{3D} sample presented in Krajnović et al. (2013) for a one component Sérsic fit. In a more recent study Cortese et al. (2016), within the SAMI project, speculate that the scatter in this relation also found in their own sample especially in the slow rotating regime is mainly due to inclination effects. Since we are able to exclude inclination effects by using the edge-on projection, we can disprove this speculation and conclude that there is no significant correlation between $\lambda_{R_{1/2}}$ and the Sérsic-Index. Hence, the Sérsic-Index as a morphological parameter of a galaxy is not a sufficient tracer for the kinematical

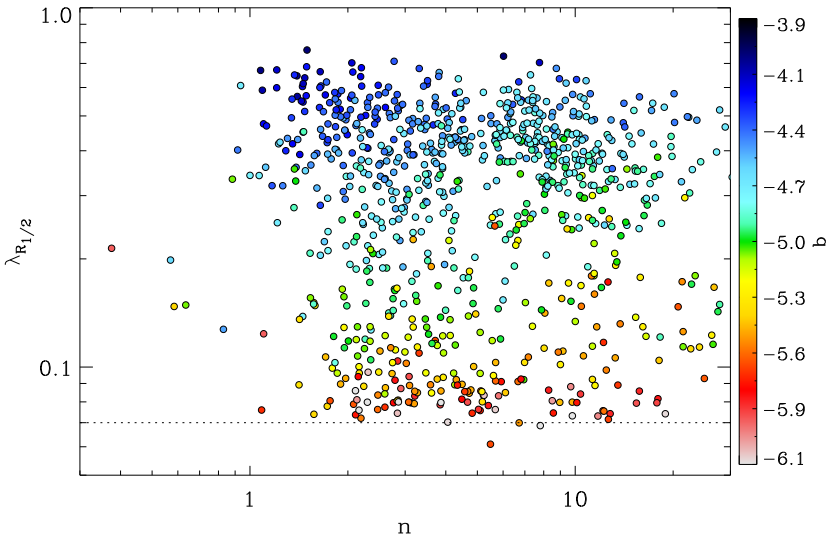

Figure 4.12: Correlation between Sérsic-index n and $\lambda_{R_{1/2}}$. The colour indicates the b-value.

state of a galaxy[4].

We also do not find a correlation between b (see upper panel of Fig. 4.13) and the Sérsic-Index. A weak, shallow, linearly decreasing trend is visible for galaxies with $b > -5.0$ while in the low-b range absolutely no correlation is present. The lower panel of Fig.4.13 explains the origin of the described behaviour by colouring fast (blue) and slow (red) rotating galaxies. A clear trend is visible for fast rotating galaxies with high n to possess a lower b in the more elliptical branch in line with what is found in Cortese et al. (2016). In contrast, the slow rotators populate the diffuse low-b region, causing the uncorrelated part of the distribution. This is again demonstrating the fundamental difference between fast and slow rotators, populating different regions of the b-n-plane.

The black symbols in the lower panel of Fig. 4.13 depict observational results from the SAMI survey (filled diamonds, Cortese et al. (2016)) and R12 (open diamonds). In the SAMI data we again only include elliptical and S0 galaxies. The *Magneticum* ETGs are in good agreement with the SAMI observations, while a significant fraction of the R12 data shows higher b-values. The disagreement with the R12 observations is most probably due to projection effects, since the angular momentum is not corrected for inclination.

4.5 Kinematical Groups

Motivated by the fundamental findings of Krajnović et al. (2011) we investigate the specific kinematical features of the line-of-sight velocity maps. The authors in that observational study define six kinematical groups based on features in the velocity maps (see Sec. 4.1 for the definition of the kinematical groups) and investigate their connection to internal properties of ETGs.

[4]However, a direct comparison of Sérsic-Indices obtained from simulations and observations has to be interpreted with caution, as they probe different radial regimes of the galaxies, since simulations do not resolve the innermost part of the galaxies while observations have difficulties in detecting the faint, low-luminosity outskirts of the galaxies.

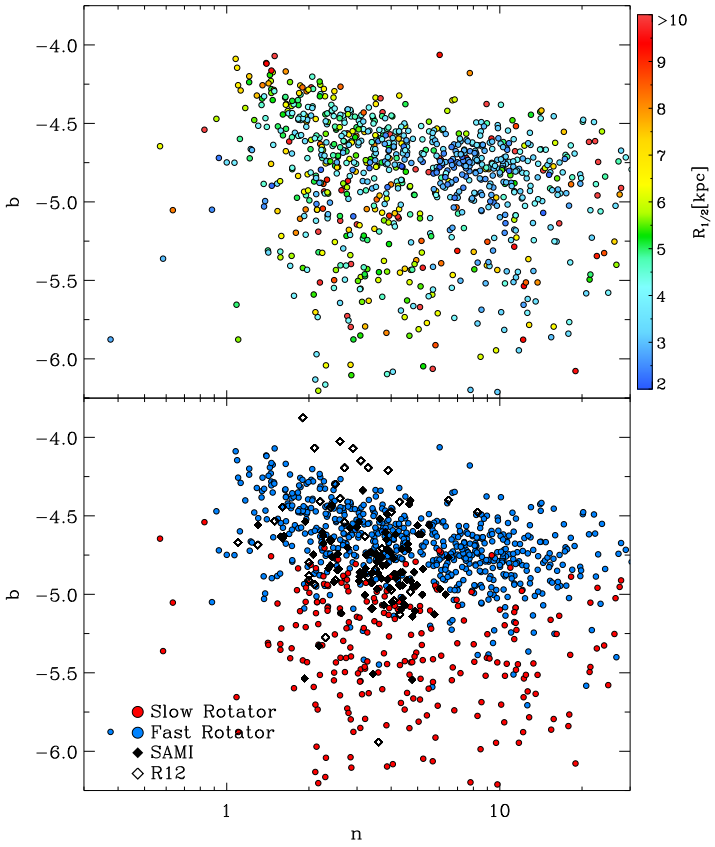

Figure 4.13: Correlation between Sérsic-index n and b-value. *Upper panel:* Colours according to $R_{1/2}$. *Lower panel:* Colours code fast rotators (blue-filled circles) and slow rotators (red-filled circles). Black filled diamonds show observations from the SAMI survey extracted from Cortese et al. (2016), while the open diamonds represent observations from R12.

4.5.1 Classification and Group Frequency

The classification method applied in this study rests upon a visual inspection of each individual velocity map in the edge-on projection. The class of 2σ galaxies is not considered. To reduce possible bias, each velocity map was classified independently by three persons. Discrepancies were solved by either assigning the class with two votes to the galaxy or, in the case of a complete disagreement, a collective reconsideration. The galaxies were classified into the following groups:

- *Regular Rotator (RR)*: The velocity map shows a well defined, ordered rotation around the minor axis, with no kinematical features.
- *Non Rotator (NR)*: The velocity map exhibits no distinct kinematical feature and low-level velocities.
- *Distinct Core (DC)*: The velocity map features a central rotating component surrounded by a low-level or non-rotating component.
- *Kinematically Distinct Core (KDC)*: The velocity map shows a central rotating compo-

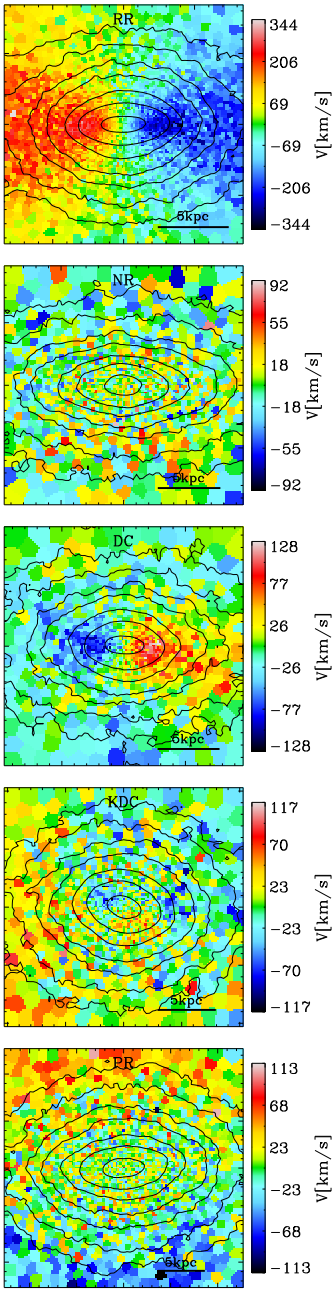

Figure 4.14: Example velocity maps for the 5 kinematical groups defined in Sec. 4.5 from top to bottom: Regular Rotator, Non Rotator, Distinct Core, Kinematically Distinct Core, and Prolate Rotator. Each map is voronoi binned to ensure a proper number of particles per bin. The scaling of the velocity is shown in the colour bar. The shown areas encompasses one half-mass radius, and the galaxies are rotated such that the long axis is along the x-direction. The solid black lines represent contours of constant density.

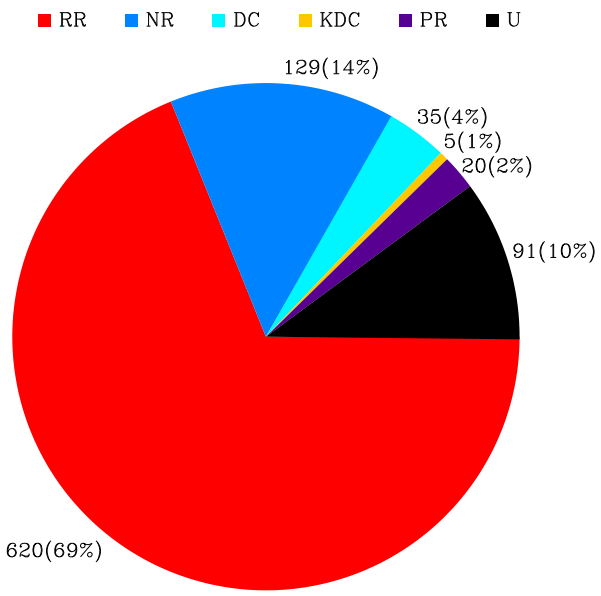

Figure 4.15: The statistical distribution of the different kinematical groups within the *Magneticum* ETGs: red are Regular Rotators, blue are Non Rotators, turquoise are Distinct Cores, yellow are Kinematically Distinct Cores, and lilac are Prolate Rotators. Unclass are shown in black.

nent surrounded by a region with inclined rotation with respect to the central component. This explicitly includes counter-rotating cores.

- *Prolate Rotator (PR)*: The velocity map shows ordered rotation around the major axis of the galaxy.

- *Unclass (U)*: The galaxy cannot be assigned to any of the previous groups.

For each class, Fig. 4.14 displays an example of a voronoi-binned line-of-sight velocity map, except for the U class. The statistical frequency of each class is summarised in a pie chart in Fig. 4.15. In agreement with observations, the RR are the most common group in the *Magneticum* sample (69%) followed by the NR (14%). 4% of the *Magneticum* ETGs are assigned to the class of DC corresponding to 35 objects. The reason for the low number of five KDCs (1%) is most probably a resolution issue, since KDCs in ATLAS^{3D} are located in the very centre of the galaxy, which is not resolved in the simulation.

The group of PR contains 20 galaxies, which corresponds to 2% of the total sample. Preliminary results from the M3G-project using the MUSE instrument suggest that at stellar masses above $10^{11.5} M_{\odot}$ those galaxies are more frequent. The PRs in our sample follow a similar mass distribution, being more prominent at higher masses, with a significant increase around $10^{11.5} M_{\odot}$ (see middle panel of 4.20). This is in good agreement with the results from ATLAS^{3D} and CALIFA sample which show a rise in the prolate rotator fraction in the same mass regime, reported in Tsatsi et al. (2017). Interestingly, the number of PRs is rather constant over the complete mass range covered by the *Magneticum* ETGs (see upper panel of 4.20). This implies, that the increase in the fraction of PRs with higher mass is due to the decrease of the number of other objects. This is in agreement with results found in the Illustris simulation (Ebrová and Łokas, 2017). Thus, we conclude, that *Magneticum*

represents a powerful tool to investigate their formation and compare to upcoming results from M3G, MASSIVE, CALIFA and MaNGA, which will be addressed in a future paper.

A direct comparison to the results by Krajnović et al. (2011) is difficult due to the differences in the underlying classification mechanism. Especially the group of PR is not included in the ATLAS^{3D} classification. Furthermore, many of the kinematical features found in the ATLAS^{3D} reside within $0.5R_{1/2}$, which, for various of the *Magneticum* ETGs, is in the region where spatial resolution issues become relevant and it is not possible to detect features which are smaller than the spatial resolution of the velocity map. In order to explore the impact of mass resolution on the velocity maps we applied a bootstrapping algorithm to galaxies with the smallest amount of stellar particles. It revealed that the kinematical features in our sample are not sensitive to the particle binning.

4.5.2 Kinematical Groups and Global Galaxy Properties

The distribution of the five kinematical groups in the $\lambda_{R_{1/2}}$-ϵ plane is shown in the central panel of Fig. 4.16 for the edge-on projection, while the sideways panels display cumulative distributions of $\lambda_{R_{1/2}}$ and ϵ with a different linestyle for each group. As expected the NR they exclusively populate the low-$\lambda_{R_{1/2}}$ regime, while spanning a wide range of ϵ with a peak at $\epsilon \approx 0.35$ and are slow rotating. The RRs populate the fast rotating regime, with only a small number of objects in the slow rotating region. The slow rotating RRs show a RR velocity pattern, however their dispersion maps reach higher values than those of the fast rotating RRs, with a comparable rotational velocity, effectively causing the low $\lambda_{R_{1/2}}$ values. Four of the five KDCs found in the *Magneticum* ETGs are, in agreement with ATLAS^{3D} observations, classified as slow rotators, while one KDC lays close to the threshold.

For the DCs, the distribution is not as obvious as for the other classes. They span the complete $\lambda_{R_{1/2}}$ range up to ≈ 0.5, with a larger fraction in the fast rotating regime. The reason for the wide spread within this class is the strong difference in the spatial extend of the rotating component: since the non-rotating surrounding is causing a lower $\lambda_{R_{1/2}}$-value the total $\lambda_{R_{1/2}}$ decreases with smaller radial extend of the rotating component. The DCs with the slowest rotation have small rotating discs in the centre, with an extent of only a third of $R_{1/2}$.

Except for three members, all PRs are located in the slow rotating regime. This is an unexpected behaviour since per definition the stars show a distinct rotation around a common axis. However, a similar behaviour was found for prolate rotating galaxies in the Illustris simulation as presented in Li et al. (2018a). Therefore, slow rotation seem to be a fundamental property of PRs. Detailed Schwarzschild modelling of the prolate rotating galaxy NGC 4365 by van den Bosch et al. (2008) gives a hint at origin of the slow rotation. The modelling shows that most of the stars are rotating around the minor axis, however approximately an equal fraction of stars are on prograde and retrograde orbits leading to a low net angular momentum and high velocity dispersion. Although the stars rotating around the major axis are only a minor contribution their angular momentum dominates the appearance of the velocity field.

As the formation of those objects is still a matter of debate, we can only speculate about the origin of the low $\lambda_{R_{1/2}}$ values. From basic physics it is clear that smoothly accreted gas cooling to the centre of a halo always forms a disk rotating around the minor axis. Therefore, the most probable mechanisms to form prolate rotation are galaxy mergers or a flyby interaction with another galaxy. In the context of dwarf spheroidal galaxies, Ebrová and Łokas (2015) showed that mergers of two dwarf disk galaxies can indeed result in prolate rotation,

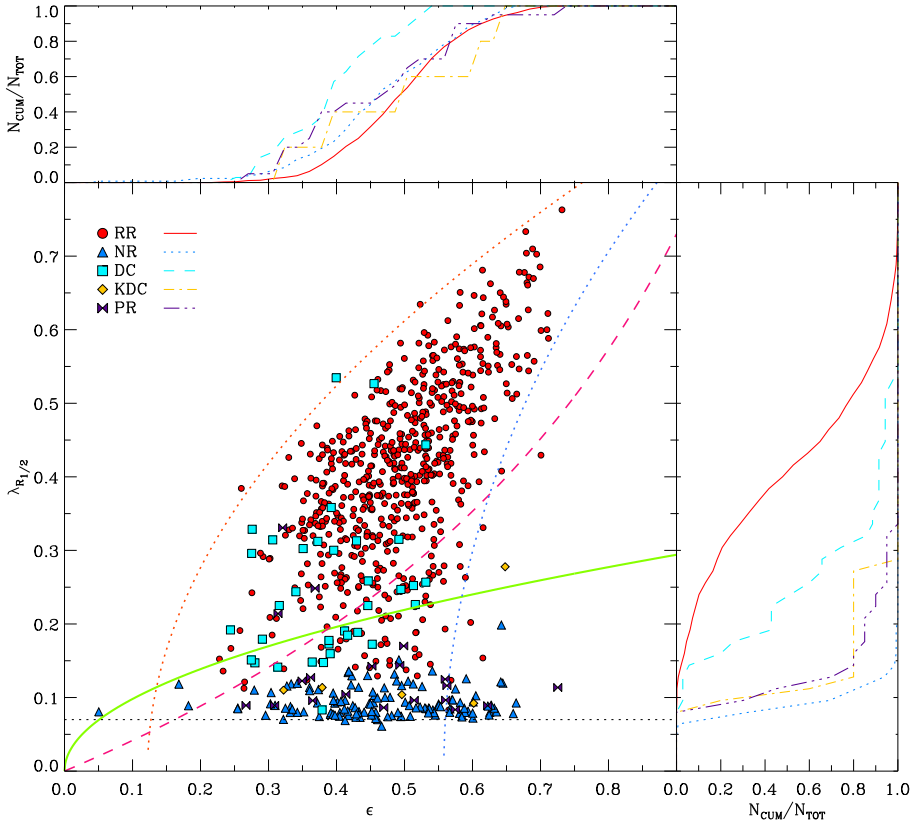

Figure 4.16: *Main panel*: The $\lambda_{R_{1/2}}$-ϵ plane for the *Magneticum* ETGs subdivided into the kinematical groups defined in Sec. 4.5 at $z = 0$: red circles are PR, blue triangles are NR, turquoise rectangles are DC, yellow diamonds are KDC, and lilac bow ties are PR. The lines are as in Fig. 4.9. *Side panels* show the cumulative number of galaxies (N_{CUM}) normalised by the total number of galaxies (N_{TOT}) of the respective sample split up into the various kinematical groups.

using a collisionless N-Body simulation. They found the most significant prolate rotation in the remnant of a nearly face-on merger of two identical disk dwarfs on a perfectly radial orbit. In a pure N-Body simulation with this settings, the prolate rotation is a consequence of angular momentum conservation around the merger axis. The possibility to form PRs in binary N-Body simulations of more massive non-dwarf galaxies is shown in Tsatsi et al. (2017), where the authors form PRs in a polar merger with the amplitude of prolate rotations depending on the bulge-to-total ration of the progenitors. Of course, the scenario gets significantly more complicated when involving a gaseous component and allowing for non-radial orbits in a fully cosmological environment: Ebrová and Łokas (2017) showed that in the fully cosmological Illustris simulation the merger configurations leading to prolate rotation span a large parameter space in regarding mass ratio, merger time, radiality of the progenitor orbits, and the relative orientations of spins of the progenitors with respect to the orbital angular momenta. Furthermore, they find that about 50% of their prolate rotators were formed during a gas-rich merger.

To further explore the properties of the kinematical groups, Fig. 4.17 shows the three correlations investigated in the previous sections, split up into the kinematical groups. The upper left panel shows the between $\lambda_{R_{1/2}}$ and the Sérsic-index. None of the groups shows

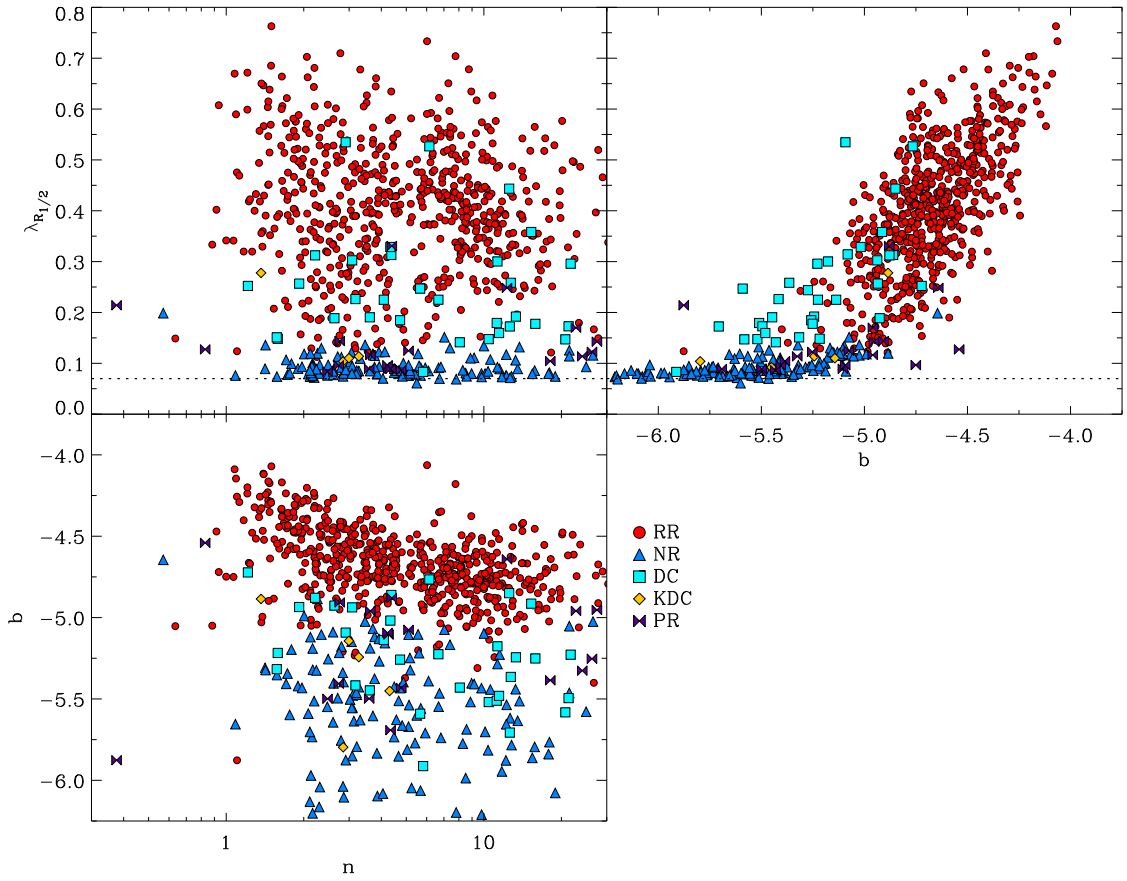

Figure 4.17: Various parameter correlations split up into kinematical groups. *Left upper panel*: Correlation between $\lambda_{R_{1/2}}$ and Sérsic index. *Right upper panel*: Correlation between $\lambda_{R_{1/2}}$ and b. *Left lower panel*: Correlation between b and Sérsic index. In the upper row the black dashed line marks the resolution limit for $\lambda_{R_{1/2}}$.

a correlation between those parameters. Except for the KDC, which have n in the range $1 < n < 4$, all groups populate a large range in n. Hence, the formation of the various kinematical features do not leave a signature in the stellar density profile out to large radii. We want to allude, that the region where the defining features for the kinematical groups are located is explicitly excluded from the fitting range. Therefore we can not exclude to find group specific features in the stellar density profile when investigating only the central region within one half-mass radius.

In the correlation between n and b (lower left panel of Fig. 4.17) we see that the uncorrelated lower region is build up by the NR, DC, KDC and PR, while the correlation is build up by the RR. We can furthermore conclude, that RR exhibit more disc-like b-values than all the other kinematical groups, while the b-value cannot be used to distinguish the other kinematical groups from each other.

This is also visible in the upper right panel where the connection between b and $\lambda_{R_{1/2}}$ is displayed. The only group which populates a distinct region in this plane are the RRs. Interestingly, the special group of PRs covers a large range in b, not reaching the high disc-like values.

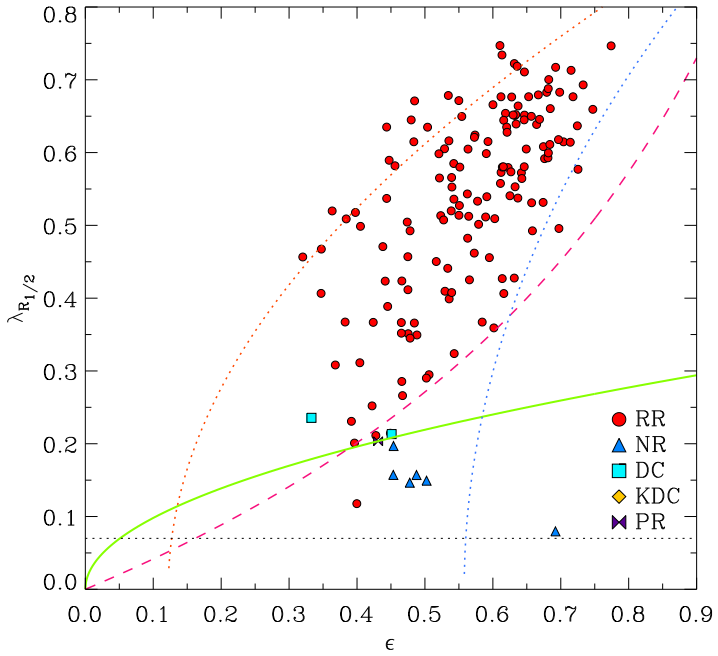

Figure 4.18: *Main panel:* The $\lambda_{R_{1/2}}$-ϵ plane for the *Magneticum* ETGs subdivided into the kinematical groups at $z = 2$. The lines are the same as in Fig. 4.16.

Therefore, we conclude that it is not possible to disentangle the kinematical groups using global galaxy parameter. This suggests that the signature of their respective formation histories are encoded in local parameters restricted to the central region of the galaxy.

4.5.3 Kinematical Groups at $z = 2$

For the 161 galaxies classified as ETGs at $z = 2$, we apply the same classification according to the kinematical features as for the ETGs at $z = 0$. From these 161 ETGs, 158 had maps resolved enough for such classifications, while only 3 could not be classified. Fig. 4.18 shows the $\lambda_{R_{1/2}}$-$\epsilon_{R_{1/2}}$ plane for the ETGs at $z = 2$, with different symbols and colours marking the same kinematical groups as before. Most of the ETGs at $z = 2$ are regular rotators (92%), and nearly all fast rotators belong to this kinematical group. Only two fast rotators do not classify as regular rotators but have a clearly visible decoupled core. Both galaxies with decoupled cores live in the transition region, however, it is not possible to conclude from only two objects a "typical" behaviour.

As can clearly be seen, all galaxies (but two) that belong to the slow rotator regime are classified as non-rotators (4%) suggesting that the split-up between non-rotators and fast-rotators is already established at $z = 2$. Interestingly, we find a galaxy that already exhibits a prolate rotation at $z = 2$. We trace this galaxy from $z = 2$ to $z = 0$ and find that the prolate rotation of this object is present at all redshifts, and that its $\lambda_{R_{1/2}}$ does not change much with time. In our sample at $z = 2$, there is no galaxy with a kinematically distinct core, however, these galaxies are also rare at $z = 0$ and thus the lack of such galaxies in our box at $z = 2$ does not indicate that such galaxies cannot exist at $z = 2$.

We conclude that the most common kinematical classes are already present at $z = 2$, and

that regular rotators are more frequent at higher redshifts, in agreement with the current picture of non-rotator formation. Furthermore, we already find special kinematic features like decoupled cores and prolate rotation at $z = 2$, proving that the formation pathways that produce such kinematical features can also occur at redshifts higher than $z = 2$. As all our ETGs have gas fractions below $f_{\rm gas} = 0.1$, none of these galaxies classify as blue nuggets, but several of them have rather small half-mass radii and as such classify as red nuggets.

4.6 Summary and Conclusion

Recent observations revealed a shift in the existing paradigm for early-type galaxies, away from the classical morphological separation into elliptical galaxies and S0 mostly driven by the observed ellipticities, towards a classification based on fundamental kinematical properties. The picture of early-type galaxies to be kinematically unimpressive has been revolutionised by observing a richness of complex kinematical structures, suggesting a variety of formation histories.

In this study we investigated the kinematical properties of a sample of 900 early-type galaxies at $z = 0$ extracted from the *Magneticum Pathfinder* simulation, which are a set of hydrodynamic simulations performed with the Tree/SPH code GADGET-3. We selected all galaxies with $M_* > 2 \cdot 10^{10} M_\odot$ and a cold gas fraction below $f_{\rm gas} < 0.1$, to ensure maximal comparability to the galaxy selection process adopted for the observations. Furthermore, we follow the evolution of the properties of ETGs from $z = 2$ to $z = 0$ in a statistical manner applying the same selection criteria.

To characterise the kinematical state of the *Magneticum* ETGs, voronoi-binned line-of-sight velocity maps were constructed and $\lambda_{\rm R_{1/2}}$ is calculated for all galaxies. In addition, we investigate our sample with regard to various parameters characterising ETGs like the b-value, anisotropy, ellipticity, and Sérsic-index.

In the first step we compare the distribution of our sample at $z = 0$ in the $\lambda_{\rm R_{1/2}}$-ϵ plane to the distribution found by ATLAS$^{\rm 3D}$, CALIFA, SLUGGS and SAMI. With 70% of the sample being classified as fast rotators and 30% as slow rotators, *Magneticum* successfully reproduces the observed strong trend of fast rotators being the dominant kinematical state of early-type galaxies. While the overall distribution is in quantitative agreement with observations, the simulation generates a non-negligible fraction of elongated SR with $\epsilon > 0.4$ that is not found in the observed sample. However, this seems to be a common feature of numerical simulations since this issue was already reported in previous studies (Bois et al., 2010; Naab et al., 2014; Penoyre et al., 2017).

While the observations are constrained to the fixed given projection on the sky, we investigate the $\lambda_{\rm R_{1/2}}$-ϵ plane in the more physical edge-on projection. We find that in the edge-on projection two distinct populations are present, clearly separated by an underpopulated region. In substantial agreement with the theoretical prediction by Cappellari et al. (2007) the vast majority of the fast rotators lie above the $\delta = 0.8\epsilon_{\rm intr}$ curve, which represents the steepest allowed relation according to the analytic model presented in Cappellari et al. (2007).

Furthermore, we investigate the anisotropy distribution of the *Magneticum* ETGs in the $\lambda_{\rm R_{1/2}}$-ϵ plane considering a analytic model and true anisotropies, calculated from the particle distribution. We find a substantial agreement between the model predictions and the true anisotropy allowing to determine the anisotropy of a galaxy from the position in the edge-on $\lambda_{\rm R_{1/2}}$-ϵ plane. The fast rotating population is very well encompassed by the two limiting

curves of the model prediction for a constant anisotropy of 0.1 and 0.5 and the empirical fast-slow rotator separation curve.

Studying the evolution of the $\lambda_{R_{1/2}}$-ϵ plane with redshift, we find that the fast rotating population is already in place at $z = 2$, while only a small fraction of ETGs occupy the slow rotating regime. With decreasing redshift, the statistical frequency of the SR increases gradually from 8% to 30%. We therefore conclude that the mechanism which forms slow rotators becomes more frequent at redshifts below $z = 2$. Accordingly, the frequency of fast rotators decreases from 92% at $z = 2$ to 70% at $z = 0$. This strongly indicates that dry (minor) merger events play an important role in the formation of slow rotators as discussed in previous studies (Moody et al., 2014; Naab et al., 2014). Investigating the evolution of $\lambda_{R_{1/2}}$ for individual slow rotators we find that at least 30% of the slow rotators at $z = 0$ experience a rapid decrease of $\lambda_{R_{1/2}}$ on a timescale of 0.5Gyr associated with a significant merger event.

Considering the fast rotators, we find the general trend of a spin-down and a shift towards rounder shapes, consistent with the findings of Choi and Yi (2017a). The described behaviour is also present when considering all galaxies that satisfy the resolution criteria (i.e. disks and galaxies undergoing a merger event). Clearly demonstrating that the recent formation of the slow rotating population and the spin-down are not due to a galaxy selection bias but in fact driven by physical processes in the low-z Universe.

We show that, adopting the b-value from Teklu et al. (2015), the fundamental M_*-j_* plane is tightly connected to the $\lambda_{R_{1/2}}$-ϵ plane. The continuous change of the b-value in the $\lambda_{R_{1/2}}$-ϵ plane implies a simultaneous movement in both planes when a galaxy is influenced by external processes like merging, harassment or stripping. We suggest merging as a possible process that is able to cause the observed distributions in both planes.

We find a strong correlation between $\lambda_{R_{1/2}}$ and the b-value. This correlation and the associated scatter is already in place at $z = 2$. Using a toy model to estimate the functional form of the correlation, we show that the scatter in the relation is inherited from the scatter in the mass-size relation.

In order to investigate the connection between morphology and kinematics, we determine the Sérsic-index n as a proxy for the morphology of galaxies. We recover the general trend found in Krajnović et al. (2013) that ETGs with $n < 1.5$ are preferentially classified as fast rotators, while n is not adequate to disentangle fast and slow rotators.

Furthermore, we classify the *Magneticum* ETGs into five kinematical groups according to visual features in their velocity maps. Our sample includes all features stated in Krajnović et al. (2011), except for the 2σ galaxies which by definition are not considered in our study. 69% of our ETGs show a regular rotation pattern in excellent agreement with observational results. The class of non-rotating ETGs comprise 14% of the *Magneticum* ETGs, while 4% exhibit a distinct core and 1% show a kinematically distinct rotating core in the centre.

We find a non-neglectable number (20) of ETGs which show prolate rotation around the morphological major axis. Although this only represents a small fraction of 2% of our total sample their existence confirms that *Magneticum* comprises all the physics to form those observationally discovered objects. Interestingly, except for three galaxies, all PRs are classified as slow rotators. Investigating the mass dependence of the PR fraction we find a relatively flat distribution in the range $10.3 < \log(M_*) < 12$. In contrast, the fraction of the other groups decreases significantly leading to a rise of the fraction of prolate rotators. The increase in the statistical frequency of prolate rotators is in agreement with recent observational results of CALIFA and ATLAS^{3D}, as reported in Tsatsi et al. (2017) and theoretical results from the

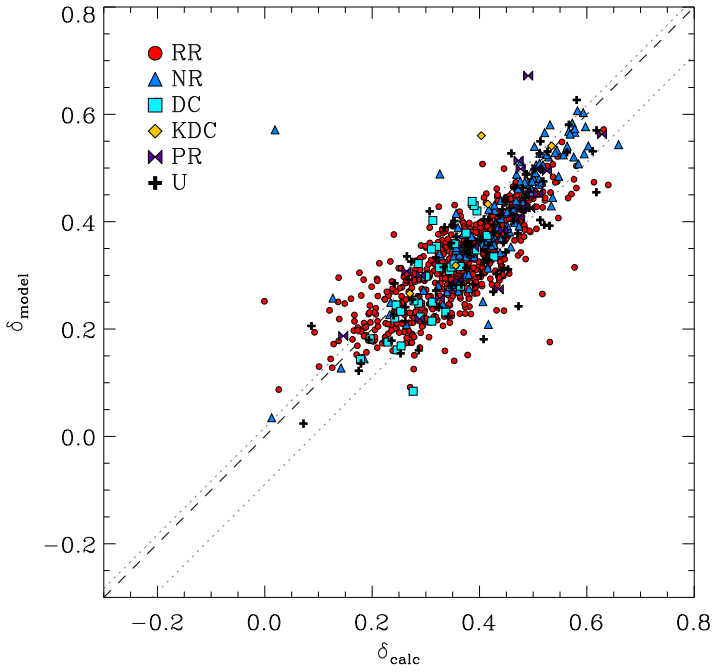

Figure 4.19: Real anisotropy δ_{calc} calculated from the particle distribution using Eq. 4.10 against anisotropy obtained from the theoretical model δ_{model} using Eq. 4.11, for each ETG. The colours and symbols show the different kinematical groups, as described in the legend and Sec. 4.5.1. The grey dotted lines show the orthogonal 1σ scatter with respect to the 1:1 relation (dashed black line).

Illustris simulation (Ebrová and Łokas, 2017).

4.A Theoretical versus Real Anisotropy in ETGs

In Sec. 4.3.3, we discussed the differences between the global anisotropy of an ETG calculated directly from the stellar particles, and the global anisotropy obtained from theoretical modelling using Eq. 4.11. Fig. 4.19 shows the correlation between both anisotropies found for each ETG in the *Magneticum* sample. There is a clear, almost 1:1, correlation between these anisotropies (dashed line in Fig. 4.19) with a weak trends for $\delta_{\rm calc}$ to be slightly larger than $\delta_{\rm model}$. This is reflected in the orthogonal antisymmetric 1σ scatter of $(0.016, -0.089)$ with respect to the 1:1 relation (grey dotted lines in Fig. 4.19).

The symbols in Fig. 4.19 demonstrate the aforementioned effect, that slow-rotators tend to have slightly higher anisotropies than fast rotators as can be seen in that the non-rotators generally occupy the area of higher anisotropies than the regular rotators in both anisotropy-measurement methods. The ETGs with decoupled cores tend to have smaller anisotropies than the non-rotators, populating the regular rotator regime, in both anisotropy methods. Prolate rotators occupy the same anisotropy-range as the other classes, showing no distinct difference in the anisotropy behaviour.

We also tested the anisotropy correlation for the galaxies where a kinematical classification was not possible, but we did not find any difference in their behaviour with respect to the correlation between the real and the calculated anisotropies.

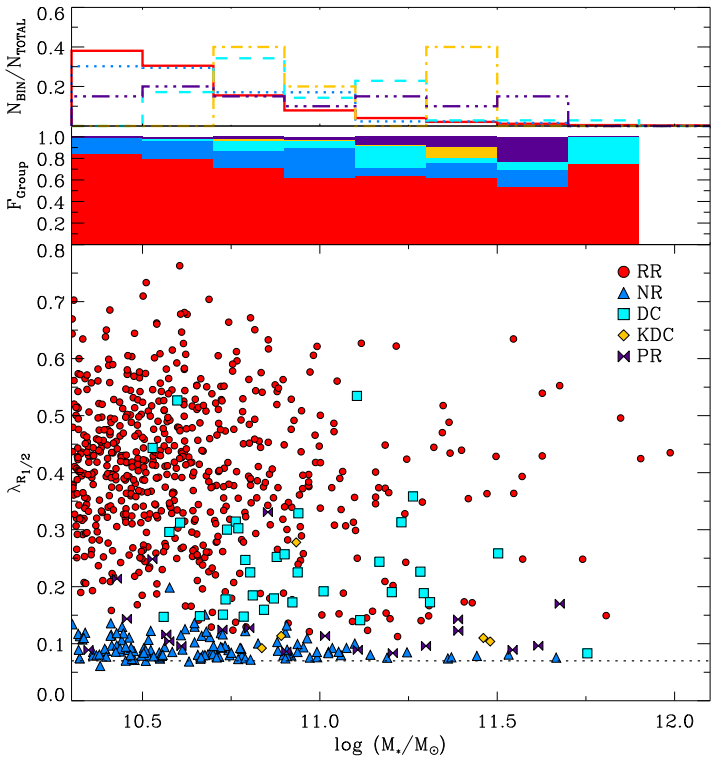

Figure 4.20: *Lower (main) panel*: $\lambda_{R_{1/2}}$ versus M_* for all ETGs in the *Magneticum* simulation. Regular Rotators (RR) are shown as red filled circles, Non-Rotators (NR) as blue filled triangles, Decoupled Core (DC) galaxies as cyan filled squares, Kinematically Distinct Core (KDC) galaxies as yellow filled diamonds, and Prolate Rotators (PR) as violet filled bowties. *Upper panel*: The number of galaxies of a certain kinematical group at different stellar mass bins normalised by the total number of galaxies within each group. The different kinematical groups are colour-coded according to the symbol colour in the lower panel. *Middle panel*: Relative percentage of each kinematical group at the different stellar mass bins, colour-coded as in the lower panel.

4.B $\lambda_{R_{1/2}}$–M_* Relation

Observations revealed that very massive ETGs usually tend to be round and often slowly rotating ETGs, while the high $\lambda_{R_{1/2}}$ range is preferentially populated by less massive galaxies (e.g. Emsellem et al., 2011). One possible explanation for this behaviour is the formation of such massive systems through multiple minor merger (e.g. Naab et al., 2014; Moody et al., 2014). However, more recently, Ebrová and Łokas (2017) showed that many of the highest massive systems are prolate rotating, albeit the formation channel of these systems is still under debate, as discussed in Sec. 4.5.2.

The main panel (lowest) of Fig. 4.20 shows $\lambda_{R_{1/2}}$ against the stellar mass M_* for all ETGs (upper panel), with colours and symbols indicating the different kinematical groups introduced in Sec. 4.5.1. As can clearly be seen, the regular rotating galaxies dominate the lower mass regime, while non-rotators are present but not common. At the high-mass end, the regular rotators become less dominant, while the fraction of galaxies with decoupled cores or prolate rotation increases (as can also be seen from the middle panel of Fig. 4.20, where the relative fractions of the different kinematical groups within each mass bin are shown). Especially the prolate rotators account for a significant fraction of the ETGs at the high-mass end, in good

agreement with recent observations by Tsatsi et al. (2017). The fraction of non-rotators, interestingly, is at about 10% regardless of the stellar mass, clearly showing that non-rotators occur on all mass bins. Nevertheless, at the highest mass bin above $M_* = 10^{11.75} M_\odot$, where the number of galaxies in the simulation is low, all ETGs are regular rotators with high values of $\lambda_{R_{1/2}}$, in contrast to observations.

The upper panel of Fig. 4.20 shows the number of ETGs within a given kinematical group in each mass bin, normalised to the total number of all ETGs of that group. Both, regular rotators and non-rotators, are most frequent at the low-mass end, and become less frequent with increasing mass. On the contrary, distinct cores and kinematically distinct cores are features that become much more frequent at the higher mass end, albeit this could be a result of the resolution limitation of the simulation, as the sampling of particles at the low-mass end enhances the noise in the kinematical maps and therefore could suppress the signal of such features in the maps.

However, most interestingly, the relative number of prolate rotators is constant over all mass bins. Thus, while prolate rotators become more frequent at the high-mass bin due to the decreasing number of galaxies with other kinematic features, their effective occurrence is independent of the mass, which is clearly in agreement with the observational fact that such prolate rotating galaxies are also seen at the dwarf-galaxy mass end (Ho et al., 2012; Ebrová and Łokas, 2015). Therefore, a more detailed investigation of the formation mechanisms that lead to prolate rotation features, is needed in the future.

4.C Redshift Evolution of the $\lambda_{R_{1/2}}$-ϵ Distribution for all Galaxies in the *Magneticum* Simulation

As the classification criteria for galaxies into early- and late-type galaxies strongly vary between different surveys and especially redshifts, it is important to demonstrate that the redshifts trends found for galaxies in the $\lambda_{R_{1/2}}$-ϵ-plane in this paper are not biased by the classification. Therefore, Fig. 4.21 shows the same as Fig. 4.6, but for all galaxies in the *Magneticum* simulation above the resolution limit. Those galaxies that were classified as ETGs are shown as circles, while the galaxies that were rejected (see Sec. 4.2.1 for the classification criteria) are shown as diamonds, independent whether they are disk-like galaxies, merging systems, or rejected due to other reasons.

As can be seen, there is a clear tendency for all galaxies regardless of their morphology, to have higher $\lambda_{R_{1/2}}$ (and thus be more rotation dominated) and larger ellipticities at higher redshifts, clearly indicating that there exists a general spin-down for disk galaxies towards lower redshifts as well. This indicates that also disk galaxies might suffer from multiple minor merger event, without destroying the disk-like structures (see e.g. Karademir et al., 2019). At $z = 2$, the slow-rotator regime remains nearly empty, and is populated subsequently at lower redshifts with the advent of more massive galaxies and an increasing fraction of ETGs. At all redshifts, the higher-$\lambda_{R_{1/2}}$-regions are occupied by rejected galaxies (as expected since these galaxies include the disk-like galaxies).

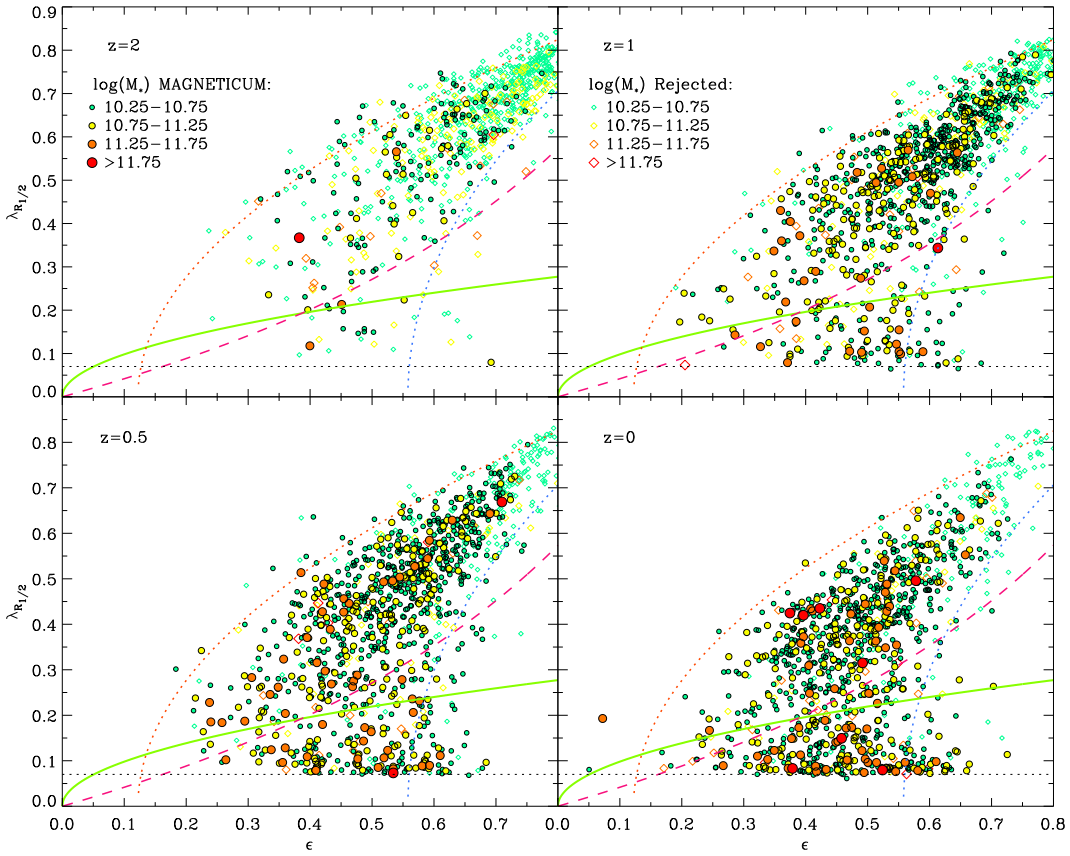

Figure 4.21: $\lambda_{R_{1/2}}$-ϵ-plane for all galaxies satisfying the resolution criteria, with *Magneticum* ETGs shown as filled circles and the rejected galaxies shown as open diamonds. Different colours and symbol-sizes indicate the mass of the galaxy. Upper left panel: $z = 2$; upper right panel: $z = 1$; lower left panel: $z = 0.5$; Lower right panel: $z = 0$. Lines are as in Fig. 4.6.

Chapter 5

Kinematics, Stability and Lifetime of a Kinematically Distinct Core

This chapter has been published by Schulze et al. (2017) [1]

Abstract

We present a case study of a early-type galaxy (ETG) hosting a kinematically distinct core (KDC) formed in a binary high resolution 1:1 spiral galaxy merger simulation. The runtime of the simulation is pushed up to 10 Gyr to follow the complete evolution of various physical properties. To investigate the origin of the KDC, the stellar component residing within the KDC is dissected, revealing that the rotational signal is purely generated by stars that belong to the KDC for at least 0.5 Gyr and are newly formed during the merging process. Following the orientation of the total stellar angular momentum of the KDC, we show that it performs a motion comparable to the precession of a gyroscope in a gravitational potential. We draw the conclusion that the motion of the KDC is a superposition of an intrinsic rotation and a global precession that gets gradually damped over cosmic time. Finally, the stability of the KDC over the complete runtime of the simulation is investigated by tracing the evolution of the widely used λ_R parameter and the misalignment angle distribution. We find that the KDC is stable for about 3 Gyr after the merger and subsequently disperses completely on a timescale of $\approx$1.5 Gyr.

5.1 Kinematically Distinct Cores in Galaxies

The stellar kinematics of galaxies represent a meaningful benchmark for modern models of galaxy formation. Recent advances in integral field spectroscopy revealed a rich variety of kinematical features in the line-of-sight velocity distribution (LOSVD), especially in early-type galaxies (Emsellem et al., 2004; Krajnović et al., 2011). These features embody the final state of a complex assembly history and evolution shaping the dynamical and kinematic appearance of galaxies. A particularly interesting class of kinematic appearances are galaxies that exhibit kinematically distinct cores (KDCs), which are kinematically decoupled from

[1] The section describing the details of the merger simulations is omitted since it is already contained in Chap. 3 of this thesis.

their host galaxy, often visible in an inclined net rotation of the central core component. Providing full two-dimensional observations of the stellar kinematics of statistically meaningful samples, the ATLAS^{3D} (Cappellari et al., 2011a) and CALIFA (Sánchez et al., 2012) surveys unveiled a significant fraction of ETGs exhibiting KDCs.

Results from McDermid et al. (2006a), who investigated the central region of ETGs using the OASIS spectrograph, suggest two fundamental types of KDCs: the first type are KDCs that exhibit an old stellar population (> 8 Gyr) contemporary to the surrounding host galaxy. This indicates that those KDCs are not a result of recent merging and were more likely to be formed through accreted material or merging at earlier times. KDCs of this type are typically extended to kpc scale while residing in non-rotating galaxies. The second type of KDCs are comprised of a more compact younger stellar population extending characteristically out to a few 100 pc. These KDCs characteristically exist in fast rotating galaxies emphasising the different formation histories of the two types.

A diagnostically conclusive method to probe the general formation pathways of KDCs is to utilise binary merger simulations of spiral galaxies. Within this framework, it is possible to follow the evolution of galaxy properties in great detail. Early theoretical studies suggest that young KDCs can arise from a binary galaxy merger on a retrograde orbit via in-situ star formation (Balcells and Quinn, 1990; Hernquist and Barnes, 1991). In a more recent study, Tsatsi et al. (2015) showed that old KDCs can also originate from a initially prograde merger through a reversal of the orbital spin induced by reactive forces due to substantial mass loss. Furthermore, Hoffman et al. (2010) showed that the initial gas fraction (f_{gas}) of the progenitors has a substantial impact on the existence of a KDC in the centre of the merger remnant. Analysing a sample of 56 1:1 binary spiral mergers with varying orbital parameters and f_{gas}, they show that, for $f_{gas} < 10\%$, the remnants do not host a KDC, while, for $10\% < f_{gas} < 40\%$, the fraction of remnants hosting a KDC increases. However, while the origin of young KDCs seem to be well understood by now, their stability and lifetime has not been studied in great detail.

In this chapter we present a case-study for the evolution of a second-type KDC formed in a major merger event, demonstrating that these structures might only be visible for a short timespan.

5.2 Global Properties

Before investigating the kinematics of the KDC in detail, we have to determine the spatial extent of the KDC. Fig. 5.1 shows the LOSVD of the merger remnant projection onto the three coordinate planes after a simulation runtime of 2.7 Gyr that is 1.5 Gyr after the second encounter. As can clearly be seen, the merger remnant hosts a distinct central rotating feature that is present in all three projections (i.e., never seen face-on) and is clearly misaligned to the rotation of its surroundings. From the visual appearance of the LOSVD map, we conservatively estimate the radius of the KDC to be 1.5 kpc, as shown by the solid black circle in Fig. 5.1. This corresponds roughly to a third of the stellar half-mass radius ($r_{1/2} = 5.2$ kpc) of the remnant, which is illustrated by the black dashed line, and therefore much larger than the resolution limit. The half-mass radius is determined to be the radius of a three-dimensional sphere containing half of the total stellar mass centred on the galaxy centre of mass.

Fig. 5.2 displays the temporal evolution of the stellar (green) and gaseous (blue) mass within the core as well as the total SFR of the galaxy in black. The starting point in time is

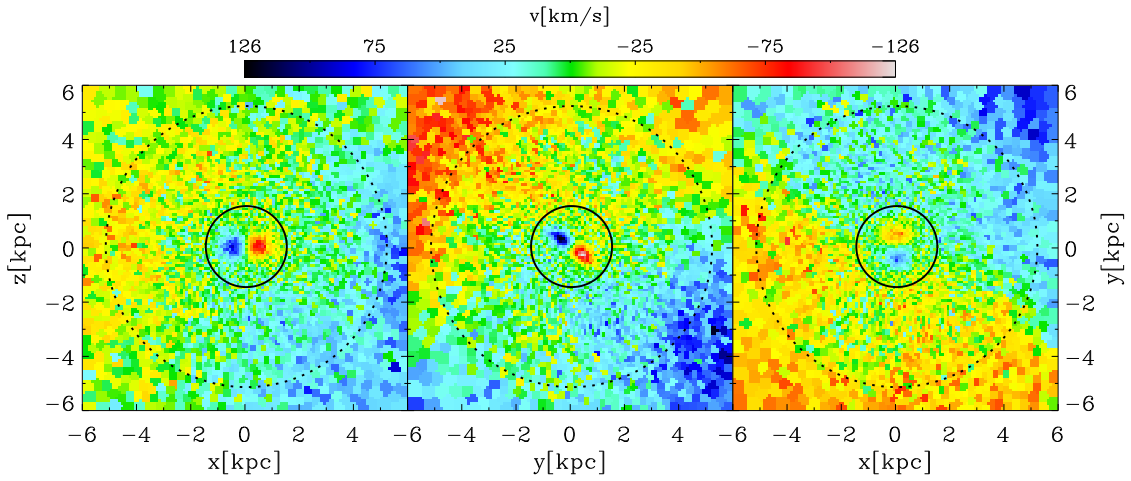

Figure 5.1: Each panel displays a LOSVD map of the central region of the merger remnant hosting the KDC in different projections at $t = 2.7$ Gyr. From left to right: x–z plane, y–z plane and x–y plane. The colour bar on the top indicates the velocity scaling adapted individually for each panel. The black solid circle marks the estimated KDC radius of 1.5 kpc, while the dashed circle indicates the half-mass radius.

chosen to be directly before the second encounter to also capture the starburst triggered by the second encounter. This starburst lasts for approximately 0.7 Gyr, with a maximum SFR of 28 $M_\odot$/yr. During this period, the stellar mass inside the KDC increases until it plateaus at $\approx 3 \cdot 10^{10}$ $M_\odot$. Afterwards, M_{STAR} stays constant, excluding significant infall of stars. Consistently with a starburst, the amount of gas in the KDC decreases drastically by roughly one order of magnitude within this timeframe. The subsequent modest decrease of M_{GAS} suggest ongoing star formation activity within the KDC, however at much lower rates.

5.3 Dissecting the KDC

To investigate the origin of the KDC signal in the LOSVD maps, we explore the contributions of stellar populations with different properties to the signal. We distinguish between stars that are set up in the initial conditions and stars that are produced during the runtime of the simulation, denoting them *'Initial Stars (IS)'* and *'Newly Formed Stars (NFS)'*. The initial gas from which the NFS are formed is expected to form a disc in the centre during the merger due to its hydrodynamic nature and therefore generates a orbital configuration characteristic for discs. In contrast, the IS are only affected by violent relaxation and dynamical friction. Of course, the interplay between those processes and their efficiency is complex and depends on the parameters of the merger and hence cannot be predicted easily.

In addition, we split the stars inside the core into two groups, independently of whether they are IS or NFS: stellar particles that are permanently located within the KDC are classified as *'Permanent Core Stars (PCS)'*, and stars which are localised only temporarily within the core denoted *'Temporary Core Stars (TCS)'*. TCS are expected to move on highly elliptical orbits with apocenters beyond the KDC radius. For this purpose, we use a algorithm that iteratively removes particles that move outside of the KDC. At a runtime of 2.2 Gyr, where the KDC is fully evolved, the algorithm selects all stellar particles within the KDC radius, traces this parent sample of stars to the consecutive snapshot, and removes the particles that leave the KDC radius from the sample. This procedure is reiterated for 24 subsequent snapshots

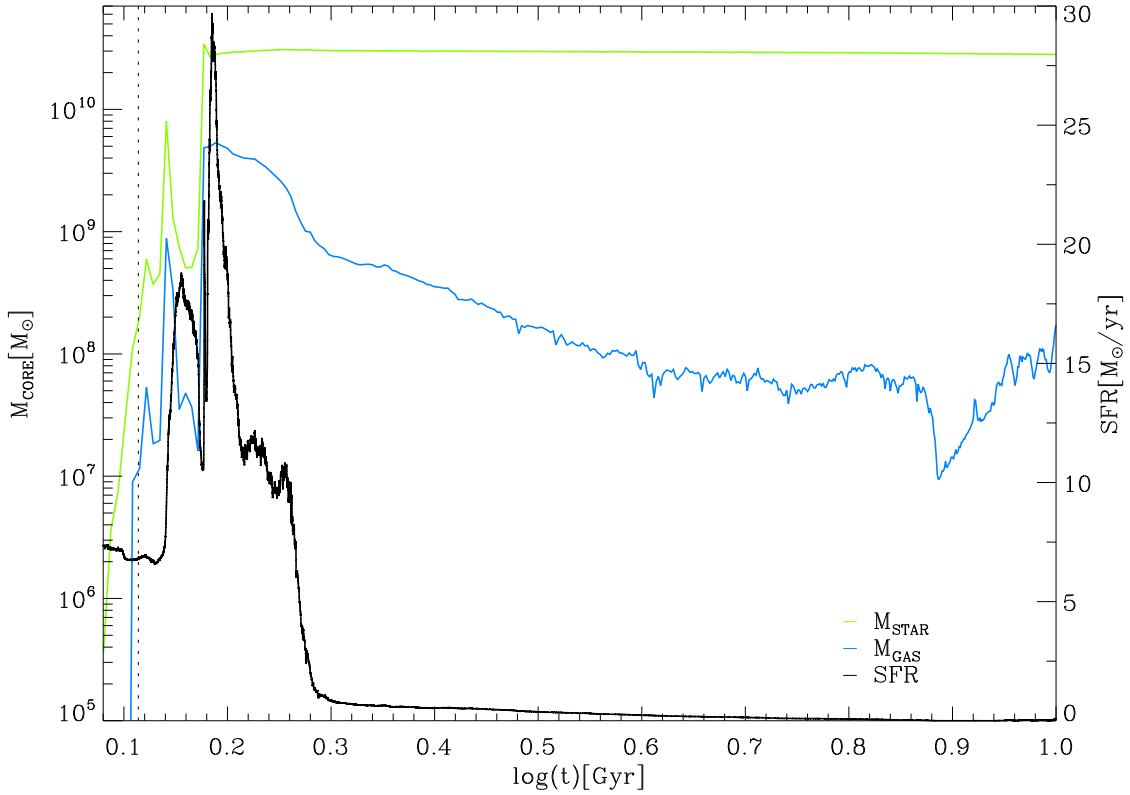

Figure 5.2: Temporal evolution of global core properties and the total star formation rate (SFR) of the complete galaxy. The black line indicates the SFR of the entire galaxy, while the green and blue curves represent the total stellar and gaseous mass within the KDC, respectively. The vertical dashed line marks the moment of the second encounter.

until a runtime of 2.7 Gyr. In this manner, the algorithm creates a sample of stellar particles that reside within the KDC for at least 0.5 Gyr. This corresponds to approximately one characteristic orbital period within the KDC. By construction, this algorithm also disregards stellar particles falling into the KDC during the application of the procedure from the sample.

Fig. 5.3 directly compares the visual contribution of the PCS and TCS to the rotational signature in the LOSVD map at $t = 2.7$ Gyr. The left panel displays a zoom-in onto the KDC including all stellar particles in the line-of-sight. Velocity maps for the TCS and PCS are shown in the central and right panel, respectively. As can clearly be seen, the rotational signal is the net rotation induced by the PCS component overlaying the TCS component, which is dominated by random motion. The fact that the maximum velocities reached by the PCS is higher than those of the full stellar sample infers that the random moving component diminishes the signal as expected.

As we are interested in the origin of the KDC, we further separate the PCS into the two populations of IS and NFS. The result is displayed in Fig. 5.4: the left velocity map replicates the central panel of Fig. 5.3, while the central and right panels show the subdivision into IS and NFS, respectively. Comparing the central and right panels demonstrates that the KDC is dominated by the newly formed stars in agreement with the results from Hoffman et al. (2010). The NFS component exhibits a peak velocity that is a roughly a factor of two higher than the peak velocity of the IS component. We reason that the minor rotation in the IS

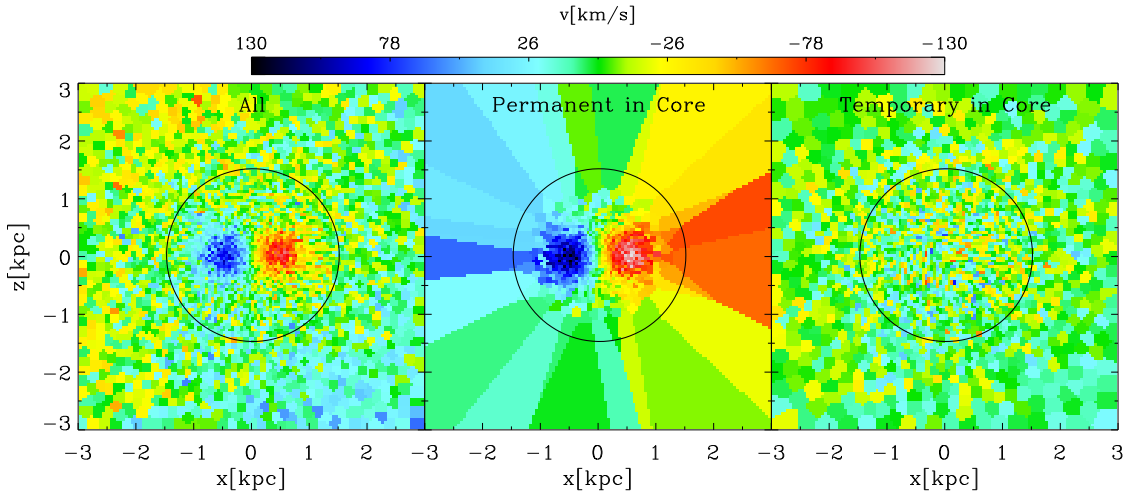

Figure 5.3: *Left panel*: LOSVD of the central 3 kpc in the x–z projection considering all stars in the line-of sight; *central panel*: LOSVD map of the central 3 kpc in the x–z projection taking into account stars that are determined to belong permanently to the KDC; *right panel*: LOSVD map of the central 3 kpc in the x–z projection including stars that only temporarily reside in the core. The panels share a common velocity scaling given in the colourbar. The solid black circle indicates the core radius of $r_{CORE} = 1.5$ kpc.

component might be generated by the drag caused by the fast rotating particles.

From our analysis we can conclude that the KDC signal in the merger remnant is generated mainly by stellar particles that permanently reside within the core and are formed during the merging process in situ. Therefore, the KDC seems to be in agreement with the younger more compact KDCs found observationally by McDermid et al. (2006a).

5.4 Evolution of Stellar KDC Kinematics

To understand the evolution of the KDC, we investigate its kinematic behaviour over time with respect to the kinematic behaviour of the surrounding host galaxy. The previous section revealed that the actual KDC is composed of stellar particles formed in-situ during the merger and hence might retain a fraction of the orbital angular momentum. To measure the orientation of the KDC, we calculate the total angular momentum of all stars located inside the KDC ($J_{STAR,CORE}$) for each snapshot, and calculate its angle to the three coordinate axes. In addition, the same angles are determined for the host galaxy to exclude a global mutual motion of the KDC and the galaxy within the simulated box. The temporal evolution of the angles is shown in the main panel of Fig. 5.5. The red, black and green curves represent the angles between the KDC and the coordinate axes, while the orange line marks the angle between the angular momentum of the host galaxy and the z-axis.

The KDC angular momentum follows a completely unexpected behaviour: subsequent to a violent phase of relaxation lasting until $t = 1.7$ Gyr, the angles with respect to the coordinate axes reveal an oscillation of the KDC, which gets gradually dampened in the further evolution. The imprint of the oscillation is visible up to $t \approx 7$ Gyr, and the period of the oscillation is nearly equal for each axis and is determined to be $\delta t \approx 0.5$ Gyr. As a two-dimensional visualisation, the upper and lower rows of Fig. 5.5 show the velocity field in the x–z plane projection at six points in times equally distributed over one oscillation period: from an initial alignment with the x-axis at 2.7Gyr, the KDC turns upwards by 90° at $t \approx 2.93$ Gyr. In the

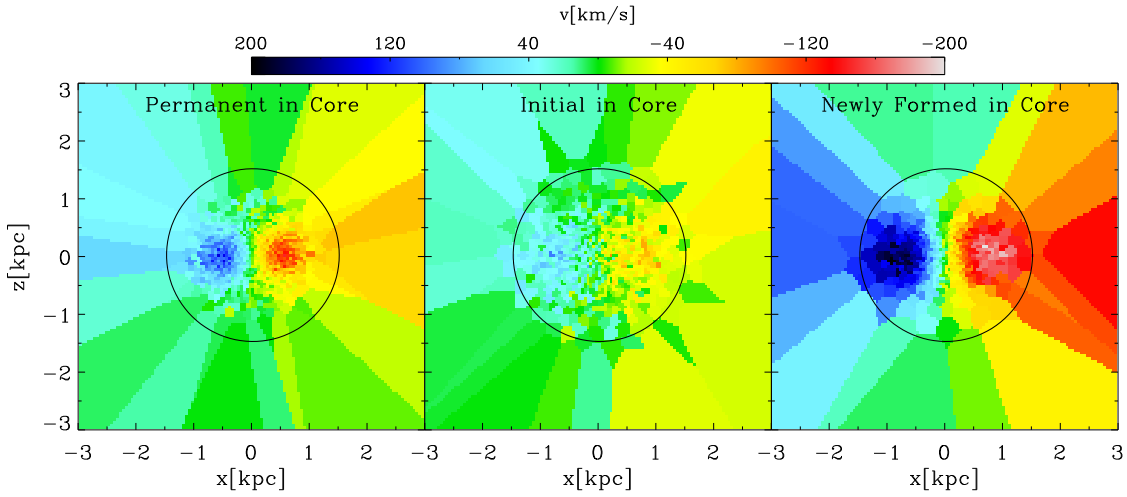

Figure 5.4: LOSVD maps of the central 3 kpc in the x–z projection. *Left panel*: all permanent core stars; *central panel*: permanent core stars that are initially in one of the progenitors; *right panel*: permanent core stars that are formed in situ during the simulation. The panels share a common velocity scaling given in the colour bar. The solid black circle indicates the core radius of $r_{CORE} = 1.5$ kpc.

following snapshot, it gets more diffuse and almost disappears until it reverts to its initial configuration at $t = 3.27$ Gyr. The last panel shows the initiation of a new oscillation cycle indicated by the slight upturn.

Of course, the projected appearance in the velocity maps is strongly influenced by the rotation of the KDC around the other two coordinate axes. Furthermore, it is difficult to deduce the actual movement in three dimensions from the angles and the velocity maps. Therefore, Fig. 5.6 illustrates the direction of the angular momentum vector of the KDC in three-dimensional space at three points in time. The curves drawn on the coordinate planes visualise the projected track of the vector's until its current position. In all three projections, the tracks describe slightly distorted circles that get smaller due to the damping of the oscillation until the angular momentum stabilises in direction.

From our analysis, we conclude that the total stellar angular momentum of the KDC performs a three-dimensional motion comparable to the precession of a gyroscope in a gravitational potential superimposed with a general tilt of the precession axis. From this, we infer that the kinematics of the KDC can be subdivided into an intrinsic rotation and a superimposed global figure rotation.

This result raises the questions of which mechanism generates this periodic, well-defined motion of the KDC and how it is damped. In the previous section we showed that the rotating component of the KDC comprises stars formed during the merger and that the intrinsic rotation is the result of the process, whereby gas condenses into a disc. We speculate that the precession is a residue of the orbital angular momentum of the merger event retained by the gaseous component.

5.5 Fading of the KDC

After revealing the origin and kinematics of the KDC in the previous sections, we now examine the temporal stability of the KDC with regard to its kinematic properties. The timescale

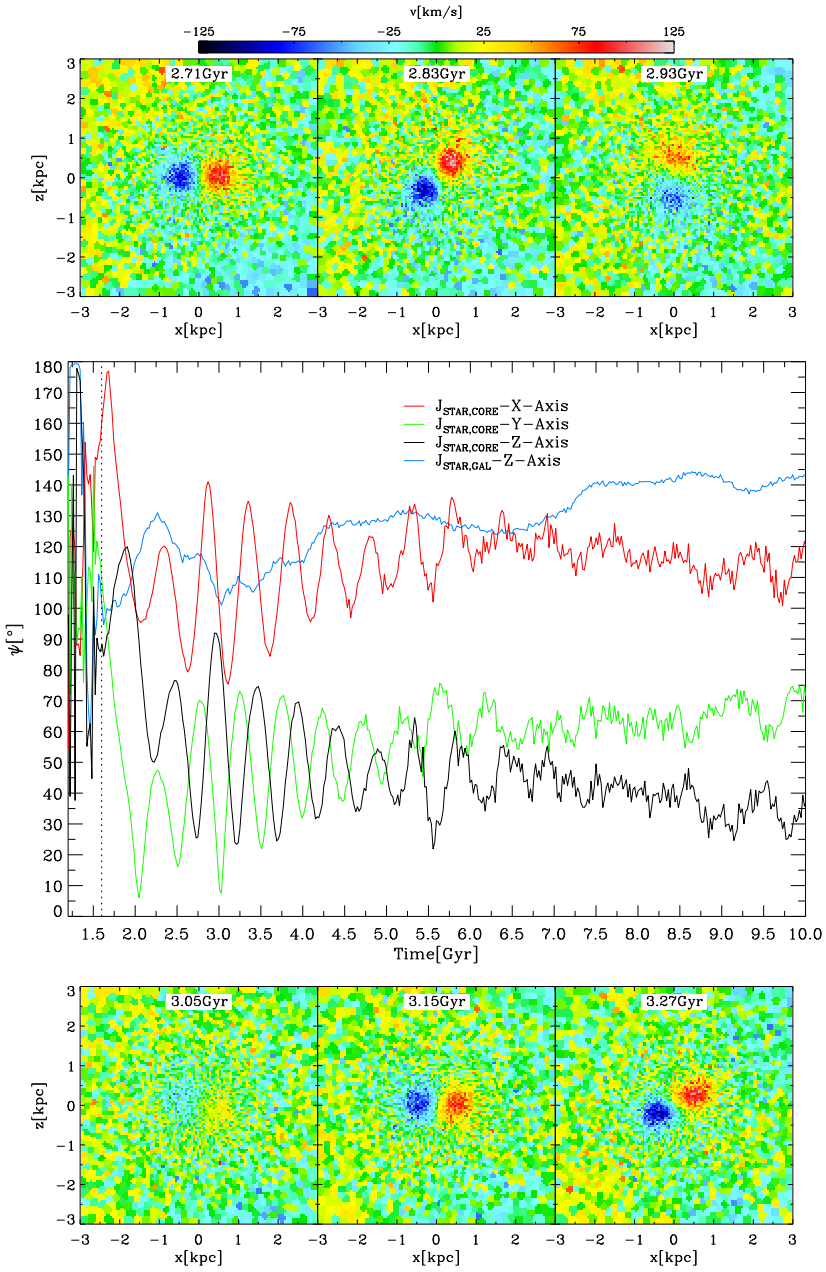

Figure 5.5: The main panel shows the temporal evolution of the angle between the total stellar angular momentum of the KDC and the three coordinate axes as given in the legend. The blue line for comparison shows the evolution of the angle between the angular momentum of the surrounding galaxy and the z-axis. The dashed vertical line marks the time at which the stellar mass accretion of the KDC is finished (see Figure 5.5). The upper and lower rows display a temporal sequence of the LOSVD map of the central 3 kpc in the x–z projection.

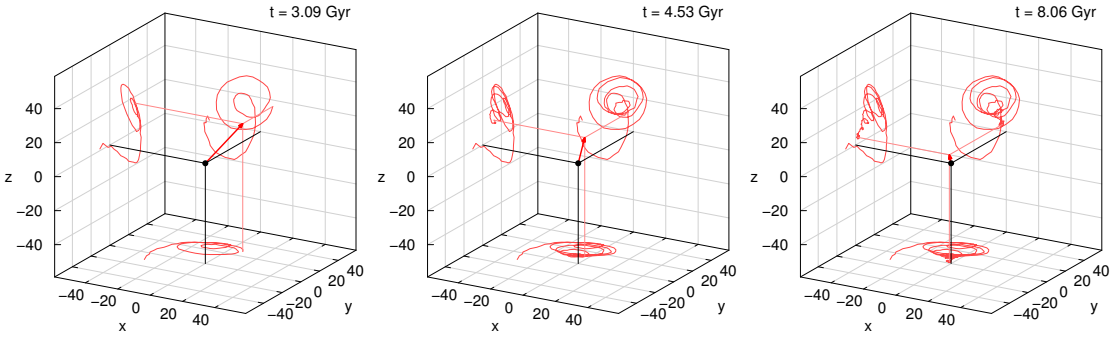

Figure 5.6: Illustration of the direction of the total stellar angular momentum in three-dimensional space as a red vector at three different time steps, of the simulation as given in the label. The red curves drawn on the coordinate planes trace the projected paths of the vector's endpoint until its current position.

on which the young compact KDCs are stable is still widely unknown since only numerical simulations with sufficient resolution can trace their evolution. In contrast, classical old KDCs are expected to be stable for up to 10 Gyr since their stellar population is indistinguishable from their host galaxy.

One of the few investigations of KDC stability was conducted by McDermid et al. (2006b) using a simulation based on SSP model spectra. They find that the KDC is fading due to the stellar evolution of the young KDC stars, as their luminosity-weighted contribution is diminished due to a increasing mass-to-light ratio. Following this argument, the KDC is still present, however forced to the background of the velocity field.

As shown in the previous section, our analysis provides a reasonable dissection of the core into its rotating and dispersion dominated component by differentiating the IS and NFS components confirmed by their visual appearance in the LOSVD maps.

A sequence of LOSVD maps in various decisive steps of the KDC evolution considering all stars in the line-of-sight from $t = 3.6$ Gyr to $t = 5.2$ Gyr are shown in the upper and lower rows of Fig. 5.7. The projection plane is held constant in all panels. After a runtime of 3.63 Gyr, the KDC is still clearly visible performing a precession in the two following snapshots. Between $t = 4.27$ Gyr and $t = 5.33$ Gyr, the KDC signal gradually gets weaker until it vanishes almost completely. By testing different projections, we confirmed that this fading is real and not just due to a precession of the core, as in the previous time steps where a weakening of the KDC signal could be detected in one projection, while it strengthened in another projection. Up to the full time of the simulation, the KDC does not build up again in any projection, clearly indicating that the KDC was dissolved. Hence, we conclude that the KDC is fading on a timescale of 1.6 Gyr.

In order to quantify the rotational support of the stellar populations of the KDC, we calculate the λ_R parameter for the core, which is given by

$$\lambda_R = \frac{\langle R\ |V|\rangle}{\langle R\ \sqrt{V^2+\sigma^2}\rangle} = \frac{\sum_{i=1}^{N_p} F_i\ R_i\ |\overline{V}_i|}{\sum_{i=1}^{N_p} F_i\ R_i\ \sqrt{\overline{V}_i^2+\sigma_i^2}}, \tag{5.1}$$

where the summation runs over each pixel within the chosen aperture. F_i, R_i, $\left|\overline{V}_i\right|$ and σ_i are the flux, projected distance to the galaxy centre, mean stellar velocity and velocity dispersion of the ith pixel, respectively (Emsellem et al., 2007). For simulations, the fluxes are replaced by stellar masses as we do not have luminosities, while assuming a constant mass-to-light ratio

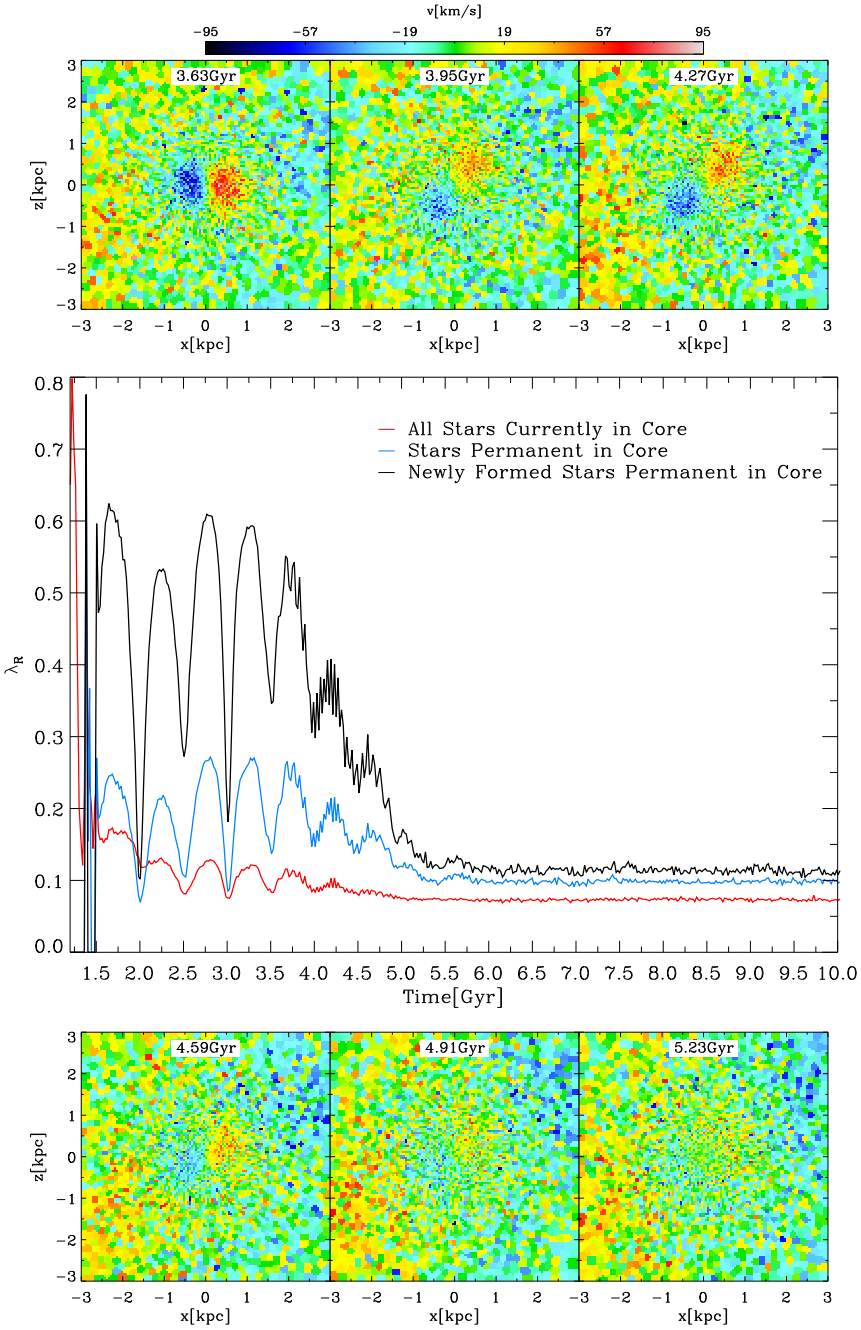

Figure 5.7: The upper and lower rows display a temporal sequence of the LOSVD maps of the central 3 kpc in the x–z projection visualising the gradual fade of the KDC. The main panel shows the temporal evolution of λ_R in the x–z projection split up into three stellar populations: All stars that reside inside the core at a given time are represented by the red curve, while the blue and black curve trace the evolution for the permanent core stars and the newly formed permanent core stars, respectively.

within each galaxy. λ_R is a measure of the ratio of random to ordered motion. Furthermore, λ_R is an observationally accessible quantity, albeit sensitive to projection effects.

The temporal evolution of λ_R in the core region, measured in the x–z plane and considering different populations of stars, is displayed in the main panel of Fig. 5.7. The red curve shows λ_R for all stellar particles within the KDC at each time step, while blue and black curves represent the PCS and newly formed PCS population, respectively. A common feature of all three populations is an imprinted oscillation, reflecting the projection effects induced by the precession of the KDC revealed in the previous section.

Comparing the mean level of λ_R for the three populations, the red and blue curves exhibit significantly less rotational support than the black curve. For the total population, this is due to the included, highly dispersive TCS component. In the case of the PCS, we showed that the IS subcomponent gets partly dragged into rotation, however, at a factor of two slower than the NFS subcomponent. Thus, the dispersion within the PCS is still rather large and explains the lower λ_R values of the blue curve.

The newly formed PCS component shows λ_R-values as high as $\lambda_R \approx 0.6$, which is a clearly rotation-dominated signal. However, due to the precession of the core, it can reach values as low as $\lambda_R \approx 0.1$ when the core precesses out of the x–z-plane, extinguishing any rotational signal. Between $t = 3.75$ Gyr and $t = 5.25$ Gyr, we find a gradual decrease to $\lambda_R \approx 0.13$, which is clearly in the slow rotating regime populated by non-rotating early-type galaxies, on a timescale of 1.5 Gyr. This is in agreement with the fading timescale inferred from the inspection of the LOSVD maps.

To further constrain the fading of the KDC, we take full advantage of the three-dimensional information from the simulation. A useful method to determine the degree of ordered rotation within a system of particles is to calculate the distribution of the angles between the angular momentum of each particle and the total angular momentum vector of the complete system. For a rotating system, the distribution of these angles is expected to feature a peak at small angles, while a completely dispersion-dominated system is expected to show a random distribution. The distribution of these angles at two points in time for the PCS is displayed in Fig. 5.8 separated for the IS (blue) and NFS (red) populations. The highlighted times are chosen such that, at the earlier point ($t = 2.76$ Gyr), the KDC is fully developed, while, at the later time ($t = 10$ Gyr), the KDC is completely dispersed.

The angle distributions shown in Fig. 5.8 conclusively confirm the kinematic difference between the IS and NFS population already found in Section 5.3. Already at $t = 2.7$ Gyr, the IS component shows a nearly randomised distribution of angles, indicating a dispersion dominated system. In contrast, the distribution for the NFS population completely changes its shape over the period of 7.3 Gyr. At $t = 2.7$ Gyr, the distribution features a clear peak at low angles, indicating ordered rotation in the system. At $t = 10$ Gyr, the alignment disappears entirely, evolving into a purely random distribution. Therefore, we conclude that the population of NFS generating the KDC signal at earlier times disperses in its further evolution. This is most likely caused by the interaction between the PCS and the dispersion dominated TCS component. We conclude that, depending on the mass ratio between the two populations, mixing drives the combined system towards a homogeneous distribution in phase space, dissolving the KDC.

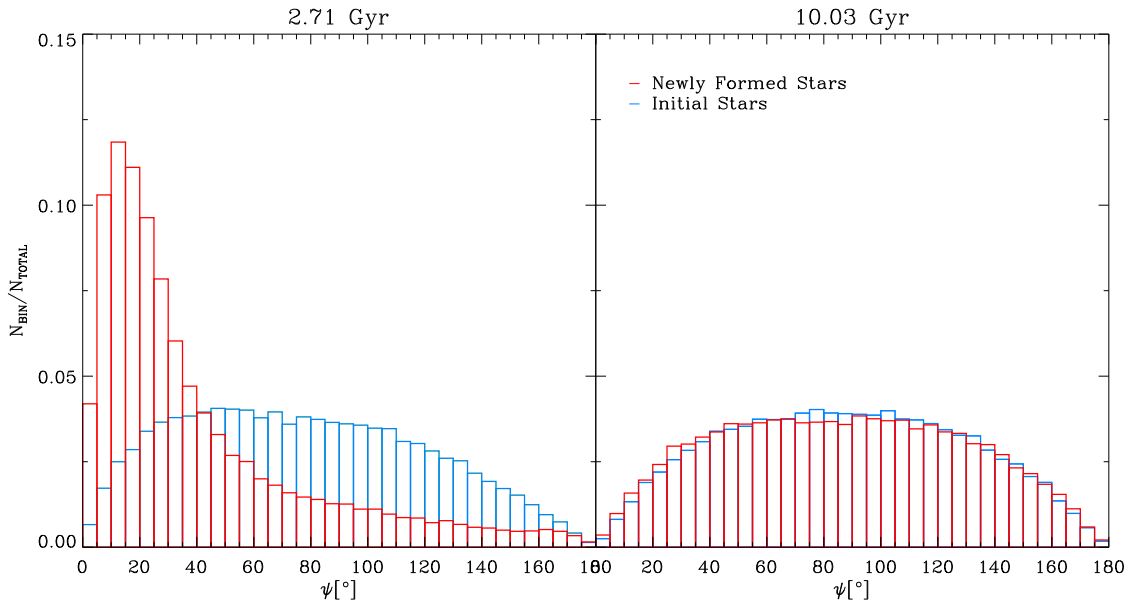

Figure 5.8: Distribution of the misalignment angles between the total stellar angular momentum vector of the KDC and the angular momentum vectors of the individual stars inside the KDC. The newly formed stars are represented by the red histograms, while the blue histograms illustrate the initial stars. *left*: $t = 2.71$ Gyr; *right*: $t = 10$ Gyr.

5.6 Summary and Conclusion

Results from highly resolved IFU observations suggest a dichotomy of KDCs found in the centres of galaxies. We present an extensive case study of a KDC formed in a high resolved 1:1 binary disc galaxy merger simulation. We identify the KDC to be consistent with the class of young and compact KDCs, where the rotational signal is mainly generated by stars that are formed in-situ during the merger event. Furthermore, the dissection of the KDC reveals a significant dispersion dominated population of stars following highly elliptical orbits permeating the KDC.

We trace the kinematic properties of the KDC over cosmic time, revealing a global gyroscopic precession motion of the KDC. From this result, we infer a superimposed motion of the KDC consisting of an intrinsic rotation and a global precession of the complete system. We suspect the precession to be induced by the orbital angular momentum of the merger retained in the gaseous component.

Furthermore, we demonstrate that the KDC is stable for about 3 Gyr after the merger event. We show that the amount of ordered motion within the KDC subsequently drops significantly on a timescale of 1.5 Gyr, leading to a dispersion of the KDC. This dispersion happens on a similar timescale on which the global precession of the KDC fades. We suspect that the effect of gravitational mixing between the rotational component and the intruding, permeating dispersion-dominated population causes the KDC to disperse. Therefore, we conclude that the visibility of a young KDC in the cores of early-type galaxies indicates a (recent) dominant merger event; however, a more statistical approach is required for a generalised statement regarding this matter.

Chapter 6

Stellar Kinematics of Galaxies out to Large Radii

This chapter has been published by Schulze et al. (2020)[1]

Abstract

We investigate the stellar kinematics of a sample of galaxies extracted from the hydrodynamic cosmological *Magneticum Pathfinder* simulations out to 5 half-mass radii. We construct differential radial stellar spin profiles quantified by the observationally widely used λ and the closely related (V/σ) parameters. We find three characteristic profile shapes: profiles exhibiting a (i) peak within 2.5 half-mass radii and a subsequent decrease (ii) continuous increase that plateaus at larger radii typically with a high amplitude (iii) completely flat behaviour typically with low amplitude, in agreement with observations. This shows that the kinematic state of the stellar component can vary significantly with radius, suggesting a distinct interplay between in-situ star formation and ex-situ accretion of stars. Following the evolution of our sample through time, we provide evidence that the accretion history of galaxies with decreasing profiles is dominated by the anisotropic accretion of low mass satellites that get disrupted beyond $\sim$ 2.0 half-mass radii, building up a stellar halo with non-ordered motion while maintaining the central rotation already present at $z = 2$. In fact, at $z = 2$ decreasing profiles are the predominant profile class. Hence, we can predict a distinct formation pathway for galaxies with a decreasing profile and show that the centre resembles an old embedded disk. Furthermore, we show that the radius of the kinematic transition provides a good estimation for the transition radius from in-situ stars in the centre to accreted stars in the halo.

6.1 From Central to Halo Kinematics

Within the ΛCDM paradigm, dark matter structures merge hierarchically at high redshift, leading to the build-up of deep potential wells that efficiently funnel gas into the centre of halos, proceeding the galaxy formation via primordial in-situ star formation at the very centre of a galaxy. Subsequent to this dissipative epoch, below $z \approx 2$ the dominant process

[1]The section describing the details of the Magneticum simulations and the merger tree construction is omitted since it is already contained in Chap. 3 of this thesis.

shaping the properties of galaxies is galactic mergers (Oser et al., 2010; Huang et al., 2013). A main driver of the relative importance of dissipative and merging processes is the stellar mass (Clauwens et al., 2018). While this multi phase scenario represents a suitable picture of galaxy formation on cosmological time-scales, the mechanisms determining the detailed inner baryonic structure of galaxies are still not completely understood (Naab and Ostriker, 2017).

The broad morphological distinction into late-type galaxies (LTGs) and early-type galaxies (ETGs) is mainly driven by the low-redshift evolution of galaxies. While late-type galaxies are expected to experience a quiet formation pathway, mostly driven by internal secular processes that leave the disc structure in the centre intact, early-type galaxies are subject to a complex interplay between environmental processes like mergers, tidal striping, ram-pressure stripping, harassment and strangulation.

Early observations based on photometry perceived ETGs as fairly simple objects without significant internal structure. In contrast to the accepted picture at that time, Bender et al. (1988) showed that isophotes of ETGs differ from ellipses and can be either 'boxy' or 'discy'. Together with the discovery that discy ETGs seemed to rotate more rapidly than boxy ETGs, the correlation between the isophotal shape and the central surface density slope led to a revision of the formation picture of ETGs (Kormendy and Bender, 1996; Faber et al., 1997).

Environmental effects play a fundamental role in determining the present-day properties of galaxies, especially for ETGs. Due to the short mixing time-scales in the centre of galaxies it is difficult to decipher the imprints of these effects in the central kinematics. Since the mixing time-scales in the stellar halos of galaxies are substantially longer than in the centre, stellar halos represent an excellent laboratory to probe the accretion histories of galaxies. Furthermore, the connection between the central and halo stellar kinematics encodes information about the formation pathway of galaxies.

As a main driver of galaxy formation, galaxy mergers are one of the most important environmental effects. However, the impact of mergers at lower redshift is not trivial to predict. The morphology of (dry) major merger [2] remnants naturally resembles a puffed-up spheroidal due to the predominant effect of violent relaxation, capable of drastically altering the global orbital configuration of the progenitors (Hoffman et al., 2010; Moody et al., 2014). In contrast, the mass accreted through dry minor mergers is in general deposited in the outskirts of the galaxy, leading to a less concentrated remnant, influencing the galaxy properties at larger radii beyond $\sim 1R_{\rm e}$ (Hilz et al., 2012; Lackner et al., 2012; Karademir et al., 2019). Thus, galaxies are expected to display structural variations in radial profiles of properties such as the surface brightness (D'Souza et al., 2014; Spavone et al., 2017; Cooper et al., 2013; Abadi et al., 2006, Remus&Forbes 2019, in prep), age and metallicity (El-Badry et al., 2016; Pastorello et al., 2014, 2015; Forbes and Remus, 2018), and stellar kinematics.

Noticeable progress in understanding stellar halo kinematics has been made using spatially sparse tracer measurements beyond $1R_{\rm e}$ using planetary nebulae (Coccato et al., 2009; Méndez et al., 2009; Pulsoni et al., 2018) and globular clusters (Méndez et al., 2001; Strader et al., 2011; Arnold et al., 2011; Pota et al., 2013). Especially Coccato et al. (2009) present pioneering kinematic measurements based on planetary nebulae out to $\sim 10R_{\rm e}$. While these studies represent an important advance in understanding the kinematics of the stellar halo, they are limited by a small sample size (some focusing on single galaxies), and therefore do not provide statistically representative results.

[2] Note, however, that wet major merger can also lead to the formation of a disk galaxy, see Sparre and Springel (2017).

Within the SAGES Legacy Unifying Globulars and GalaxieS (SLUGGS, Brodie et al. (2014)) survey, Arnold et al. (2014) compiled differential specific angular momentum profiles out to $\sim 2-4R_{\rm e}$ for 22 ETGs using multiple slitmask spectra (SKiMS). For a significant fraction of galaxies they found that the kinematic state observed within $1R_{\rm e}$ could change drastically at larger radii. While centrally slow rotating galaxies typically remain dispersion dominated in the outskirts, centrally fast rotating galaxies show profiles ranging from rapidly increasing to declining at larger radii. The declining profiles are interpreted as a sign for a kinematic subcomponent, i.e. an embedded disk. This result was later confirmed by Foster et al. (2016) using a similar but slightly extended sample of 25 ETGs. In contrast, drops in stellar spin reported by Raskutti et al. (2014) and Boardman et al. (2017) were not as strong as reported for the SLUGGS galaxies. The discrepancies are mainly attributed to small sample sizes and selection biases. The physical meaning of embedded disks has been emphasised by Savorgnan and Graham (2016a) and Graham et al. (2016) who showed that they are a key component to correctly model galaxies with respect to photometry and the related black hole mass. A general connection between the disk/bulge fraction and the kinematics has been found in several former studies (Cappellari et al., 2011b, 2013a; Cappellari, 2016; Falcón-Barroso et al., 2019b). Krajnović et al. (2013) found a strong trend for the stellar spin to increase with increasing disk-to-total ratios. Furthermore, Graham et al. (2016) proposed a transition from slow rotators to fast rotators driven by the presence and size of a stellar disk quantified by the bulge-to-total ratio.

In a first step to understand radially-varying kinematics, more recent studies investigated the connection between the modulations of the stellar spin profile and the visual morphology of galaxies. Within the CALIFA project, Falcón-Barroso et al. (2019b) found a continuous sequence spanning high to low rotational support when going from later to earlier galaxy types at all radii out to $3R_{\rm e}$. It is, however, not straight-forward to compare the results of this study to results from the SLUGGS survey since the authors calculate stellar spin profiles in an integrated manner rather than differential. Focusing only on ETGs, Bellstedt et al. (2017) observed a clear difference in the local stellar spin profiles between lenticular (S0) and elliptical (E) galaxies within their sample of 28 SLUGGS ETGs. While the vast majority of S0 galaxies show a rapidly rising profile with a plateau at larger radii, a significant fraction of ellipticals exhibit a completely flat or declining profile. A connection between the apparent morphology and the rotational support was also found by Foster et al. (2018) for a significantly larger galaxy sample including late-type galaxies. In one of the few theoretical studies, Wu et al. (2014) investigated the stellar kinematics of 42 zoom simulations of galaxies out to $\sim 6R_{\rm e}$. Consistent with the observations, the simulation produces inclining, declining and constant radial angular momentum profiles.

Very recently, the boundaries of observing stellar halo kinematics has been further pushed by Pulsoni et al. (2018). Using planetary nebulae as tracers for the underlying stellar velocity field, they observed stellar kinematics out to typically $\sim 6R_{\rm e}$, with a range of $[3R_{\rm e}-13R_{\rm e}]$. Interestingly, they found that the majority of centrally fast-rotating ETGs exhibit declining V/σ profiles as well as declining velocity amplitudes. In contrast, slow rotators typically show higher rotational support in the stellar halo than within $1R_{\rm e}$. The authors conclude that the varying rotational support of fast rotators is due to a more or less prominent disk in the centre which fades towards larger radii. As these transitions occur usually at larger radii than most studies have been covering so far, a statistical significance in the appearance of the different radial behaviour could not yet be established and is one of the major goals of the work presented here.

Therefore, the following chapter uses data from the fully cosmological hydrodynamic *Magneticum Pathfinder* simulations to investigate the stellar kinematics of massive galaxies out to ~ 5 half-mass radii ($R_{1/2}$) in a statistical manner and understand the origin of the different radial behaviours present in observations with special emphasis on the declining stellar spin profiles. This chapter is structured as follows: Details of the methodology of the galaxy analysis as well as the sample selection are presented in Sec. 6.2. In Sec. 6.3 we conduct a first qualitative investigation of the radial stellar spin profiles and compare to recent observations. Furthermore, we introduce a new classification based on the shape of the spin profiles that gets explored in detail throughout the study. Therefore, Sec. 6.4 investigates the connection between the stellar large scale kinematics and fundamental galaxy properties like central stellar kinematics, stellar mass, and morphology. Exploiting the full power of the simulation, in Sec. 6.5 we follow the evolution of our sample through cosmic time and investigate the imprint of the accretion history on the stellar large scale kinematics. We conclude in Sec. 6.7 with a summary and conclusion.

6.2 Sample Selection and Analysis

6.2.1 Sample Selection

We select all halos identified by SUBFIND with a stellar mass $M_* > 2 \times 10^{10} M_\odot$ to ensure that the galaxy is sampled with a sufficient number of stellar particles. We find 1147 halos in *Magneticum* Box4 that obey this mass limit. In the next step we discard all galaxies with a stellar half-mass radius[3] $R_{1/2} < 1.4$ kpc h^{-1}, corresponding to twice the stellar gravitational softening length for stars in the simulation. This selection criterion ensures an adequate spatial resolution, excluding galaxies dominated by the unresolved central region.

This leaves us with a sample of 1132 halos, equivalent to the galaxies used in Schulze et al. (2018) and van de Sande et al. (2019). For this sample the aforementioned studies have shown that they successfully reproduce the observed distribution of stellar kinematic properties within $1R_{1/2}$.

Additionally, we discard galaxies from the sample whose stellar kinematics are not resolved beyond $3R_{1/2}$ due to the lack of particles (see Sec. 6.2.2 for more details). After this step the sample contains 492 objects, with 320 of them being centrals and 172 being satellites.

In summary, we cover a mass range from $2 \times 10^{10} \mathrm{M}_\odot$ up to $\approx 1.7 \times 10^{12} \mathrm{M}_\odot$ with decreasing completeness towards higher and lower masses. At the high-mass end this is due to the limited box -size that does not allow for the formation of a significant number of massive object with $M_* > 10^{12}$. Towards lower masses this is driven by the lack of particles in the galaxies leading to kinematic profiles that do not reach radii beyond $3R_{1/2}$ and are therefore discarded from the sample due to our selection criteria.

In order to investigate the properties of our sample in more detail we apply a visual kinematic classification capturing specific kinematic features in the velocity maps of the central $1R_{1/2}$ analogous to Schulze et al. (2018) (see also Krajnović et al., 2011), and split our sample in five kinematic classes:

[3]The half-mass radius $R_{1/2}$ is defined to be the radius of a three dimensional sphere containing half of the total stellar mass. Throughout this study $R_{1/2}$ is considered to be equal to the observationally accessible effective radius R_e.

- *Regular-Rotator (RR):* The velocity map shows an ordered rotation pattern around the morphological minor axis.
- *Non-Rotator (NR):* The velocity map does not show any signs of ordered motion and low level velocities.
- *Distinct-Core (DC):* The velocity map shows a kinematically decoupled structure in the centre. This includes especially misaligned rotating structures with respect to the surrounding rotating galaxy, and rotating structures embedded in the centre of a non-rotating galaxy.
- *Prolate-Rotator (PR):* The velocity map shows ordered rotation around the morphological major axis.
- *Disks (D):* The velocity map shows a high degree of ordered rotation and a b-value (Eqn. 6.1) larger than -4.35, which is the threshold for pure disk galaxies determined in Teklu et al. (2015).

Discarding all galaxies that can not be classified into one of the above kinematic classes leaves us with a final sample of 450 objects. Not classifiable galaxies typically exhibit unstructured velocity maps often caused by environmental effects, as tidal interactions with other objects. This selection process ensures that our sample is as clean as possible with regard to peculiar objects and interacting galaxies.

To classify our sample by morphology we resort to the fundamental findings by Fall (1983): investigating the stellar mass $\log(\mathrm{M}_*)$ and the specific angular momentum $\log(\mathrm{j}_*)$ of galaxies they found that LTGs and ETGs follow a parallel sequence. Studies based on larger samples confirmed a continuous parallel sequence from pure disks to pure bulges in this plane corresponding to a shift of the bulge-to-total ratio from 0 to 1 (Fall and Romanowsky, 2013; Obreschkow and Glazebrook, 2014; Cortese et al., 2016; Fall and Romanowsky, 2018; Sweet et al., 2018). Furthermore, these results are in agreement with predictions from cosmological simulations Teklu et al. (2015); Genel et al. (2015); Zavala et al. (2016); Lagos et al. (2017b). Teklu et al. (2015) hence introduced the so called b-value as a proxy for morphology:

$$b = \log_{10}\left(\frac{j_*}{\text{kpc km/s}}\right) - \frac{2}{3}\log_{10}\left(\frac{M_*}{M_\odot}\right) \tag{6.1}$$

As found by Romanowsky and Fall (2012) and Teklu et al. (2015), galaxies with $b \approx -4$ are disc-like galaxies, followed by a smooth transition to lenticular and elliptical galaxies with decreasing b-value.

Following Teklu et al. (2015) we classify our galaxies according to their b-value as:

- Disk: $b > -4.35$
- Intermediate: $-4.73 < b < -4.35$
- Spheroidal: $b < -4.73$

Fig. 6.1 summarises the properties of our sample with regard to the introduced classifications. It shows the stellar mass of each galaxy versus the b-value. The symbols and colours distinguish RRs (red circles), NRs (blue triangles), DCs (cyan square), PRs (lilac bowtie), and Ds (yellow stars). The horizontal dashed lines separate Disks, Intermediates and Spheroids.

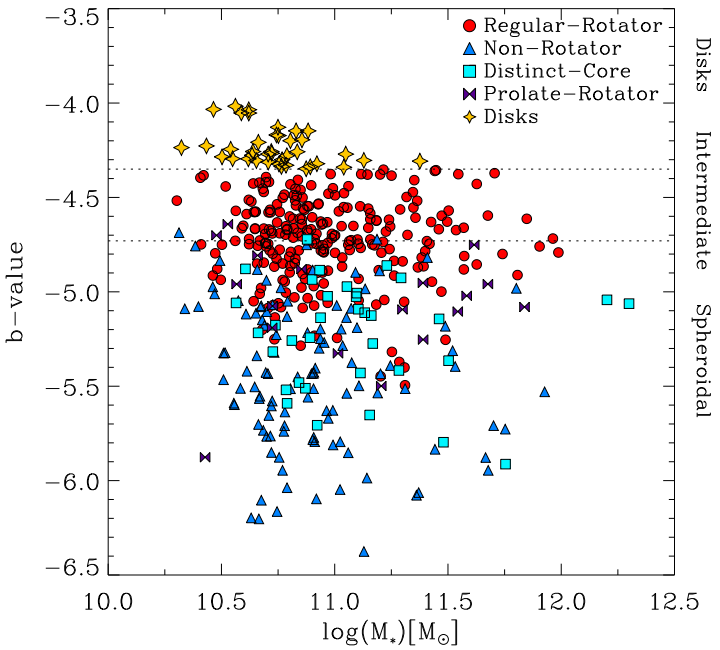

Figure 6.1: The b-value as proxy for the morphology versus the stellar mass for the sample selected from the simulation. The symbols discriminate Regular-Rotators (red circles), Non-Rotators (blue triangles), Distinct-Cores (cyan square), Prolate-Rotators (lilac bowtie), and Disks (yellow stars). The horizontal dashed lines indicate the threshold between Disks, Intermediates and Spheroidals as given in Sec. 6.2.1.

The final galaxy sample studied in this work contains 39 (9%) Disks, 140 (31%)) Intermediates and 271 (60%) Spheriodals. Furthermore, the sample comprises 245 (54%) Regular-Rotators, 113 (25%) Non-Rotators, 35 (8%) Distinct-Cores, 18 (4%) Prolate-Rotators, and 39 (9%) Disks. In comparison to the statistically larger sample investigated in Schulze et al. (2018) the distribution is quite similar, demonstrating the completeness with regard to the kinematic classes. As expected the Regular-Rotators populate the high b-values range, while the Non-Rotators and the complex kinematic structures exhibit lower b-values in line with Schulze et al. (2018).

6.2.2 Stellar Spin Analysis

To investigate the stellar kinematics of galaxies in the *Magneticum* simulations, we construct two-dimensional spatially resolved line-of-sight velocity and velocity dispersion maps, and analyse their properties. This enables us to directly compare and apply the results to the wealth of observational IFS studies that have been carried out during the past decade and will be conducted in the future. Therefore, the construction of the kinematic maps should be as similar as possible to the methods used for the observations, while taking the properties and limitation of simulated data into account. The methods used in this study resemble the methods outlined in Schulze et al. (2018).

Due to the limited mass resolution of the simulation, low particle numbers can cause statistical errors when sampling stellar particles onto a grid. To avoid statistical noise, we apply the following procedure to each galaxy in our sample: For a given spatial region and projection of interest the stellar particles are sampled onto a simple rectangular grid with a resolution comparable to modern IFS instruments of 0.3kpc. Subsequently, we apply a Cen-

troidal Voronoi Tessellation (CVT), which ensures a sufficient particle number per cell while maintaining an adequate spatial resolution (see Cappellari and Copin, 2003). To construct the final kinematic maps the mean velocity

$$\overline{V}_i = \frac{\sum_{j=1}^{N_c} V_j}{N_c} \tag{6.2}$$

and the velocity dispersion

$$\sigma_i = \sqrt{\frac{\sum_{j=1}^{N_c} V_j^2}{N_c} - \left(\frac{\sum_{j=1}^{N_c} V_j}{N_c}\right)^2} \tag{6.3}$$

are calculated within each CVT cell. Here, V_j is the particle velocity, and the sum runs over all N_c particles within the cell.

During the course of this paper we will use the $\lambda_{\rm R}$ parameter which was introduced by Emsellem et al. (2007) and has been extensively studied in great detail since then for many sets of observations (Emsellem et al., 2011; Krajnović et al., 2013; Fogarty et al., 2014; Cortese et al., 2016; van de Sande et al., 2017a; Brough et al., 2017; Greene et al., 2017; Veale et al., 2017a; Falcón-Barroso et al., 2019a) and simulations (Jesseit et al., 2009; Bois et al., 2011; Naab et al., 2014; Moody et al., 2014; Penoyre et al., 2017; Choi and Yi, 2017b; Choi et al., 2018; Schulze et al., 2018). For a given set of observed kinematic maps it is defined as

$$\lambda_R = \frac{\sum_{i=1}^{N_p} F_i \; R_i \; |\overline{V}_i|}{\sum_{i=1}^{N_p} F_i \; R_i \; \sqrt{\overline{V}_i^2 + \sigma_i^2}}, \tag{6.4}$$

with the sum running over all pixels in the considered field of view. F_i, R_i, $\left|\overline{V}_i\right|$, and σ_i are the flux, projected distance to the galaxy centre, mean stellar velocity, and velocity dispersion of the i$^{\rm th}$ photometric bin, respectively. For simulated data we replace the fluxes in Eq. 6.4 by stellar masses, assuming a constant mass-to-light ratio, as been done in various former theoretical studies (Bois et al., 2011; Naab et al., 2014; Moody et al., 2014; Penoyre et al., 2017; Schulze et al., 2018).

$\lambda_{\rm R}$ obviously depends on the projection direction of the velocity map. In practice, we choose the morphological edge-on projection, since this maximises $\lambda_{\rm R}$. Furthermore, the spatial region over which the summation in Eq. 6.4 is done, is given by an ellipse with the corresponding axis ratio $q_{\rm morph}$ of the galaxy and an area of $A_{\rm ellipse} = \pi \; R_{1/2}$. This is indicated by appending the subscript '1/2' to the parameter name $\lambda_{\rm R_{1/2}}$.

Since we aim to quantify the local variations of the kinematic state of galaxies, we calculate radial differential λ profiles for our sample. Calculating the profile in a differential manner, instead of cumulative, helps to capture kinematic transitions and the related profile gradients in more detail (Bellstedt et al., 2017). Furthermore, using λ as proxy for the local stellar spin ensures a proper comparability to results from current and future IFS observations.

In order to determine the local λ, we construct kinematic IFS mock observations of the line-of-sight velocity and velocity dispersion out to $5R_{1/2}$, using a CVT as described above. The velocities are transformed into the centre-of-mass system of the stars inside $1R_{1/2}$. Throughout this study we will refer to the local λ by $\lambda(R)$.

The CVT maps are the maximal statistically reliable information that can be extracted from the particle data. We intentionally refuse to apply interpolation techniques to the map

that are not physically motivated since they might introduce artificial values. Therefore, we proceed by binning the CVT maps onto a rectangular grid to increases the resolution of the maps. Then we calculate $\lambda(R)$ within elliptical annuli:

$$\lambda(R) = \frac{\sum_{i=1}^{N_p} R_{i,c} \, |\overline{V}_i|}{\sum_{i=1}^{N_p} R_{i,c} \, \sqrt{\overline{V}_i^2 + \sigma_i^2}}, \tag{6.5}$$

where summations run over all pixels within the annulus. Here, R_i, V_i and σ_i are the circularised projected distance to the galaxy centre, the mean stellar line-of-sight velocity and the velocity dispersion of the i$^{\text{th}}$ photometric bin, respectively. The circularised distance is given by R_c:

$$R_\text{c} = \sqrt{x^2 \; q_\text{morph} \; + \; y^2 / q_\text{morph}}, \tag{6.6}$$

where q_morph is the morphological axis ratio of the galaxy. This transformation maps a given ellipse onto a circle with radius R_c. The borders of the annuli are determined by demanding a minimum of 1500 particles per radial bin. This ensures a proper equal statistical weighting of each annuli from the particle data. To reduce small scale noise the resulting radial profile is smoothed using an adaptive Gaussian kernel which uses 6 neighbouring data points.

Using a fixed number of particles per radial bin leads to unequal bin sizes. Since we calculate mean quantities within fixed radial ranges in our further analysis of the profiles, this is a undesired behaviour. Therefore, we apply an additional cubic spline interpolation to the profile, generating a profile with 400 equidistant sample points.

Demanding a constant number of particles per annuli introduces a natural limit for the radial extent of the kinematic profiles. If there are fewer than 1500 particles beyond the last considered sampling point, the profile is truncated.

6.2.3 Merger Mass Fraction Determination

In Sec. 6.5 we will follow the evolution of individual halos through cosmic time to explore the processes that lead to their $z = 0$ properties. Within the ΛCDM paradigm, structures grow hierarchically through mergers that inevitably affect the galaxies that reside within halos. Thus, merger trees, which comprise information about progenitors, are key to understanding the processes shaping the present-day properties of galaxies. Details about the merger tree construction method used in this work are outlined in Sec. 3.2.1.

While merger trees provides a meaningful way to trace the main central structure of a halo, it gives rise to an issue when calculating mass-ratios of two merging objects: At the time of the merger identification z_merg, the objects could potentially have experienced significant tidal stripping and other environmental effects, leading to an artificially false estimate of the mass. We correct for this effect by defining the mass of the less massive merger participant M_sat to be its maximum mass before the merger is identified:

$$M_\text{Sat} = \max\left([M_*(z) : z > z_\text{merg}]\right) \tag{6.7}$$

The corresponding mass of the host M_Host is determined at the same moment in time z_max:

$$M_\text{Host} = M_*(z_\text{max}) \tag{6.8}$$

Throughout this study we classify a merger event into three merger classes based on the mass-ratio $M_\text{Sat}/M_\text{Host}$:

- **Mini merger:**

$$0.1 > \frac{M_{\rm Sat}}{M_{\rm Host}} \tag{6.9}$$

- **Minor merger:**

$$0.3 > \frac{M_{\rm Sat}}{M_{\rm Host}} > 0.1 \tag{6.10}$$

- **Major merger:**

$$\frac{M_{\rm Sat}}{M_{\rm Host}} > 0.3. \tag{6.11}$$

Merger events with $M_{\rm Sat}/M_{\rm Host} < 0.01$ are considered to be smooth accretion.

6.3 Radial $\lambda(R)$ Profiles out to $5R_{1/2}$

6.3.1 Qualitative Connection Between Kinematic Features and the $\lambda(R)$ Profile Shape

To visualise the connection between the kinematic maps and the $\lambda(R)$ profile, each row in Fig. 6.2 shows an example of the five kinematic groups defined in 6.2.1. For the group of DCs we show two examples illustrating the two kinds of kinematic configurations comprised in this group. From left to right the panels display a density map with isophotes, velocity map on a scale of $1R_{1/2}$, velocity map on a scale of $5R_{1/2}$, and the corresponding $\lambda(R)$ (solid), $(V/\sigma)(R)$ (dotted), $\sigma(R)$ (dashed), and $V(R)$ (dashed-dotted) radial profiles. The dashed black ellipses in the velocity maps mark isophotes with semi-major axis length of integer multiples of $R_{1/2}$.

The RR (first row) shows the characteristic velocity pattern of a centrally fast rotator. Accordingly, this galaxy has $\lambda_{\rm R_{1/2}} = 0.42$ clearly in the fast rotating regime. The regular rotation pattern extends beyond $1R_{1/2}$ with a mild decrease in the velocity amplitude. This behaviour is reflected in the $\lambda(R)$ profile: it increases steeply in the very centre, followed by an almost constant section with a mild decrease beyond $2R_{1/2}$. At $\sim 5R_{1/2}$, the profile reaches its minimum of ~ 0.35 still, in the fast rotating regime.

The NR (second row) represents a typical example of a non-rotating slow rotator based on its velocity field in the centre as well as based on its stellar spin $\lambda_{\rm R_{1/2}} = 0.07$. The profile exhibits only minor variations out to $3R_{1/2}$, and a moderate increase beyond this radius out to the maximal probed radius. With a maximum of ~ 0.15 the galaxy exhibits low rotational support in the entire investigated radial range.

The first DC (third row) shows significant variations in the velocity map and the $\lambda(R)$ profile: this galaxy exhibits an apparent rotating core with a non-rotating surrounding stellar halo. Already towards the centre, there is an apparent drop in the amplitude of the velocity. Furthermore, the regular rotating velocity pattern disperses within $2R_{1/2}$. Beyond this radius there is only minor evidence of low level rotation. The appearance of the velocity maps is consistent with a rotating disk embedded in a non-rotating stellar halo. The $\lambda(R)$ profile shows a peak in the centre followed by a drastic decrease out to $2.5R_{1/2}$, and a subsequent mild incline capturing the transition from the rotating core to the non-rotating surroundings.

The second DC (fourth row) shows a rotating core component that is embedded in a halo that rotates with a kinematic position angle close to 180° with respect to the centre. Accordingly, $\lambda(R)$ has a significant depression exactly at the transition radius between the

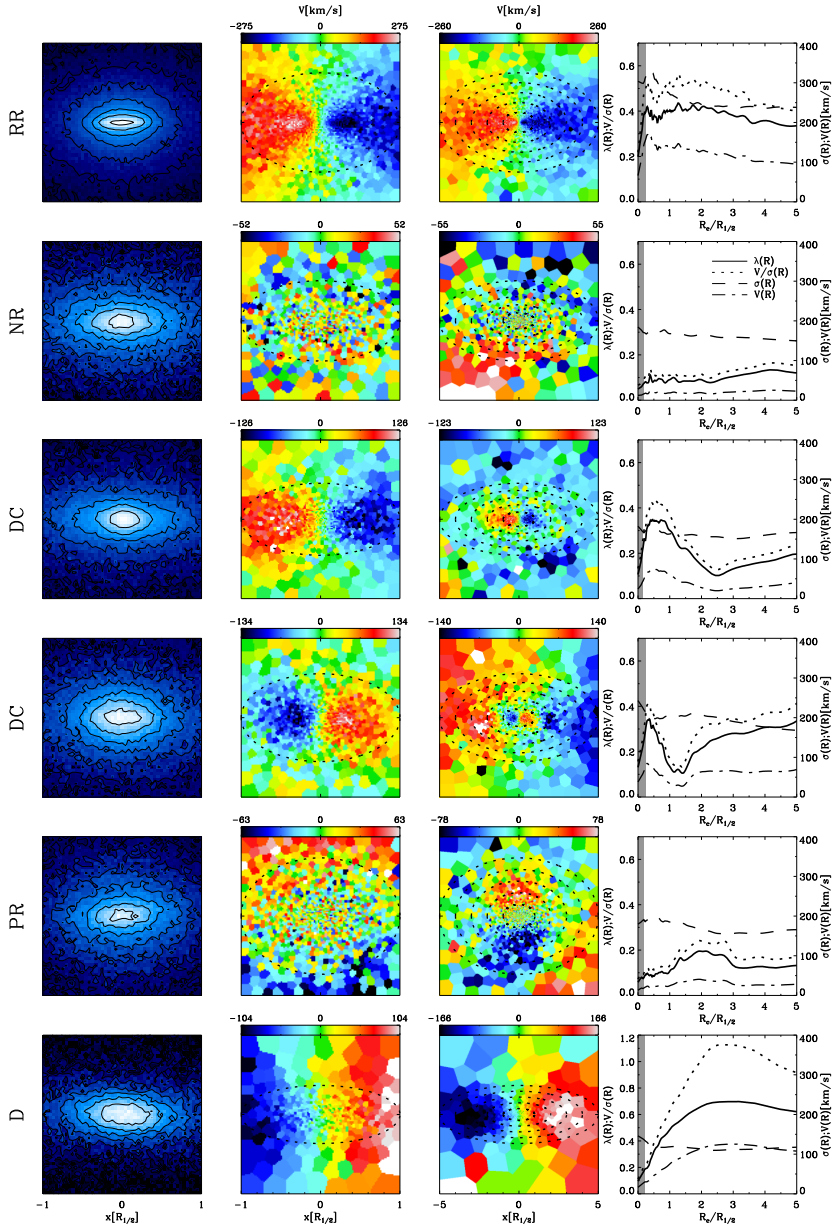

Figure 6.2: Each row displays an example of a typical kinematic feature found in the centre of the *Magneticum* galaxies. From top to bottom: Regular-Rotator, Non-Rotator, Distinct-Core, Distinct-Core, Prolate-Rotator, and Disk. From left to right the panels show the density map, line-of-sight velocity map on a scale of $1R_{1/2}$, a zoom-out line-of-sight velocity map to $5R_{1/2}$, and the corresponding radial $\lambda(R)$ (solid), $(V/\sigma)(R)$ (dotted), velocity (dashed dotted), and dispersion (dashed) profile. The dashed black lines in the velocity maps show ellipses with the galaxies' axis ratio and semi-major axis length of integer multiples of $R_{1/2}$. The grey shaded area in right panels marks the unresolved region below two softening length.

two kinematic subcomponents. Subsequently, the profile plateaus at $3R_{1/2}$ followed by a moderate increase.

The fifth row displays a member of the special group of PRs. These galaxies show ordered rotation around the morphological major axis. Within $1R_{1/2}$, the velocity map resembles that of a slow rotator. In the radial range of $1 - 2R_{1/2}$, the prolate rotation is apparent. Beyond $3R_{1/2}$, the velocity pattern becomes asymmetric: While the rotation in the upper part vanishes completely, the rotation in the lower part of the map extends significantly further out. The asymmetric lower part might be caused by stripped particles of an infalling galaxy which caused the prolate rotation signal. Within the Illustris simulation Ebrová and Łokas (2017) found that prolate rotation is strongly correlated with the last significant merger a galaxy experienced. Furthermore, slight asymmetries in the velocity map during the relaxation process after the merger, as found in our example, are possible to occur. However, investigating this in more detail is beyond the scope of this paper.

As expected, the D in the last row shows flatter isophotes than the other examples. The ordered motion is apparent out to a scale of $5R_{1/2}$. The $\lambda(R)$ profile reaches up to values of ≈ 0.7 and therefore the extremely rotationally supported range. This is mainly due to the low $\sigma(R)$ in comparison to the RR example. This is the only example where we find a crossing of of $V(R)$ and $\sigma(R)$ at $\approx 2R_{1/2}$, implying clear rotational support.

Comparing the RCs and RR clearly shows that galaxies that exhibit a similar velocity feature and $\lambda(R)$ profile within $1R_{1/2}$ can have very different outer halo kinematics. Hence, it is not sufficient to solely investigate the central $1R_{1/2}$ to assess the full kinematic state of a galaxy. Furthermore, these variations in the halo kinematics are connected to the distinct formation pathway of a galaxy and therefore encode valuable information about the processes that shape the galaxy.

The $(V/\sigma)(R)$ profile shows the same behaviour as $\lambda(R)$ in every aspect and thus can also be used to trace the radial behaviour (see also Sec. 6.6).

6.3.2 Quantifying Profile Shape

We compare the shape of the $\lambda(R)$ profiles in the simulation to recent observations from the SLUGGS (Bellstedt et al., 2017), SAMI (Foster et al., 2018), and ePN.S (Pulsoni et al., 2018) survey. Due to the challenging task of observing spectra at low surface brightnesses in the stellar halo, the three observational comparison samples use different methods to determine velocity maps out to large radii. Foster et al. (2018) uses direct integral-field observations with a radial coverage out to typically ~ 1.5–$2.5R_{\rm e}$. Bellstedt et al. (2017) utilises the SKiMS technique which uses DEIMOS slit observations to capture the underlying stellar velocity field and apply a novel interpolation method to obtain a continuous velocity map with a radial coverage out to ~ 2–$3R_{\rm e}$. A similar approach is used by Pulsoni et al. (2018), however using planetary nebulae as discrete tracers, which allow for a significantly larger radial coverage out to typically $\sim 6R_{\rm e}$.

Fig. 6.3 shows the two point gradient of the $\lambda(R)$ profile measured at different points versus the local $\lambda(1R_{1/2})$ for our sample, split up into the kinematic groups, in comparison to the above mentioned observations. The upper panel shows $\lambda(1.5R_{1/2}) - \lambda(0.5R_{1/2})$ vs. $\lambda(1R_{1/2})$ in comparison to SAMI, while the middle panel shows $\lambda(2.0R_{1/2}) - \lambda(0.5R_{1/2})$ vs. $\lambda(1R_{1/2})$ in comparison to SAMI and SLUGGS. The lower panel shows the $\lambda(R_{max}) - \lambda(1.0R_{1/2})$ vs. $\lambda(1R_{1/2})$ in direct comparison to ePN.S. The SLUGGS sample contains 15 S0 galaxies and 13 elliptical galaxies, while the SAMI survey provides $\lambda(2.0R_{1/2}) - \lambda(0.5R_{1/2})$

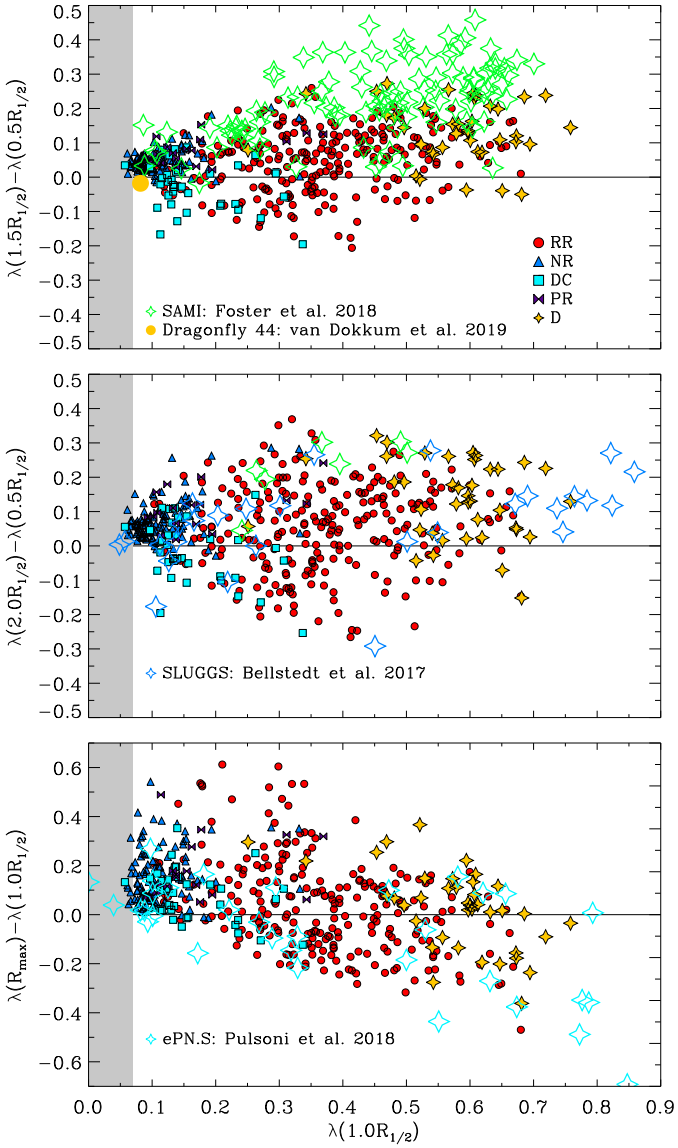

Figure 6.3: *Upper Panel:* Gradient in $\lambda(R)$ profile between $1.5R_{1/2}$ and $0.5R_{1/2}$ versus the local $\lambda(R)$ measured at $1.0R_{1/2}$. The *Magneticum* galaxies are subdivided according to their central kinematic group Regular-Rotators (red circles), Non-Rotators (blue triangles), Distinct-Cores (cyan square), Prolate-Rotators (lilac bowtie), and Disks (yellow stars). The grey shaded region marks the due to resolution unreachable region. Green symbols show observational results from the SAMI survey (Foster et al., 2018), and the orange symbol marks Dragonfly 44 (van Dokkum et al., 2019). *Middle Panel:* Same as upper panel, however the gradient is calculated between $2.0R_{1/2}$ and $0.5R_{1/2}$. We include observations from the SAMI survey (green) and the SLUGGS survey (blue, Bellstedt et al., 2017). *Lower Panel:* Same as the upper two panels with the gradient calculated between the outermost data point $R_{\rm max}$ and $1.0R_{1/2}$. The cyan symbols represent observations from the ePN.S survey extracted from Pulsoni et al. (2018).

values for 7 galaxies where we do not have access to a morphological classification. In addition, we have $\lambda(1.5R_{1/2}) - \lambda(0.5R_{1/2})$ values for 107 galaxies of mixed morphologies, including late-type galaxies, from the SAMI survey. From the ePN.S survey we include 33 ETGs. Here, we have access to $\lambda(R_{max}) - \lambda(1.0R_{1/2})$, where R_{max} is in the ranges $3.0R_{1/2}$-$13R_{1/2}$. We also derive a $\lambda(R)$ profile for the ultra diffuse galaxy Dragonfly 44 from the data provided in van Dokkum et al. (2019). For the simulation, we calculate the gradients always in the same radial range as the comparison observations.

The middle and lower panels show a good agreement between the simulated sample and the observations. The *Magneticum* galaxies cover the same range of gradients [−0.3-0.35] as the observations. Minor discrepancies are visible in the high $1.0R_{1/2}$ range where the SLUGGS survey reaches values of 0.85 which are not found in the simulated sample. We suspect, that this might me due to the still to high dispersion in disk galaxies formed in the simulation. More significant disagreements are apparent in the upper panel: The SAMI galaxies exhibit significantly larger gradients than the *Magneticum* galaxies. This is even more surprising considering that SAMI does not favour the edge-on projection in the sample selection, which would maximise the gradient, like we are. Furthermore, there is only one object with negative gradient. The low number of objects with negative gradients with respect to the SLUGGS sample was already stated in Foster et al. (2018) and quantitatively resolved by accounting for differences in the sample selection and observational effects. One side note, the ultra diffuse galaxy Dragonfly 44 (orange symbol) is a regular galaxy in the plane exhibiting low rotation in the centre and only very minor variations in the $\lambda(R)$ profile.

For the simulated sample, the overall distribution of kinematic groups is as expected in all panels: The RRs and Ds show the largest gradients, while the NR and PRs predominately populate the small gradient regime below ~ 0.1. Furthermore, most of the DCs have negative gradients, reflecting the drop in the rotational support seen in the velocity map. Interestingly, the gradient for RRs and Ds shift significantly to negative values when the outer sampling point is shifted to larger radii in agreement with the observations. This reflects that many of these object have a centrally increasing profile ($< R_{1/2}$) that decreases at larger radii.

Apart from the radial variations in the profile, the maximum amplitude is a characteristic quantity describing radial profiles. Therefore, Fig. 6.4 shows the correlation between the stellar mass and the maximum amplitude of the $(V/\sigma)(R)$ profiles (upper panel) and the $\lambda(R)$ profiles (lower panel), denoted as $(V/\sigma)_{\rm max}$ and $\lambda_{\rm max}$, respectively. The symbols are coloured according to the b-value as a proxy for morphology. It represents the direct comparison with Figure 4 of Foster et al. (2018). Although Fig. 6.4 covers a larger mass range than Foster et al. (2018), we confirm the trend that there is no overall correlation between the profile maximum and the stellar mass. This holds true for the directly comparable $(V/\sigma)_{\rm max}$ as well as for $\lambda_{\rm max}$. However, a clear correlation between the b-value, and therefore the morphology, and the location in this plane is visible: There is a continuous sequence of decreasing b-values with decreasing $(V/\sigma)_{\rm max}$ and $\lambda_{\rm max}$, which reflects the higher rotational support of late-type galaxies. Such a connection has already been reported by Schulze et al. (2018) for the *Magneticum* simulation for the central region within $1R_{1/2}$. It is, however, difficult to judge whether galaxies of equal b-value lie on relations with varying slope as found by Foster et al. (2018) for different morphological types, given the large scatter. The observed connection between the b-value and the $\lambda_{\rm max}$ is perfectly in line with the results form Falcón-Barroso et al. (2019b). Using data from the CALIFA survey they calculated cumulative $\lambda(R)$ profiles out to $3R_{\rm e}$ and found a strong continuous trend of increasing profile amplitude when going form earlier to later Hubble types.

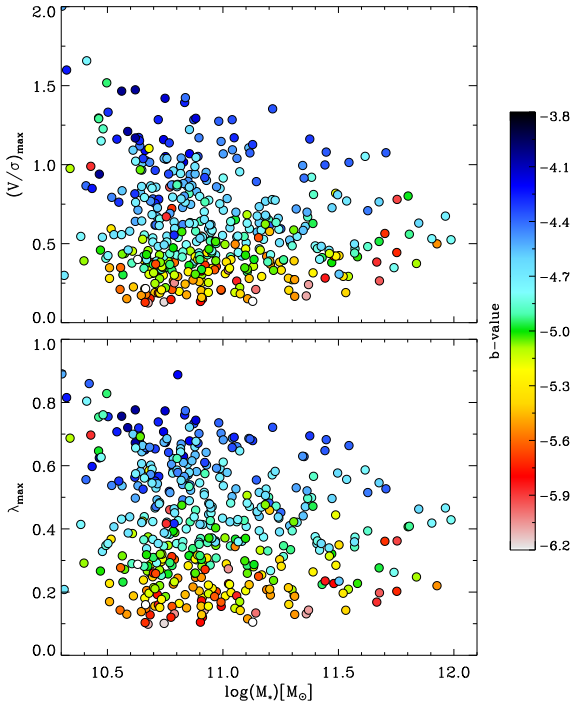

Figure 6.4: The maximum of the $(V/\sigma)(R)$ profile (*upper panel*) and the $\lambda(R)$ profile (*lower panel*) as function of stellar mass for the *Magneticum* sample. Data points are colour-coded according to their b-value as an proxy for their morphology. A b-value larger than -4.3 is characteristic for disc galaxies, while the morphology transitions to earlier types with decreasing b-value.

As discussed in Sec. 6.3.1, galaxies can show significantly different $\lambda(R)$ profile shapes. While the examples shown in Fig. 6.2 represent single example cases, the aim of this study is to analyse our sample of galaxies in a statistical manner. In order to find statistical meaningful trends, it is necessary to quantify the shapes of the radial $\lambda(R)$ profiles and, if possible, to classify them.

A comprehensive visual inspection of our sample revealed three characteristic shapes:

- Decreasing Profile: Galaxies showing a central peak and a subsequent decrease in the outer region. The position of the peak ranges from $\sim 0.5R_{1/2}$ to $\sim 2.0R_{1/2}$.
- Increasing Profile: Galaxies showing a continuous increase out to the maximally probed radius. The increase is either close to linear with varying slope or shows a steep increase in the inner region followed by a plateau at larger radii.
- Flat Profile: Galaxies showing only minor variations over the entire radial range. The amplitude of the profile ranges from low $\lambda(R)$ values in the slow rotating regime to high fast rotating values, albeit the former case is much more frequent.

Earlier observational studies use the gradient of the $\lambda(R)$ or $(V/\sigma)(R)$ profile calculated from two sampling points in the inner region ($\sim 0.5R_{1/2}$) and outer region ($\sim 1.5 - 2R_{1/2}$) depending on the covered radial range (Arnold et al., 2014; Bellstedt et al., 2017; Foster et al., 2018; Pulsoni et al., 2018) as discussed before.

Fig. 6.5 shows an example for each of the three classes. From left to right: Decreaser, Increaser and Flat. In each panel the various lines display the $\lambda(R)$ (solid), $(V/\sigma)(R)$ (dotted),

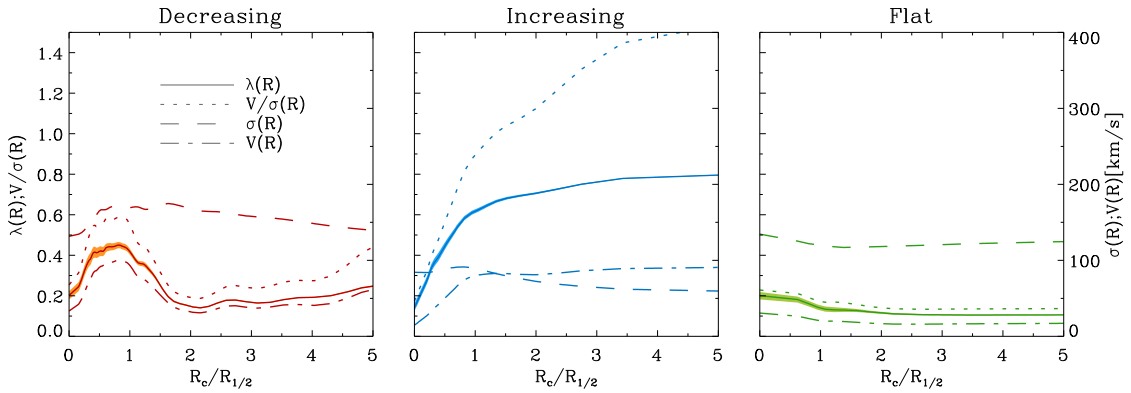

Figure 6.5: Hand-picked examples from the *Magneticum* sample for a decreasing (*left panel*), increasing (*middle panel*) and flat profile (*right panel*). In each panel the different lines distinguish $\lambda(R)$ (solid), $V/\sigma(R)$ (dotted), $\sigma(R)$ (dashed) and $V(R)$ (dashed dotted). The shaded area around the $\lambda(R)$ profiles marks the 16th and 84th percentile of a bootstrapping.

$\sigma(R)$ (dashed) and $V(R)$ (dashed-dotted) profiles. The shaded areas mark the 1σconfidence interval derived from 500 bootstraps within each radial bin, demonstrating the minor statistical noise in the profiles. While the last two categories can be captured by a simple gradient with two sampling points, the varying position of the peak for the decreasing profiles makes this simple approach unsuitable.

Visual inspection and of the profiles showed that the following classification disentangles the three characteristic shapes:

- *Decreasing:*
$$\overline{\lambda\big(2.0 < R < 3.5\big)} - \overline{\lambda\big(0.5 < R < 2.0\big)} < -0.04 \tag{6.12}$$
- *Increasing:*
$$\overline{\lambda\big(2.0 < R < 3.5\big)} - \overline{\lambda\big(0.5 < R < 2.0\big)} > 0.04 \tag{6.13}$$
- *Flat:*
$$\begin{aligned} |\overline{\lambda\big(0.5 < R < R_{\max}\big)} - \lambda_{\max}| < 0.09 \;\; \& \\ |\overline{\lambda\big(0.5 < R < R_{\max}\big)} - \lambda_{\min}| < 0.09 \end{aligned} \tag{6.14}$$

$\lambda_{\max}$ and $\lambda_{\min}$ are the maximum and minimum values reached by $\lambda(R)$, respectively. Throughout this paper we will use this classification, correlate it with various galaxy properties, and investigate its connection to the formation history of the galaxy.

In total, 84% of the sample can be assigned to one of the defined classes. Accordingly, 16% are unclassified. These galaxies typically show large variation in their profile with several maxima and minima, and are tidally interacting or in the process of merging.

Increasing profiles comprise 47% of our total sample and therefore represent the most frequent profile type. Decreasing and flat profiles are equally abundant with 19% and 18%, respectively. The predominance of increasing profiles is in qualitative agreement with former observational studies by Bellstedt et al. (2017), Foster et al. (2018) and Arnold et al. (2014). While these studies find disagreements in the actual numbers, which might be due to small sample sizes and selection biases, they consistently find a significantly larger fraction of increasing profiles than other shapes. As shown in App. 6.6 this also holds when using the V/σ instead of λ.

6.4 Profile Shape Correlation with Galaxy Properties

To examine the imprint of the large-scale stellar kinematics on other fundamental galaxy properties, we investigate the connection between the $\lambda(R)$ profile shape and the central stellar kinematics, the stellar mass, and the morphology via the b-value. Several earlier studies have addressed this topic in the past: Having access to a large sample of 384 galaxies, Foster et al. (2018) found that the radial dynamical support is linked to the visual morphology, however with a significant intrinsic scatter. Furthermore, Bellstedt et al. (2017) found a strong separation between elliptical galaxies and S0 galaxies in the plane of stellar spin gradient and local stellar spin at $1\mathrm{R}_{1/2}$, giving more physical meaning to the morphological distinction. More general, a very clear trend between the Hubble type and the rotational support at all radii out to $\sim 3R_{1/2}$ has been reported recently by Falcón-Barroso et al. (2019b) from the CALIFA project.

6.4.1 Correlation with Central Stellar Kinematics

First we investigate the connection between profile shape and the notion of centrally fast and slow rotators. Therefore, the lower panel of Fig. 6.6 displays the widely used $\lambda_{\mathrm{R}_{1/2}}$-$\epsilon$ plane which relates the stellar spin to the apparent ellipticity. The threshold between fast and slow rotators is marked by the green line, while the magenta lines show the theoretical prediction for an edge-on isotropic galaxy (dotted) and a galaxy with anisotropy $\delta = 0.8 \times \epsilon$ (dashed).

To distinguish between fast and slow rotators, we use the quantity $\lambda_{\mathrm{F/S}} = \lambda_{\mathrm{R}_{1/2}}/0.31\sqrt{\epsilon}$, with fast rotators having ($\lambda_{\mathrm{F/S}} > 1$) and slow rotators having ($\lambda_{\mathrm{F/S}} < 1$) according to the criterion introduced by Emsellem et al. (2011) and corresponding to the green line in the lower panel. The upper panel of Fig. 6.6 relates this quantity to λ_{max}, which is the maximal amplitude of the $\lambda(R)$ profile, for increaser (triangles), decreaser (circles), and flats (diamonds). The top panel displays the cumulative distribution of $\lambda_{\mathrm{F/S}}$ for each class normalised to the number of members of the respective class.

The increasers cover the full range of measured $\lambda_{\mathrm{F/S}}$, and therefore contain both fast and slow rotators. Approximately 50% are classified as fast rotators, and 50% as slow rotators. In general, the increasers are separated from the other two classes having larger λ_{max} values at all $\lambda_{\mathrm{F/S}}$. Only in the high $\lambda_{\mathrm{F/S}}$ regime we find a minor overlap with the decreasing class. The maximum λ_{max} reached by increasers is 0.9, which is in the extremely rotational dominated domain. The distribution features a well defined lower envelop: with increasing $\lambda_{\mathrm{F/S}}$ the minimum λ_{max} increases accordingly. For a given $\lambda_{\mathrm{F/S}}$, the increasing profiles show a significantly larger vertical scatter than the two other classes.

Similar to the increasers, the flats cover a wide range of $\lambda_{\mathrm{F/S}}$, and hence comprise slow and fast rotators. However, the concentration of the distribution is located in the slow rotating regime. Approximately 70% are centrally slow rotating, while 30% are fast rotating. It might be that the fast rotating flats are actually increasers, but low mass and therefore the steep inner rise of the profile falls below the resolution limit. Those objects show a constant rotational support over the whole range of investigated radii.

The overall distribution of flats is well constrained by an upper and lower envelope following a very similar relation, describing a fairly tight connection: as $\lambda_{\mathrm{F/S}}$ increases, λ_{max} increases as well. This class also contains an extreme outlier with a $\lambda_{\mathrm{max}} = 0.24$ and a anomalous low $\lambda_{\mathrm{F/S}}$. We checked this object and found that it is unusually round, which causes $\lambda_{\mathrm{F/S}}$ to be small. This particular object is an outlier in every correlation investigated in Schulze

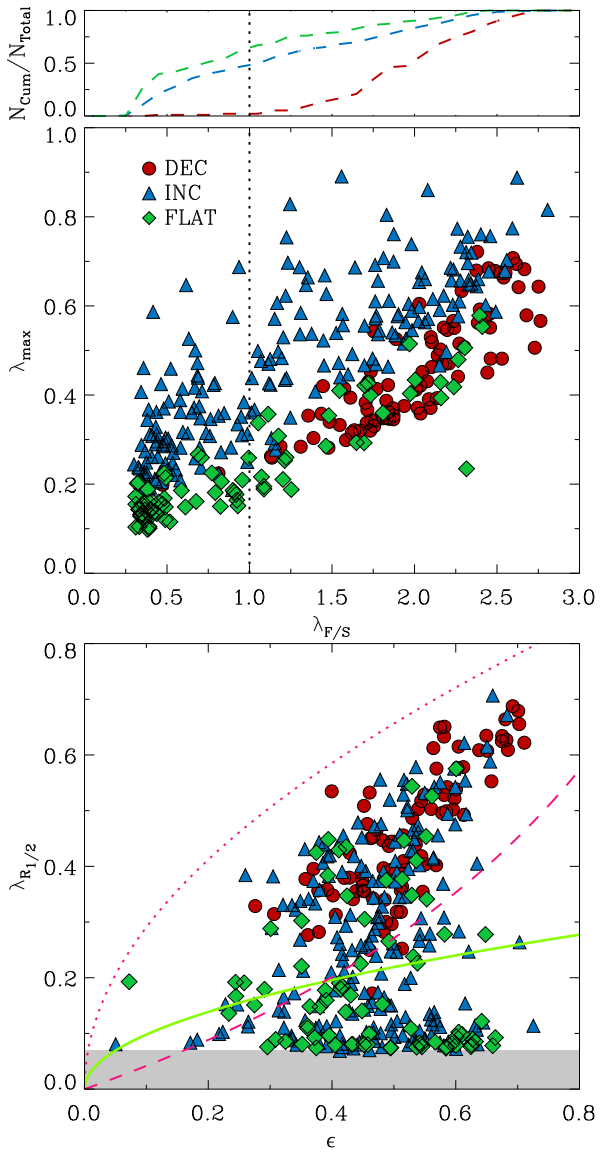

Figure 6.6: *Upper panels:* The quantity $\lambda_{F/S} = \lambda_{R_{1/2}}/0.31\sqrt{\epsilon}$ versus the maximal amplitude of the $\lambda(R)$ profile λ_{max} for the *Magneticum* galaxies. For fast rotators, $\lambda_{F/S}$ is larger than one, accordingly $\lambda_{F/S}$ is smaller than one for slow rotators. The *top panel* shows the cumulative number of galaxies (N_{Cum}) normalised by the total number of galaxies (N_{Total}) for each class. *Lower panel:* The edge-on $\lambda_{R_{1/2}}$-ϵ plane for decreasing (red circles), increasing (blue triangles) and flat (green diamonds) profiles. The green line marks the threshold between slow and fast rotators, while the magenta dashed and dotted lines show the theoretical position of an edge-on galaxy with anisotropy $\delta = 0.8 \times \epsilon$ and $\delta = 0$, respectively. The grey shaded region marks the, due to resolution, inaccessible $\lambda_{R_{1/2}}$ values for the simulation.

Table 6.1: The statistical distribution of decreasing, increasing and flat profiles within the five kinematic groups.

	Decreasing	Increasing	Flat	N_{gal}
RR	36%	49%	15%	208
NR	1%	61%	38%	101
DC	15%	48%	37%	27
PR	0%	100%	0%	14
D	37%	63%	0%	30

et al. (2018). However, looking into this in detail is beyond the scope of this paper.

The decreasing profiles populate the high $\lambda_{F/S}$ regime separated from the increasers by generally lower λ_{max} values. Interestingly, except for one object, all of the decreasers are classified as central fast rotators. This supports the findings of Arnold et al. (2014) and Foster et al. (2018) that these profiles resemble stellar rotating structures embedded in a non-rotating halo. As aforementioned, we find a minor overlap between decreasers and increasers at high $\lambda_{F/S}$ values. Similar to the flats the decreasers exhibit a rather tight correlation that increases with increasing $\lambda_{F/S}$. This trend is expected since decreasing profiles reach their $\lambda_{F/S}$ at low radii close to where $\lambda_{F/S}$ is measured.

Overall, the three classes populate distinctly different regions in this plane with only minor overlaps. This separation is not as clear in the lower panel of Fig. 6.6. This shows that taking the large scale kinematics, quantified by λ_{max} here, into account is crucial to assess the full dynamical state of galaxies. Comparing the flat and decreasing profiles, it seems like the decreasers represent a natural extension of the relation found for flats to larger $\lambda_{F/S}$. We suspect that there is an evolution channel from decreasers to flats: decreasers seem to evolve towards flat profiles due to a less significant peak in the centre. We therefore suspect the decreasing and flat profiles to have a similar merger history however the flat profiles experience at least one high mass fraction merger that kills off the rotation in the centre and transform an decreaser into a flat.

In order to investigate how the profile shape is connected to a refined classification of the central kinematics, we apply the central kinematic classification introduced in Sec. 6.3.1. Tab. 6.1 summarises the fraction of decreasing, increasing and flat profiles for each kinematic group.

The RRs comprise objects from all three profile groups. As expected, the most frequent group within the RRs are the increasers with 49%. The decreaseres encompass 36% of the RR, while 15% are flat. The flat profiles in this group correspond to the fast rotating flats in Fig. 6.6 exhibiting high amplitudes in the profile.

As expected, the NRs are in general less rotationally support than the RRs. The fraction of flat profiles is 38% and therefore twice as frequent as for the RRs. Therefore, objects with low rotational support in the centre stay relatively often pressure supported out to $5R_{1/2}$. This reflects the low number of fast rotating flats found in Fig. 6.6. Interestingly, the NRs include a large fraction of increasers of 61% even higher than the average. However, the shape of the increasing profiles of the NRs differs from the RRs: The amplitude is in general smaller. Furthermore, the increase is more modest and closer to linear.

An interesting feature of the DCs is the fact, that they comprise a similar fraction of flats (37%) and increasers (48%), and only a small fraction of decreasers (15%). Due to the

definition of DCs one would expect to preferentially find decreasing profiles in this kinematic group, since a decrease of the rotation in the LOSV-map is characteristic for this group, except for the members with counter rotation which are however extremely rare (5 galaxies). Hence, the visual appearance of the LOSV-map within the central $1R_{1/2}$ is not always sufficient to deduce the profile shape at larger radii demonstrating the complex connection between central and halo kinematics.

All of the 14 PRs have an increasing $\lambda(R)$ profile. This signal shows that for PRs the central and halo kinematics are coupled and are determined by a process that affects the centre and the halo. This is in line with the findings of Ebrová and Łokas (2017) that a significant merger sets the prolate rotation which can alter the orbital configuration in the centre and the halo.

A noticeable feature in the D group is the occurrence of increasing and decreasing $\lambda(R)$ and $(V/\sigma)(R)$ profiles. This means, that extremely rotational support disks can exist within a rotating (63% increaser) and non-rotating (37% decreaser) halo, i.e. 1/3 in a non-rotating halo. Therefore, the process causing the pressure support in the halo, and hence the difference in the formation of the halo, does not effect the very centre of the galaxy.

6.4.2 Correlation with Stellar Mass

Earlier studies found a strong correlation between the stellar mass of a galaxy and its central kinematics. According to these studies the fraction of slow rotators increases significantly with stellar mass (Brough et al., 2017; Jimmy et al., 2013; Veale et al., 2017a). In order to extend this to the halo kinematics, we study the relation between the profile shape and stellar mass.

Fig. 6.7 shows the stellar mass distribution of the three profile classes in 6 bins. To investigate the distribution within each bin the lower panel depicts the fraction of increasing (blue), decreasing (red) and flat (green) profiles normalised within each mass-bin. In contrast, the upper panel shows the distribution of the total number of galaxies (N_{Bin}) normalised to the total number of galaxies N_{Total} (solid line), and the cumulative fraction (dashed line) in each individual class. We emphasise that, due to the limited box size of the simulation, our sample is not complete in the high mass regime.

Throughout the whole probed mass range, the increasers are the most frequent class. In the lowest mass bin, the increasers represent 87% of the total sample. For higher masses, the fraction of increasing profiles drops to $\approx 50\%$ and shows no further mass dependence. This is a first hint towards a connection between the profile shape and the morphology of galaxies, since we expect the largest fraction of rotational supported late-type and S0 galaxies in the low mass bin.

The fraction of decreaser and flats rises concurrently from $\approx 7\%$ at $\log(M_*/M_\odot) = 10.5$ up to $\approx 25\%$ at $\log(M_*/M_\odot) = 11.1$. Beyond $\log(M_*/M_\odot) = 11.1$, the decreasers become more frequent, rising up to 40% and then gradually dropping back to 20%. The flats show a contrasting behaviour with a minor degression and a subsequent rise. Therefore, the relative fraction of decreasing and flat profiles stays constant within the considered mass range.

Investigating the normalised distribution for each individual class in the upper panel of Fig. 6.7, we find a similar behaviour for the three classes: All distributions peak in the mass-bin centred on $\log(M_*/M_\odot) = 10.75$ and show a gradual decrease towards higher masses. The flattening of the cumulative distributions above $\log(M_*) = 11.5$ is mainly driven by the lack of high mass objects due to the limited size of the simulated box. According to conclusions drawn

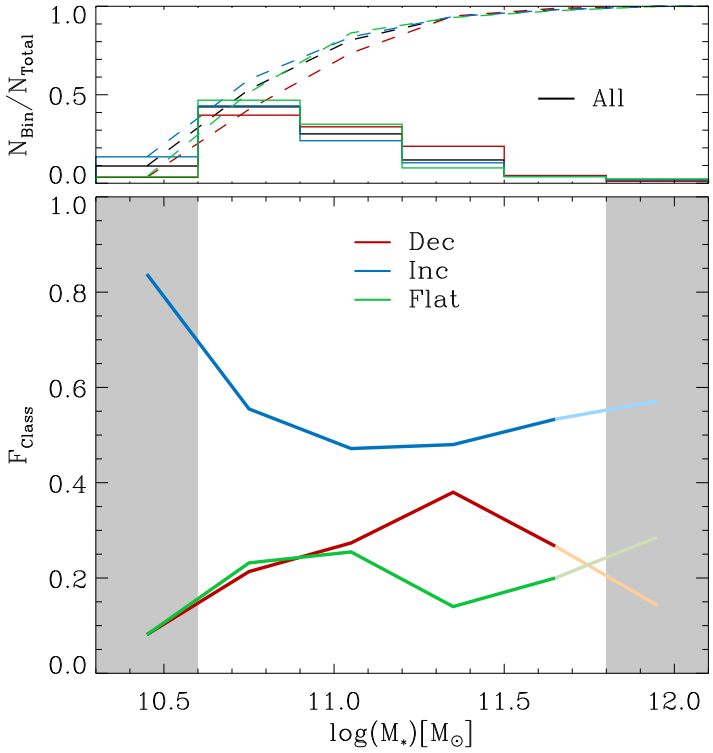

Figure 6.7: The *lower panel* depicts the connection between the fraction F_{Class} of increasing (blue), decreasing (red) and flat (green) profiles and the stellar mass normalised within each mass-bin for the *Magneticum* galaxies. The grey shaded region marks the, due to resolution and box-size, unreliable mass-range. Bins with less than 10 galaxies are shown in lighter colours. The histogram in the *upper panel* shows the absolute number of galaxies in each mass bin (N_{Bin})normalised by the total number of galaxies (N_{Total}) of the respective class, while the dashed line represents the according cumulative distribution. The black curves represent the all galaxies in the sample.

from the distribution in the lower panel increasers exhibit the largest excess with respect to the other groups in the lowest mass bin. Overall, we do not find a significant difference in the individual mass dependence among the three classes. In line with our findings, using $(V/\sigma)(R)$ profiles, which are closely related to $\lambda(R)$, Foster et al. (2018) found only a weak trend for more massive galaxies to have slightly larger $(V/\sigma)(1.5R_e) - (V/\sigma)(0.5R_e)$ gradients.

6.4.3 Correlation with Morphology via the b-value

A connection between the V/σ gradient with morphology was reported for the SLUGGS survey by Arnold et al. (2014) and Bellstedt et al. (2017), and especially by Foster et al. (2018) for the SAMI survey. According to these studies the gradients in the V/σ profiles get larger when going from early-type to late-type galaxies. Furthermore, Foster et al. (2018) found a clear morphology trend in the $(V/\sigma)_{max}$-log(M_*) plane that can be understood by the Faber-Jackson (Faber and Jackson, 1976) and Tully-Fisher relation (Tully and Fisher, 1977).

Fig. 6.8 displays the connection between the b-value and the gradient $\lambda(2.0R_{1/2})$-$\lambda(0.5R_{1/2})$. The sample is split up into increasing, decreasing and flat profiles as given in the legend. The

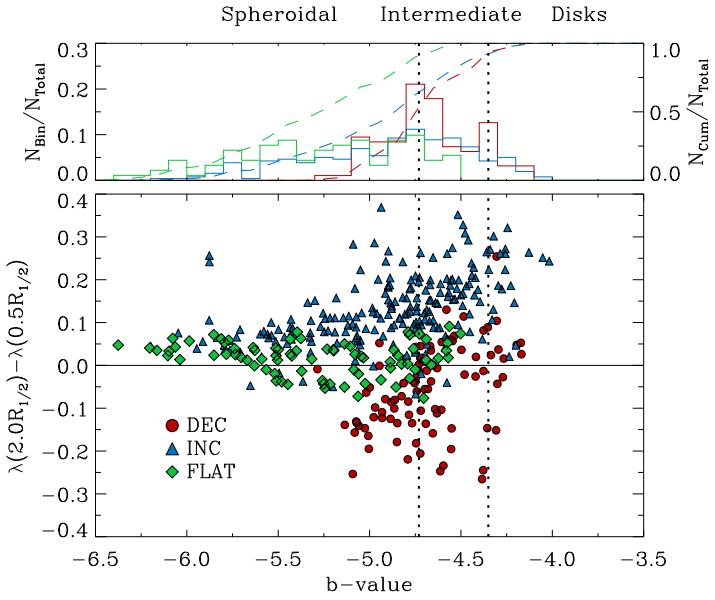

Figure 6.8: Gradient in $\lambda(R)$ profile between $2.0R_{1/2}$ and $0.5R_{1/2}$ versus the b-value for the *Magneticum* sample. The sample is subdivided into decreasing profiles (filled red circles), increasing profiles (blue filled triangles), and flat profiles (green squares). The top panel shows the normalised distribution for the three profiles types (solid lines) together with the according cumulative distributions (dashed lines).

upper panel shows the normalised cumulative (dashed) and differential (solid) distribution of b-values for increasing (blue), decreasing (red) and flat (green) profiles.

The increasers cover a large range from disk-like b-values down to spheroidal-like b-values. Their distribution shows no sharp peaks or substructure indicative of sub populations. Furthermore, the increasers feature the most disk-like morphologies (largest b-value). The flat profiles show a similar distribution to the increasers, however shifted to smaller b-values with a significant overlap. No flats are classified as disk galaxies according to their b-values. Furthermore, the lowest b-values are reached by this class. For the decreasers we find the narrowest distribution of the three classes, reaching up to the extremely disk-like b-values. Around $b = -4.7$ (in the "intermediate" morphological region) the distribution features a peak encompassing $\approx 37\%$ of all decreasers. Hence, decreasing profiles are preferentially in the transition range between pure spheroidals and pure disks, not showing tail to low b-values.

Investigating the overall distribution in the lower panel of Fig. 6.8, the maximum absolute value of the gradients increase towards higher, and therefore more disk-like, b-values confirming the finding from Bellstedt et al. (2017) and Foster et al. (2018). In general the three classes populate distinct regions in this plane. This separation is, as expected from the definition of the classes, mainly driven by the gradient. Overall, the distribution is not symmetric around 0, but offset of positive gradients.

Interestingly, we find a significant fraction of decreasing profiles with positive gradient, representing 31% of the decreasing sample, which is counterintuitive. This can be explained by the varying position of the central maximum present for the vast majority of the decreasers. For these galaxies the maximum is at larger radii such that the profiles is indeed decreasing at $\lambda(2.0\mathrm{R}_{1/2})$ but didn't fall below the amplitude at $\lambda(0.5\mathrm{R}_{1/2})$. Furthermore, this is the reason for the overlap of flats and decreasers at $b \approx -4.7$. The overlap between the increasers and

decreasers highlights that the introduced classification is useful since it recovers decreasers which are consistent with no or even positive gradient. In addition, we even find 8 increasers with negative gradients. These galaxies show a common characteristic shape: starting from $0.5R_{1/2}$ the profiles are falling until they reach a minimum in the range $1.0R_{1/2}$-$2.0R_{1/2}$ and subsequently increase. These two examples show that a simple gradient with two sampling points doesn't capture the diversity of the profiles properly and the classification introduced in this study is required.

6.5 Dissecting the Formation Pathways of Galaxies using Halo Kinematics

In the previous section we analysed the stellar large-scale kinematics at $z = 0$ in detail, and their connection to global galaxy properties. However, the simulations enable us to investigate the formation pathways of these galaxies over cosmic time and connect the present-day profile shape to merger characteristics of the individual galaxy and therefore identify imprints of the accretion history in the profiles.

6.5.1 Connection to Profile Shape

To understand the information about the accretion history encoded in the large scale kinematics, Fig. 6.9 shows a summary of the merger history for increasing (blue), decreasing (red), and flat (green) profiles condensed into two parameters: The upper panel shows the stellar mass accreted through the various merger types since $z = 2$, where ΔM_* is normalised by the $z = 0$ stellar mass M_* for each profiles class. Similar to the upper panel of Fig. 6.9, the lower panel investigates the amount of gas accreted via the different types of merger since $z = 2$. This is a direct measure of the available fuel for potential star formation and the build-up of new dynamically cold components.

In total, increasers accrete on average 55% of their present day stellar mass through mergers, and therefore $\approx$ 17% more than decreasers, which accrete 38%. Flat profiles gain 50% of their stellar mass via mergers, and hence lie between increaser and decreaser.

The largest difference between the classes is apparent for mass gained through major mergers: While decreasing profiles accrete 13% of their stellar mass through this channel, increaser accrete with 32% almost a factor 3 more stellar mass via major merger. The flat profile galaxies again reside in the intermediate region, gaining 22% of their stellar mass through major merger. It seems like there is a sequence from increaser over flats to decreaser driven by the total amount of accreted stellar mass and the importance of major merger since $z = 2$.

The amount of stellar mass accreted through minor and mini mergers is similar for the three classes. All classes gain more mass via minor mergers than mini mergers. However, the relative importance of the mini and minor mergers differs strongly between the different classes. Especially, the difference between increasers and decreasers is significant: The mass accreted via mini and major mergers for decreasers is 6% larger than the mass gained through major merger. In contrast, increasers accumulate 11% less via minor and mini merger. Flats are again between the two classes, gaining slightly more stellar mass via mini and minor mergers than through major mergers. Therefore, we conclude, that the merger history of decreasing profiles is dominated by mini and minor mergers that lead to the characteristic

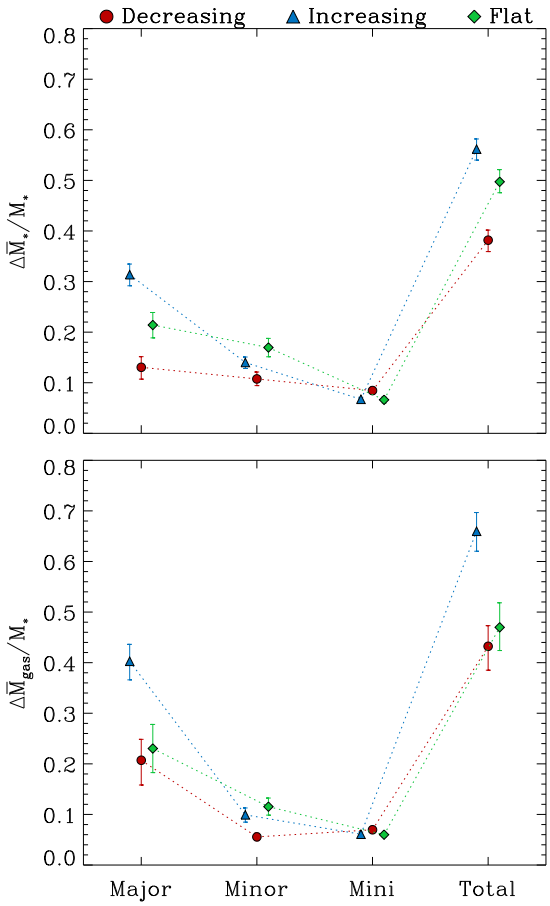

Figure 6.9: Both panels shows an averaged quantity related to the accretion history of the *Magneticum* galaxies. Different colours and symbols separate the three profile classes decreasing (red filled circles), increasing (blue triangle), and flat (green diamonds). We distinguish between contributions by major, minor, mini and all mergers from left to right. The error associated with each point is derived from 500 bootstraps and error bars correspond to the 1σ confidence interval. *Top panel:* Average stellar mass accreted since $z = 2.0$ normalised by the stellar mass at $z = 0$. *Lower Panel:* Average gaseous mass accreted since $z = 2.0$ normalised by the stellar mass at $z = 0$.

profile shape.

Regarding the gaseous mass accreted through mergers for the different classes, we find a similar picture: the decreasing and flat profiles show a very similar behaviour for all merger types, accreting $\approx 45\%$ of their present day stellar mass in gas via merger events and $\approx 7\%$ through each minor and mini merger.Both classes gain $\approx 20\%$ gas mass via major merger. The increasers are clearly separated from the other classes in the total amount of gaseous mass gained through merger events. With 60% gas mass relative to the total stellar mass, this class accretes a factor 1.5 more gas than decreasers and flats. This behaviour is clearly driven by the major merger component: While the increasers gain a comparable amount of gas through minor and mini merger, they gain a factor 2 more via major merger than the other classes.

An interesting feature for the increasers is that, when considering the total accreted baryonic mass ($M_* + M_{gas}$), they assemble more than their present day stellar mass in contrast to the other classes. This suggests, that the increasers exhibit a higher gas-mass fraction

and potentially more star formation than the decreasers and flats. Analysing the gas mass fractions confirms this conclusion.

Summarising the conclusion from Fig. 6.9, we find distinct differences in the global accretion history of the three profile classes which motivate the following idea for the formation pathway: The merger history of the increasing class is dominated by gas-rich major merging. Depending on the orbital configuration major mergers are believed to enhance the dispersion of the velocity distribution down to the very centre of the halo where the galaxy is located. However, we find a significant amount of gas that is provided by the major merger which potentially can build up a new kinematic cold component as demonstrated in Sparre and Springel (2017). An increasing $\lambda(R)$ profile is compatible with an exponential disk with a flat rotation curve (Romanowsky and Fall, 2012). Therefore, we suspect that the gas-rich major mergers for increasing profiles happened rather early before $z \sim 1$, allowing for the build-up of a kinematic cold disk in the centre that is aligned with the stars stripped during the infall. In contrast decreasing profiles are clearly mini and minor merger dominated. Earlier studies have shown that these low-mass satellites, especially the mini merger, never reach the centre of the host halo, getting disrupted in the halo and therefore building up the stellar halo (Amorisco, 2017; Karademir et al., 2019). Assuming an anisotropic accretion of the satellites, we expect this disruption process to enhance the dispersion in the halo without affecting the central embedded disk. The formation of the decreasing profiles is discussed in more detail Sec. 6.5.3. The flat profiles seem to be in a transition state driven by the ratio of minor+mini to major merger accretion.

In order to elaborate our interpretation of Fig. 6.9 in more detail, Fig. 6.10 shows two more quantities extracted from the merger trees. The right column displays the fraction of galaxies that underwent N_{merger} major (upper panel), minor (central panel) and mini merger split up into decreasing (red circles), increasing (blue triangles) and flat (green diamonds) profiles.

As expected from Fig. 6.9, we find the most sever differences between the classes in the major merger regime. The three classes feature a similar distribution for the fraction to increase towards lower numbers of merger. We find that 61% of the decreasers do not undergo a major merger, and 27% have one merger in their formation history since $z = 2$. The increasers show a reversed trend, with the majority of 53% experiencing a single major merger and 30% not having a major merger. The flats are in an intermediate state with approximately the same fraction ($\sim 40\%$) of the sample having 0 or 1 major merger. While almost none of the galaxies has more than three minor mergers, $\sim 40\%$ of the sample does not undergo a minor merger at all, similar for the three classes. Furthermore, the distribution for the minor merger exhibits a strong increase towards lower numbers, independent of the profile type. In contrast, in the mini merger case, the distribution declines towards lower and larger numbers with a maximum at $2 - 3$ mergers similar for all three profile classes.

The left column shows the fraction of galaxies that experienced their last mini (lower panel), minor (central panel) and major (upper panel) merger within a time interval of $\pm$1Gyr around the plotted look-back time (lbt). This means that we only include galaxies that actually experienced a merger of the respective type[4].

[4]As already discussed in Sec. 6.2.3, in the context of estimating the mass fraction of a merger, determining the precise point in time when a merger happens is notoriously difficult. This is on the one hand due to the algorithm that constructs the merger trees. On the other hand defining a physically meaningful single 'merger time' rather than a period of interaction is also degenerate. Hence, we only focus on overall trends and significant differences in the left column to not over interpret the artificial definition of a merger time in

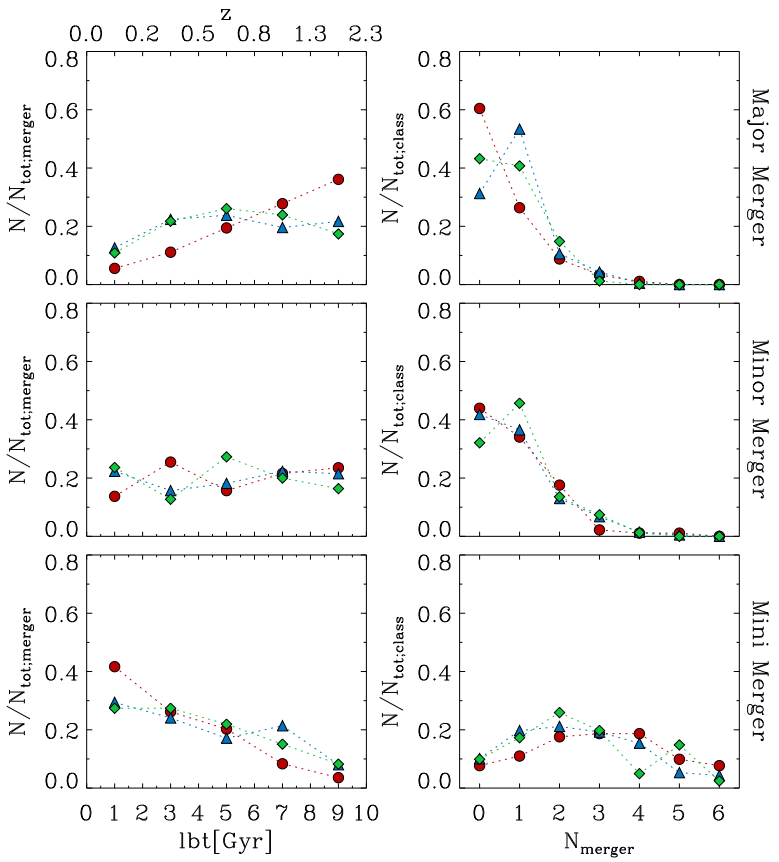

Figure 6.10: *Left Column:* The fraction of *Magneticum* galaxies that had their last mini (lower panel), minor (central panel) and major (upper panel) merger within a time interval of ±1Gyr around the plotted look-back time (lbt). *Right Column:* The fraction of galaxies that experienced N_{merger} of a given type. In all panels the different colours and symbols separate decreasing (red circles), increasing (blue triangles) and flat (green diamonds) profiles.

The major merger (left upper panel) show a contrary trend than the mini mergers (left lower panel): A larger fraction of galaxies experienced an early major merger and no subsequent major merger. This holds true for all three profile classes. While the increasers and flats exhibit a similar distribution the decreasers again stand out: The outlined trend is significantly stronger for galaxies with decreasing profiles than for galaxies with increasing or flat profiles. About 90% of the decreasers that experienced a major merger in their formation underwent the merger more than 5Gyr ago. In contrast, for the increasers and flats this fraction is $\sim 60\%$. Therefore, we conclude that the recent accretion history (lbt < 5Gyr) of decreasers that experience a major merger is dominated by mini and minor mergers compared to major mergers. Combined with the finding that only 40% of this class does undergo a major merger at all, this represents a clear and strong signal.

For the minor mergers (central panel) we do not find the same general trend of earlier accretion as for the major merger. The distribution is relatively flat without substantial differences between the profile classes.

The lower left panel shows the general trend that a larger fraction of galaxies had their last

the merger trees.

mini merger more recently independent of the profile class. The increasers and flats exhibit a very similar evolution with approximately 28% of the sample having their last mini merger in the past 2Gyr, while 8% did not experience a mini merger in the past 9Gyr. The trend is strongest for the decreasers with 42% experiencing the last mini merger in the past 2Gyr, while only 3% had their last mini merger 9Gyr ago. Therefore, the fraction of galaxies with lbt $<$ 2Gyr is significantly larger for decreasers than for increasers and flats.

6.5.2 Profile Classes at Higher Redshift

To investigate if the class frequencies evolve over time, we applied our classification scheme at $z = 2$, $z = 1$, and $z = 0.5$ using the same selection criteria as outlined in Sec. 6.2.1, yielding a samples of 243, 785, and 805 galaxies, respectively. Tab. 6.2 summarises the class frequencies at the considered redshifts. We find that the decreasers account for 37% of the $z = 2$ sample, while 18% are increasers and 17% are flats. With decreasing redshift, the fraction of decreasers declines to 19% at $z = 0$. The largest change in the decreaser fraction happens between $z = 2$ and $z = 1$. In contrast, the fraction of increasing profiles increases for lower redshift from 18% at $z = 2$ to 47% at $z = 0$. The fraction of flats does not vary significantly with redshift.

At high redshift, a decreasing $\lambda(R)$ profile is the predominant class in contrast to $z = 0$, where the increasers comprise half of the total sample. This implies that there has to be an evolutionary path between decreasing and increasing profiles to explain the class frequencies found at $z = 0$. Since the decreasing feature is already in place at $z = 2$, present-day decreaser must have an accretion history that does not destroy this feature while building up a non-rotating stellar halo, in agreement with our result, that decreasers essentially grew through mini/minor mergers since $z = 2$. The origin and nature of decreasing profiles is investigated in more detail in the following chapter.

In total, 28% of our $z = 2$ galaxies are unclassified, representing an increase of 12% in comparison to $z = 0$. This is due to a significantly stepper increase of the profiles inside $0.5R_{1/2}$ for these galaxies and less variation at larger radii, implying that our $z = 0$ classification is less distinctive at higher redshift. This reflects the different evolutionary state of the galaxies at $z = 2$, strongly dominated by dissipative processes like gas accretion and in-situ star formation.

Fig. 6.11 shows the evolution of the distribution in more detail: The class frequency of decreasers (left), increasers (middle), and (flats) is presented in mass bins at the four considered redshifts. It shows that the trends found for the total fractions above is apparent in every mass bin: With decreasing redshift, the frequency of decreasers declines, while the fraction of increasers inclines, independent of mass. Furthermore, we find a general increase in the fraction of decreasers towards higher stellar masses at all redshift, while the increasers show a contrary behaviour. The galaxies with flat profiles do not show an overall trend with redshift.

For lower-masses ($\log(M_*/M_\odot) < 11$), the most significant drop for decreasers occurs between $z = 0.5$ and $z = 0$, while for higher masses ($\log(M_*/M_\odot) > 11$) the decline is strongest already between $z = 2$ and $z = 1$, as implied by the varying slope with redshift. This behaviour suggests that the process that drives the evolution of F_{Class} acts at different times for different stellar masses. In contrast, the relatively constant slope for the increasers implies a concurrent rise of the fraction, independent of stellar mass. Only in the lowest mass bin we find a significantly larger jump between $z = 0.5$ and $z = 0$ than between the other

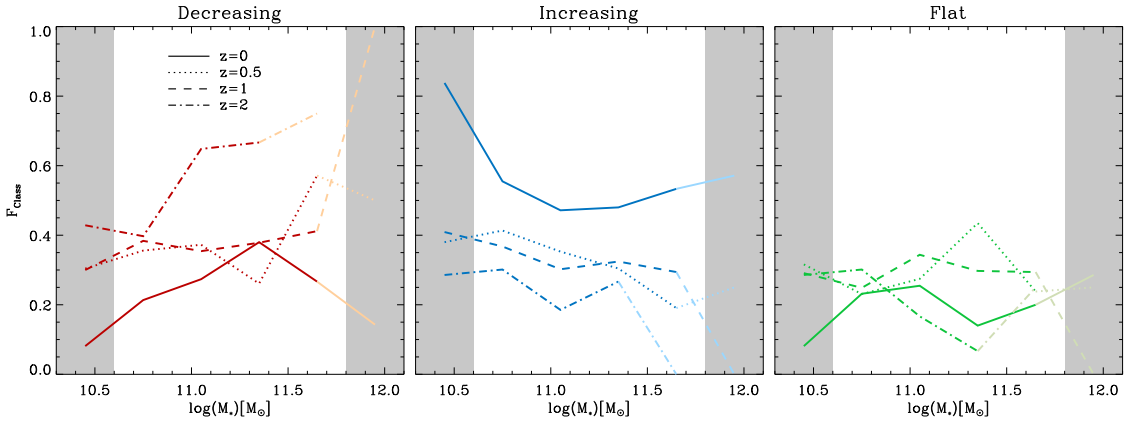

Figure 6.11: Each Panel shows the fraction of decreasers (left), increasers (middle), and flats (right) in mass bins with 0.3dex width at $z = 0$, $z = 0.5$, $z = 1.5$, and $z = 2.0$. Grey regions mark the bins that are impacted by resolution and the limited box-size. Bins with less than 10 galaxies are shown in lighter colours.

Table 6.2: The statistical distribution of decreasing, increasing, flat, and unclassified profiles at different redshifts.

z	Decreasing	Increasing	Flat	Unclass	N_{gal}
0	19%	47%	18%	16%	450
0.5	27%	30%	22%	21%	805
1	23%	30%	22%	25%	785
2	37%	18%	17%	28%	243

redshifts.

6.5.3 Formation of Decreasing Profiles at $z = 0$

As shown in Sec. 6.5.1 the formation of present-day decreasing profiles is dominated by low mass-fraction mergers at late times. We suspect that the anisotropic accretion of those satellites and their subsequent disruption in the halo randomises the velocities and hence enhances the dispersion in the halo, while maintaining the central rotating in-situ component. In order to further corroborate this concept, we investigate the evolution of an example galaxy exhibiting a decreasing $\lambda(R)$ profile at $z = 0$ in detail.

The left central panel of Fig. 6.12 depicts the evolution of the stellar mass for the example galaxy over cosmic time from $z = 2$ down to $z = 0$. Vertical dashed lines mark minor (green) and mini (blue) merger as defined in Sec. 6.2.3. This particular example does not experience a major merger in the considered redshift interval. The galaxy experiences two mini and two minor mergers below $z = 1$. Relating the example to Fig. 6.9, for minor mergers $\Delta M_*/M_* = 0.29$, for mini merger $\Delta M_*/M_* = 0.03$, and for total merger $\Delta M_*/M_* = 0.39$. Therefore, this halo is an example of a minor merger dominated stellar accretion history. For the gaseous component, we find $\Delta M_{gas}/M_* = 0.23$ for minor merger, for mini merger $\Delta M_{gas}/M_* = 0.04$, and for total merger $\Delta M_{gas}/M_* = 0.35$.

The left upper and lower panels show the projected stellar density within a cube of 70kpc, corresponding to $7R_{1/2}$ at $z = 0$, around the galaxy centre at six distinctive times as indicated. The extend of the central disk does not increase significantly for lbt $<$ 6.7Gry, while the

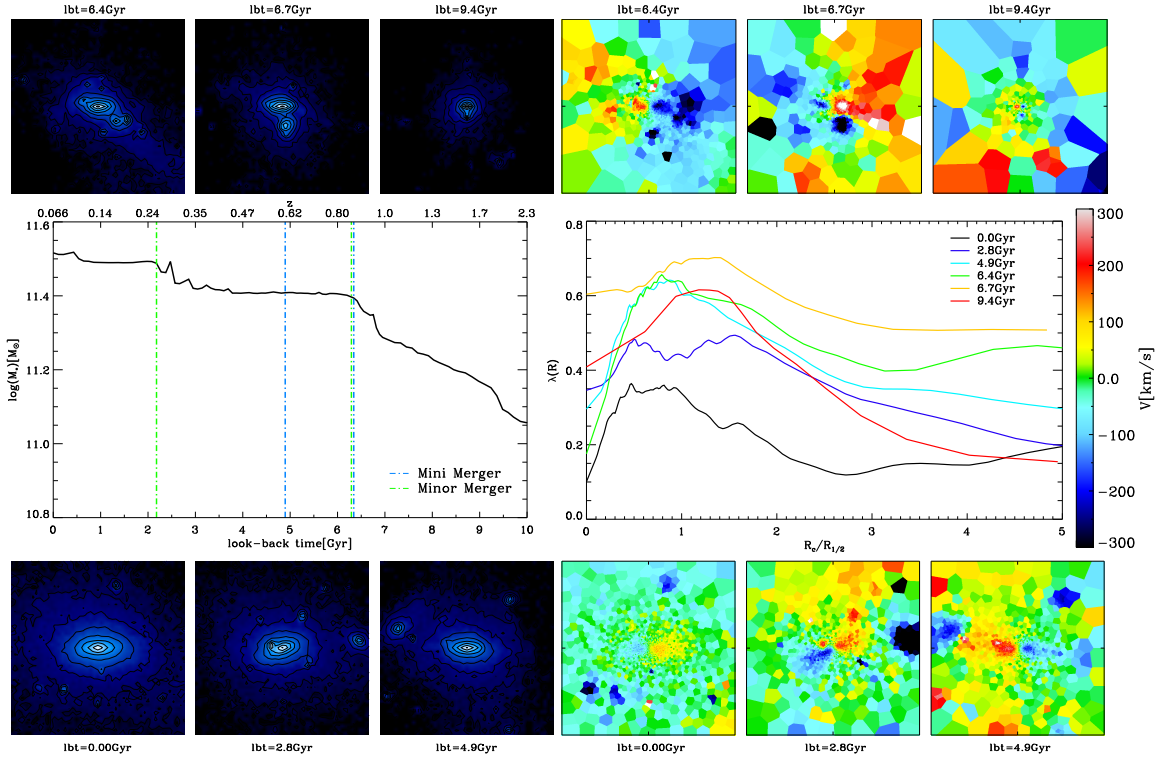

Figure 6.12: Visualisation of the temporal morphological and kinematic evolution of the *Magneticum* example galaxy with decreasing profile at $z = 0$. In the central panel on the left the black solid line illustrates the evolution of the stellar mass with look-back time (lbt). Vertical dashed-dotted lines mark the moment at which a merger is identified. Colours distinguish minor merger (green), and mini merger (blue). The top and bottom panels show the projected stellar density map within a square of 70kpc side length at various distinctive times as given in the panel annotation. The central panel on the right shows the $\lambda(R)$ profile at the same moments in time. Corresponding velocity maps are displayed on the top and the bottom on the right.

surrounding stellar halo gets more prominent with time. Although we are not able to trace the orbit of the in-falling satellites in detail, their position suggests that they get accreted from anisotropic directions.

In the velocity maps (right upper and lower panels) we clearly see that the rotating stellar core already present at lbt = 9.4Gyr is visible at all times, and gets not destroyed during the evolution of the galaxy. It gets more pronounced and grows in size towards lower redshift. The accreted satellites are clearly visible in the velocity maps. Especially at lbt = 6.4Gyr, we see a coherent velocity structure in the right upper corner which is most probably caused by stripped stars from the in falling satellite. However, the tail is not dense enough to be identified in the density map. The galaxy never shows an ordered rotating motion in the halo, which is reflected in the $\lambda(R)$ profile: At all times the profile is decreasing and maintains its central peak. In general, the entire profile spins down at all radii.

Fig. 6.13 shows various radial properties of the example galaxy at $z = 0$, demonstrating the dynamic and kinematic composition of the halo. We select all particles of a merging satellite at the moment when the merger takes place and identify them at $z = 0$, for all mergers happening below $z = 2$. Furthermore, we follow the complete evolution of the galaxy to identify the stars that have been formed in-situ and stars that have been formed outside and later on got accreted onto the halo. Note that we follow the accreted and in-situ component

down to the first identification of the halo, while we only consider merger events below $z = 2$. Therefore, the merger components do not fully add up to the total accreted component.

The upper panel of Fig. 6.13 shows the density profile of the different components: total density profile (black solid), accreted (solid blue), in-situ (solid red), mini merger (dotted blue) since $z = 2$, and minor merger (dashed blue) since $z = 2$ ($n = 300$ equal particle bin).

The total profile is well-described by a Sersic profile with a Sersic index of $n = 3.0$, consistent with an elliptical galaxy. Decomposing the profile into accreted and in-situ shows that the individual components are closer to an exponential than the total profile. At $\sim 1.2R_{1/2}$, the accreted and in-situ profiles cross, marking the transition from the in-situ dominated centre to the accretion dominated halo. This is in line with our hypothesis that the decline in the $\lambda(R)$ profile marks a transition of this kind. The stacked mini merger profile contributes only marginally to the total density. In contrast, the minor mergers are a significant contribution to the accreted component. At $\sim 1.7R_{1/2}$, we find a transition between the minor merger profile and the in-situ profile.

In the lower panel of Fig. 6.13 we connect the density profile to the kinematic $\lambda(R)$ profile. The black solid line shows the $\lambda(R)$ profile for all stars, while the other curves decompose the profile in the same manner as in the upper panel. Note that due to the lack of particles it is not possible to construct a $\lambda(R)$ profile for the mini mergers.

The total $\lambda(R)$ profile exhibits a steep incline in the centre within $0.5R_{1/2}$ up to a peak at $\sim 1.0R_{1/2}$. Beyond $\sim 1.0R_{1/2}$ the profile decreases significantly to a minimum at $\sim 2.0R_{1/2}$, followed by a mild increases beyond that radius. Interestingly, the radial transition range, in which the in-situ and accreted density profiles cross, coincides with the declining section of the total $\lambda(R)$ profile. The $\lambda(R)$ profile for the in-situ component follows a similar shape, however with a much stronger increase in the centre and accordingly a higher peak. At radii larger than $\sim 2.0R_{1/2}$, the in-situ profile has only very few data points, reflecting the drop in density.

The profile for the accreted component does not show much variation except for a mild increase in the outer radial range. It does not follow the peak of the in-situ profile in the centre, hence mitigating the peak of the total profile to lie below the in-situ profile. For radii larger than $2.5R_{1/2}$, the $\lambda(R)$ profile of the accreted component coincides with the $\lambda(R)$ profile of the total and the minor merger.

This finding clearly shows that the transition from high rotational support at the peak radius to a less rotational dominated region is driven by the transition from an in-situ dominated inner part to an accretion-dominated halo. In this particular example the halo kinematics are dominated by the stars accreted through minor merger that were stripped from the satellite during the infall.

It also supports the idea, presented by Foster et al. (2018), Bellstedt et al. (2017), and Arnold et al. (2014) that the declining profiles indicate an embedded in-situ disk, albeit this disk seems to be rather old. Investigating the age distribution of the in-situ formed stars revealed that 60% of the in-situ stars, which form the highly rotating central disk at $z = 0$, were formed before $z = 2$, and only 17% below $z = 1$. We find a similar behaviour for all our decreasing galaxies at $z = 0$, clearly highlighting that the decreasing signal in $\lambda(R)$ really represents a indication for an old embedded stellar disk with a purely mini/minor merger dominated formation history.

In the previous we showed for an example galaxy with decreasing profile, that the rotating inner part was formed in-situ while the outer halo was formed by only mini and minor mergers. We now test if this is generally the case by investigating where the accreted stars get deposited

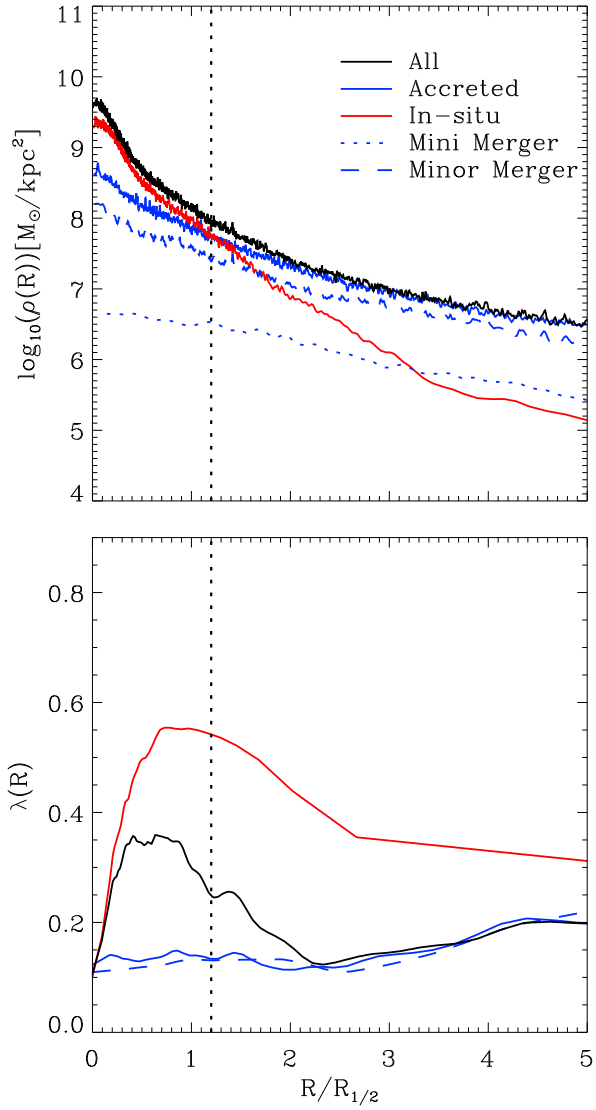

Figure 6.13: Further analysis of the *Magneticum* example galaxy investigated in Fig. 6.12. *Upper Panel:* Stellar density profile of the example galaxy at $z = 0$ split up into several components. The black solid line shows the profile for all stars while the red and blue solid lines depict the contributions from the in-situ and accreted component constructed from the complete evolution of the galaxy. Blue dashed and dash-dotted curves show the contribution of stars accreted via minor and mini merger since $z = 2.0$. *Lower Panel:* $\lambda(R)$ profile split up in the same manner as in the upper panel. Note that it is not possible to construct a $\lambda(R)$ profile for the mini merger stars due to the lack of particles. Vertical lines mark the crossing of the in-situ and accreted density profiles.

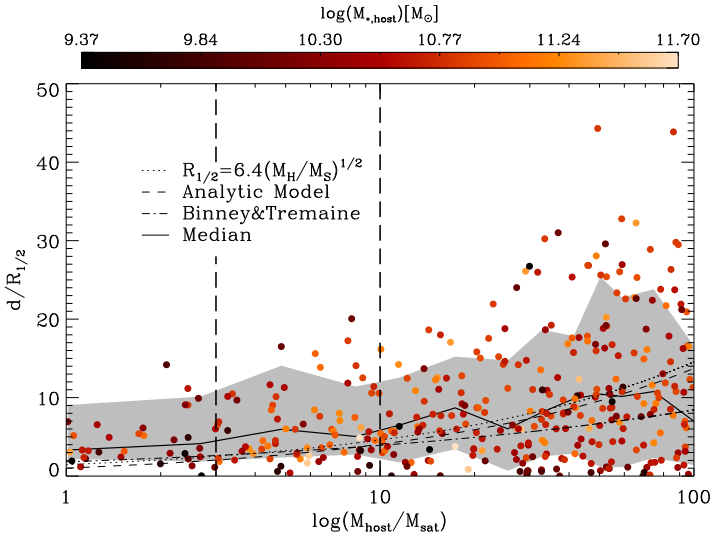

Figure 6.14: Half-mass distribution radius d normalised by $R_{1/2}$ of the host at the moment of the merger event in dependence of the mass-ratio stacked for all merger events experienced by *Magneticum* galaxies with decreasing profiles. The colour encodes the stellar mass of the host at the moment of the merger event. Vertical dashed lines visualise the borders between major, minor and mini merger. The black solid line shows the median of the distribution within bins while the grey shaded area mark the corresponding 16th and 84th percentile. The dashed, dotted and dash-dotted curves show predictions from theoretical models extracted from Karademir et al. (2019).

for a larger sample of galaxies. We quantify this by the half-mass distribution radius d: for every single merger event of all decreasing galaxies we select the accreted stars at the moment of the merger and identify them within the halo at $z = 0$. The half-mass distribution radius d is then defined to be the radius of a sphere containing half of the total mass of the accreted stars. Therefore, d represents a measure for the radius at which the merger deposited its stars.

Fig. 6.14 shows d, normalised by $R_{1/2}$ at the moment of the merger event, versus the mass ratio of the merger, colour-coded according to the stellar mass of the host at the time of the merger. The solid black curve represents the median within bins of 30 data points, while the grey shaded area marks the 16th and 84th percentile. The three non-solid lines show the prediction from three analytic models presented by Karademir et al. (2019). Vertical dashed lines visualise the borders between major, minor, and mini merger.

The median curve shows a continuous incline with increasing mass fraction following the behaviour of the analytic models from Karademir et al. (2019) (dashed and dotted). Therefore, lower mass satellites get stripped at larger radii. Similarly, the scatter becomes significantly larger with increasing mass-fraction. While the major merger cover a comparably small range below $d/R_{1/2} = 14$, minor and mini merger populate a significantly broader range. This can be explained by the influence of the orbital configuration of the merger, as found by Karademir et al. (2019). Investigating a large set of idealised merger simulations with varying orbital configurations and mass-fractions, they showed that major mergers always reach the galaxy at the centre of the halo, regardless of the orbit. In contrast, for minor and especially mini mergers, d is much more sensitive to the orbital configuration and can build up a stellar halo while not affecting the central galaxy. Therefore, minor and mini merger represent a suitable process that leaves the rotating component in the centre intact while building up a

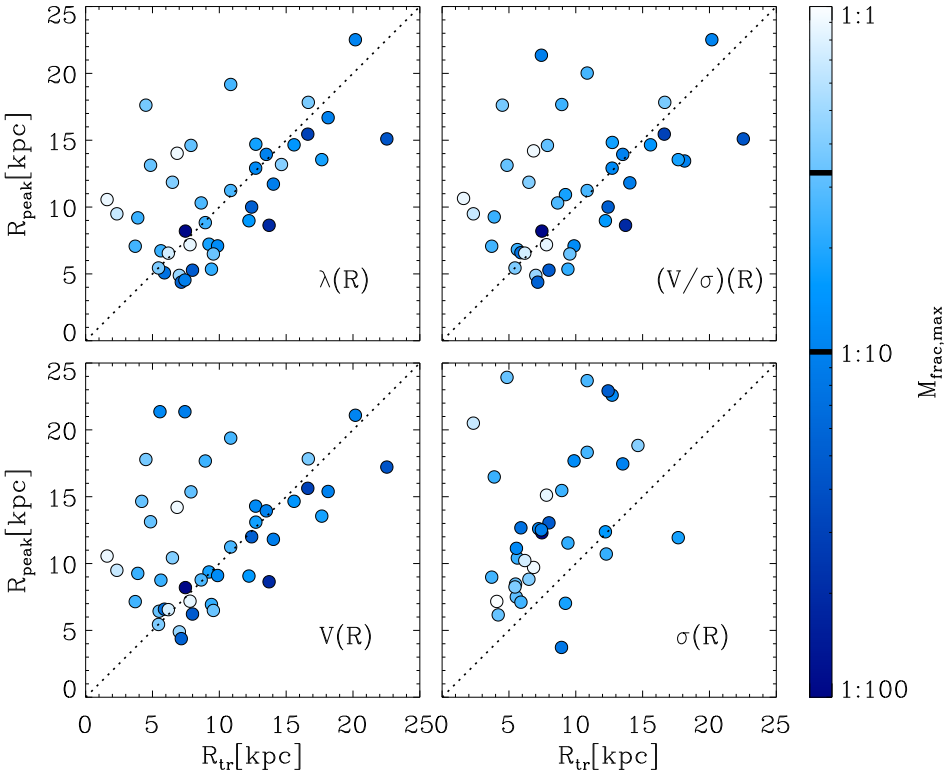

Figure 6.15: Radius of the maximum of the $\lambda(R)$ profile $R_{\rm peak}$ versus the transition radius $R_{\rm tr}$ at which the accreted component begins to dominate the stellar density profile for *Magneticum* decreasers. The colour encodes the mass-ratio of the most massive merger the galaxy experienced during its formation since $z = 2.0$.

kinematic distinct stellar halo.

To further explore the connection between the kinematic transition and the transition from in-situ to accreted stars we investigate the connection between the position of the maximum of the kinematic profiles $R_{\rm peak}$ and the density-profile of accreted and in-situ stars for a subset of 43 decreasers. For this subsample we have access to a well-defined transition radius $\mathrm{R_{tr}}$ that is defined to be the radius at which the density profile of in-situ and accreted stars intersect.

Fig. 6.15 correlates $\mathrm{R_{tr}}$ with $R_{\rm peak}$ for the $\lambda(R)$ profile (upper left), $(V/\sigma)(R)$ profile (right upper), V(R) profile (left lower), and $\sigma(R)$ profile (right lower). The colour encodes the mass-ratio of the most massive merger experienced by the galaxy since $z = 2$.

In the upper left panel we can clearly see that there is a apparent trend for $\mathrm{R_{peak}}$ to increase with increasing $R_{\rm tr}$. The lower right region below the 1:1 line of the diagram is completely unoccupied. Above the 1:1 relation we find a larger orthogonal scatter. The galaxies with the largest distance to the 1:1 line have all experienced major mergers as indicated by the colour. Therefore, the scatter around the 1:1 becomes considerably smaller when only considering the objects that did not undergo a major merger in their evolution. However, a certain scatter in the correlation is expected since in the transition region, where the accreted and in-situ component overlap, the combined kinematics are eminently complex.

As expected, a very similar behaviour is visible for the $(V/\sigma)(R)$ profile, however with a slightly larger scatter. Decomposing the $(V/\sigma)(R)$ profile in the lower two panels reveals that the velocity is the main driver for the correlation found in the upper panels: While for V the correlation has a comparable scatter around the 1:1 line and with $\mathrm{M_{frac,max}}$, σ does not show

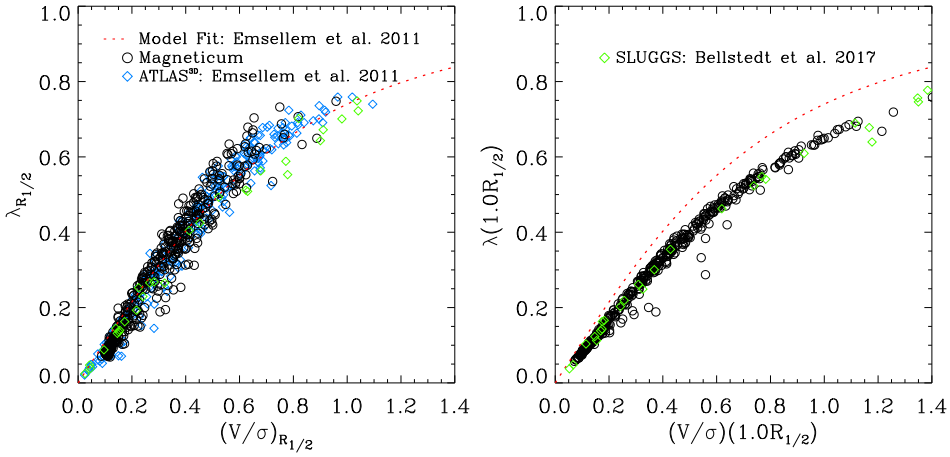

Figure 6.16: Correlation between λ and (V/σ) at a scale of $1.0\mathrm{R}_{1/2}$. The *left panel* displays the quantities integrated within $\mathrm{R}_{1/2}$. The right panel shows the local quantities calculated within a elliptical shell at $1.0\mathrm{R}_{1/2}$. Black circles mark the simulated *Magneticum* galaxies, while the red dashed line is the best fitting relation from Emsellem et al. (2011) obtained from dynamical modelling. Blue open diamonds mark observations from the ATLAS^{3D} survey, while green open diamonds mark observations from the SLUGGS survey extracted from Bellstedt et al. (2017).

a correlation close to the 1:1 line at all.

Based on this finding we conclude that, for galaxies with decreasing profiles, the kinematic transition is closely correlated with the transition from an in-situ dominated centre to accretion dominated halo. Furthermore, we predict, that $\mathrm{R}_{\mathrm{peak}}$ represents a good estimator for this transition region in many cases. Since $\mathrm{R}_{\mathrm{peak}}$ can be observed with a sufficient radial coverage, as has been done in Pulsoni et al. (2018), in contrast to R_{tr} this represents a meaningful tool to estimate the transition region in observations.

6.6 λ versus V/σ

In Emsellem et al. (2007) and Emsellem et al. (2011) it has been shown that the integrated $\lambda_{R_{1/2}}$ and (V/σ) tightly correlate with the form

$$\lambda_{\mathrm{R}_{1/2}} = \frac{\kappa (V/\sigma)_{\mathrm{R}_{1/2}}}{\sqrt{1+\kappa^2 (V/\sigma)^2_{\mathrm{R}_{1/2}}}} \tag{6.15}$$

where κ is estimated to be ~ 1.1. Given that we study local $\lambda(R)$ and $(V/\sigma)(R)$, we want to investigate the connection between λ and (V/σ) measured locally to show that our results are not dependent on whether $\lambda(R)$ or $(V/\sigma)(R)$ is used.

Fig. 6.16 shows the correlation between λ and (V/σ) integrated within $1\mathrm{R}_{1/2}$ in the left panel and the local values at $1.0\mathrm{R}_{1/2}$ on the right. Black circles represent the Magneticum galaxies, while the red dashed lines and the blue diamonds in the left panel mark the best model fit and observations extracted from Emsellem et al. (2011). Observations from the SLUGGS survey extracted from Bellstedt et al. (2017) are marked by green diamonds. For the integrated quantities, the *Magneticum* galaxies are in good agreement with the theoretical model prediction, however with a slightly steeper slope. A steeper slope, with respect to the model, is also apparent in the observed ATLAS^{3D} sample. The SLUGGS galaxies exhibit a

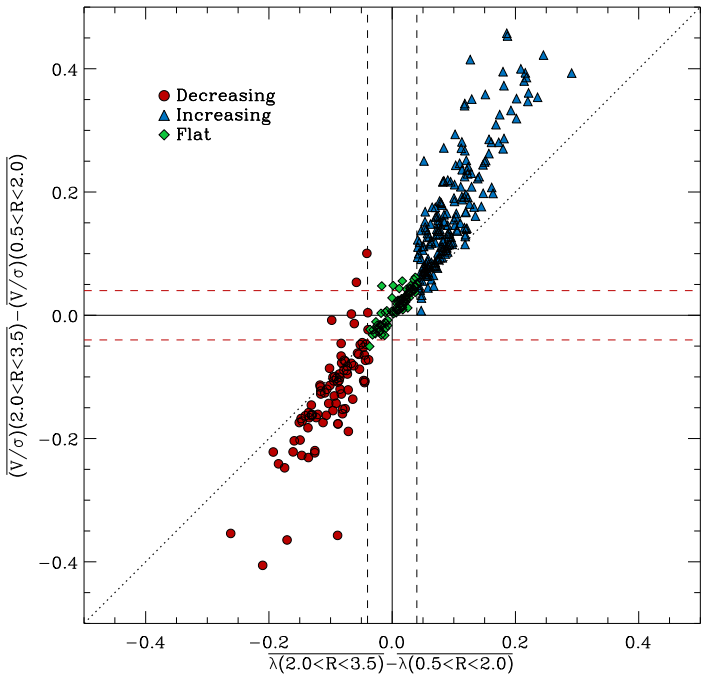

Figure 6.17: Gradient determining the classification in decreasing, increasing and flat given in Eqn. 6.12 for the *Magneticum* sample. The x-axis displays the gradient for $\lambda(R)$ profile, while the y-axis displays the corresponding gradient of the $(V/\sigma)(R)$ profile. The sample is split up into decreasing (red circles), increasing (blue triangles), and flat (green diamonds) based on the $\lambda(R)$ profile. The vertical dashed lines illustrate the chosen boundaries of the three groups, while the dotted line marks the 1:1 relation.

slightly shallower slope in the high spin regime than than ATLAS^{3D} and the Magneticum galaxies.

For the locally measured quantities, the correlation is tighter than in the integrated case. This is due to the larger area considered by the integration and therefore more variations in the kinematic maps. In contrast, the calculation of the local values is only based on the area close to an isophote, excluding regions with large variations in the kinematic maps. Although it follows a similar shape, the local correlation exhibit a shallower slope with respect to the model prediction and the correlation found for the integrated values. This can be explained by the way we calculate the local values: Using the circularised radius in Eq. 6.5 explicitly drops the radial dependence of $\lambda(R)$ calculated on an isophote, suggesting $\kappa = 1.0$ in Eq. 6.15 corresponding to a shallower slope of the relation than for $\kappa = 1.1$. We find the same behaviour for the SLUGGS sample.

The profile classification applied in this study is mainly based on the difference between the inner ($0.5\mathrm{R}_{1/2} < R < 2.0\mathrm{R}_{1/2}$) and outer ($2.0\mathrm{R}_{1/2} < R < 3.5\mathrm{R}_{1/2}$) mean of the λ(R) profile by using a fine tuned threshold of ± 0.04 to separate increasing and decreasing profiles. Fig. 6.17 shows this gradient for the λ(R) profile versus the gradient of the $(V/\sigma)(R)$ profile at the same radii. The 1-1 relation is given by the dotted line, while the vertical dashed lines mark the 0.04 threshold. Furthermore, the sample is split up into the three profile classes marked by the symbols as indicated in the legend.

As expected from Fig. 6.16, the two gradients correlate strongly. In the small gradient regime, which is populated by flat profiles, the distribution follows the 1-1 relation closely. Only for more negative and positive gradients, the gradients in the $(V/\sigma)(R)$ profile diverge to

lower and larger values, respectively. This is most probably due the flattening of the relation at larger values seen in Fig. 6.16, since a stronger gradient suggests larger amplitude values in the flatter regime of the relation. However, it is evident that the chosen threshold value for the $\lambda(R)$ gradient also represents a meaningful differentiation in the $(V/\sigma)(R)$ gradients as illustrated by the red dashed line with only few misclassified galaxies. Therefore, we conclude that utilising the $(V/\sigma)(R)$ profile for classification would not alter the results of the study.

6.7 Summary and Conclusion

We have investigated the kinematic properties of a sample of 450 galaxies, extracted from the *Magneticum Pathfinder* simulations out to $5R_{1/2}$. For this sample we construct $\lambda(R)$ and $(V/\sigma)(R)$ profiles to assess the local kinematic state, and analyse them with regard to galaxy properties and implications on the formation of the galaxies and the halo it resides in.

In a first step we quantify the shape of the $\lambda(R)$ profiles by a simple two-point gradient and compare this to observations from the SAMI, SLUGGS, and ePN.S surveys. Overall, we find an excellent agreement with the SLUGGS and ePN.S observations, while SAMI finds significantly larger gradients also in comparison to the other observational samples. In agreement with the observations, we find negative gradients for a significant fraction of centrally regular rotating objects, with an increasing fraction when the outer sampling point is shifted to larger radii. This suggests that these galaxies exhibit a rotating component in the centre which is embedded in a less rotationally supported halo, supporting the assumption from Arnold et al. (2014) and Foster et al. (2018) that these galaxies are disks embedded in a non-rotating stellar halo.

Visually examining the $\lambda(R)$ profiles for our simulated sample reveals three characteristic shapes:

a) Decreasing: The profiles exhibits a central peak in the range $0.5R_{1/2}$-$2.0R_{1/2}$.

b) Increasing: The profile is continuously increasing with varying slope until it reaches a plateau.

c) Flat: The profile features only minor variations and stays constant out to the maximally probed radii.

Approximately 50% of the sample have an increasing profile, while 20% are decreasing, and 20% are flat. The predominance of of increasing profiles is in agreement with observations by Bellstedt et al. (2017), Foster et al. (2018), and Arnold et al. (2014).

We find that the vast majority of flats are centrally slow rotating galaxies, while the increasing profiles are equally distributed among centrally fast and slow rotators (50%), however showing larger maximum amplitudes in $\lambda(R)$ in the fast rotating regime. Except for one galaxy all the decreasing profiles are classified as centrally fast rotating, reflecting the peak of the profile in the centre.

In order to understand the origin of the different $\lambda(R)$ profile shapes we exploit the full power of the simulation and follow the evolution of our sample through cosmic time. Since galaxy mergers represent one of the major drivers of galaxy evolution at lower redshift, we analyse our sample with respect to merger events. In particular, decreasing profiles show a distinct accretion behaviour: They gain most of their stellar mass via minor and mini merger and not through major merger as the increasing profiles. Analysing the accretion history in

more detail for an example galaxy with decreasing profile we find that the central peak in the profile is generated by stars that were formed in-situ at early times, while the slow rotation at larger radii is generated by stars that got accreted in low mass-fraction merger events. This is supported by the finding that at $z = 2$ decreasing profiles are, with 37% of the total sample, the predominant class showing that the central peak in the profile is already in place at this time. Furthermore, the radial range of the decline coincides with the transition from in-situ to accreted domination in the density profile. This suggests a formation pathway in which the galaxy merges with low mass galaxies from random direction that get disrupted in the halo due to tidal forces and build up a non-rotating halo while leaving the rotating component in the centre unimpaired.

We support this notion by investigating the distribution of stars being accreted in merger events within the halo at $z = 0$. We find that stars that got accreted in minor and mini merger get preferentially deposited at larger radii in comparison to major merger building up the stellar halo. By correlating the position of the peak of the $\lambda(R)$ profile for decreasing profiles with the transition from in-situ to accreted domination in the density profile we predict, that the peak radius represents a good proxy for the transition radius. Since position of the peak of the $\lambda(R)$ profile can be observed, with a sufficient radial coverage, this provides a meaningful tool to estimate the transition radius in observations.

In conclusion we find that galaxies generally show three characteristic local kinematic profiles shapes quantified by $\lambda(R)$. Our conclusions do not change when using $(V/\sigma)(R)$ as a proxy for the local kinematics. We find clear evidence, that the profiles shape encode information about the accretion history of galaxies, especially for the galaxies with decreasing profiles at $z = 0$. For these galaxies we can constrain the accretion history to an early in-situ disk formation at $z \geq 2$ and subsequent mini and minor merger that build up the stellar halo. Therefore, decreasing profiles resemble an old disk embedded in a non-rotating accreted halo. Furthermore, $\lambda(R)$ represent a meaningful diagnostic to constrain the radial range where the in-situ or accreted stars dominate the galaxy/halo dynamics. Therefore, our study provides meaningful interpretations and predictions for current and future observations for the formation of galaxies and their stellar halo that can be deduced from the stellar central and halo kinematics.

Chapter 7

Extending the Analysis to Higher-Order Moments

This chapter will be published in Schulze et al., to be submitted[1]

Abstract

The kinematics of galaxies has been shown to be an excellent tracer of the galaxy formation pathway, however, the possible formation pathways are rather diverse. To further disentangle the formation histories we analyse the line-of-sight velocity distribution (LOSVD) of galaxies extracted from the hydrodynamic cosmological *Magneticum Pathfinder* simulations also considering the third and fourth kinematic moments, i.e. h_3 and h_4. This extends previous studies based on isolated merger and zoom-in simulations for the first time to a fully cosmological environment. Focusing on the global higher-order moments, we find evidence for a shift towards a peaked LOSVD with increasing stellar mass, indicative of an increased radial anisotropy, in agreement with observations. We find a strong trend for galaxies with $\langle h_4 \rangle < 0$ to have significantly larger in-situ fractions than galaxies with $\langle h_4 \rangle > 0$, reflecting the different origin of the orbital structure encoded in h_4. Following our sample through cosmic time reveals that dry accretion is an important process driving the variations in the slope of the spatially resolved (V/σ)-h_3 relation, with steeper anticorrelation resulting from increased dry accretion through major mergers, while the strength of the correlation does not correlate clearly with the stellar and gaseous mass accreted via merger. Instead, the evolution of galaxies with strong anti-/correlations is governed by enhanced internal star formation fuelled by smooth gas accretion. Furthermore, we show that including the higher-order moments beyond one half-mass radius is a useful tool to further quantify the different accretion histories of regular rotating galaxies: dry massive mergers lead to an overall non-correlated (V/σ)-h_3 relation, wet massive mergers are indicated by centrally anticorrelation and non-correlated (V/σ)-h_3 relation in the outskirts, while galaxies with anticorrelation in the centre and outskirts are dominated by internal evolution and small mass accretion.

[1]The section describing the details of the Magneticum simulations is omitted since it is already contained in Chap. 3 of this thesis.

7.1 Higher-Order Kinematic Moments in Galaxies

The stellar kinematics of galaxies has been subject to many observational and theoretical studies over the past decade, since it encodes information about the internal and external processes that determine the present day properties of galaxies. The understanding of galaxy dynamics and kinematics has been advanced significantly by the development of integral-field spectroscopy, allowing to observe stellar kinematics and populations in a spatially resolved fashion. Large observational IFS surveys provide insight into the kinematic properties of thousands of galaxies in a statistical reliable manner, e.g. SAURON (Bacon et al., 2001), ATLAS^{3D} (Cappellari et al., 2011a), SAMI (Croom et al., 2012), CALIFA (Sánchez et al., 2012), MaNGA (Drory et al., 2015), MASSIVE (Ma et al., 2014). Especially the analysis of the structure of the LOSVD, quantified by the first two kinematic moments line-of-sight velocity and line-of-sight dispersion, significantly improved our knowledge of galaxy properties, such as fast and slow rotation of ETGs (Emsellem et al., 2007; Cappellari et al., 2007; van de Sande et al., 2020), complex kinematic substructures (McDermid et al., 2006b; Krajnović et al., 2011), kinematic morphology-density relation (Fogarty et al., 2014; Brough et al., 2017), and prolate rotation of the most massive galaxies (Tsatsi et al., 2017; Krajnović et al., 2018), but also of dwarf galaxies (Ebrová and Łokas, 2015).

Additional, kinematic information is encoded in the higher-order moments of the LOSVD, in particular h_3 and h_4, which describe the higher-order deviation of the LOSVD from a perfect Gaussian distribution. The first study to investigate the higher-orders of the LOSVD for a statistically meaningful and unbiased sample was Bender et al. (1994). They investigate the LOSVD of 44 ETGs up to h_4 using a long-slit spectroscopic approach and found that the deviation from a Gaussian distribution is generally small of order $\sim 10\%$, while asymmetric deviations (h_3) are more prominent than symmetric deviations (h_4). In general, the presence of a stellar disk produces a asymmetric LOSVD (Gerhard, 1993; van der Marel and Franx, 1993). Furthermore, for fast rotating galaxies h_3 shows a strong anticorrelation with (V/σ) (Bender et al., 1994; Halliday et al., 2001; Chung and Bureau, 2004; Spiniello et al., 2015; Forbes et al., 2016; Bellstedt et al., 2017). More complex substructures, as bars and KDCs, can manifest in different correlations of kinematic moments (e.g. Bureau and Athanassoula, 2005; Iannuzzi and Athanassoula, 2015; Du et al., 2016; Johnston et al., 2018; Blaña Díaz et al., 2018).

Strong anticorrelation between h_3 and (V/σ) was also found by Krajnović et al. (2006) and Krajnović et al. (2011) for ETGs within the SAURON and ATLAS^{3D} survey, respectively. Krajnović et al. (2013) interprets the presence of the anticorrelation in ETGs as evidence for an embedded stellar disc. A particularly detailed analysis of the higher-order moments was conducted by van de Sande et al. (2017a), using IFS data from the SAMI survey for 315 galaxies. Motivated by insights from cosmological simulations by Naab et al. (2014), the authors classify galaxies according to their distribution in the h_3-(V/σ) plane. As a result, they identify five classes of distinct h_3-(V/σ) structures, varying from sharp vertical relations to strong anticorrelation, and analyse the class properties with regard to other galaxy properties. They show that the h_3-(V/σ) signature of galaxies does not necessarily distinguish galaxies in the $\lambda_{R_{1/2}}$-ϵ plane. By comparing their classification to the classification introduced in Naab et al. (2014), they constrain the merger history of the different types of h_3-(V/σ) signature galaxies.

Using IFS data from the MASSIVE survey for 41 massive ETGs, Veale et al. (2017b) showed that, while the distribution of the average h_3 is symmetric around 0 with low values

as expected for the most massive galaxies, the average h_4 is positive for the complete sample. Further studies found correlations between higher-order moments and galaxy properties, e.g. morphology (Vudragović et al., 2016) and metallicity gradients (Greene et al., 2019; Ferré-Mateu et al., 2019).

The interpretation of higher order moments in observations is in general not trivial. On the one hand, h_3 and h_4 are obviously determined from a certain projection, and therefore susceptible to degeneracies and projection effects. On the other hand, it is difficult to disentangle the influence of substructures, as bars and bulges and their superposition, on the higher order moments. Therefore, several studies have employed numerical simulations in order to give meaningful interpretations of observed LOSVD structure and predictions for future surveys.

Early simulations have shown that the remnants of collisionless binary mergers typically show a positive correlation between h_3 and (V/σ) due to the superposition of minor-axis tube and box orbits (Bendo and Barnes, 2000; Jesseit et al., 2007). More recently, Tsatsi et al. (2017) investigated the origin of prolate rotation and its signature in the LOSVD in a series of four N-body polar major merger simulations. The authors conclude that all remnants exhibit clear prolate rotation and a characteristic positive correlation between h_3 and (V/σ) for low (V/σ) and an anticorrelation for large (V/σ), generating a S-shaped distribution. Involving a dissipational gas component, Hoffman et al. (2009) investigated the impact of the progenitor gas-fraction $f_{\rm gas}$ in 1:1 isolated bulgeless disk mergers on the remnant LOSVD by varying $f_{\rm gas}$ from 0% to 40%, finding a continuous transition of the h_3-(V/σ) signature from no correlation for low $f_{\rm gas}$ ($< 15\%$) to strong anticorrelation for high $f_{\rm gas}$ ($> 15\%$), concluding that strong anticorrelation is a good tracer for a gas-rich merger that leads to the formation of a stellar disk from the progenitor gas (see also Naab and Burkert, 2001; Meza et al., 2003; Jesseit et al., 2005; Naab et al., 2006; Hoffman et al., 2010). While these studies provided meaningful insight into the impact of mergers on the LOSVD, the cosmological environment in which galaxies evolve is not considered. Therefore, Naab et al. (2014) extended the analysis to 44 zoom-in simulations capturing the cosmological environment. By classifying the sample according to their merger history, they confirm that recent gas-rich accretion, either gradual through minor mergers or through individual major mergers, generate the anticorrelation signal in the h_3-(V/σ) plane. Based on the same set of zoom-in simulations, Röttgers et al. (2014) related the kinematic properties and formation history to detailed orbit families. They show, that the h_3-(V/σ) anticorrelation originates from a dissipative formation history that leads to an increased fraction of z-tube orbits. In a very detailed analysis of the LOSVD of 20 cosmological zoom-in simulations focusing on the effect of AGN feedback, Frigo et al. (2019) showed that AGN activity has a strong influence on the LOSVD and the underlying orbital distribution by regulating in-situ star formation.

In the this chapter we investigate the properties of galaxies galaxies extracted from the fully cosmological *Magneticum Pathfinder* Simulations with regard to higher-order moments. In order to cover a large range in stellar masses we select galaxies from Box4 uhr and Box2 hr being cautious about resolution effects. The methodological details of the galaxy analysis and classification are outlined in Sec. 7.2. In Sec. 7.3 we conduct a first qualitative investigation of the connection between the first four moments, i.e. $\overline{V}$, σ, h_3, and h_4 for different kinematic galaxy types. In addition, this section analyses the connection of the averaged higher-order moments to further global galaxy properties as stellar mass, fast/slow rotation, and in-situ fraction. In order to investigate the velocity moments in more detail Sec. 7.4 explores the V/σ-h_3 plane for individual galaxies and connects it to global galaxy properties. Exploiting

the full power of the simulation we furthermore follow the individual galaxies through cosmic time and identify the imprints of the formation history on the V/σ-h_3 distribution. We extend our analysis to radii beyond one half-mass radius in Sec. 7.5, attempting to disentangle the group of regular rotating galaxies. We conclude with a discussion and summary in Sec. 7.6.

7.2 Galaxy Analysis and Classification

7.2.1 Classifications

To investigate the properties of our sample in detail we adopt the visual classification of the kinematic maps within $1R_{1/2}$, similar to Schulze et al. (2018), in five kinematic classes:

- *Regular-Rotator (RR):* The velocity map features regular rotation around the morphological minor axis.
- *Non-Rotator (NR):* The velocity map show low level velocities and no indication of ordered motion.
- *Distinct-Core (DC):* The velocity map hosts a dynamically decoupled substructure in the centre. This involves misaligned rotating central substructures with respect to the surrounding galaxy, and rotating substructures embedded in the centre of a non-rotating galaxy.
- *Prolate-Rotator (PR):* The velocity map features regular rotation around the morphological major axis.
- *Disks (D):* The velocity map shows pronounced ordered rotation around the minor axis, and the galaxies (see Eq. 7.1) b-value larger than -4.35, which is the threshold for pure disk galaxies as defined by Teklu et al. (2015).

The b-value adopted to identify pure disk galaxies is defined as

$$b = \log_{10}\left(\frac{j_*}{\text{kpc km/s}}\right) - \frac{2}{3}\log_{10}\left(\frac{M_*}{M_\odot}\right), \tag{7.1}$$

i.e. it describes the position of a galaxy in the stellar mass-angular momentum-plane. As shown by observations (Fall, 1983; Fall and Romanowsky, 2013; Obreschkow and Glazebrook, 2014; Cortese et al., 2016; Fall and Romanowsky, 2018; Sweet et al., 2018) and simulations (Teklu et al., 2015; Genel et al., 2015; Zavala et al., 2016; Lagos et al., 2017b; Schulze et al., 2018), this is a good approximate for galaxies morphology.

In our final samples we only include galaxies that can be classified in the kinematic classes in leaving us with 667 galaxies in Box4 uhr with stellar masses above $M_* = 3 \times 10^{10} M_\odot$ and 397 galaxies with stellar masses above $M_* = 1 \times 10^{12} M_\odot$ in Box2 hr. The class frequencies within the Box4 and Box2 galaxy sample are summarised in Tab. 7.1. It clearly shows the expected decrease in the frequency of RR and the increase in the frequency of NR when comparing the lower mass Box4 sample and the extreme high-mass Box2 sample. In the following study we will use the Box2 sample mainly as the comparison sample for data from the MASSIVE survey (Veale et al., 2017b) and as indicator for trends at higher stellar masses, while physical conclusions are drawn from the better resolved Box4 sample.

Table 7.1: The statistical distribution of the kinematic classes within the Box4 and Box2 sample.

	Box4 uhr		**Box2 hr**	
Groups	$N_{\rm gal}$	Percentage	$N_{\rm gal}$	Percentage
RR	428	63%	72	18%
NR	123	18%	273	69%
DC	39	6%	20	8%
PR	19	3%	32	5%
Disks	68	10%	0	0
Total	677		397	

7.2.2 Line-of-Sight-Velocity Distribution Analysis

In this chapter we will investigate the global and local moments of the LOSVD of the simulated galaxies in detail. Therefore, we construct projected two-dimensional line-of-sight maps of the first four velocity moments, i.e. mean velocity $\overline{V}$, dispersion σ, h_3, and h_4. The applied methodology is as comparable as possible to the methodology used in observations to be able to conduct a meaningful comparison and to provide meaningful predictions for future surveys, while accounting for the specific limitations of the simulated data.

The procedure to determine the $\overline{V}$ and σ maps is conceptional equivalent to that presented in Chaps. 4 and 6: Subsequent to a Nearest-Neighbor sampling of the stellar particles onto a rectangular grid with 0.3kpc resolution, we apply a Centroidal Voronoi Tesselation (CVT, Cappellari and Copin, 2003) to ensure a minimum number of particles per bin to reduce statistical particle noise. The procedure to determine the first four moments of the LOSVD proceeds as follows: The LOSVD within an individual CVT bin is approximated by a Gaussian distribution with higher order corrections applying the method introduced by van der Marel and Franx (1993):

$$f(v_{\rm los}) \propto e^{-\frac{1}{2}\omega^2} \left[1 + h_3 H_3(\omega) + h_4 H_4(\omega)\right] \tag{7.2}$$

with $w = (v_{\rm los} - \overline{V})/\sigma$, and where

$$H_{\rm m}(\omega) = \frac{1}{\sqrt{m!}} e^{\omega^2} \left(-\frac{1}{\sqrt{2}} \frac{\partial}{\partial \omega}\right)^m e^{-\omega^2} \tag{7.3}$$

are the Hermite polynomials. Due to the nature of simulated data, choosing an appropriate target particle number is a crucial trade-off between statistical meaningfulness of each CVT bin and spatial resolution of the generated map, i.e. we want the statistical error of the fitting parameters in one cell to be smaller than the difference of the absolute values between to neighbouring cells, while maintaining an adequate spatial resolution to resolve the kinematic features of the map. Fig.7.1 displays the result of a bootstrapping procedure deployed to determine the appropriate target particle number. In order to quantify the effect of varying particle number we selected six adjacent CVT bins with a target particle number of maximum 400 for a well resolved non-rotating galaxy where we expect minor variations within the maps. An increasing number of particles is randomly drawn within each of the six CVT bins to determine the four kinematic moments. Each random number of particles is drawn 300 times to estimate the statistical error. The arithmetic mean and the corresponding bootstrapping error of the moments for the six CVT bins are shown in Fig.7.1 in different colours. As can be seen the statistical error decreases with increasing number of drawn particles. Above 200

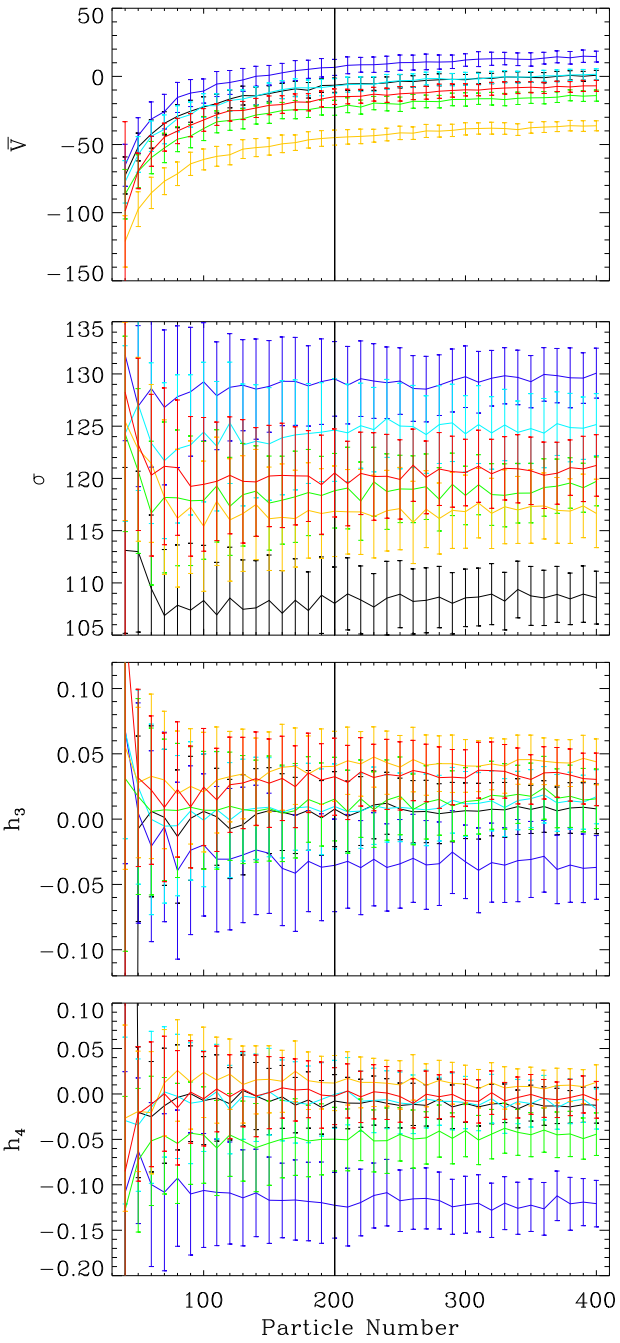

Figure 7.1: Results from a bootstrapping procedure for the four moments of the LOSVD, i.e. from top to bottom $\overline{V}$, σ and higher moments h_3 and h_4. Each colour shows the dependence on particle number of the mean value and the corresponding bootstrapping error for individual adjacent CVT bins. For every particle number 300 bootstrapping steps are performed.

particles it is possible to confidently distinguish between values of two neighbouring cells. Therefore, we chose a target particle number of 200 to generate the kinematic maps.

To quantify the global behaviour of the kinematic maps, we utilize the λ_{R} parameter (Emsellem et al., 2007), that has been subject to many former observational and theoretical studies. It is defined as

$$\lambda_R = \frac{\sum_{i=1}^{N_p} M_i \; R_i \; |\overline{V}_i|}{\sum_{i=1}^{N_p} M_i \; R_i \; \sqrt{\overline{V}_i^2 + \sigma_i^2}}, \tag{7.4}$$

where M_{i}, R_{i},$\overline{V}_{\mathrm{i}}$, and σ_{i} are the stellar mass, radius, mean velocity, and velocity dispersion of the i^{th} CVT bin, respectively. The sum in Eq. 7.4 runs over all CVT bins in the considered aperture. In addition we determine global $\langle h_3 \rangle$ and $\langle h_4 \rangle$ by fitting Eq. 7.2 to the total LOSVD instead of the individual CVT bins. Obviously, the LOSVD analysis depends on the specific projection. Throughout this study the edge-on projection of the galaxy is chosen as the line-of-sight to maximise any physical signal.

7.3 Higher Order Moments for Different Classes of Galaxies

In this section the connection between higher order moments and other galaxy properties is studied. Therefore, we will identify statistical trends between global galaxy properties quantifies by $\langle h_3 \rangle$ and $\langle h_4 \rangle$ for galaxies with different kinematic features and discuss this in the context of different formation pathways. Furthermore, the (V/σ)-h_3 and (V/σ)-h_4 distributions for individual Voronoi-Bins are analysed in detail and connected to tracers of the formation history of the galaxies.

7.3.1 Qualitative Connection Between Kinematic Features and Higher Order Moments

To visualise the connection between typical kinematic features and the higher-order moments, each row of Fig. 7.2 shows $\overline{V}$, σ, h_3, and h_4 maps for a poster-child example of the kinematic groups in the edge-on projection. The physical side-length of each panel is $2\mathrm{R}_{1/2}$, while the black bar in the right lower corner of the $\overline{V}$ map indicates 5kpc.

The regular-rotator in the first row shows distinct regular rotation around the minor-axis in the $\overline{V}$-map, characteristic for a fast rotator. The σ–map exhibits a high degree of symmetry. Two clear minima are visible along the major-axis that coincide with the region of fastest rotation. This structure is indicative of a stellar disk embedded in a rotating spheroidal component. In contrast, along the minor-axis two maxima are present. This central structure is embedded in a low σ surrounding. Similarly, the h_3-map shows clear structure in the form of opposing minimum and maximum, symmetric around the minor axis indicating strong leading wings in the LOSVD. The maxima/minima in the h_3-map are inverted with respect to the $\overline{V}$-map, suggesting an anticorrelation between h_3 and $\overline{V}$. The h_4-map has a double-ring feature with a ring of positive values corresponding to a peaked LOSVD surrounded by a ring of negative values indicating a flat LOSVD, however, the signal in h_4 is very weak.

The non-rotator represents a typical example of a slow rotator. The $\overline{V}$–map as well as the h_3-map and h_4-map do not show any coherent patterns. Solely the σ-map shows a maximum in the centre and a continuous gradual decrease towards larger radii.

A distinct rotating structure embedded in a non-rotating surrounding is visible in the $\overline{V}$-map of the distinct-core. Interestingly, the σ-map shows a distinct structure, however

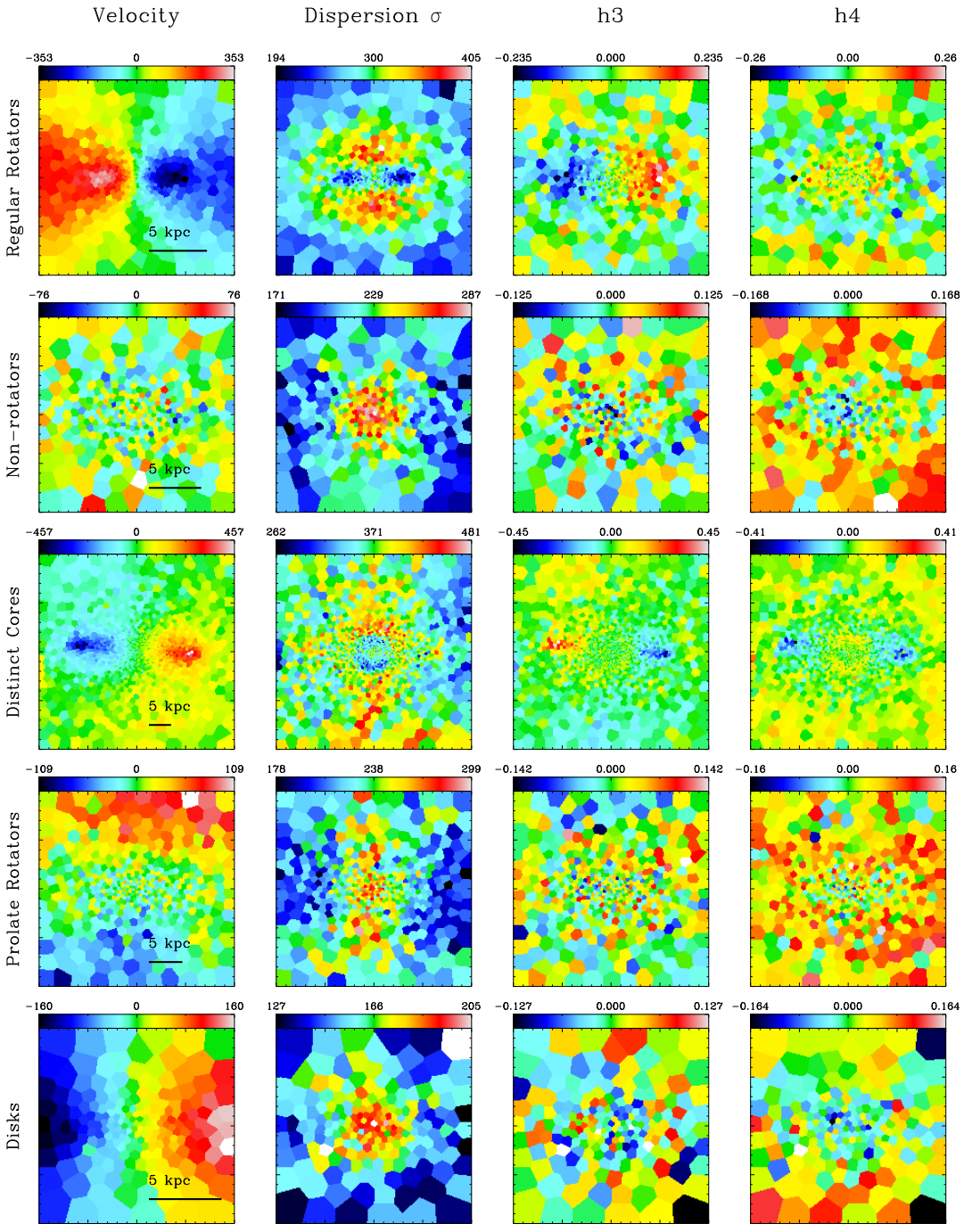

Figure 7.2: Example maps of the kinematic moments for galaxies of the five kinematic classes. From left to right each row displays the four moments, i.e. $\overline{V}$, σ, h_3, and h_4, of a galaxy representative of one kinematic class. The physical side-length of the panels is $2R_{1/2}$ and the black bar indicates a scale of 5kpc.

does not show the disk-like feature as the regular-rotator. In the centre a ring-like feature of lower dispersion is visible surrounded by a high dispersion structure that extends along the minor-axis. The h_3-map is anticorrelated with respect to the $\overline{V}$–map, similarly to the regular-rotator, however with a larger low h_3 region in the centre. A very distinct pattern is present in the h_4-map: We find a ring of enhanced h_4 values in the centre coinciding with the ring of lower values in the h_3-map. This ring-like feature is similar to the one found for the regular rotator. Along the major axis beyond this ring two clear minima are visible, indicating a more flat-topped velocity distribution and thus more tangential orbits. The spread in h_4 is the largest of all examples, suggesting a distinct change in the orbital configurations. Negative values of h_4 are typically associated with an increased tangential anisotropy, whereas positive h_4 are indicative of increased radial anisotropy (Gerhard et al., 1998; Thomas et al., 2007).

The fourth row displays the kinematic maps for a prolate-rotator, which show clear rotation around the major-axis in the $\overline{V}$-map. Furthermore, the rotation pattern does not reach to the very centre in contrast to the regular-rotator. The σ-map shows a maximum in the centre that extends along the minor-axis towards the rotating region and a rapid decrease along the major-axis. In the lateral regions σ is approximately a factor two lower than the in the centre. The h_3-map does not show a prominent feature. Interestingly, we do not find any sign of anticorrelation between h_3 and $\overline{V}$ as expected for rotation originating from in-situ star formation (Naab et al., 2014). This might be a hint that the prolate rotation in this case is not caused by an in-situ dissipational process, in line with the findings from Tsatsi et al. (2017). However, Tsatsi et al. (2017) also found a characteristic S-shape distribution in the h_3-(V/σ) plane of PRs which is not obvious in the maps for our example PR.

The lower row shows the maps for an example Disk. While the $\overline{V}$ map shows clear ordered rotation, the σ map does not feature a cold, low-dispersion disk, as found for the regular-rotator example. Furthermore, the σ map is most comparable to the non-rotator, showing a central region with enhanced σ. An extremely weak sign of anticorrelation between $\overline{V}$ and h_3 is visible in the very centre, however, much weaker than for the regular-rotator and the distinct core. Apart from a dip in the centre, the h_4 map is virtually featureless.

This first quantitative study of example maps revealed substantial differences between the kinematic classes that motivates a further more detailed investigation of the kinematic maps that is conducted in Sec. 7.4.

7.3.2 Connecting Global Galaxy Properties to Higher-Order Moments

To identify and investigate global statistical trends for different kinematic types of galaxies we analyse correlations of $\langle h_3 \rangle$ and $\langle h_4 \rangle$ with global galaxy parameters. Therefore, Fig. 7.3 presents the connection between $\langle h_3 \rangle$ (left panel), $\langle h_4 \rangle$ (right panel) and stellar mass M_*, for the five kinematic groups. In order to extend the sample to very massive objects Fig. 7.3 includes the Box2 sample marked by the grey shaded area. Additionally, the purple diamonds show the observational results from Veale et al. (2017b).

For $\langle h_3 \rangle$ we find a symmetric distribution around 0, independent of M_* and kinematic group. For $\log(\mathrm{M}_*) < 11$ a weak tendency towards positive values is visible. Interestingly, the kinematic groups cover a similar range in $\langle h_3 \rangle$ across the whole considered mass range even at the extreme high mass end. Hence, $\langle h_3 \rangle$ is not a sensitive quantifier of the internal kinematics, since it averages over the complete orbital composition.

The transition region $11.5 < \log(M_*) < 12$ between the two boxes is not sufficiently sampled. Unfortunately, this is the mass range where the observational comparison sample

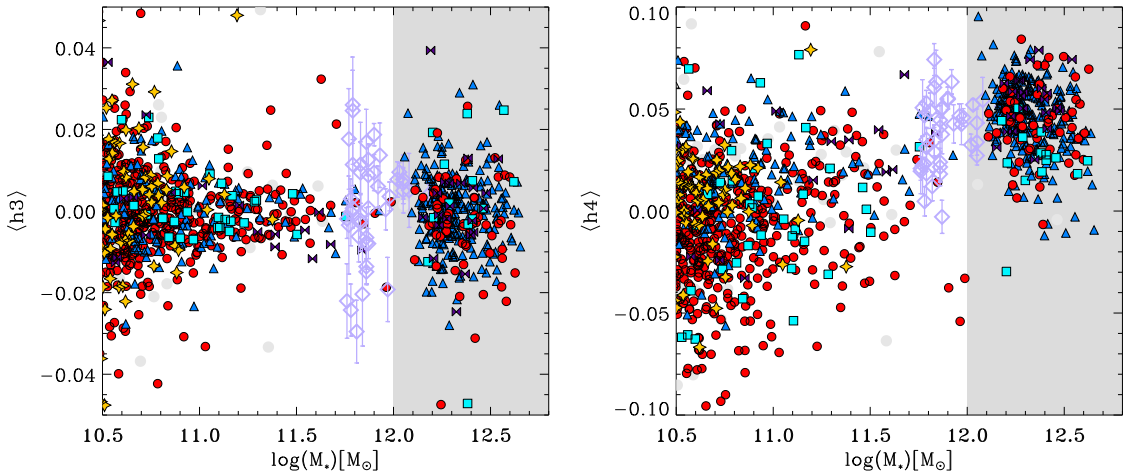

Figure 7.3: Higher order kinematic moments versus stellar mass M_* for all simulated galaxies, with colors and symbols separating the different kinematic classes. *Left panel:* Correlation between $\langle h_3 \rangle$ and for the simulated sample. *Right panel:* Correlation between $\langle h_4 \rangle$ and the stellar mass M_*. Both panels show the Box4 uhr and the Box2 hr sample. The transition between the boxes is marked by the grey shading. The purple symbols mark observations by the MASSIVE survey (Veale et al., 2017b).

is located, not allowing for a rigorous comparison. The NR dominated Box2 sample covers a similar range in $\langle h_3 \rangle$ than the low mass galaxies, not extending the trend of decreasing scatter found at lower masses. The scatter in the high mass sample is consistent with the observational sample. A more detailed comparison would require to analyse a medium sized simulated box with intermediate mass resolution which is beyond the scope of this paper.

In contrast to $\langle h_3 \rangle$, the $\langle h_4 \rangle$ distribution in the right panel of Fig. 7.3 shows a clear trend with stellar mass: For $\log(\mathrm{M}_*) < 11$, the total distribution is reasonably symmetric around 0, with 51% having negative $\langle h_4 \rangle$ and accordingly 49% positive $\langle h_4 \rangle$. With increasing stellar mass, the fraction of galaxies with negative $\langle h_4 \rangle$, and therefore a flattened LOSVD, reduces. This trend is already present for the Box4 sample, and the box2 sample as well as the observations naturally extend this trend. In the observational sample, only one galaxy (2%) exhibits a negative $\langle h_4 \rangle$, while for Box2 6 galaxies (2%) have negative $\langle h_4 \rangle$. Therefore, the orbital structure in the simulated galaxies changes towards higher masses favouring configurations with more peaked LOSVDs, making $\langle h_4 \rangle$ a particularly interesting parameter to study with regard to imprints of the formation history.

We further investigate the relation between the average moments and the notion of fast and slow rotators (Emsellem et al., 2007, 2011). Fig. 7.4 shows the $\lambda_{\mathrm{R}_{1/2}} - \epsilon$ plane colour coded according to $\langle h_3 \rangle$ (left panel) and $\langle h_4 \rangle$ (right panel) for the Box4 sample. There is no apparent systematic difference between fast and slow rotators, threshold indicated by the green line, with regard to $\langle h_3 \rangle$. Furthermore, neither $\lambda_{\mathrm{R}_{1/2}}$ nor ϵ correlates with $\langle h_3 \rangle$.

In contrast, we find a statistical difference between the fast and slow rotator populations in $\langle h_4 \rangle$ (right panel of Fig. 7.4): fast rotators preferentially have a flat top LOSVD indicative of more circular orbits (van der Marel and Franx, 1993), manifesting in an overall negative $\overline{\langle h_4 \rangle} = -0.035$. Slow rotators generally have a more peaked LOSVD with $\overline{\langle h_4 \rangle} = 0.017$. Therefore, in addition to the mass trend in Fig. 7.3, $\langle h_4 \rangle$ is also related to the fast and slow rotation. It has been shown in former studies (e.g. Jesseit et al., 2009; Naab et al., 2014;

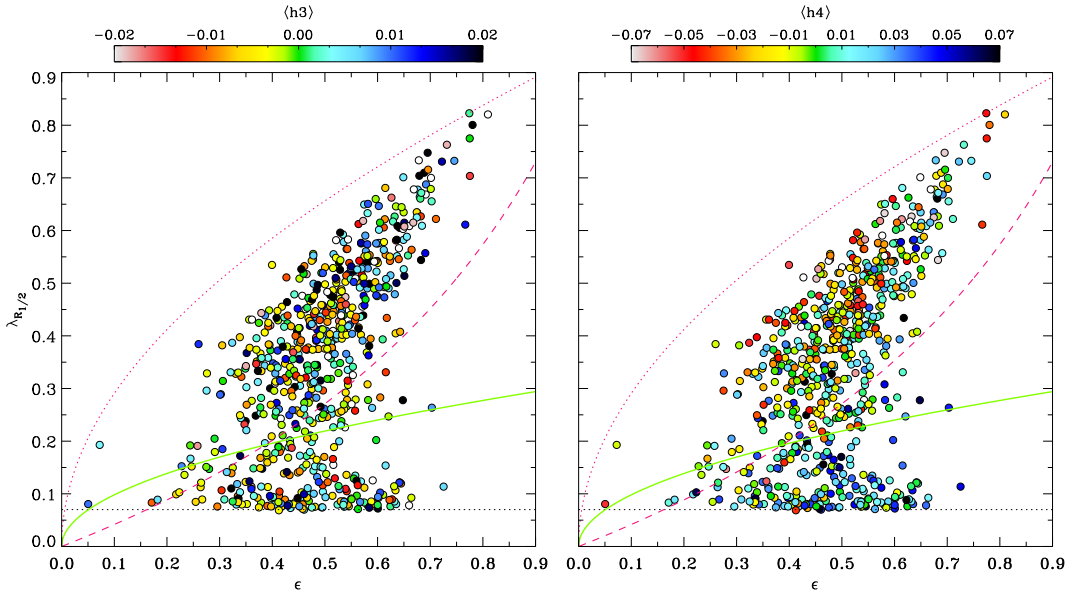

Figure 7.4: Both panels show the edge-on $\lambda_{R_{1/2}} - \epsilon$ plane for the *Magneticum* galaxies extracted from Box4. Symbols are coloured according to $\langle h_3 \rangle$ (left panel) and $\langle h_4 \rangle$ (right panel). The magenta line shows the theoretical position of edge-on viewed ellipsoidal galaxies with an anisotropy parameter $\delta = 0.7 \times \epsilon_{intr}$, while the magenta dashed line corresponds to a factor of 0.8 (for further details see Cappellari et al. (2007)). Accordingly the dotted magenta line represents the theoretical position for edge-on projected isotropic galaxies with $\delta = 0$.

Moody et al., 2014; Choi and Yi, 2017b; Schulze et al., 2018; Lagos et al., 2020), that slow rotators are the result of a single or a serious of non-dissipative accretion events that leave an imprint on the orbital structure that also seems to manifest in the averaged $\langle h_4 \rangle$ parameter.

To further investigate the origin of the trends found for $\langle h_4 \rangle$, we explore its connection to the in-situ fraction f_{insitu} in Box4, as can be seen in Fig. 7.5. The in-situ fraction f_{insitu} is a direct measurement of the integrated star formation of the galaxy with respect to the amount of stars that are accreted from the environment, e.g. through merger (for more details see Remus and Forbes, 2021). To be consistent only stellar particles within $1\mathrm{R}_{1/2}$ are considered in the calculation of f_{insitu}.

For the complete sample we find a substantial difference in the f_{insitu} distributions for $\langle h_4 \rangle < 0$ and $\langle h_4 \rangle > 0$: Galaxies exhibiting a flat-top LOSVD ($\langle h_4 \rangle < 0$) have $f_{\mathrm{insitu}} > 50\%$, with the peak of the distribution at $f_{\mathrm{insitu}} > 90\%$. Furthermore, with decreasing $\langle h_4 \rangle > 0$ the lower bound of the distribution shifts to larger in-situ fractions. Hence, the probability to find a galaxy with large in-situ fraction rises with decreasing $\langle h_4 \rangle$. In contrast, galaxies having peaked LOSVD ($\langle h_4 \rangle > 0$) show a wider and more uniform distribution covering the range between $15\% - 95\%$ in-situ fraction. Only two outliers have smaller f_{insitu}. Therefore, the centre of the distribution resides at a significantly lower in-situ fraction. Furthermore, the upper envelope of the distribution shifts to smaller f_{insitu} with increasing $\langle h_4 \rangle$, corresponding to an increase in the probability to measure a galaxy with low in-situ fraction. Hence, we conclude that $\langle h_4 \rangle$ is a surprisingly good estimator of the in-situ fraction especially for negative $\langle h_4 \rangle$. The process triggering and providing the fuel for in-situ star formation and its influence on the higher-order moments is studied in Sec. 7.4.2 in more detail.

Focusing on the kinematic groups reveals that the correlation described above is present

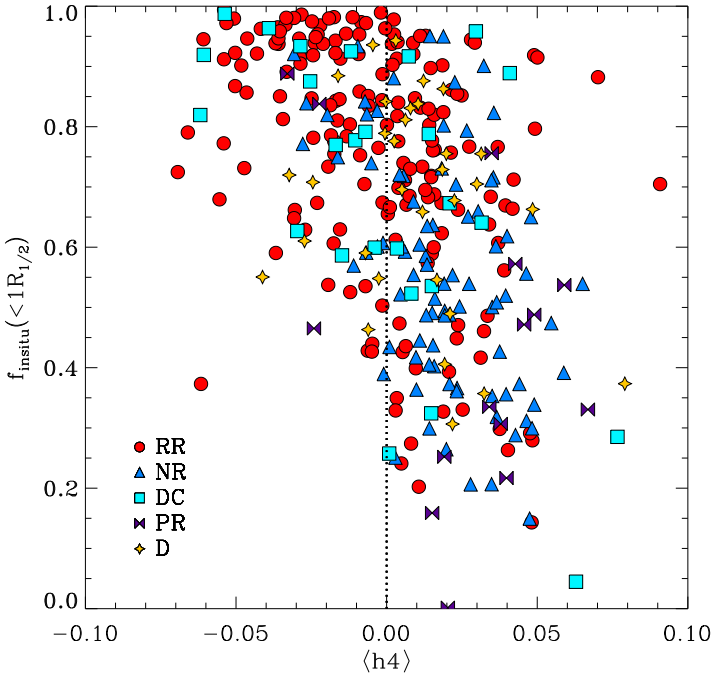

Figure 7.5: $\langle h_4 \rangle$ vs. in-situ fraction f_{insitu} within $1\mathrm{R}_{1/2}$ for the Box4 sample split up into the five kinematic groups as given in the legend. The dotted line marks $\langle h_4 \rangle = 0$.

for every group, however with varying strength. The RRs reach the highest in-situ fractions and show the strongest correlation. This is consistent with the picture, that their strong rotational support originates from in-situ star formation fuelled by either wet merging or smooth gas accretion (Naab et al., 2014; Röttgers et al., 2014; Penoyre et al., 2017). NRs typically exhibit positive $\langle h_4 \rangle$ and lower f_{insitu}, also in agreement with the general picture of slow/non rotator formation.

7.4 Connecting Velocity Moments for Different Types of Galaxies

In order to quantify the connection between the four velocity moments $\overline{V}$, σ, h_3, and h_4 for different types of galaxies, we investigate the (V/σ)-h_3 and (V/σ)-h_4 planes. Therefore, we analyse the distributions of the individual Voronoi-Bins of single galaxies as well as the stacked distribution for different galaxy classes in these planes. This approach has been applied in former studies and has proven to be a useful diagnostics to classify galaxies and to constrain the formation history in a cosmological context (Hoffman et al., 2009; Naab et al., 2014; van de Sande et al., 2017a).

In Fig. 7.6, we present the stacked distributions within $1\mathrm{R}_{1/2}$ for the five kinematic groups. The colour represents the distance of the Voronoi-Bin to the centre of the galaxy as given in the colourbar. The kinematic groups show distinctly different distributions in the (V/σ)–h_3 and (V/σ)-h_4 planes, reflecting the different kinematic states of the member galaxies.

The RRs cover a large range of h_3 and (V/σ) values as expected from their rotation dominated velocity pattern. A weak trend of anticorrelation is visible, generated by the high

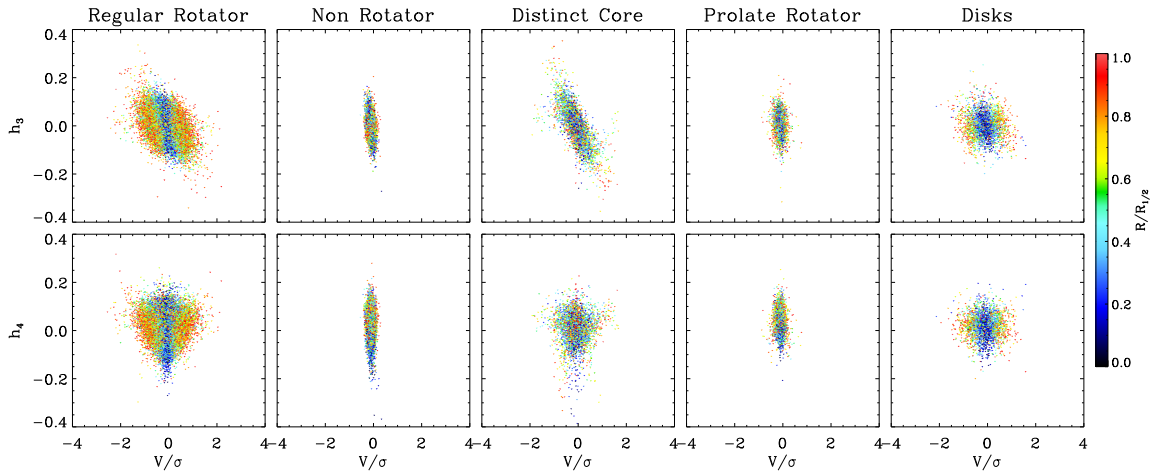

Figure 7.6: Higher-order moments $h3$ (top row) and $h4$ (bottom row) versus (V/σ) for the *Magneticum* galaxies stacked for different kinematic groups as indicated by the column title. In the individual panels, each data point represents a single Voronoi-bin in a galaxy from the respective group. The colour is chosen according to the distance of the Voronoi-bin to the center of the galaxy in units of $R_{1/2}$. We only include Voronoi-bins within an aperture of $1R_{1/2}$.

(V/σ) wings that reach larger absolute h_3 values. Interestingly, a similar range of h_3 values is covered for all radii, while the high (V/σ) range is solely reached outside of $\sim 0.5R_{1/2}$. Central bins typically have $(V/\sigma) < 0.5$, hence have stronger random motion than bins at larger radii. The central bins seem to form a vertical anticorrelation. Note, however, that this region is prone to artificial resolution effects due to the gravitational softening of the simulation.

The distribution in the (V/σ)-h_4 plane forms a characteristic symmetric heart shape. The lowest h_4 bins originate from bins close to the centre, while bins at larger radii generally have larger h_4 values. The general shape along with the radial trends are in good quantitative agreement with the observational results from van de Sande et al. (2017a) and Krajnović et al. (2008, 2011).

The second column displays the relations for the group of NR. While the range covered by h_3 and h_4 is similar to the RRs, smaller (V/σ) are covered, as expected for NRs. We do not find any significant radial trends except for the lowest h_4 originating from central bins similar to the RRs. A weak tilt towards an anticorrelation in the (V/σ)-h_3 plane is visible. Again, the distributions for the NRs is in quantitatively good agreement with observational results by van de Sande et al. (2017a) and Krajnović et al. (2008, 2011).

A particularly interesting kinematic groups are the DCs since they comprise two kinematic structures, i.e. a rotating component in the very centre and no or misaligned rotation in the outskirts. The stacked (V/σ)-h_3 distribution occupies similar (V/σ) and h_3 ranges than the RRs, however with a much more prominent anticorrelation. This anticorrelation seems to be present at all radii, which might be a results of the stacked plotting, given this group includes different kinds of DCs. The presence and interpretation of double slopes and radial variations in general will be discussed in Sec. 7.5. The (V/σ)-h_4 distribution resembles the heart shape found for the RRs, however, the radial trend of high (V/σ) bins at larger radii is much weaker.

The fourth column displays the relations for the group of PRs, which has been studied more intensively in the past few years and are believed to be a frequent dynamic configuration

for high mass galaxies (Tsatsi et al., 2017; Ebrová and Łokas, 2017; Krajnović et al., 2018). Although the velocity maps of the PRs exhibit a regular rotation pattern, the shapes of the distributions for both h_3 and h_4 closely resemble that of the NR. This can be interpreted as a sign that the rotation in PRs originates from a different process than in the RRs and the DCs. Furthermore, we do not find any sign of an S-shaped distribution in the (V/σ)-h_3 plane as found by Tsatsi et al. (2017), who proposed a binary polar merger as origin of the prolate rotation.

For the group of Disks we find a rather surprising distribution since one would expect a clear sign of anticorrelation for this rotation dominated group in the (V/σ)-h_3 plane, but instead we find a more round shape without any flattening. On the other hand, the distribution in the (V/σ)-h_4 plane shows a similar behaviour and radial trend as the RRs. However, the highest (V/σ) values originate from bins at large radii, as for the RRs.

Our investigation in this section shows that the *Magneticum* simulation is in qualitatively good agreement with observations regarding higher-order velocity moments. Furthermore, different types of galaxies cover a similar range in h_3 and h_4, but show different correlations with (V/σ) and different radial trends that might be imprints of the respective formation history.

7.4.1 Quantifying the (V/σ)-h_3 and (V/σ)-h_4 Distributions and their Correlation to Global Galaxy Properties

In the previous section we identified distinct differences and similarities between kinematic groups in the stacked (V/σ)-h_3 and (V/σ)-h_4 distributions. To expand the analysis, we now study the (V/σ)-h_3 distribution for individual galaxies in more detail and connect it to global galaxy properties to identify statistical trends.

To quantify the shape of the distribution we perform a linear regression to the (V/σ)-h_3 relation which yields the slope $\Delta h_3/\Delta(V/\sigma)$ and the Pearson correlation coefficient for every individual galaxy. The Pearson correlation coefficient measures the strength of a linear correlation and takes values between -1 and 1, where -1 indicates an anticorrelation, 0 no correlation, and 1 a correlation.

Fig. 7.7 shows the correlation between $\Delta h_3/\Delta(V/\sigma)$ and M_* for our sample. To extend our sample to higher masses we include galaxies extracted from Box2 hr highlighted in with grey shading. The upper panel shows the distribution for the *Magneticum* galaxies marked according to their kinematic group. The lower panel presents observations from the MASSIVE survey (Veale et al., 2017b), SAMI survey (van de Sande et al., 2017a), and SLUGGS survey (Bellstedt et al., 2017), in direct comparison to the simulation indicated by the blue number density.

In the mass regime above $10^{11} M_\odot$, the slopes of the simulated sample are consistent with the observations from the SAMI and SLUGGS survey. The SAMI and SLUGGS samples only show minor variation of the slope within this mass regime. However, the simulation produces significantly more galaxies with positive slopes than are observed at the low-mass end for $M_* < 11.0$. Since positive slopes are interpreted as a sign for bar-like orbits that occur in late-type galaxies, differences in the morphological sample selection could be an explanation for this tension, as SLUGGS only includes ETGs. However, the SAMI sample specifically includes barred late-type galaxies. Another potential explanation are inclination effects, since the SAMI galaxies are usually not observed in the edge-on projection. Although investigating this in more detail is beyond the scope of this study it would be interesting to

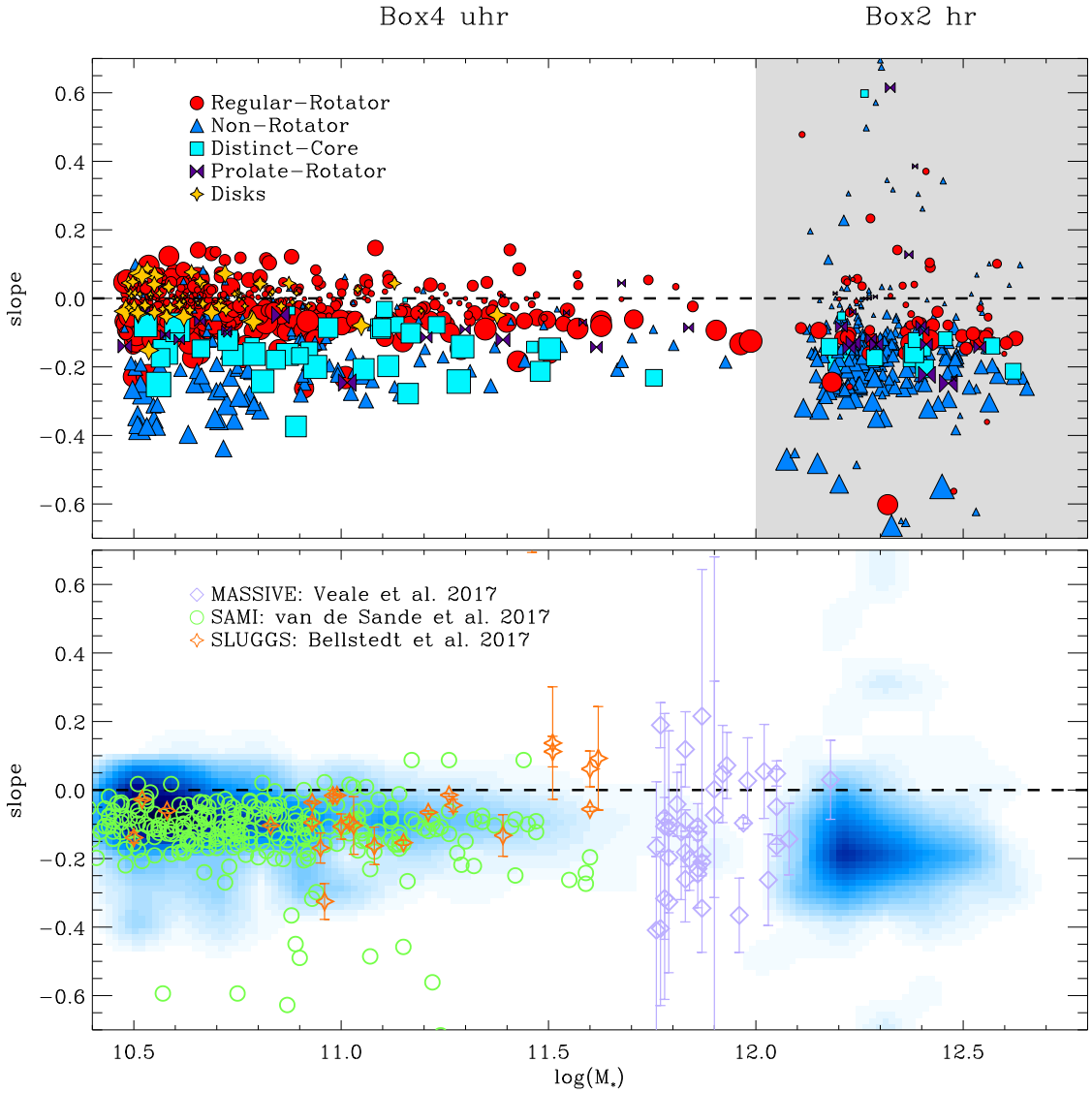

Figure 7.7: *Upper Panel:* Stellar mass vs. $\Delta h_3/\Delta(V/\sigma)$ for individual galaxies from the *Magneticum* simulation Box4 uhr and Box2 hr spilt up into the five kinematic groups. The symbols size is according to the absolute value of the correlation coefficient. *Lower Panel:* Stellar mass vs. $\Delta h_3/\Delta(V/\sigma)$ for different observational data sets. Lilac symbols mark observations by he MASSIVE survey (Veale et al., 2017b), while green circles and orange stars show data from the SAMI (Bellstedt et al., 2017) and SLUGGS survey (van de Sande et al., 2017a), respectively. For comparison the shading shows the number density of the combined *Magneticum* sample.

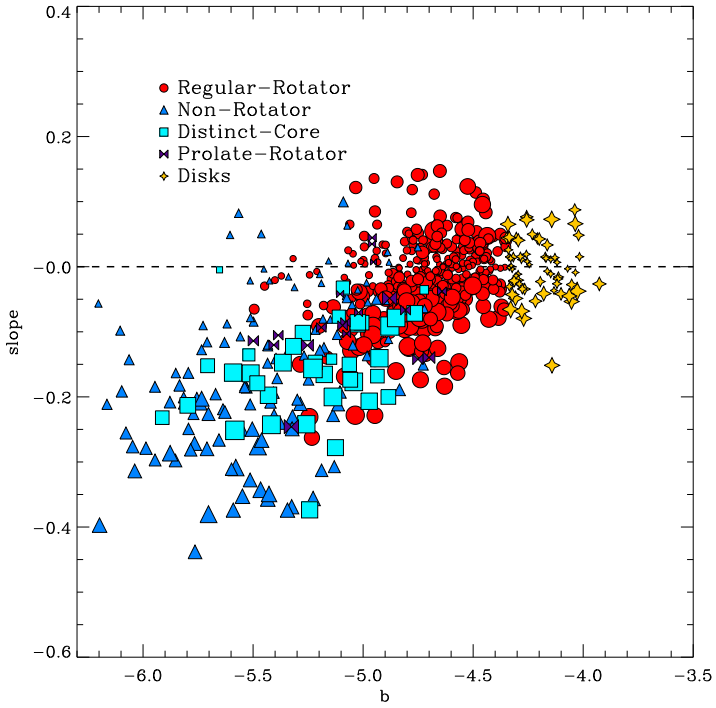

Figure 7.8: Correlation between the b-value and $\Delta h_3/\Delta(V/\sigma)$ for the Box4 sample. Symbols and colours are according to the five kinematic groups. The symbol-size indicates the correlation coefficient.

explore if this discrepancy is intrinsic to simulations in general.

In the intermediate regime $M_* = 10^{11.5}$-$10^{12.1} M_\odot$, where the observations from the MASSIVE survey are located, we are not able perform a meaningful comparison due to the low number of simulated galaxies in this mass range. However, including the Box2 sample, we find a similar trend than the observations: Towards higher masses the scatter for the slopes increases. Furthermore, with increasing mass the frequency of galaxies with $\Delta h_3/\Delta(V/\sigma) > -0.1$ decreases. In the simulated sample this trend is generated by the declining number of objects with regular rotation patterns, i.e. RRs, DCs and Disks, which occupy this range at lower masses. Moreover, the frequency of NRs increases with mass, but NRs show no change in slope with mass. Therefore, the trend in the slopes with increasing mass is mainly driven by the change in the group frequencies rather than a physical kinematic evolution within the kinematic groups.

We find, however, a clear correlation between slope and morphology, as can be seen in Fig. 7.8. Here morphology is represented by the b-value (Eq. 7.1) as discussed above.

For larger b-value, the slope of the $(V/\sigma) - h_3$ anticorrelation gets continuously shallower. Therefore, galaxies with more speroidal-like b-values tend to exhibit a steeper slope than those having a more disk-like b-value. Interestingly, also the peculiar galaxies with $\Delta h_3/\Delta(V/\sigma) > 0$ cover the correct b-value range to preserve the correlation. For b-values larger than ~ -4.6, i.e. disk-like regime, the correlation flattens and becomes fairly symmetric around 0. Except for the Disks, which lie in the flattened part of the relation, all kinematic groups independently follow this trend, even the special class of PRs. Furthermore, the kinematic groups occupy different ranges along the correlation, transitioning fairly smoothly from NR to DC to RR to Disks, however with some overlap. PRs cover a similar region than the DCs in this plane.

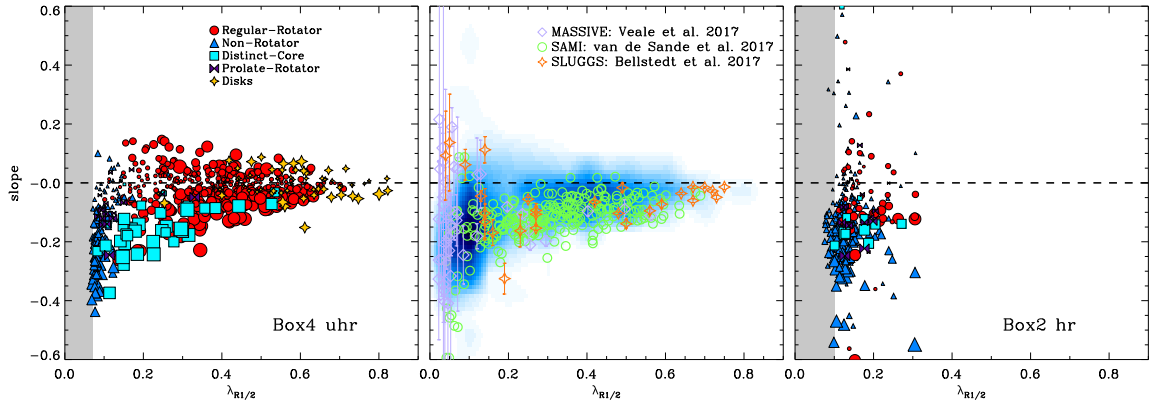

Figure 7.9: $\Delta h_3/\Delta(V/\sigma)$ against $\lambda_{R_{1/2}}$. The *left panel* utilises galaxies extracted from Box4 uhr, while the *right panel* uses galaxies from Box2 hr split up into kinematic groups as given in the legend. In both panel the symbol size corresponds to the absolute value of C_{corr}. The central panel displays observational data samples from the MASSIVE survey (Veale et al., 2017b), SAMI survey (van de Sande et al., 2017a), and SLUGGS survey (Bellstedt et al., 2017) as given in the legend.

Fig. 7.9 shows the correlation between $\Delta h_3/\Delta(V/\sigma)$ and $\lambda_{R_{1/2}}$ for our simulated sample. While the left panel shows the sample from Box4, the right panel comprises galaxies from Box2. The grey shaded areas mark the $\lambda_{R_{1/2}}$ range that is not accessible in the simulation due to resolution effects. The central panel directly compares the combined simulated sample from Box4 and Box2 as blue shaded area with the observational data sets.

For the Box4 sample, we find a significant trend for the slope to become shallower with increasing $\lambda_{R_{1/2}}$, in excellent agreement with observational data, although the overabundance of galaxies with positive $\Delta h_3/\Delta(V/\sigma)$ is again apparent. This overabundance is present throughout the entire fast rotating regime ($\lambda_{R_{1/2}} > 0.15$), except for the largest $\lambda_{R_{1/2}}$ values. In the slow rotator regime, the comparison is not straight forward, since $\lambda_{R_{1/2}}$ is artificially enhanced by resolution effects. However, we can state that the scatter to more negative slopes in this regime and the covered range of slopes is in good agreement with the observations.

As expected, the high-mass Box2 sample covers the low $\lambda_{R_{1/2}}$ regime, mainly containing slow rotators. Therefore, no reliable statement can be made about the trend towards larger $\lambda_{R_{1/2}}$. However, in the covered range an increase of the slope is visible comparable to the distribution in the Box4 sample. The Box2 sample contains some outliers scattering to steeper $\Delta h_3/\Delta(V/\sigma)$, still consistent with the MASSIVE data within the error bars.

Focusing on the slope distribution for the kinematic groups in Box4 and Box2, we find significant differences: The two classes with regular rotation pattern, i.e. RRs and Disks, cover a symmetric range in $\Delta h_3/\Delta(V/\sigma)$, however with a larger fraction of galaxies having negative values. In contrast, almost all NRs, DCs, and PRs have negative slopes. The steepest negative slopes are reached by the NRs which, in general, have lower correlation coefficients indicative of a less pronounced linear relation. For negative slopes, we find a rather smooth transition of kinematic groups from NR to DC to RR to Disks along the rising correlation between slope and $\lambda_{R_{1/2}}$. This highlights that the difference in the kinematic state of the kinematic groups not only manifests in $\lambda_{R_{1/2}}$ but also in the higher-order moments.

Interestingly, a non-negligible fraction of RRs exhibit positive slopes, however with smaller correlation coefficients than RRs with negative slopes. A correlation between (V/σ) and

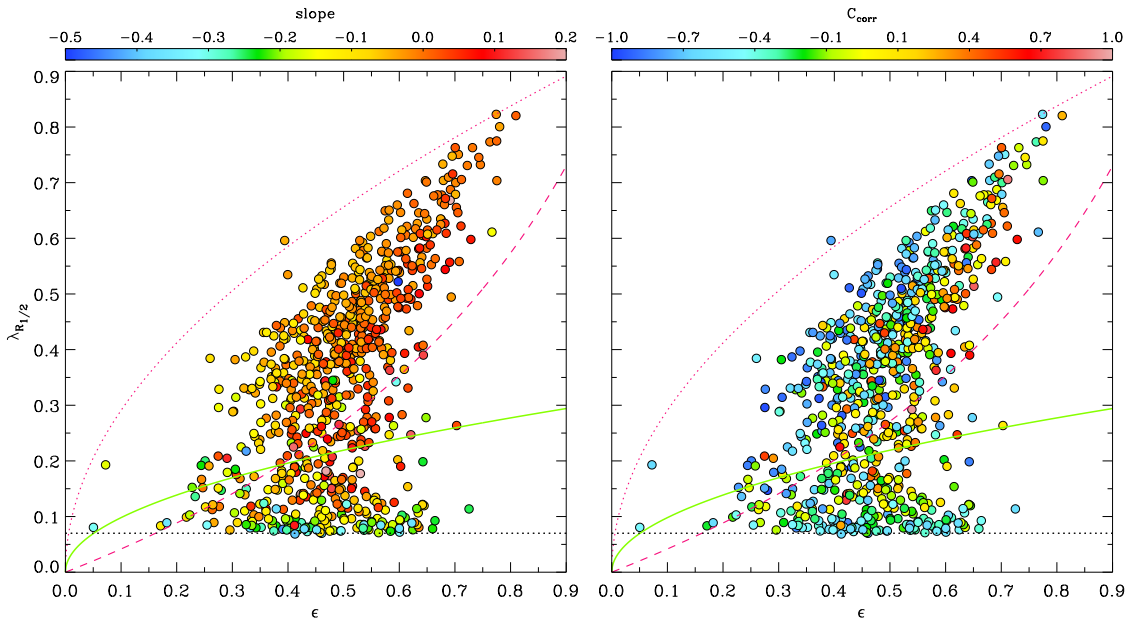

Figure 7.10: The edge-on $\lambda_{R_{1/2}} - \epsilon$ plane for the *Magneticum* galaxies extracted from Box4 uhr. *Left Panel:* Symbols are coloured according to the slope of the $(V/\sigma) - h_3$ correlation. *Right Panel:* Symbols are coloured according to C_{corr}. The magenta line shows the theoretical position of edge-on viewed ellipsoidal galaxies with an anisotropy parameter $\delta = 0.7 \times \epsilon_{intr}$, while the magenta dashed line corresponds to a factor of 0.8 (for further details see Cappellari et al., 2007). Accordingly the dotted magenta line represents the theoretical position for edge-on projected isotropic galaxies with $\delta = 0$.

h_3 is generally associated with a bar-like structure (Chung and Bureau, 2004; Bureau and Athanassoula, 2005; Li et al., 2018b). It is therefore consistent that the vast majority of galaxies with positive slope are classified as RRs or Disks. Note, however, that we do not expect to form realistic bars with regard to size and structure in the simulation due to the insufficient resolution. A general orbital distribution comparable with bars, i.e. non-circular streaming motions, might, however, potentially form.

In Fig. 7.10, the analysis is extended to the full $\lambda_{R_{1/2}}$-ϵ plane for Box4 that has been studied in great detail Chaps. 4 and 6. While the left panel shows the $\lambda_{R_{1/2}} - \epsilon$ plane for Box4 colour coded according to $\Delta h_3/\Delta(V/\sigma)$, the colour in the right panel indicates the correlation coefficient C_{corr} of the $(V/\sigma) - h_3$ relation. In addition, the symbol size in the left panel corresponds to C_{corr}.

The clear trend for the slope to increase with rising $\lambda_{R_{1/2}}$ is clearly visible. Fast rotators have an average of $\Delta h_3/\Delta(V/\sigma) = -0.016$, while slow rotators have steeper relations with an average of $\Delta h_3/\Delta(V/\sigma) = -0.12$. Focusing on the fast rotators another interesting trend is visible: For a given $\lambda_{R_{1/2}}$, the slopes mildly increase with the flattening of the galaxy. The fast/slow rotator separation line (green) approximately marks the threshold where this trend breaks down. Since $\lambda_{R_{1/2}}$ is constant along this gradient this shift corresponds to a change in the h_3 distribution. As shown in Schulze et al. (2018), this horizontal trend corresponds to a shift in anisotropy, hence we expect to find a correlation between $\Delta h_3/\Delta(V/\sigma)$ and the anisotropy for the fast rotators.

A similar behaviour is visible in the right panel of Fig. 7.10. While the difference between slow ($\overline{C}_{corr} = -0.32$) and fast rotators ($\overline{C}_{corr} = -0.24$) is not as pronounced as for

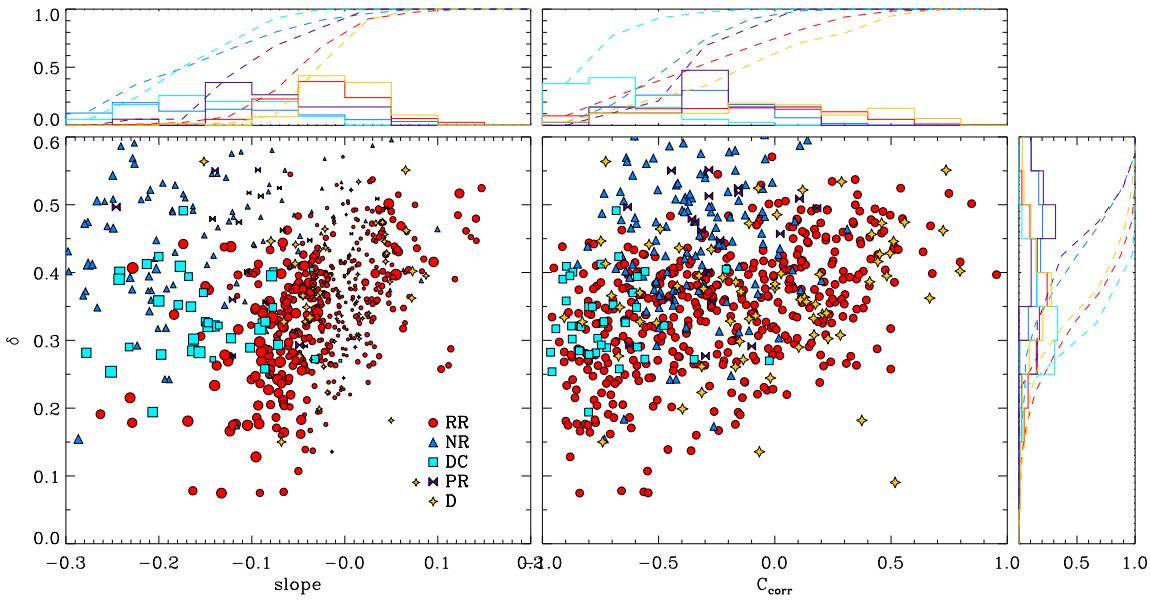

Figure 7.11: Anisotropy vs. $\Delta h_3/\Delta(V/\sigma)$ (*left panel*) and $C_{\rm corr}$ (*right panel)*) split up into kinematic groups as given in the legend. Symbol-size in the left panel is according to $C_{\rm corr}$. Lateral panels show the distributions of the shown parameters for the individual kinematic groups.

$\Delta h_3/\Delta(V/\sigma)$, the strongest correlations and anticorrelations are found in the fast rotator population. In the fast rotator regime we again find a horizontal gradient in colour corresponding to a shift from a strong anticorrelation to correlation for a given $\lambda_{\rm R_{1/2}}$ with increasing ϵ. Hence, we also expect $\overline{C}_{\rm corr}$ to correlate with the anisotropy.

Fig. 7.11 confirms the expected correlations by directly correlating the slope (left panel) and $C_{\rm corr}$ (right panel) with the anisotropy, split up into the kinematic groups. Following Cappellari et al. (2007), the anisotropy parameter is defined as

$$\delta = 1 - \frac{\Pi_{zz}}{\Pi_{xx}} = 1 - \frac{\sum_{i=1}^{N} M_i\ \sigma_{z,i}^2}{\sum_{i=1}^{N} M_i\ \sigma_{x,i}^2}, \tag{7.5}$$

where M_i, $\sigma_{z,i}$, and $\sigma_{x,i}$ are the stellar mass, velocity dispersion in z- and x-direction of the $\rm i^{th}$ cell. The sum runs over a spherical volume with radius $1{\rm R}_{1/2}$. Lateral panels show the statistical distributions for the kinematic groups.

For the RRs and Disks, a clear correlation between the slope and the anisotropy is present, although with significant scatter, while the remaining groups do not extend this correlation due to a shift to larger anisotropy values. The lateral histograms elucidate this, where the RRs and Disks show a very similar distribution discerned from the other groups. Especially RRs and Disks with positive slope have a significantly higher probability to exhibit an anisotropy larger than 0.35. Therefore, for galaxies with regular rotation pattern the slope becomes increasingly larger for orbital configurations with a more anisotropic stress-tensor. Interestingly, the DCs, which per definition host a regular rotating component, occupy a different parameter space in this plane than the RRs and Disks, closer to the NRs. This emphasises the special orbital structure of the DCs, consisting of a superposition of multiple kinematic structures causing larger anisotropy.

Table 7.2: The statistical distribution of various C_{corr} bins at different redshifts given in percentages of the total sample.

z	[-1,-0.8]	[-0.8,-0.6]	[-0.6,-0.4]	[-0.4,-0.2]	[-0.2,0]	[0,0.2]	[0.2,0.5]	[0.5,1]
0	8 (63)	16 (123)	16 (118)	17 (129)	15 (114)	12 (93)	12 (88)	4 (29)
0.5	3 (24)	14 (118)	20 (166)	22 (180)	16 (136)	12 (101)	11 (94)	1 (9)
1	3 (20)	11 (90)	20 (154)	23 (185)	18 (144)	14 (116)	8 (62)	2 (17)
2	4 (22)	10 (52)	18 (98)	19 (103)	20 (106)	16 (84)	10 (54)	2 (13)

Similar to the slope, C_{corr} also shows the trend to increase with rising anisotropy for the RRs and the Disks, however, with a substantial scatter. The DCs show a stronger overlap with the RRs in this plane, indicating that the slope is the parameters which distinguishes the RRs and DCs in this anisotropy range. NRs and PRs are offset from this increasing relation towards larger δ not showing any correlation between δ and C_{corr}.

7.4.2 Connecting (V/σ)-h_3 Plane to the Evolution of Galaxies

Naab et al. (2014) showed, for a sample of zoom-in simulations without AGN, that in a cosmological context the existence of a (V/σ)-h_3 correlation is a result of a dissipational accretion history .Furthermore, Hoffman et al. (2009) investigated the imprint of dissipation on the shapes of the LOSVD of merger remnants from isolated merger simulations, showing that the gas-fraction of a merger has a strong influence on the non-Gaussian shape of the LOSVD, with higher gas-fractions generally resulting in a stronger anticorrelation between (V/σ) and h_3. Here, we extend this analysis to a fully cosmological hydrodynamic simulation without selection bias and for a statistically representative galaxy sample.

To investigate the connection between the formation history and the higher-order moments reported in previous studies, we exploit the full power of the simulation showing the $\lambda_{R_{1/2}}$-ϵ plane at $z = 0.5$, $z = 1$ and $z = 2$ in Fig. 7.12. In the upper row, colour corresponds to the slope $\Delta h_3/\Delta(V/\sigma)$, while in the lower row it indicates C_{corr}. At $z = 2$, the slow rotator population has not developed yet and the barycentre of the fast rotators is shifted to higher $\lambda_{R_{1/2}}$ and ϵ values.

The correlation between $\lambda_{R_{1/2}}$ and $\Delta h_3/\Delta(V/\sigma)$ is present at all considered redshift (albeit at $z = 2$ the number of slow rotators is small, not allowing for a statistically meaningful statement in this regime). Therefore, this correlation is most probably caused by internal processes, since at $z > 1$ the predominant processes within galaxies are in-situ (Oser et al., 2010). In the fast rotator regime the horizontal gradient is not as pronounced at higher redhifts then at $z = 0$ and seems to develop gradually over time suggesting that this is driven by internal mixing and relaxation processes. The only observable evolution is the emergence of the steepest anticorrelations with the build up of the slow rotator population. Hence, this is a hint that slow rotation and the steepest anticorrelations originate from the same physical processes in the evolution.

A similar evolution is present for C_{corr} in the lower row. The horizontal gradient for the fast rotators becomes clearer with decreasing redshift. Interestingly, we find galaxies with strong anticorrelation and correlation already at $z = 2$. Tab. 7.2 summarises the evolution of C_{corr} by defining eight C_{corr} bins and showing the frequency of each bin at four different redshifts. The bins are chosen such that each bin contains a relatively reliable number of galaxies. While each bin is populated at every redshift, we do not find a strong evolution in

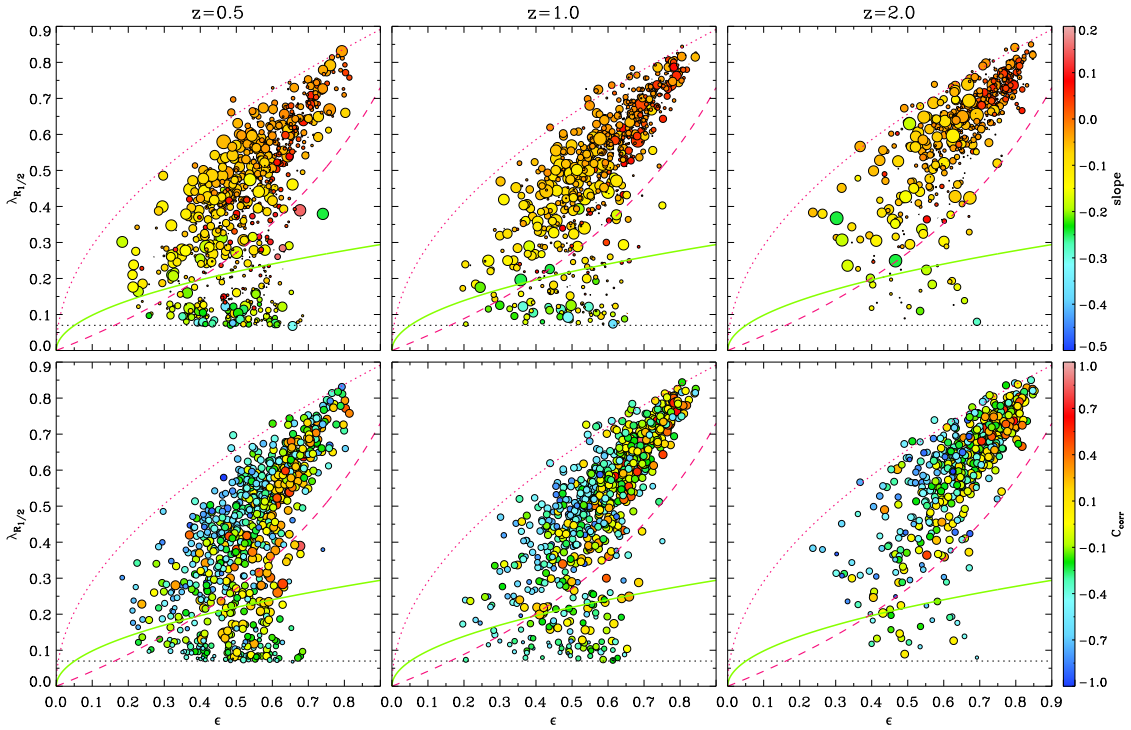

Figure 7.12: Evolution of the the edge-on $\lambda_{R_{1/2}} - \epsilon$ plane for the *Magneticum* galaxies extracted from Box4 uhr at four different redshifts . *Upper Row:* Symbols are coloured according to the slope of the $(V/\sigma) - h_3$ correlation, while the symbol size corresponds to the correlation coefficient. *Lower Row:* Colour is corresponds to $C_{\rm corr}$. The magenta line shows the theoretical position of edge-on viewed ellipsoidal galaxies with an anisotropy parameter $\delta = 0.7 \times \epsilon_{intr}$, while the magenta dashed line corresponds to a factor of 0.8 (for further details see Cappellari et al. (2007)). Accordingly the dotted magenta line represents the theoretical position for edge-on projected isotropic galaxies with $\delta = 0$.

any of the bins. Solely the most extreme bins $[-1, -0.8]$ and $[0, 5.1.0]$ show a noticeable jump from $z = 0.5$ to $z = 0$.

In Fig. 7.13 and Fig. 7.14 we study the influence of the merging history on the slope and correlation coefficient of the $(V/\sigma) - h_3$ relation within our Box4 sample. In both plots the upper panel shows the average stellar mass accreted through major, minor, mini, and all mergers since $z = 2$, where ΔM_* is normalised by the $z = 0$ stellar mass M_*. Similar to the upper panel, the lower panel shows the amount of gas accreted via the different types of merger since $z = 2$. This is a direct measure of the available fuel for potential star formation and the formation of new kinematic cold components.

While we do find significant differences between the slope bins for the total stellar mass accreted, there is no continuous trend with slope visible in the upper panel of Fig. 7.13. Although we find that a steeper anticorrelation typically correspond to more total stellar accretion, the trend is broken by the galaxies in the bin with the steepest anticorrelation (red) which have an intermediate value of 42%. With 55%, galaxies in the $[-0.3, -0.2]$ bin (orange) have the most dry accretion, while the two bins around 0 have the least dry accretion with 33% and 35%. Since the different bins behave very similar for the minor and mini mergers the variation in the total accretion is predominately driven by major mergers. Here, the most significant difference is between galaxies in the $[-0.3, -0.2]$ bin, gaining 35% of its stellar

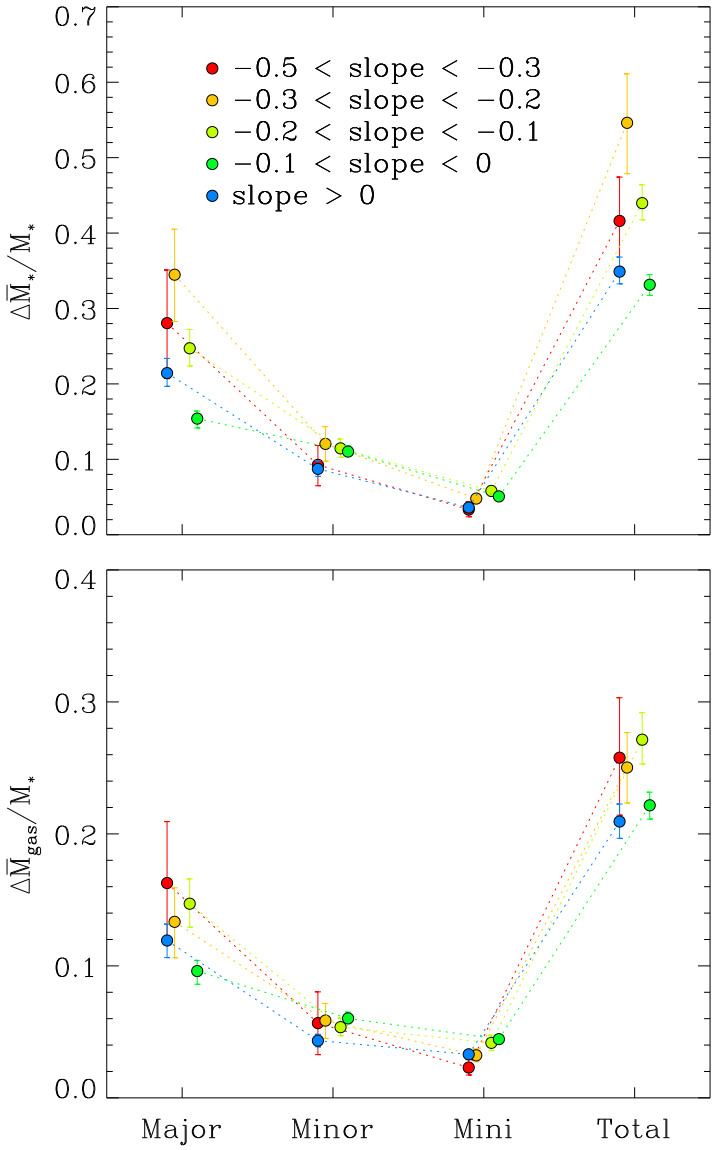

Figure 7.13: Both panels shows an averaged quantity related to the accretion history of the Magneticum galaxies. Different colours separate five slope bins defined at $z = 0$. We distinguish between contributions by major, minor, mini and all mergers from left to right. The error associated with each point is derived from 500 bootstraps and error bars correspond to the 1σ confidence interval. Top panel: Average stellar mass accreted since $z = 2$ normalised by the stellar mass at $z = 0$. Lower Panel: Average gaseous mass accreted since $z = 2$ normalised by the stellar mass at $z = 0$.

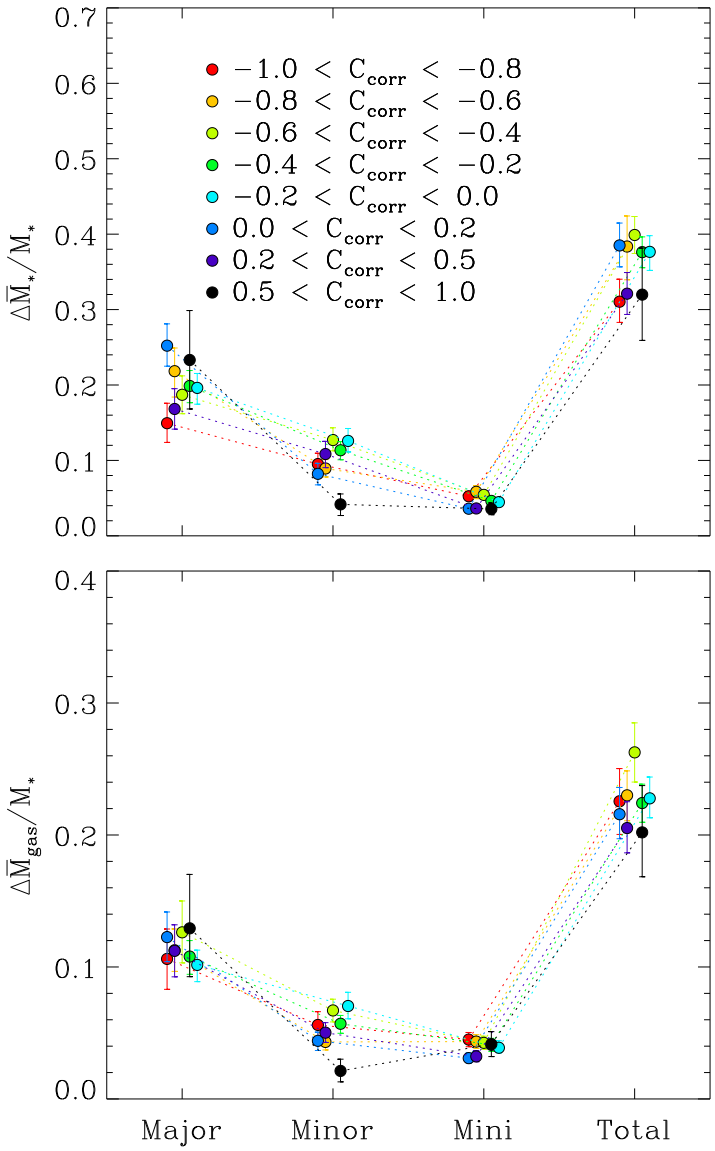

Figure 7.14: Same as Fig. 7.13 for eight correlation coefficient bins defined at $z = 0$.

mass via major merger, and the galaxies in the $[-0.1, 0]$ bin with 15%. For the total gas mass accreted since $z = 2$ the difference between the slope bins is smaller than for the stellar mass. However, the bins with the steeper anticorrelation (red, orange, bright green) tend to accrete more gas then the two bin around 0 (green, blue). This is again driven by the major mergers, which show the same trend than the total accretion. From this analysis we can therefore state that major merger play an important role in determining the $z = 0$ slope of the $(V/\sigma) - h_3$ correlation, with steeper anticorrelations typically resulting from more accretion of stellar and gaseous mass through major mergers.

Overall, we do not find substantial differences between the various correlation coefficient bins in Fig. 7.14. The average total amount of accreted stars since $z = 2$ range between 30%-40% of the present day stellar mass for all bins. For the mini mergers, the bins are even more consistent around 5%. A similar distribution is visible for minor merger, however with a clear outlier: All bins are between 10%-15% except for the bin with the largest correlation coefficient (black), which only accretes $\sim 3\%$ through minor mergers. Furthermore, the bin with the strongest anticorrelation (red) gains approximately a quarter less stellar mass through major mergers than the other bins. Investigating the gas mass accreted through mergers since $z = 2$ in the lower panel, the differences between the bins are even smaller. Only the bin with the strongest correlation again is an outlier, gaining less gas mass through minor mergers than the other bins. Therefore, we conclude, that the total amount of stars and gas accreted since $z = 2$ is not the determining process for the existence and strength of an anti-/correlation between (V/σ) and h_3. It is important to note, that we are not considering the timing and orbit of the individual mergers, which can have a significant impact on the properties of the merger remnant.

After investigating the influence of external accretion through mergers on the $(V/\sigma) - h_3$ correlation, we extend our analysis to internal processes. We will focus on C_{corr}, since we aim to analyse what drives the actual existence of a correlation/anticorrelation between (V/σ) and h_3. Therefore, we follow the evolution of the cold-gas fraction $f_{\rm gas} = M_{\rm coldgas}/M_*$ and the tightly connected specific star-formation rate $sSFR$ for all galaxies in the Box4 sample individually. These two parameters are influenced by various relevant processes, e.g. feedback and environment, hence providing a suitable diagnostics to trace the internal state of galaxies as has been applied to higher-order moments by Hoffman et al. (2009) and Naab et al. (2014).

Fig. 7.15 shows the temporal evolution of the median $f_{\rm coldgas}$ (upper panel) and $sSFR$ (lower panel) distributions for eight $C_{\rm corr}$ bins selected at $z = 0$ for the Box4 sample. As reference, the dotted line marks the evolution for all galaxies. We specifically only consider the contribution from particles within $1{\rm R}_{1/2}$ to be consistent with the determination of $C_{\rm corr}$.

In line with the general picture of galaxy evolution within the ΛCDM paradigm, the cold-gas fraction as well as the $sSFR$ declines strongly towards lower redshift (Madau and Dickinson, 2014; Lagos et al., 2014) for all bins. For redshifts below ~ 0.8, the median drops to 0 for all bins, indicating that the vast majority of galaxies are quenched by this redshift.

There are clear differences between the bins visible, however there is no completely continuous trend with $C_{\rm corr}$, although in the anticorrelated regime a more negative $C_{\rm corr}$ corresponds to larger $f_{\rm coldgas}$ and $sSFR$. This holds for all considered redshift. A striking feature is the large difference between the galaxies in the two symmetric bins around 0. Although both of these bins are only weakly correlated with a small tendency towards anti-/correlation, galaxies in the $[0, 0.2]$ bin have a significantly larger $f_{\rm coldgas}$ and $sSFR$ in the evolution since $z = 2$. Furthermore, while galaxies in the $[-0.2, 0]$ bin get quenched gradually, the galaxies

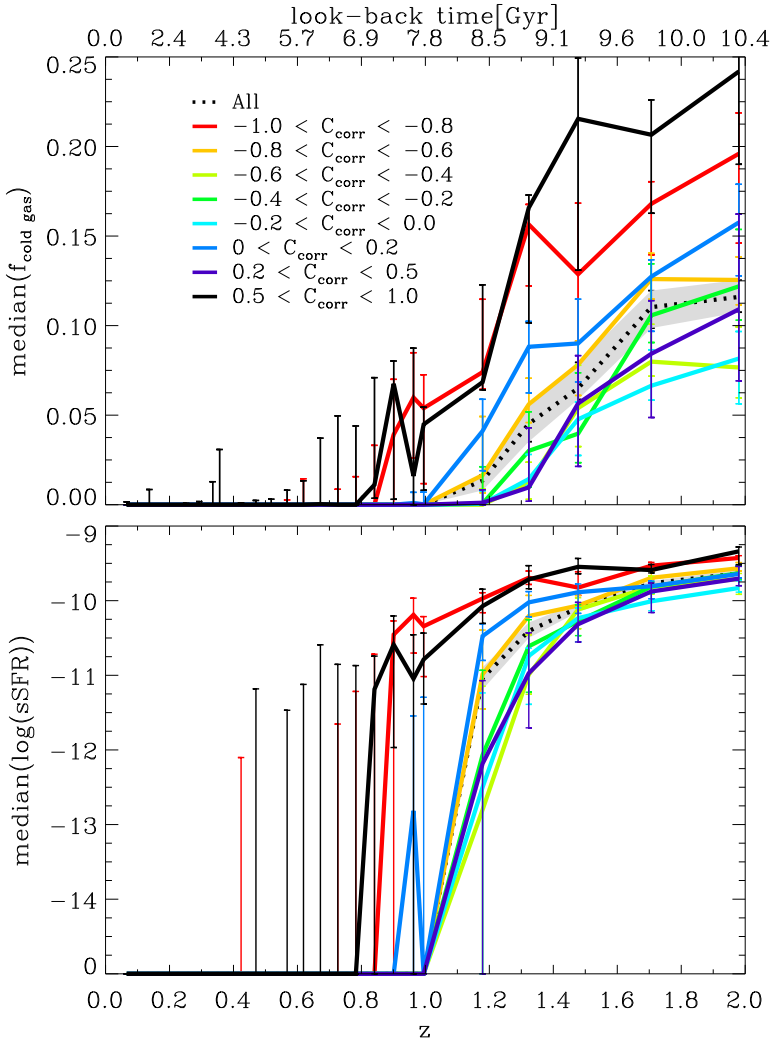

Figure 7.15: The evolution of the median cold-gas fraction $f_{\rm coldgas}$ *(upper panel)* and the median specific star formation rate $sSFR$ *(lower panel)* inside $1\mathrm{R}_{1/2}$ for eight $C_{\rm corr}$ bins selected at $z = 0$ for the Box4 sample. The solid line shows the median values of the distribution at each time-step for the individual bins, while the dotted line includes all galaxies. Error-bars and the grey shaded area mark the 1σ confidence interval drawn from 1000 bootstraps.

in the $[0, 0.2]$ bin have only a weakly decreasing $sSFR$ before $z \sim 1.4$ and gets quenched comparably rapid subsequently. This suggest, that the transition from negative to positive $C_{\rm corr}$ is physically connected to internal galaxy processes.

The most apparent feature in Fig. 7.15 is the evolution of the galaxies that have the strongest anticorrelation (red) and correlation (black). While they show the same overall evolution of decreasing $f_{\rm coldgas}$ and $sSFR$, they are clearly separated from the remaining galaxies. At all redshifts they exhibit a clearly enhanced $f_{\rm coldgas}$ and $sSFR$ in comparison to galaxies with weaker anti-/correlations. Furthermore, these galaxies sustain their star-formation and cold-gas for $\sim$ 1Gyr longer in comparison to others. Focusing on the bootstrap error-bars we furthermore see, that also for $z < 0.8$ galaxies of these two bins can show non-negligible $f_{\rm coldgas}$ and $sSFR$ down to $z \sim 0.4$. Considering the results from Fig. 7.14, where we found only minor differences in the total gaseous accretion via merger, this suggests that the existence of a strong anti-/correlation is regulated by the internal processing of the gas. This has been suggested in former studies of either isolated merger or zoom-in simulation for a low number of galaxies (Hoffman et al., 2009; Naab et al., 2014; Röttgers et al., 2014). Our study extends this to a statistically meaningful sample in a fully consistent cosmological context. However, from Figs. 7.15 and 7.14, we cannot conclusively exclude that mergers play a role in the development of an anti-/correlation, since we are not able to investigate the orbital parameters of the mergers and therefore the angular momentum of the incoming gas. Nevertheless, we find strong indication, that galaxies of these two bins accrete a larger fraction of gas via smooth or clumpy accretion of gas that fuels star formation in a disk leading to the observed trends in Fig. 7.15 and 7.14.

7.5 Extending the Analysis to Larger Radii

In the previous chapters we investigated the kinematic state of galaxies within $1{\rm R}_{1/2}$ in great detail, quantified by the higher-order moments, and connecting it to the formation history of galaxies. The aperture of $1{\rm R}_{1/2}$ is mainly motivated by the available observational data, which is typically constrained to $1{\rm R}_{\rm e}$ due to available apertures. However, in the course of the past decade, several observational and theoretical studies have shown that valuable information about the formation of galaxies is encoded beyond this characteristic radius, especially with regard to the merging history (Coccato et al., 2009; Arnold et al., 2014; Foster et al., 2016; Spavone et al., 2017; Bellstedt et al., 2017; Forbes and Remus, 2018; Pulsoni et al., 2018; Foster et al., 2018; Falcón-Barroso et al., 2019b; Schulze et al., 2020; Pulsoni et al., 2020). However, higher-order moments have not been studied in this context yet. Therefore, we will extend our analysis of higher-order moments to larger radii in the following section.

7.5.1 The (V/σ)-h_3 Plane out to $5{\rm R}_{1/2}$

We extend the radial range of voronoi-bins included in the (V/σ)-h_3 and (V/σ)-h_4 plane to $5{\rm R}_{1/2}$ in Fig. 7.16 that shows the stacked distribution for the kinematic groups equivalent to Fig. 7.6 but for the extended aperture. The solid and dashed contours mark where 75% of the bins within $1{\rm R}_{1/2}$ and in the range $1{\rm R}_{1/2} < R < 5{\rm R}_{1/2}$ are.

The stacked RRs show a similar distribution in the centre and at larger radii in the h_3-(V/σ) plane, and a slightly anticorrelated broad total distribution. The central distribution is more concentrated and seems to be slightly less elongated than the outskirt distribution driven by less prominent high (V/σ) wings. For the h_4-(V/σ) plane the central bins resemble

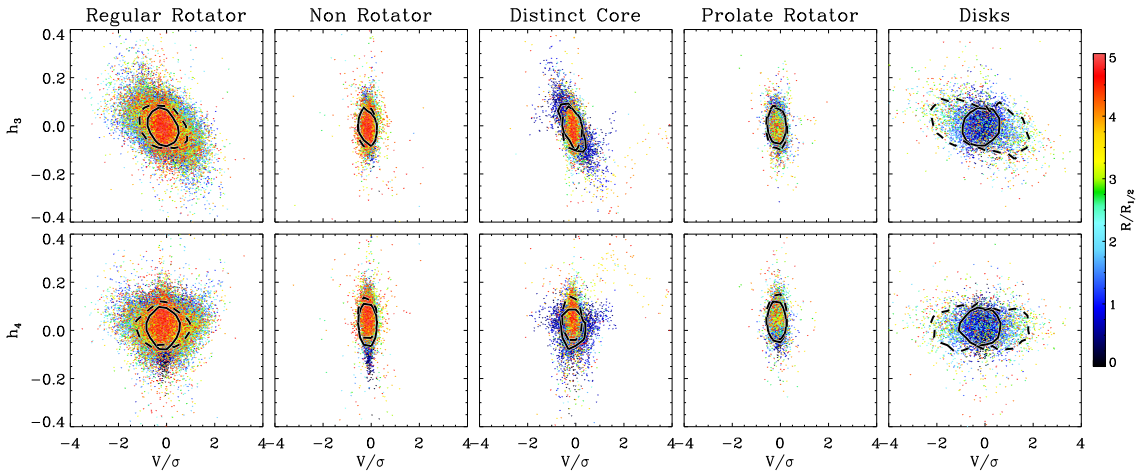

Figure 7.16: h_3 (top row) and h_4 (bottom row) versus (V/σ) for the *Magneticum* galaxies stacked for different kinematic groups as indicated by the column title. In the individual panels, each data point represents a single voronoi-bin in a galaxy from the respective group. The colour is according to the distance of the voronoi-bin to the centre of the galaxy in units of $R_{1/2}$. We extend the radial range to include all bins within an aperture of $5R_{1/2}$. The black solid contour show where 75% of the bins within an aperture of $1R_{1/2}$ are. Accordingly the black dashed contour marks where 75% of the bins in the radial range $1R_{1/2} < R < 5R_{1/2}$ are.

the characteristic heart shape found in former studies van de Sande et al. (e.g. 2017a), and the high (V/σ) bins at larger radii generate a widening of the distribution close to $h_4 = 0$. Furthermore, an interesting feature is that the low h_4 tail mainly consists of bins located in the very centre ($R < 0.5R_{1/2}$). This signature is present for all types except for the Disks, in varying strength. We suspect that this is caused by a central bulge component dominated by random motion, i.e. low (V/σ) values.

Consistently, the stacked h_3-(V/σ) plane for the NRs is vertical, independent of radius without any sign of anti/-correlation. Therefore, the lack of rotation in the stellar halo for this type of galaxies found by Schulze et al. (2020) is also apparent in the higher-order moments. Similar to the RRs, the h_4 distribution for the central parts is offset to lower values in comparison to larger radii.

A clear radial change in the h_3-(V/σ) plane is visible for the stacked DC distribution. The central bins form a distinct anticorrelation, while bins at larger radii have a vertical distribution, covering a significantly smaller range in both parameters. The transition between the two components is relatively abrupt and is determined by the extend of the rotating core. In the h_4-(V/σ) plane, the high (V/σ) wings for the central bins show the typical heart shape for rotation supported components, but that is gone for larger radii.

The PRs exhibit a vertical distribution in both planes with no signs of anti/-correlation comparable to the NRs, however less elongated towards higher/lower h_3 and h_4. Furthermore, there is no evidence for radial variations of h_3, and only a slight trend for larger values in h_4 at larger radii, weaker than in the other groups.

For the Disks, we find a rather unexpected behaviour. They show a distinctly different distribution in both planes than the other groups. The central bins form an uncorrelated distribution reaching only low h_3 values in comparison to the RRs and DCs. However, in comparison to the NRs higher (V/σ) values are reached leading to a spherical shape of the distribution. Going to lager radii, much larger (V/σ) are reached, generating a weak anti-

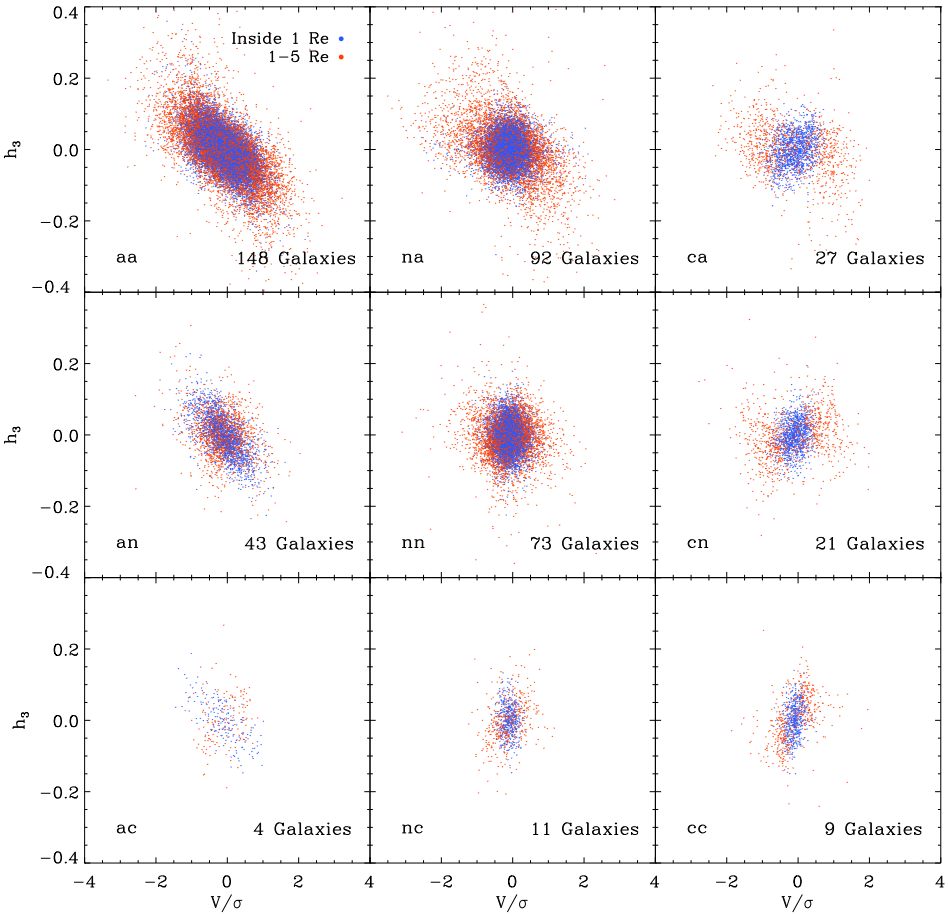

Figure 7.17: The $(V/\sigma) - h_3$ plane for newly introduced 9 subclasses, based on the correlation coefficient at small and large radii, of RRs (see Tab. 7.3). Each panel shows the stacked distribution for all the members of the respective groups. To illustrate the class definition we show bins within $1R_{1/2}$ in red and bins with $1R_{1/2} < R < 5R_{1/2}$ in blue. The columns distinguish the different kinds of correlations (anticorrelated, uncorrelated and correlated) for the central bins, while the rows distinguish the type of correlation for the bins in the outskirts, as marked by the lateral labels. The number of galaxies in each class is given in the label in lower right corner of the panel.

correlation. A very similar behaviour is present in the h_4-(V/σ) plane, however with a flat connection for the bins at larger radii. The unexpected trends found for the Disks might originate from stacking galaxies with varying slope resulting in a rather uncorrelated distribution.

7.5.2 Disentangle the Class of Regular Rotators

As described above, the scatter of the (V/σ)-h_3 plane for the RRs out to large radii is rather large (Fig. 7.16), indicating towards differences in slope and correlation coefficient for individual galaxies. In fact, we find different trends of the (V/σ)-h_3 correlation with radius inside the group of RRs, which motivates a more detailed classification within this kinematic group according to the (V/σ)-h_3 correlation at different radii. Therefore, we classify the RRs into further subgroups based on each galaxy's correlation coefficients inside $1R_{1/2}$, $C^{\rm in}_{\rm corr}$, and for

Table 7.3: The statistical distribution of the RR subclasses. Columns distinguish the connection type in the centre ($R < 1R_{1/2}$. Rows distinguish the connection type at larger radii ($1R_{1/2} < R < 5R_{1/2}$)

.

	a	n	c	Total
a	35%	21%	6%	62%
n	10%	17%	5%	32%
c	1%	3%	2%	6%
Total	46%	41%	13%	

$1R_{1/2} < R < 5R_{1/2}$, $C_{\rm corr}^{\rm out}$. We apply a threshold of -0.3 and 0.3 to these two parameters to distinguish the type of connection, i.e. anticorrelation, no correlation and correlation, hence defining 9 subclasses. This threshold is chosen based on visual inspection of various distributions, and is generally accepted as the threshold for moderate liner correlation strength. Note, the purpose of this classification is not to provide a comprehensive classification, but to identify physical differences within the group of RRs and connect those to galaxy properties and formation histories. In Fig. 7.21 the classification and distributions of the two parameters are visualised showing $C_{\rm corr}^{\rm in}$ versus $C_{\rm corr}^{\rm out}$.

Fig. 7.17 presents the stacked (V/σ)-h_3 distributions for the 9 classes. Columns separate the three types of connection in the centre, while rows distinguish the connection type at larger radii. In the following, we will label the classes using 'a' for anticorrelated, 'n' for uncorrelated, and 'c' for correlated, e.g. a galaxy with an anticorrelation in the centre and no-correlation in the outskirt is labelled 'an' and so on. The resulting class frequencies are listed in Tab. 7.3.

Summing up the individual rows in Tab. 7.3 reveals that also at larger radii every type of correlation exists. The vast majority of RR galaxies exhibit an anticorrelation or no correlation in the centre. The fraction of galaxies with a correlation at larger radii (6%) is considerably smaller than in the centre (13%). Interestingly, the frequency of galaxies with anticorrelation at larger radii (62%) is significantly larger than for the bins in the centre (46%). Although the radial range $1R_{1/2} < R < 5R_{1/2}$ comprises a fraction of the central rotating component, the accreted halo is not expected to strengthen the anticorrelation.

Considering both $C_{\rm corr}^{\rm in}$ and $C_{\rm corr}^{\rm out}$, the most common class is the double anticorrelation (aa), indicating that rotation is also present in the stellar halo. With 21%, 17%, and 10% the na, nn, and an classes also comprise a significant fraction of our sample. As expected from the rarity of correlations at both radial scales, classes involving a correlation (ac, nc, cc, cn, ca) have very low percentages. Thus, we combine all galaxies with a correlation in the centre into one class ('cx') to increase the statistical relevance and to gain more insight into their properties. Since a correlation between (V/σ) and h_3 is considered to be a sign of a triaxial component, their origin is probably a results of very specific merger configurations, environmental effects, or secular evolution, and hence difficult to determine given the temporal resolution of the stored simulation output.

In the following we explore the classification introduced above with regard to well known scaling relations, i.e. mass-size relation, dark-matter-fraction-mass relation, and $\lambda_{R_{1/2}}$-ϵ plane for the most frequent classes, i.e. aa, na, nn, an, cx.

Fig. 7.18 shows the correlation of $R_{1/2}$ (upper panel) and the dark-matter fraction $f_{\rm DM} = M_{\rm DM}(R < R_{1/2})/M_{\rm TOT}(R < R_{1/2})$ (lower panel) with stellar mass for the different classes of RRs. For the calculation of $f_{\rm DM}$, we consider all particles within a spherical volume

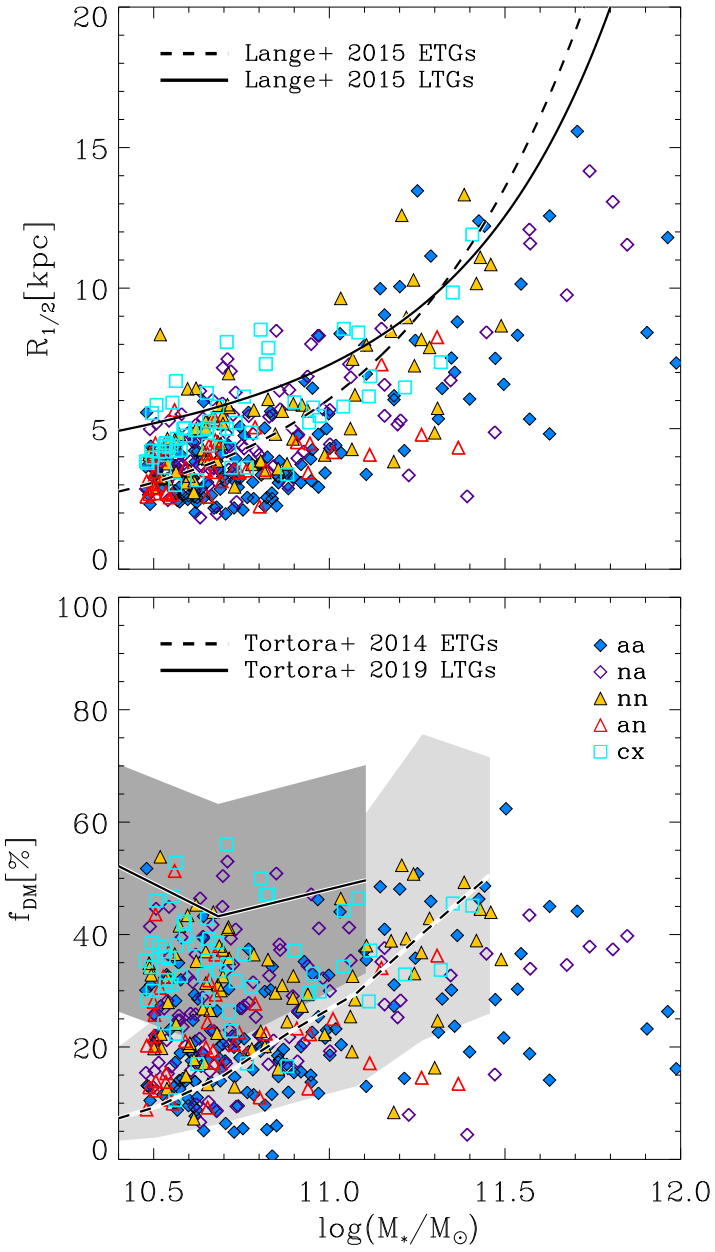

Figure 7.18: The dependence of the half-mass radius $R_{1/2}$ (upper panel) and central dark matter fraction f_{DM} (lower panel) on stellar mass split up into classification introduced in Sec. 7.5.2 and the 'cx' class as given in the legend. As reference we include observed mass-size relations for ETGs (dashed line) and LTGs (solid line) from Lange et al. (2015) in the upper panel. The lower panel includes observational results from Tortora et al. (2014) for ETGs (dashed line) and from Tortora et al. (2019) for LTGs (solid line).

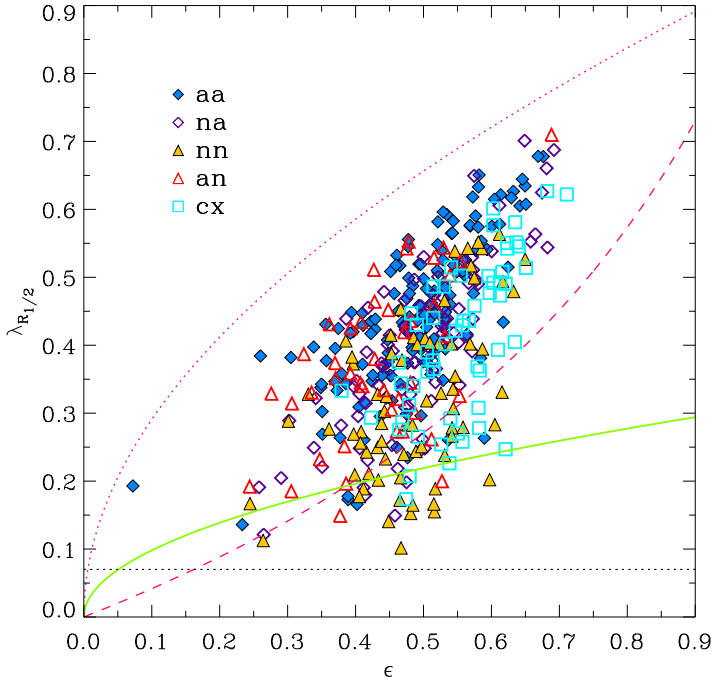

Figure 7.19: The $\lambda_{R_{1/2}}$-ϵ for the most frequent classes 'aa', 'na', 'nn', and 'an' as defined in Fig. 7.17, per definition only comprising Regular-Rotators. We also include the special 'cx' class. The curves are equivalent to Fig. 7.10.

with radius $R_{1/2}$. Overall the simulated sample follows the observed ETG relations in both panels, however, with noticeable differences between the groups. The stellar body of galaxies with an anticorrelation in the centre (aa, an) are on average more compact than the classes with no-correlation in the centre (na,nn), independent of the relation type in the halo. The independence of the halo relation type suggests that the processes determining the relation type in the centre and at larger radii act somewhat independently, i.e. accretion versus internal processes. Interestingly, for a given M_*, the cx group is offset towards larger $R_{1/2}$ from the rest of the galaxies, behaving more LTG like. Similar trends are visible in the lower panel for f_{DM}: Galaxies with anticorrelation in the centre typically have lower f_{DM} than the na and nn classes, although the scatter reaches up to the highest fractions. The most distinct signal is visible for the cx group showing the smallest scatter and on average highest f_{DM}, again clearest resembling the disks.

In Fig. 7.19 we investigate the influence of the relation type at larger radii on the central $\lambda_{R_{1/2}}$-ϵ plane by splitting our sample into the RR classes. As expected, we do not find galaxies of the same correlation type in the halo to populate distinct regions of the plane, which would indicate a strong co-evolution of the centre and the halo given that $\lambda_{R_{1/2}}$ is calculated for the centre only. However, for the aa and nn classes we find a clear difference in the distributions, with the aa typically having larger $\lambda_{R_{1/2}}$ values than the nn, driven by the central kinematics highlighting the rather distinct kinematic evolution of the galaxy centre and the stellar halo. The most apparent signal is visible for the cx galaxies, which for a given $\lambda_{R_{1/2}}$ occupy the high ϵ region with comparably small scatter, in line with Fig. 7.10 indicative of a larger anisotropy.

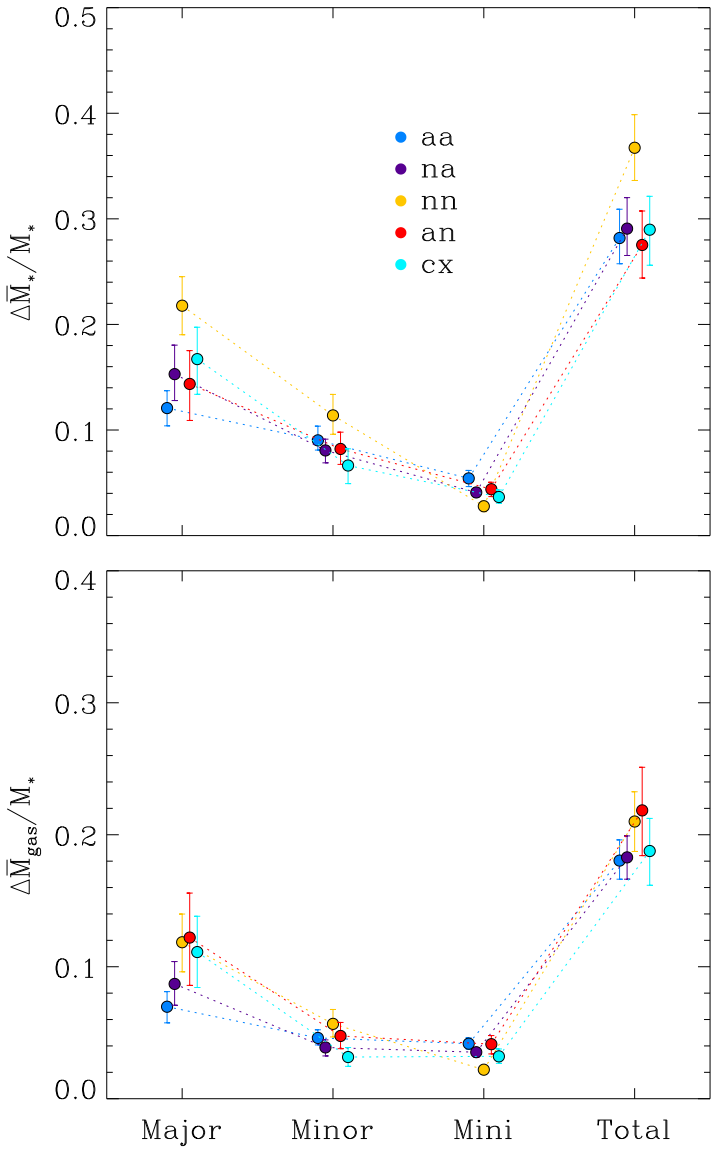

Figure 7.20: Both panels shows an averaged quantity related to the accretion history of the simulated galaxies including the 'aa', 'na', 'nn', 'an' classes. We also show the special 'cx' class, which combines 'cc', 'ca', and 'cn'. The plot is conceptionally equivalent to Fig. 7.13.

In Sec. 7.4.2 we have shown that especially wet merging plays a secondary role in determining $C^{\rm in}_{\rm corr}$, while we find a much stronger signal in the evolution of the cold-gas fraction and the specific-star formation rate. However, in the newly introduced classification the kinematics at larger radii, which are strongly influenced by merging, are taken into account. Therefore, Fig. 7.20 shows the median accreted stellar and gaseous mass in major, minor, and mini mergers as well as the total accreted mass for the new classes.

Except for the mini merger regime, the nn group is offset from the other groups towards larger $\Delta\overline{\rm M}_*/{\rm M}_*$. This trend is strongest for the major mergers where this group accretes 22% in stars and 12% in gas, hence a factor ~ 2 more stars than the aa class which has the least amount of mass accreted through major merger. Comparing the accretion history to the other class with no-correlation at larger radii, i.e. an, we see that the an class accretes significantly less stars via mergers but accretes the largest amount of gas through mergers (23%). This is predominately driven by the major mergers which contribute 12% of the present day stellar mass in gas, hence approximately a factor 2 more than the aa group.

For galaxies with anticorrelation at all radii, aa, we see a very different picture: The most frequent class accretes the least amount of stellar as well as gaseous mass in major mergers, while it behaves similar to the other classes in the minor and mini merger regime. Accordingly, in total it gains the least fraction of gas mass (17%) and the second least fraction of stellar mass (28%) since $z = 2$. Therefore, the accretion history of this class since $z = 2$ is less violent and stronger influenced by low-mass mergers than for the other classes.

For the class of na galaxies no clear trends could be found and we suspect the orbital accretion setting to be important for this class of galaxies. The special class of cx does not provide a signal that allows us to make a meaningful statement about its origin based on its accretion history. It shows a weak trend to be stronger influenced by major mergers in the stellar and gaseous accretion, since it is among the strongest accreting classes in the major merger regime and among the weakest accreting classes for minor and mini merger. Most likely this class is strongly influenced by internal secular evolution triggered by instabilities and perturbations as proposed for the formation of stellar bars.

Hence, for the most common classes taking the kinematics at larger radii into account revealed clear differences in the merger history. A compatible formation scenario for the an group would be a gas-rich major merger which transforms the galaxy to nn, however providing enough gas to build up a new dynamically cold component in the centre generating the anti-correlation. The nn galaxies were formed through dry mergers, with significant contribution from major mergers. The aa galaxies, however, are dominated by internal evolution processes and minor mergers.

7.6 Summary and Conclusion

We investigate the structure of the LOSVD for a sample of galaxies extracted from the fully cosmological hydrodynamic *Magneticum Pathfinder* simulations based on the first four line-of-sight velocity moments, i.e. $\overline{V}$, σ, h_3, and h_4. The main analysis sample is selected from Box4 uhr, since the resolution allows to extract reliable kinematic moments for galaxies down to a stellar mass of ${\rm M}_* = 3 \cdot 10^{10}{\rm M}_\odot$. Due to the small volume of this Box the sample gets increasingly incomplete towards higher masses and does not contain galaxies with ${\rm M}_* > 10^{12}{\rm M}_\odot$. Hence, a second sample of galaxies from the larger but lower resolution Box2 is selected to also probe the extreme high-mass end beyond $10^{12}{\rm M}_\odot$. The final galaxy

samples are classified based on characteristic features in the $\overline{V}$-maps into regular-rotators, non-rotators, distinct-cores, prolate rotators, and pure Disks. The sample selection procedure leaves us with statistical meaningful samples of 677 galaxies from Box4 and 397 galaxies from Box2.

In summary our major results are:

- We find an overall consistency with the observations from MASSIVE (Veale et al., 2017b) regarding the mass dependence of the average higher-order moments $\langle h_3 \rangle$ and $\langle h_4 \rangle$. While we find no clear trend with stellar mass for $\langle h_3 \rangle$, there is a strong evolution of $\langle h_4 \rangle$ to increase with stellar mass, reflecting the change in orbital structure towards higher stellar masses.

- We find a remarkable correlation between $\langle h_4 \rangle$ and f_{insitu}: Galaxies with negative $\langle h_4 \rangle$ have $f_{\mathrm{insitu}} > 50\%$ within $1\mathrm{R}_{1/2}$, with a large fraction even at $\sim 100\%$, while for $\langle h_4 \rangle > 0$ the f_{insitu} distribution is completely different, being relatively homogeneous between 20% and 100%. This clearly shows that negative $\langle h_4 \rangle$ correlates strongly with intrinsic processes being the dominating formation channel.

- Spatially resolved, we find very different stacked distributions for (V/σ) versus h_3 for the five kinematic classes. The RRs and DCs show an anticorrelation between (V/σ) and h_3, while NRs ans PRs do not. Surprisingly, the disk do not show a clear sign of anticorrelation which might originate from varying slopes of the individual galaxies.

- We quantify the linear relation between (V/σ) and h_3 by the fitted slope and the corresponding Pearson correlation coefficient C_{corr}. We find the slope to be consistent with observations over several orders of magnitude in stellar mass. The only discrepancy is the overabundance of objects with positive slope in the simulation, which is not due to morphological sample selection. Correlations are usually associated with stellar bars, which we do not resolve in the simulation, however we might have bar-like orbital configuration in the simulation albeit with too large radial extends. The slope also strongly correlates with the morphology via the b-value, independent of kinematic class. Furthermore, we find a clear trend that the slopes get flatter with increasing $\lambda_{\mathrm{R}_{1/2}}$ in substantial agreement with observations. In addition, $\mathrm{C}_{\mathrm{corr}}$ increases towards larger $\lambda_{\mathrm{R}_{1/2}}$ indicating tighter linear correlations.

- In the $\lambda_{\mathrm{R}_{1/2}}$-$\epsilon$ plane we find a horizontal change of the slope for a given $\lambda_{\mathrm{R}_{1/2}}$ in the fast rotator regime. This directly translates into a correlation between the anisotropy and the slope. A similar however weaker trend is present for C_{corr}.

- With increasing steepness of the anticorrelation the fraction of accreted stars, especially via major mergers, tend to rise. This signal is less clear for the gaseous accretion. The galaxies with positive slope have the lowest accretion fraction in stars and gas. For the tightness of the correlation we do not find a clear signal in the accretion fractions of the gaseous and stellar component. Only for the strongest correlations, the accretion is slightly dominated by major mergers.

- We investigate the internal gas evolution with regard to C_{corr} by following the evolution of the cold-gas fraction f_{coldgas} and $sSFR$ within $1\mathrm{R}_{1/2}$. We find clear evidence that the galaxies with the strongest correlations and anticorrelations have significantly higher

$f_{\rm coldgas}$ and $sSFR$ below $z = 2$ than galaxies with weaker linear relations and the total sample and get quenched later at $z \sim 0.8$. Also for $z < 0.8$ the scatter towards higher $f_{\rm coldgas}$ and $sSFR$ is larger, although the majority of galaxies is quenched. Overall, we find large differences in the star formation history for galaxies with different $C_{\rm corr}$, however there is no clear overall continuous trend.

- Extending our analysis to $5{\rm R}_{1/2}$ a rather complex picture emerges in the (V/σ)-h_3 and (V/σ)-h_4 planes, especially for regular rotating galaxies. We calculate the correlation coefficient in the centre and at larger radii to identify different classes of regular rotating galaxies. We define the classes aa=double anticorrelation, na=no-correlation/anticorrelation, nn=double no-correlation, an=anticorrelation/no-correla–tion, cx=everything with correlation in centre. Galaxies with a correlation in the centre tend to be more compact and have larger dark-matter fraction for a given M_* than the other galaxies. However, we do not find substantial differences driven by the correlation type at larger radii for the mass-size, mass-$f_{\rm DM}$ or the $\lambda_{\rm R_{1/2}}$-ϵ plane. In those global parameters, the main driver is the inner slope.

- The accretion history for the these classes are, however, very different. We find that the nn class is dominated by dry accretion via major mergers. The an group on the other hand shows enhanced wet accretion via major merger, suggesting the build up of a new cold component from the gas. The aa class has low accretion fractions in comparison to the other classes, dominated by a rather quite evolution without significant disturbance. Therefore, we conclude that the radial behaviour of the correlation between (V/σ) and h_3 is a good tracer for the different pathways that lead to the formation of regular rotating galaxies.

In conclusion, we find that the formation history of galaxies in a fully cosmological environment leaves clear imprints on the higher-order moments of the LOSVD and their connection to other galaxy properties. Especially the $\langle h_4 \rangle$ parameter and the strength of the (V/σ)-h_3 correlation are strongly connected to the star-formation history of galaxies and therefore are particularly interesting parameters to study in more detail in future theoretical and observational studies. Furthermore, combining the central higher-order moments with higher-order moments beyond $1{\rm R}_{1/2}$ is an excellent method to further disentangle the diverse formation histories of centrally regular rotating galaxies.

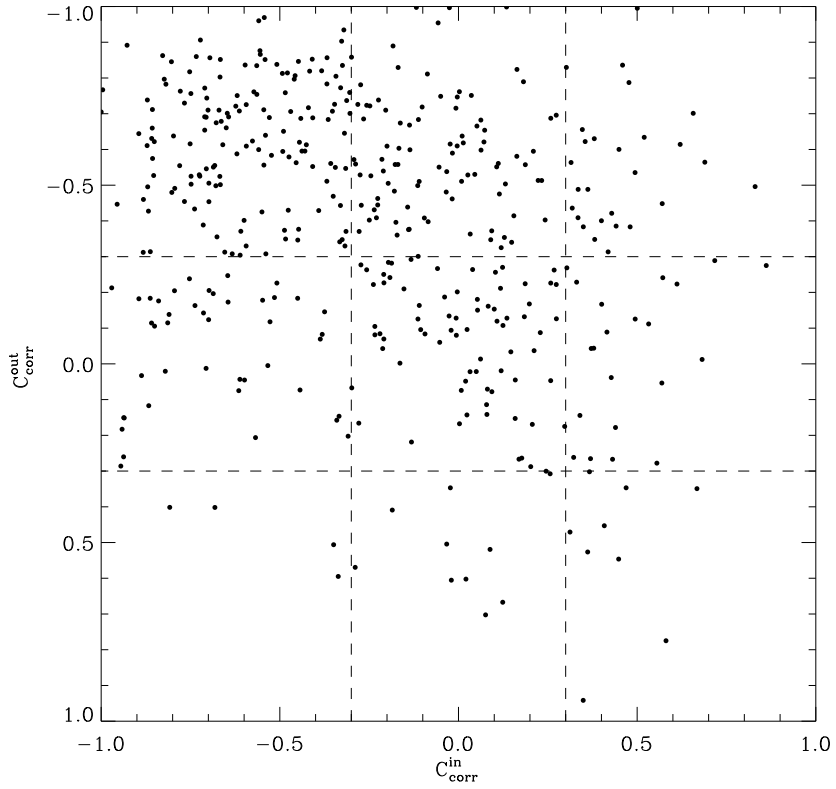

Figure 7.21: Relation between the inner C^{in}_{corr} and outer C^{out}_{corr} correlation coefficients from the linear fitting of the (V/σ)-h_3 relation within $1R_{1/2}$ and in the radial range 1-5$R_{1/2}$. The vertical and horizontal lines mark the 0.3 and -0.3 threshold separating correlation, no correlation and anticorrelation.

7.A Classification of Regular Rotators

In Sec. 7.5.2 we disentangle the class of Regular Rotators on the basis of their correlation coefficient within $1R_{1/2}$ (C^{in}_{corr}) and in the radial range 1-5$R_{1/2}$ (C^{out}_{corr}). To visualise the introduced classification Fig. 7.21 shows the direct correlation between C^{in}_{corr} and C^{out}_{corr}. The vertical and horizontal dashed lines mark the threshold values of 0.3 and -0.3 to distinguish correlation, no correlation and anticorrelation. Therefore, each of the upper left rectangle encompasses one of the classes introduced in Sec. 7.5.2, i.e. aa, na, an, and nn. The combined rectangles in the right column form the cx class.

The distribution emphasises the aforementioned result for a favouring of anticorrelations in both radial ranges. Interestingly, the right upper region is stronger populates than the lower left confirming that there is a tendency towards a anticorrelation at larger radii. Galaxies in the off-diagonal rectangles exhibit a change in the correlation type when going beyond $1R_{1/2}$.

Chapter 8

Summary and Discussion

In the current picture of structure formation in the Universe, dark matter halos build from initial density perturbations and subsequently merge in a hierarchical manner forming more massive structures. The evolution of the baryonic matter takes place within this framework, being influenced by a complex interplay of various physical processes. This thesis is dedicated to contribute to the understanding of how these processes impact the present day attributes of galaxies and how they are encoded in galaxy properties. To this end, we utilise the fully cosmological hydrodynamic *Magneticum Pathfinder* simulations, which implement a large variety of physical processes relevant for galaxy formation. The simulation provides a statistically meaningful sample of galaxies and allows to trace the evolution of galaxies with cosmic time in a fully cosmological environment. In addition, an idealised set of higher resolved binary merger simulations are analysed to perform a case study of a merger remnant. In this analysis, we focused on the dynamic and kinematic properties of galaxies, i.e. the line-of-sight velocity distribution based on its different moments, in great detail.

In the first step we constrained our analysis to the central region of ETGs within one half-mass radius. State-of-the-art intregral-field spectrograph surveys such as SAURON, ATLAS^{3D}, CALIFA, SAMI, and MaNGA provide a wealth of stellar kinematic observations in this radial range, revealing that ETGs generally come in two flavours: fast rotators and slow rotators (e.g. Emsellem et al., 2007, 2011; Cappellari, 2016; van de Sande et al., 2017a; Falcón-Barroso et al., 2019b; van de Sande et al., 2020). Constructing mock observational kinematic maps from the *Magneticum* simulation we find excellent agreement with observations for the fractions of fast and slow rotators, hence capturing the trend of fast rotors being the dominant kinematic state of ETGs. A strong limiting factor for observations is the constrain to a given projection in the sky, which can only be accounted for by applying modelling techniques under certain assumptions. Exploiting the three-dimensional information provided by the simulation to select the most physical edge-on projection, we find further evidence for a kinematic dichotomy. Very recently, we strengthened the existence of a bimodal distribution in a joint project with the SAMI survey team, statistically analysing a sample of $\sim$ 1800 observed galaxies and samples from different cosmological simulations including *Magneticum* (see App. A.2). In this thesis we extend our analysis to a visual inspection of the kinematic maps to identify specific kinematic features, as for example kinematically distinct cores, motivated by the observational findings by Krajnović et al. (2011). The simulations successfully reproduce the primary velocity features and frequency trends found in observations, suggesting that the simulation accounts for all the relevant physical processes

that shape the stellar kinematics of galaxies. Having a simulated sample of galaxies with realistic stellar kinematics enables us to revisit an analytic theoretical model introduced by Binney (2005), which connects the position in the $\lambda_{R_{1/2}}$-ϵ plane to the anisotropy parameter δ (see also Cappellari et al., 2007). We calculate δ directly from the particle data, finding excellent confirmation of the predictions from the theoretical model. Therefore, we confirm that this model represents a powerful tool to predict the actual anisotropy from projected quantities provided the inclination is known.

To further understand the origin of fast and slow rotation we investigate the $\lambda_{R_{1/2}}$-ϵ plane at higher redshift, i.e. $z = 0.5$, $z = 1$, and $z = 2$. Although only galaxies with $M_* > 2 \times 10^{10}$ can be considered, due to particle resolution, we show that the population of fast rotators is already in place at $z = 2$, while only very few slow rotators are present. The population of slow rotators gradually builds up at later times, with the most significant increase between $z = 0.5$ and $z = 0$. Furthermore, the dichotomy between fast and slow rotators is present at all redshift, suggesting a rather fast transition from fast to slow rotation. In the light of the two phase picture of galaxy formation (Oser et al., 2010) we conclude that merging is the predominate driver for the kinematic transformation that builds up the slow rotator population. We demonstrate that for a third of the slow rotator population this transition is rapid on a timescale of 0.5Gyr, and unambiguously associated with a massive merger event. Therefore, a significant fraction of slow rotators in the simulation originates from this process.

A particularly interesting kinematic configuration are kinematically distinct cores (KDC), since they comprise at least two kinematic components and therefore are promising candidates to encode information about the formation pathway. While it has been shown in previous studies that the formation of KDCs is tightly connected to merging, flybys, and the availability of gas, the details of their composition and lifetime is sparsely studied (McDermid et al., 2006b; Hoffman et al., 2010; Emsellem et al., 2014; Taylor et al., 2018; Omori and Takeuchi, 2020; Ebrová et al., 2020). Our study of a KDC formed in a binary merger simulation reveals that the rotating core signal is generated by stars that have been formed during the merger from the progenitor gas. Furthermore, the core stars reside within the core radius for several orbital periods, suggesting an orbit with an apocenter inside the core radius, most probable on z-tube orbits as shown by Hoffman et al. (2010). Running the simulations for 10Gyr made it possible to show that the KDC performs a distinct periodic figure rotation comparable to the precession of a gyroscope in a gravitational potential. This is due to a conservation of the orbital angular momentum of the merger in the gas component which forms the KDC via star formation. The global motion gets gradually dampened over time, simultaneously to the fading of the KDC signal $\sim$ 3Gyr after the merger. This fading of the KDC is driven by the gravitational mixing with a random motion dominated component that permeates the KDC on highly elliptical orbits. Therefore, the KDC truly disperses kinematically, in contrast to the result from McDermid et al. (2006b), who suggested that the KDC signal in luminosity weighted velocity maps fades due to the ageing and associated decrease in luminosity of the younger KDC stars to explain the lack of intermediate and old aged KDCs.

In addition to the information stored in the central region, the stellar halo of galaxies encodes valuable information about accretion events in a long term memory due to long mixing time scales. The most obvious remnant features of accretion events are shells and streams. However, the LOSVD contains information about accretion events for long time even after shells and streams are dispersed or fall below the detection limit. A highly discussed topic in this regard is the transition and relative importance of in-situ formed stars versus

ex-situ accreted stars, which holds substantial clues to the formation history (see e.g. Cooper et al., 2010; Pillepich et al., 2014; Remus et al., 2017; Kluge et al., 2020; Remus and Forbes, 2021). Also, at this radial scale stellar kinematics are a key ingredient to gain further inside into this subject.

Investigating the stellar kinematics in the simulation out to $5R_{1/2}$, we find three main types of radial variations of the amount of rotational support (λ(R)), i.e increasing, decreasing, and flat, in agreement with observations. A particularly interesting profile type are the decreasing profiles, which feature a well defined transition from rotational support for $R \lessapprox 2R_{1/2}$ to low rotational support for $2R_{1/2} < R < 5R_{1/2}$. These objects are in agreement with a stellar disk embedded in a non-rotating halo, as suggested by Arnold et al. (2014) and Foster et al. (2018). We are able to connect this characteristic profile shape to statistical characteristics in the formation pathway, which suggest a distinct accretion history. The strongly rotating central structure has already formed at $z \sim 2$ via in-situ star formation, and subsequently evolves rather undisturbed and uncorrelated form the surrounding halo through internal secular processes. In contrast, the surrounding halo gradually builds up over time by the disruption of low-mass satellites in the outskirts that get accreted from anisotropic directions, leading to non-ordered motion. Such a scenario suggests a correlation between the kinematic transition radius and the transition radius from insitu to exsitu stars. Indeed, we find a linear correlation between these two radii especially for halos that did not experience high-mass mergers. It is, however, not expected that there exists a sharp transition rather than a transition region where the in-situ and ex-situ components overlap considerably. Our results represent a meaningful interpreting for existing observations and future surveys with increased radial coverage.

In the effort to extract the maximum information from the LOSVD we extended our analysis beyond the first two moments, i.e. mean velocity and velocity dispersion, to the third and fourth moments h_3 and h_4, which assess the deviations of the LOSVD from a perfectly Gaussian distribution. This is studied for the first time in a fully cosmological simulation in this work.

In agreement with observations from Veale et al. (2017b), we find a transition in the global orbital structure with stellar mass quantified by an increase of the average $\langle h_4 \rangle$ towards higher masses. Related to that result we show that $\langle h_4 \rangle$ is tightly connected to the in-situ fraction, where galaxies with $\langle h_4 \rangle < 0$ are clearly dominated by insitu star formation in contrast to galaxies with $\langle h_4 \rangle > 0$ for which no such clear trend is visible. Therefore, we conclude that the global star formation and accretion history is encoded in the $\langle h_4 \rangle$ parameter. Earlier theoretical studies based on merger and zoom-in have found a connection between the higher-order moments and the amount of gas involved in the accretion history, manifesting in an anticorrelation between (V/σ) and h_3. This is also observed in several studies based on IFS (e.g. Krajnović et al., 2011; van de Sande et al., 2017b). We show that, in a fully cosmological environment, the slope and strength of this linear connection is not as strongly correlated to the gaseous accretion as expect from former studies. In contrast, the strength of the correlation is stronger correlated to the internal star formation rate and availability of cold gas independent of where the gas originates from. This is especially true for galaxies with strong anticorrelations and correlations. These galaxies exhibit a clearly enhanced star formation and cold gas content within one half-mass radius, sustaining star formation for a longer time. Extending the analysis to the stellar halo reveals that the correlation type between (V/σ) and h_3 can change beyond one half-mass radius. About half of the simulated regular rotators exhibits the same correlation type in the centre and the halo, while the

residual regular rotators show different combinations of correlation, anticorrelation, and no-correlation. While these varying kinematic properties within the class of regular rotators are not clearly connected to other properties, such as dark matter fractions and mass-size relation, we find clear differences in the accretion history.

In summary, we have shown that the LOSVD is a powerful tool to constrain the formation of galaxies and to assess the orbital configuration of a system from observable quantities. To this end it is crucial to combine observation and simulation to, on the one hand, evaluate the limitation and potential improvements of the simulations, and on the other hand provide meaningful interpretations of observed data from the theoretical point of view. In the future, technical and methodological advancements in both simulation and observation will allow for an even more detailed analysis of the stellar kinematics, and therefore holds great promise to further understand the formation and evolution of galaxies. In addition, a very promising approach, which is already deployed in studies (e.g. Guérou et al., 2016; Poci et al., 2019; Zhu et al., 2020, , Teklu et al. 2021 in prep.), is to add information about stellar populations to the kinematics, such as stellar ages and metallicities, in a spatially resolved manner, therefore extending the knowledge obtained through the work presented here.

Appendix A

Contributions to Other Work

During the course of my PhD I co-authored a number of institute internal and external studies which are outlined in this Appendix. My contributions range from extracting and providing data to strong involvement in the physical interpretation and discussion of the subject matter. I will briefly outline the scientific context and present the most important results without going into the profound details. For more details I refer to the respective publication.

The first two studies (Sec. A.1 and A.2) are very closely related to the main topic of this thesis investigating aspects of the central stellar kinematics of galaxies from a observational point of view based on data from the SAMI survey, however with a profound focus on the comparison to predictions from cosmological simulations. In Sec. A.3 I briefly outline the design and science goals of the MAGPI survey which is a currently ongoing survey where I contributed to the proposal as well as the outlined publication. The next two studies described in Sec. A.4 and A.5 are not as closely related to the main topic of this thesis, however also utilising the *Magneticum Pathfinder* simulations to investigate further aspects of galaxy formation and evolution. Finally, the last study outlined in Sec. A.6 is only very weakly connected to the main subject of this thesis, nonetheless investigates the very exciting evolution of protoclusters at $z \sim 4$ in the *Magneticum* simulations.

A.1 The SAMI Galaxy Survey: comparing 3D spectroscopic observations with galaxies from cosmological hydrodynamical simulations

This section is based on van de Sande et al. (2019)

Modern cosmological simulations are now capable to produce large samples of realistic galaxy populations implementing different numerical and physical models. And inevitable step to evaluate simulations is to construct mock observations for comparison with observations to assess whether meaningful conclusions and interpretations can be drawn from the simulations. In particular, the effect of processes such as merging and environmental processes on stellar kinematics are of high interest and can be studied in great detail in cosmological simulations (e.g. Penoyre et al., 2017; Schulze et al., 2018; Lagos et al., 2018b; Choi et al., 2018). Furthermore, the varieties in the predictions of cosmological simulations which differ in their

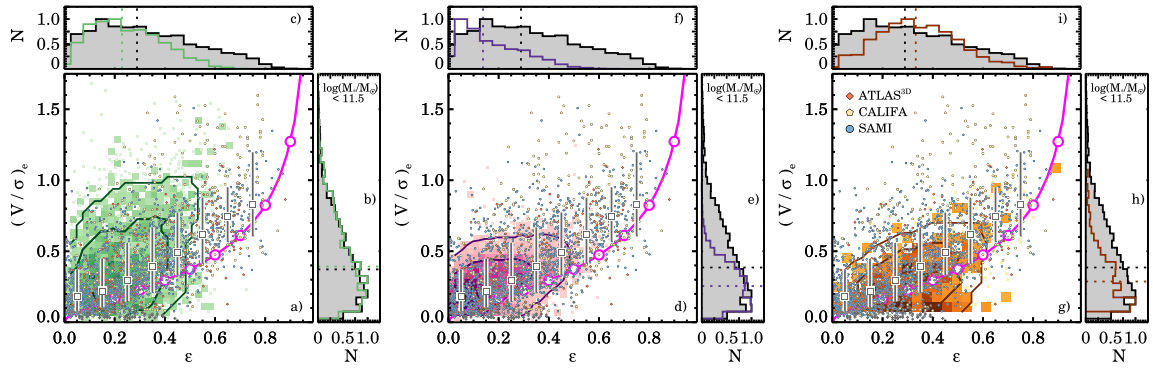

Figure A.1: Fig. 8 taken from van de Sande et al. (2019). Comparison of simulated and observed data in the (V/σ)-ϵ plane. From left to right we show the number density of EAGLE$^+$ (EAGLE+HYDRANGEA), HORIZON-AGN, and *Magneticum*. Individual symbols mark the three observational samples, i.e. ATLAS^{3D}, CALIFA, and SAMI as given in the legend. The white squares show the median of the combined observations. Similarly the grey top and lateral histograms display the distribution of the combined observational sample.

numerical methods and physical implementations can provide insight into the importance of certain processes, e.g. feedback processes. In van de Sande et al. (2019) we perform a rigorous comparison of kinematic and structural properties of galaxies predicted by the EAGLE, HYDRANGEA, HORIZON-AGN, and *Magneticum* cosmological simulations to IFS observations combining data from the SAMI, ATLAS^{3D}, CALIFA, and MASSIVE survey. The most obvious difference among the considered simulations is that HORIZON-AGN adopts the adaptive mesh refinement code RAMSES to solve the fluid equations, while EAGLE, HYDRANGEA, and *Magneticum* adopt modified versions of the SPH based GADGET code (see Sec. 3 for more details on the simulation techniques). The motivation of this study is to identify key areas of success and tension between simulation and observation.

In order to ensure a meaningful comparability a mass-matching technique is applied to sample the same fraction of galaxies from observations and simulations as a function of stellar mass. In particular, we compare correlations between stellar mass M_*, half-mass/light radius R_e, ellipticity ϵ, central velocity dispersion σ_e, dynamical mass M_{dyn}, rotational support $(V/\sigma)_e$, and stellar Age. In general we find good agreement with the observed dependence of these quantities on stellar mass in all the simulations, although the distributions of the individual quantities can differ significantly. This is also apparent when comparing the distributions amongst the different cosmological simulations. To illustrate this result Fig. A.1 shows in each panel the comparison of individual simulations with the combined observational sample in the (V/σ)-ϵ plane. While all the simulations reproduce the observed distribution in the plane and the trend towards more elongated shapes with increasing (V/σ) reasonably well there are considerable differences. The EAGLE$^+$ simulation closely matches the observed (V/σ) distribution performing better than the other simulations. However, it lacks the most elongated galaxies with typically high (V/σ). The same holds for the HORIZON-AGN simulation with the additional severe lack of strongly rotational supported galaxies. While the *Magneticum* simulation is the only simulations to recover very elongated objects the regime of very round galaxies is underpopulated. Furthermore, for a given ϵ *Magneticum* does not reach the high (V/σ) region. In this context Frigo et al. (2019) for example showed, that feedback from AGN has significant impact on the orbital structure generally lowering the rotational

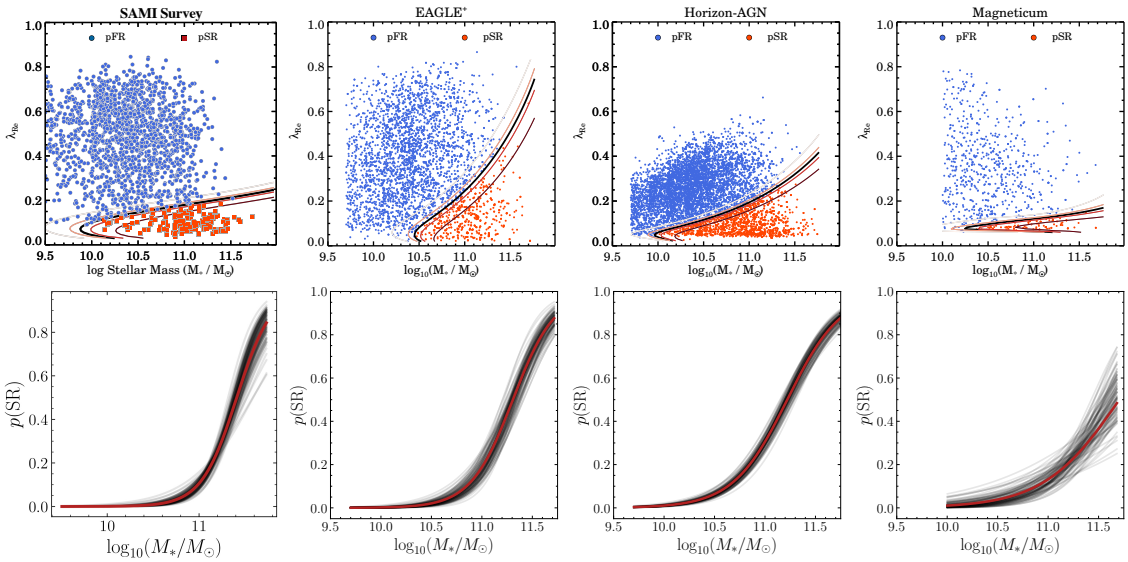

Figure A.2: Slightly modified version of Fig. 10 taken from van de Sande et al. (2020). Results from the Bayesian mixture model to detect kinematic populations in SAMI, EAGLE^{+}, HORIZON-AGN, and *Magneticum* (from left to right). The upper row shows the λ_{R_e}-log(M_*) plane which is fed to the mixture model. Orange symbols mark galaxies with a probability larger than 50% to belong to the slow rotator population (pSR) also distinguished by the black line. Accordingly blue symbols show the pFR population. The lower row displays the probability to be drawn from the pSR population as function of log(M$_*$) for 2000 model realisations (black) and their average (red).

support. Furthermore, we find, that the differences between the simulations is especially obvious when investigating stellar population properties, i.e. age of the stellar population which is directly connected to the hydrodynamic and feedback prescription.

A.2 The SAMI Galaxy Survey: Towards an Optimal Classification of Galaxy Stellar Kinematics

This section is based on van de Sande et al. (2020)

One of the earliest and most significant insight from IFS observations is the existence of least two kinematic flavours of ETGs, depending on whether they show ordered large scale rotation or not, i.e. fast and slow rotators (Emsellem et al., 2007). The evidence for these two populations has been substantiated in large samples in many studies (see Sec. 4.1). However, the overlap and possibility of a continuous transition between these two classes is still a matter of debate. In van de Sande et al. (2020) we use different classification schemes, i.e. regular and non-regular rotators using KINEMETRY, visual classification, and bayesian mixture models, to investigate if a bimodality in the kinematic properties can be identified. For the SAMI sample we find, that the mixture model predicts two kinematic populations and provides the cleanest separations. The Bayesian mixture model is applied to the λ_{R_e}-log(M_*) plane, while allowing the mixture model parameters to vary with log(M_*). Interestingly, LTGs can be described by a single beta function at all masses, while for ETGs a second beta function is required for log(M_*) > 10.5. Based on the model output we introduce the notion of probabilistic slow

(pSR) and fast (pFR) rotators, where the pSR are galaxies with a probability to be drawn from the second population larger than 50%. In the defining λ_{R_e}-ϵ plane the pSR occupy a similar region than the latest fast slow rotator separation criterion introduced in Cappellari (2016), although with slightly larger λ_{R_e} values and no incline towards larger ϵ.

Applying the mixture model to simulated data from EAGLE$^+$, Horizon-AGN and *Magneticum* also shows that a second distribution is needed which gets increasingly prominent towards higher masses in agreement with the observations. However, the location, λ_{R_e} peak, and mass dependence of the pSR population is significantly different among the simulations and with respect to the observations. Fig. A.2 summarises the outcome of the mixture model showing the distribution of pSR and pFR in the upper row and the probability to be drawn from the pSR population as function of $\log(M_*)$ for SAMI, EAGLE$^+$, HORIZON-AGN, and *Magneticum* (from left to right).

A.3 The MAGPI Survey – science goals, design, observing strategy, early results and theoretical framework

This section is based on Foster et al. (2020)

As stressed numerous times throughout this study the development of integral-field spectroscopy and its application in large survey campaigns was one of the main drivers to further understand the properties and evolution of galaxies in the past two decades. At present time multi-object integral-field spectrographs, such as SAMI (Croom et al., 2012) and MaNGA (Bundy et al., 2015) are able to provide data for sample sizes of several thousand nearby galaxies allowing for a detailed statistical investigation of stellar and gas properties in a spatially resolved manner. However, the different timescales over which processes, relevant for the evolution of galaxies, act complicates the interpretation of very low redshift observations. While the gas kinematics has been observed to redshifts of ~ 3 by various surveys (e.g. KMOS^{3D} (Wisnioski et al., 2015) and SINS (Förster Schreiber et al., 2018)) resolved stellar kinematics are more difficult to measure at high redshift due to the fainter stellar body. However, simultaneous observations of gas and stellar properties, including resolved kinematics, are a key ingredient to disentangle the formation pathway of galaxies.

In Foster et al. (2020) we present the science goals and design of the **M**iddle **A**ges **G**alaxy **P**roperties with **I**ntegral Field Spectroscopy (MAGPI) survey designed to investigate the physical processes driving the galaxy transformation at lookback time $3 - 4$Gyr ($z \sim 0.3$). Therefore, the survey targets 60 massive ($M_* > 7 \times 10^{10} M_\odot$) central galaxies in various environments and will also provide spectra for 150 satellite galaxies to study kinematic and chemical properties of stars and ionized gas. The science goals of the survey are:

- **Decoding the dynamical transformation of galaxies:** We plan to apply dynamical modelling methods such as Schwarzschild Modelling (Schwarzschild, 1979) and Jeans Anisotropic Modelling (Cappellari, 2008) to move beyond projected quantities. Schwarzschild modelling allows to assess orbital families enabling a direct comparison of orbital families at low and intermediate redshift. Combining this approach with stellar population information has shown to be a powerful tool to infer the formation history of individual galaxies (Poci et al., 2019; Zhu et al., 2020). Furthermore, JAM will provide information about the radial profiles of the dynamical mass of stars and dark matter.

- **Decipher the role of gas accretion and merging:** Recently or currently merging galaxies typically show disturbed morphologies as well as asymmetric and disturbed kinematics (e.g. Barrera-Ballesteros et al., 2015; Oh et al., 2016; Bloom et al., 2018; Feng et al., 2020). A clear sign of recent accretion is the kinematic and morphological misalignment of the stellar and gaseous component. Asymmetries in the stellar and gas kinematics can be used to infer accretion events (Davis et al., 2011; van de Voort et al., 2015; Bryant et al., 2019; Khim et al., 2020). With MAGPI we will be able to measure this misalignment 3-4Gyr ago and by comparison to low redshift observation trace its evolution.

- **Determining energy sources and feedback activity:** Feedback mechanism from stars and AGN are known to be crucial for regulating star formation in galaxies and hence the quenching of galaxies. Especially in numerical simulations feedback processes are a critical ingredient to model galaxy formation. Providing a large range of rest-frame emission lines ([OII] to [SII]) MAGPI will map the ISM properties such as metallicity, ionisation parameter, and electron density from which the trace of AGN activity and star formation can be decoded.

- **Tracing chemodynamics of galaxies:** The chemical composition of galaxies encode a wealth of information to constrain the mass assembly of LTGs and ETGs (e.g. Taylor and Kobayashi, 2017; Poci et al., 2019; Davison et al., 2021). Combined stellar and gas metallicities are sensitive to merger events, AGN feedback and star formation. In this context metallicity gradients are commonly used to quantify the chemical composition of galaxies (e.g. Sánchez-Menguiano et al., 2016; Belfiore et al., 2017; Sillero et al., 2017; Förster Schreiber et al., 2018). MAGPI will push the simultaneous measurement of resolved gas and stellar metallicity beyond $z = 0.1$. This will allow to put constraints on the quenching of star formation and for example the process of pre-processing of group galaxies prior to the accretion onto the main halo (Lotz et al., 2019; Kleiner et al., 2021).

- **Comparison to cosmological simulations:** A characteristic of the MAGPI survey is the inclusion of cosmological simulations, already in the proposal design, and the design of a comparison ready sample of mock observations. We will include data from the EAGLE, *Magneticum*, HORIZON-AGN, and Illustris-TNG100 simulations and the chemo-dynamical simulations of Taylor and Kobayashi (2015, 2017). This serves two purposes: First we aim to pin-point areas of tension and success between the observations and predictions from the simulations to investigate whether physical processes relevant to model galaxy formation are implemented properly. Secondly, the simulations will give meaningful interpretations of the observations also beyond observable quantities.

The left panel of Fig. A.3 shows the prediction from the *Magneticum* simulation for the evolution of the λ_R distribution at $z < 1$. This clearly shows how a low λ_R population builds up for lookback-times below $\sim$ 5.5Gyr and a slight spin-down of the high λ_R population. This kinematic transformation is still progressing in time interval targeted by MAGPI which is indicated by the red rectangle. The right panel shows the corresponding probability density function split up into high (grey) and low (blue) density environments. The simulation does predict a environmental dependence of λ_R where the split into two populations is more

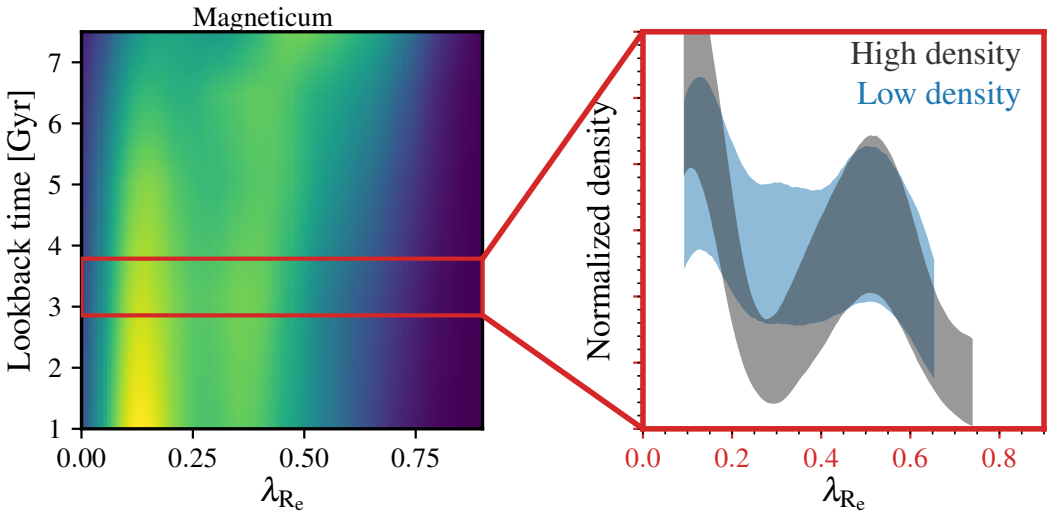

Figure A.3: Modified version of Fig. 1 taken from Foster et al. (2020). *Left Panel:* Evolution of the λ_R distribution with lookback-time in the *Magneticum* simulation for a MAGPI equivalent sample. From blue to yellow the number density of galaxies increases. *Right Panel:* Probability density function of λ_R at the MAGPI target lookback-time split up into high and low density environment.

pronounced in high density environments than in low density environments. We find that the trends stated for *Magneticum* here differ between the considered simulations. Therefore, MAGPI will be able to clarify which simulation predicts the kinematic transformation and environmental dependence most accurately.

A.4 Connecting Angular Momentum and Galactic Dynamics: The Complex Interplay between Spin, Mass, and Morphology

This section is based on Teklu et al. (2015)

The question of how galaxies and dark matter halos acquire their angular momentum is one of the most addressed questions in astronomy, since it is essential to understand galaxy formation and how it is connected to the large-scale structure of the Universe. As presented in this thesis the present-day stellar angular momentum content of galaxies varies significantly and can be attributed to different formation pathways for $z \lesssim 2$. At higher redshift, especially in the regime of linear growth, the tidal torque theory describes the growth and angular momentum acquisition of perturbation building proto-clusters and galaxies. According to this, angular momentum arises as a consequence of the tidal torque exerted from the surrounding perturbations on the halo (Peebles, 1969; Doroshkevich, 1970; White, 1984). Since the tidal torques act on both the baryons and dark matter and assuming conservation of angular momentum, the baryons are expected to have similar specific angular momentum than the hosting halo (Fall and Efstathiou, 1980). For lower redshift the angular momentum evolution is additionally influenced by non-linear processes such as merging and secular evolution which are not captured by the tidal torque theory. To further understand the connection

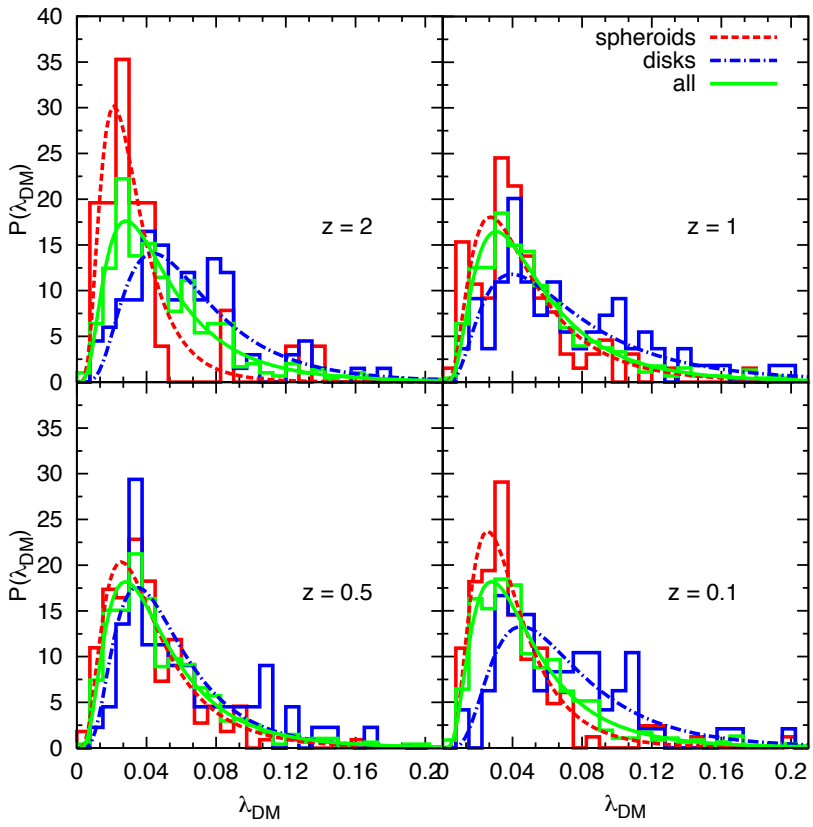

Figure A.4: Fig. 17 taken from Teklu et al. (2015). The spin parameter λ distribution for the entire dark matter halo for all (green), spheroidal (red), and disk galaxies at four different redshift. The curves show the corresponding fit of a log-normal distribution.

between the angular momentum of galaxies and the dark matter halos we investigate the angular momentum content of galaxies for different component, i.e. stars and hot/cold gas, and its relation to the angular momentum of the halo in the *Magneticum* simulations in Teklu et al. (2015). In particular we analyse the distribution of the dimensionless spin parameter $\lambda = j/\sqrt{2}R_{\rm vir}V_{\rm circ}$ (van den Bosch et al., 2002), where j is the specific angular momentum, $R_{\rm vir}$ the virial radius, and $V_{\rm circ}$ the circular velocity, as well as the angle between the angular momentum vectors of the different components.

Investigating the dependence of the stellar specific angular momentum on stellar mass we find that galaxies with similar rotational properties (circularity distribution) lie on linear parallel sequences in excellent agreement with previous studies (Fall, 1983; Romanowsky and Fall, 2012; Obreschkow and Glazebrook, 2014; Cortese et al., 2016; Lagos et al., 2017b). Furthermore, we show that galaxy properties such as cold-gas fraction, spin parameter, and angular momentum alignment transition smoothly between the parallel sequences. Therefore, parameterising the position in the stellar-mass–specific-angular-momentum plane by the y-axis intercept is a powerful way to classify galaxies capturing many of the relevant properties.

In order to understand the interplay between the dark matter halo and the baryonic component the galaxy sample is split into disk and spheroidal galaxies based on the circularity distribution and gas content. It reveals that halos hosting a disk galaxy in the centre exhibit a

slightly larger spin than halos hosting a spheroidal galaxy for $z < 2$, however most pronounced at $z = 0.1$. Fig. A.4 illustrates this results showing the λ distribution of the dark matter halo split up into all (green), spheroidal (red), and disk (blue) galaxies. At all redshifts the distributions for halos hosting a spheroidal is statistically significantly different from the halos hosting a disk. Especially at $z = 2$ and $z = 0.1$ the disk halo distribution peaks at higher λ with a more pronounced tail towards larger values. This feature is also present in a dark matter only control run, where we cross-identified the halos from the baryonic run. Therefore, the formation history of the dark matter seem to play a crucial role in regulating the morphology of galaxies. Furthermore, we find that disk galaxies tend to reside in halos with a stronger alignment between the central and total angular momentum of the dark matter, underpinning our conclusion.

A.5 Declining Rotation Curves at $z = 2$ in ΛCDM Galaxy Formation Simulations

This section is based on Teklu et al. (2018)

Since Zwicky (1933, 1937) postulated the existence of dark matter and the subsequent confirmation by Rubin et al. (1980) rotation curves of galaxies in the local Universe are studied in great detail. Rotation curves provide valuable constraints on the baryonic and dark matter mass distribution within star forming galaxies. Within the dark matter paradigm rotation curves are expected to rise in the baryonic dominated centre and to plateau with the transition to the dark matter dominated halo. A particularly interesting epoch to study the properties of galaxies is $z \sim 2$ where cosmic star formation peaks and the dominant physical processes influencing galaxy evolution are different than at present day. Genzel et al. (2017) and Lang et al. (2017) targeted exactly this redshift range measuring rotation curves for star forming galaxies from the Hα emission line out to exceptionally large radii. They find that a clear drop in the rotation velocity after the radius of maximum velocity is a common feature, opening a debate about the significance of dark matter in these galaxies. In Teklu et al. (2018) we deploy the cosmological *Magneticum* simulation to investigate whether declining rotation curves form naturally within the ΛCDM paradigm adopted in the simulation.

To this end we identify 26 poster child disk galaxies at $z = 2$ with stellar masses above $5 \times 10^{10} M_{\odot}$ based on their orbital configuration (i.e. circularity distribution) and cold gas content. 10 out of the 26 disk galaxies exhibit a clearly declining rotation curve of the cold gas component very comparable to the observations presented in Genzel et al. (2017). The left panel of Fig. A.5 shows the 10 declining rotation curves (non-solid lines) in direct comparison to the observations (solid lines) highlighting the agreement. Furthermore, the galaxies formed in the simulation have similarly low dark matter fractions than reported in Genzel et al. (2017). In line with the expectations for a dynamically young system we find significantly larger velocity dispersions than at $z = 0$ reflecting the increased turbulence in the disk at this redshift. Tracing these galaxies to $z = 0$ reveals that they experience a significant virial and stellar mass growth by a factor of typically 3.5. Furthermore, they end up in different environments and with different morphologies, some showing flat rotations curves at $z = 0$. Interestingly, the simulations also produces several spheroidal galaxies at $z = 2$ hosting a cold gas disk with decreasing rotational velocity, as can be seen in the right panel ofA.5 for five example galaxies. Overall, we conclude, that falling rotations curves are

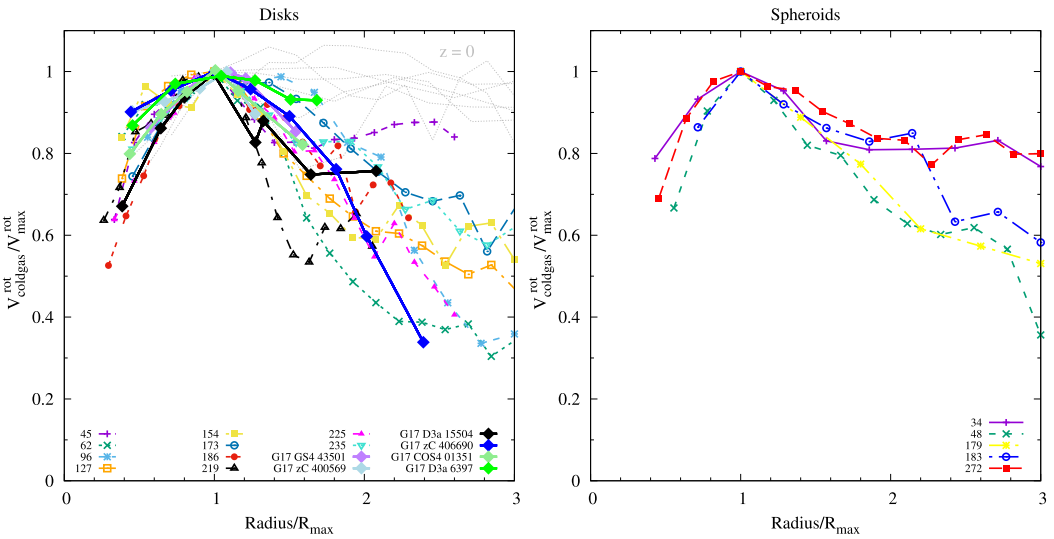

Figure A.5: Fig. 2 taken from Teklu et al. (2018). *Left Panel*: Rotation curves from the cold gas for 10 poster child disk galaxies that exhibit a distinct decline in rotational velocity at $z = 2$. The grey curves indicate the rotation curve at $z = 0$ for seven of the poster child disks. For comparison the solid lines mark the six declining rotation curves presented in Genzel et al. (2017). *Right Panel:* Declining cold gas rotation curves for five gas-rich spheroidal galaxies at $z = 2$.

a natural outcome of ΛCDM caused by a relatively turbulent disk in objects with low dark matter fractions.

A.6 The young and the wild: What happens to proto-clusters forming at $z \sim 4$

This section is based on Remus et al., to be submitted

Galaxy clusters play an important role in the discussion about structure formation in the Universe, e.g. 'top-down' vs. 'bottom-up', 'hot' vs. 'cold' dark matter. Furthermore, the cluster environment has a strong impact on galaxy formation, since dense environments are needed to form the most massive galaxies observed today (De Lucia and Blaizot, 2007). Very recently a uniquely massive and dense system, called SPT2349-56, has been observed at a redshift of ~ 4.3, hosting galaxies with extremely high star formation rates (Miller et al., 2018). Similarly, Oteo et al. (2018) detected another proto-cluster at similar redshift. These proto-clusters are believed to be the progenitors of the most massive structures in the present day Universe.

In Remus et al., to be submitted we study the formation of proto-clusters at $z \sim 4$ in Box2b of the *Magneticum* simulation, which provides a large enough volume to statistically analyse proto-clusters. Within the simulation we find structures matching the observed properties of SPT2349-56, i.e. the number of member galaxies and phase-space distribution. Furthermore, the proto-cluster galaxies in the simulation are fast rotating with rotational velocities comparable to the ones observed in SPT2349-56. In Fig. A.6 we illustrate the environment and structure of an example proto-cluster selected from the simulation. The small panels show

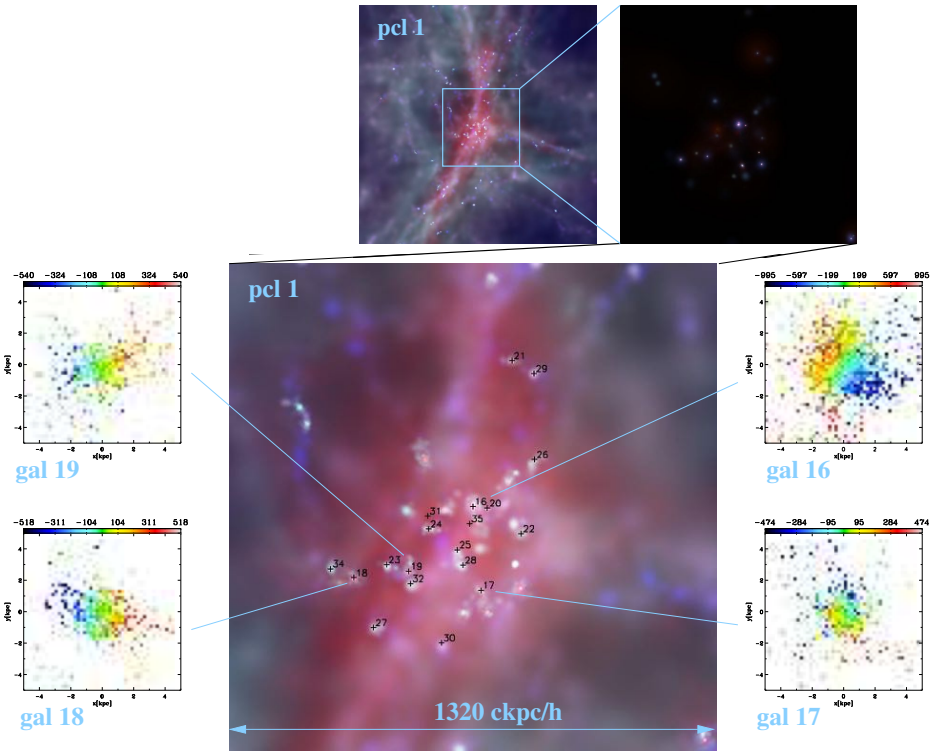

Figure A.6: *Upper left panel:* Large scale environment of a example proto-cluster at $z = 4.3$ showing the gas content from cold (blue) to hot (red). *Upper right panel:* Zoom onto the stellar component with a side-length of 353.77kpc, with the colours indicating the age of the stars from young (blue) to old (red). *Main panel:* Same zoom region with both gas and stars overlaid using the same colour scheme. The member galaxies are marked and labelled according to their stellar mass. Furthermore, the velocity maps of the gas component are shown for four example members in the lateral panels.

the clearly rotating velocity maps for four example member galaxies. As can be seen the proto-cluster is located at a knot of filaments and has already developed a hot atmosphere. Although, the member galaxies are all bound to the cluster (velocities are below the escape velocity) there is no obvious over-massive central galaxy. In fact, these galaxies will merge in the further evolution building the progenitor of the present-day cluster BCG. Following the evolution of the proto-clusters we show, that the region that will eventually collapse to form the cluster at $z = 0$ is significantly larger than the proto-cluster region at $z = 4.3$. Therefore, none of the properties virial mass, star formation rate, number of member galaxies or stellar mass used to rank the proto-clusters at $z = 4.3$ are good predictors for the mass of the final cluster at $z = 0$.

Despite the overall good agreement with the observations of SPT2349-56, the star formation rates within the proto-clusters predicted by the simulation are a factor $2-3$ smaller than inferred from the observations. This indicates that, while the average stellar mass growth down to $z = 0$ matches the observations reasonably well, the implemented sub-grid models for star formation are not able to produce sufficiently high star formation efficiencies in the environment of proto-clusters.

Bibliography

Abadi, M. G., J. F. Navarro, and M. Steinmetz
2006. Stars beyond galaxies: the origin of extended luminous haloes around galaxies. *Monthly Notices of the Royal Astronomical Society*, 365:747–758.

Albrecht, A. and P. J. Steinhardt
1982. Cosmology for Grand Unified Theories with Radiatively Induced Symmetry Breaking. *Physical Review Letters*, 48(17):1220–1223.

Amorisco, N. C.
2017. Contributions to the accreted stellar halo: an atlas of stellar deposition. *Monthly Notices of the Royal Astronomical Society*, 464(3):2882–2895.

Antoja, T., A. Helmi, M. Romero-Gómez, D. Katz, C. Babusiaux, R. Drimmel, D. W. Evans, F. Figueras, E. Poggio, C. Reylé, A. C. Robin, G. Seabroke, and C. Soubiran
2018. A dynamically young and perturbed Milky Way disk. *Nature*, 561(7723):360–362.

Arnold, J. A., A. J. Romanowsky, J. P. Brodie, L. Chomiuk, L. R. Spitler, J. Strader, A. J. Benson, and D. A. Forbes
2011. The Fossil Record of Two-phase Galaxy Assembly: Kinematics and Metallicities in the Nearest S0 Galaxy. *The Astrophysical Journal*, 736:L26.

Arnold, J. A., A. J. Romanowsky, J. P. Brodie, D. A. Forbes, J. Strader, L. R. Spitler, C. Foster, C. Blom, S. S. Kartha, N. Pastorello, V. Pota, C. Usher, and K. A. Woodley
2014. The SLUGGS Survey: Wide-field Stellar Kinematics of Early-type Galaxies. *The Astrophysical Journal*, 791:80.

Arth, A., K. Dolag, A. M. Beck, M. Petkova, and H. Lesch
2014. Anisotropic thermal conduction in galaxy clusters with MHD in Gadget. *arXiv e-prints*, P. arXiv:1412.6533.

Bacon, R.
1985. Anisotropic models of elliptical galaxies. II. The case of flattened isophotes. *Astronomy and Astrophysics*, 143:84–93.

Bacon, R., Y. Copin, G. Monnet, B. W. Miller, J. R. Allington-Smith, M. Bureau, C. M. Carollo, R. L. Davies, E. Emsellem, H. Kuntschner, R. F. Peletier, E. K. Verolme, and P. T. de Zeeuw
2001. The SAURON project - I. The panoramic integral-field spectrograph. *Monthly Notices of the Royal Astronomical Society*, 326:23–35.

Bagla, J. S. and S. Ray
2003. Performance characteristics of TreePM codes. *New Astron.*, 8(7):665–677.

Balcells, M. and P. J. Quinn
1990. The formation of counterrotating cores in elliptical galaxies. *The Astrophysical Journal*, 361:381–393.

Baldry, I. K., M. L. Balogh, R. G. Bower, K. Glazebrook, R. C. Nichol, S. P. Bamford, and T. Budavari
2006. Galaxy bimodality versus stellar mass and environment. *Monthly Notices of the Royal Astronomical Society*, 373(2):469–483.

Baldry, I. K., S. P. Driver, J. Loveday, E. N. Taylor, L. S. Kelvin, J. Liske, P. Norberg, A. S. G. Robotham, S. Brough, A. M. Hopkins, S. P. Bamford, J. A. Peacock, J. Bland-Hawthorn, C. J. Conselice, S. M. Croom, D. H. Jones, H. R. Parkinson, C. C. Popescu, M. Prescott, R. G. Sharp, and R. J. Tuffs
2012. Galaxy And Mass Assembly (GAMA): the galaxy stellar mass function at z ¡ 0.06. *Monthly Notices of the Royal Astronomical Society*, 421:621–634.

Bardeen, J. M., P. J. Steinhardt, and M. S. Turner
1983. Spontaneous creation of almost scale-free density perturbations in an inflationary universe. *Physical Review D (Particles and Fields)*, 28(4):679–693.

Barnes, J. E.
1988. Encounters of disk/halo galaxies. *The Astrophysical Journal*, 331:699–717.

Barnes, J. E.
1992. Transformations of galaxies. I - Mergers of equal-mass stellar disks. *The Astrophysical Journal*, 393:484–507.

Barnes, J. E. and L. Hernquist
1996. Transformations of Galaxies. II. Gasdynamics in Merging Disk Galaxies. *The Astrophysical Journal*, 471:115.

Barnes, J. E. and L. E. Hernquist
1991. Fueling Starburst Galaxies with Gas-rich Mergers. *The Astrophysical Journal*, 370:L65.

Barrera-Ballesteros, J. K., B. García-Lorenzo, J. Falcón-Barroso, G. van de Ven, M. Lyubenova, V. Wild, J. Méndez-Abreu, S. F. Sánchez, I. Marquez, J. Masegosa, A. Monreal-Ibero, B. Ziegler, A. del Olmo, L. Verdes-Montenegro, R. García-Benito, B. Husemann, D. Mast, C. Kehrig, J. Iglesias-Paramo, R. A. Marino, J. A. L. Aguerri, C. J. Walcher, J. M. Vílchez, D. J. Bomans, C. Cortijo-Ferrero, R. M. González Delgado, J. Bland-Hawthorn, D. H. McIntosh, and S. Bekeraitė
2015. Tracing kinematic (mis)alignments in CALIFA merging galaxies. Stellar and ionized gas kinematic orientations at every merger stage. *Astronomy and Astrophysics*, 582:A21.

Beck, A. M., G. Murante, A. Arth, R. S. Remus, A. F. Teklu, J. M. F. Donnert, S. Planelles, M. C. Beck, P. Förster, M. Imgrund, K. Dolag, and S. Borgani
2016. An improved SPH scheme for cosmological simulations. *Monthly Notices of the Royal Astronomical Society*, 455(2):2110–2130.

Belfiore, F., R. Maiolino, C. Tremonti, S. F. Sánchez, K. Bundy, M. Bershady, K. Westfall, L. Lin, N. Drory, M. Boquien, D. Thomas, and J. Brinkmann
2017. SDSS IV MaNGA - metallicity and nitrogen abundance gradients in local galaxies. *Monthly Notices of the Royal Astronomical Society*, 469(1):151–170.

Bellstedt, S., D. A. Forbes, C. Foster, A. J. Romanowsky, J. P. Brodie, N. Pastorello, A. Alabi, and A. Villaume
2017. The SLUGGS survey: using extended stellar kinematics to disentangle the formation histories of low-mass S0 galaxies. *Monthly Notices of the Royal Astronomical Society*, 467(4):4540–4557.

Bender, R., S. Doebereiner, and C. Moellenhoff
1988. Isophote shapes of elliptical galaxies. I - The data. *A&AS*, 74:385–426.

Bender, R., R. P. Saglia, and O. E. Gerhard
1994. Line-of-sight velocity distributions of elliptical galaxies. *Monthly Notices of the Royal Astronomical Society*, 269:785–813.

Bender, R., P. Surma, S. Doebereiner, C. Moellenhoff, and R. Madejsky
1989. Isophote shapes of elliptical galaxies. II - Correlations with global optical, radio and X-ray properties. *Astronomy and Astrophysics*, 217:35–43.

Bendo, G. J. and J. E. Barnes
2000. The line-of-sight velocity distributions of simulated merger remnants. *Monthly Notices of the Royal Astronomical Society*, 316(2):315–325.

Binney, J.
1977. The physics of dissipational galaxy formation. *The Astrophysical Journal*, 215:483–491.

Binney, J.
2005. Rotation and anisotropy of galaxies revisited. *Monthly Notices of the Royal Astronomical Society*, 363:937–942.

Binney, J. and O. Strimpel
1978. Predicting the X-ray brightness distributions of cluster sources - 1. Estimating the potentials. *Monthly Notices of the Royal Astronomical Society*, 185:473–484.

Binney, J. and S. Tremaine
2008. *Galactic Dynamics: Second Edition.*

Blaña Díaz, M., O. Gerhard, C. Wegg, M. Portail, M. Opitsch, R. Saglia, M. Fabricius, P. Erwin, and R. Bender
2018. Sculpting Andromeda - made-to-measure models for M31's bar and composite bulge: dynamics, stellar and dark matter mass. *Monthly Notices of the Royal Astronomical Society*, 481(3):3210–3243.

Bloom, J. V., S. M. Croom, J. J. Bryant, A. L. Schaefer, J. Bland-Hawthorn, S. Brough, J. Callingham, L. Cortese, C. Federrath, N. Scott, J. van de Sande, F. D'Eugenio, S. Sweet, C. Tonini, J. T. Allen, M. Goodwin, A. W. Green, I. S. Konstantopoulos, J. Lawrence,

N. Lorente, A. M. Medling, M. S. Owers, S. N. Richards, and R. Sharp
2018. The SAMI Galaxy Survey: gas content and interaction as the drivers of kinematic asymmetry. *Monthly Notices of the Royal Astronomical Society*, 476(2):2339–2351.

Boardman, N. F., A.-M. Weijmans, R. van den Bosch, H. Kuntschner, E. Emsellem, M. Cappellari, T. de Zeeuw, J. Falcón-Barroso, D. Krajnović, R. McDermid, T. Naab, G. van de Ven, and A. Yildirim
2017. Integral-field kinematics and stellar populations of early-type galaxies out to three half-light radii. *Monthly Notices of the Royal Astronomical Society*, 471:4005–4026.

Bode, P., J. P. Ostriker, and G. Xu
2000. The Tree Particle-Mesh N-Body Gravity Solver. *Astrophysical Journal Supplement Series*, 128(2):561–569.

Bois, M., F. Bournaud, E. Emsellem, K. Alatalo, L. Blitz, M. Bureau, M. Cappellari, R. L. Davies, T. A. Davis, P. T. de Zeeuw, P.-A. Duc, S. Khochfar, D. Krajnović, H. Kuntschner, P.-Y. Lablanche, R. M. McDermid, R. Morganti, T. Naab, T. Oosterloo, M. Sarzi, N. Scott, P. Serra, A. Weijmans, and L. M. Young
2010. Formation of slowly rotating early-type galaxies via major mergers: a resolution study. *Monthly Notices of the Royal Astronomical Society*, 406:2405–2420.

Bois, M., E. Emsellem, F. Bournaud, K. Alatalo, L. Blitz, M. Bureau, M. Cappellari, R. L. Davies, T. A. Davis, P. T. de Zeeuw, P.-A. Duc, S. Khochfar, D. Krajnović, H. Kuntschner, P.-Y. Lablanche, R. M. McDermid, R. Morganti, T. Naab, T. Oosterloo, M. Sarzi, N. Scott, P. Serra, A.-M. Weijmans, and L. M. Young
2011. The ATLAS^{3D} project - VI. Simulations of binary galaxy mergers and the link with fast rotators, slow rotators and kinematically distinct cores. *Monthly Notices of the Royal Astronomical Society*, 416:1654–1679.

Bondi, H.
1952. On spherically symmetrical accretion. *Monthly Notices of the Royal Astronomical Society*, 112:195.

Bondi, H. and F. Hoyle
1944. On the mechanism of accretion by stars. *Monthly Notices of the Royal Astronomical Society*, 104:273.

Borgani, S., K. Dolag, G. Murante, L. M. Cheng, V. Springel, A. Diaferio, L. Moscardini, G. Tormen, L. Tornatore, and P. Tozzi
2006. Hot and cooled baryons in smoothed particle hydrodynamic simulations of galaxy clusters: physics and numerics. *Monthly Notices of the Royal Astronomical Society*, 367(4):1641–1654.

Bournaud, F., C. J. Jog, and F. Combes
2005. Galaxy mergers with various mass ratios: Properties of remnants. *Astronomy and Astrophysics*, 437:69–85.

Bournaud, F., C. J. Jog, and F. Combes
2007. Multiple minor mergers: formation of elliptical galaxies and constraints for the growth of spiral disks. *Astronomy and Astrophysics*, 476:1179–1190.

Boylan-Kolchin, M., V. Springel, S. D. M. White, A. Jenkins, and G. Lemson
2009. Resolving cosmic structure formation with the Millennium-II Simulation. *Monthly Notices of the Royal Astronomical Society*, 398(3):1150–1164.

Brammer, G. B., K. E. Whitaker, P. G. van Dokkum, D. Marchesini, M. Franx, M. Kriek, I. Labbé, K. S. Lee, A. Muzzin, R. F. Quadri, G. Rudnick, and R. Williams
2011. The Number Density and Mass Density of Star-forming and Quiescent Galaxies at 0.4 ¡= z ¡= 2.2. *The Astrophysical Journal*, 739(1):24.

Brodie, J. P., A. J. Romanowsky, J. Strader, D. A. Forbes, C. Foster, Z. G. Jennings, N. Pastorello, V. Pota, C. Usher, C. Blom, J. Kader, J. C. Roediger, L. R. Spitler, A. Villaume, J. A. Arnold, S. S. Kartha, and K. A. Woodley
2014. The SAGES Legacy Unifying Globulars and GalaxieS Survey (SLUGGS): Sample Definition, Methods, and Initial Results. *The Astrophysical Journal*, 796:52.

Brough, S., J. van de Sande, M. S. Owers, F. d'Eugenio, R. Sharp, L. Cortese, N. Scott, S. M. Croom, R. Bassett, K. Bekki, J. Bland-Hawthorn, J. J. Bryant, R. Davies, M. J. Drinkwater, S. P. Driver, C. Foster, G. Goldstein, Á. R. López-Sánchez, A. M. Medling, S. M. Sweet, D. S. Taranu, C. Tonini, S. K. Yi, M. Goodwin, J. S. Lawrence, and S. N. Richards
2017. The SAMI Galaxy Survey: Mass as the Driver of the Kinematic Morphology-Density Relation in Clusters. *The Astrophysical Journal*, 844:59.

Bryant, J. J., S. M. Croom, J. van de Sande, N. Scott, L. M. R. Fogarty, J. Bland-Hawthorn, J. V. Bloom, E. N. Taylor, S. Brough, A. Robotham, L. Cortese, W. Couch, M. S. Owers, A. M. Medling, C. Federrath, K. Bekki, S. N. Richards, J. S. Lawrence, and I. S. Konstantopoulos
2019. The SAMI Galaxy Survey: stellar and gas misalignments and the origin of gas in nearby galaxies. *Monthly Notices of the Royal Astronomical Society*, 483(1):458–479.

Bundy, K., M. A. Bershady, D. R. Law, R. Yan, N. Drory, N. MacDonald, D. A. Wake, B. Cherinka, J. R. Sánchez-Gallego, A.-M. Weijmans, D. Thomas, C. Tremonti, K. Masters, L. Coccato, A. M. Diamond-Stanic, A. Aragón-Salamanca, V. Avila-Reese, C. Badenes, J. Falcón-Barroso, F. Belfiore, D. Bizyaev, G. A. Blanc, J. Bland-Hawthorn, M. R. Blanton, J. R. Brownstein, N. Byler, M. Cappellari, C. Conroy, A. A. Dutton, E. Emsellem, J. Etherington, P. M. Frinchaboy, H. Fu, J. E. Gunn, P. Harding, E. J. Johnston, G. Kauffmann, K. Kinemuchi, M. A. Klaene, J. H. Knapen, A. Leauthaud, C. Li, L. Lin, R. Maiolino, V. Malanushenko, E. Malanushenko, S. Mao, C. Maraston, R. M. McDermid, M. R. Merrifield, R. C. Nichol, D. Oravetz, K. Pan, J. K. Parejko, S. F. Sanchez, D. Schlegel, A. Simmons, O. Steele, M. Steinmetz, K. Thanjavur, B. A. Thompson, J. L. Tinker, R. C. E. van den Bosch, K. B. Westfall, D. Wilkinson, S. Wright, T. Xiao, and K. Zhang
2015. Overview of the SDSS-IV MaNGA Survey: Mapping nearby Galaxies at Apache Point Observatory. *The Astrophysical Journal*, 798(1):7.

Bureau, M. and E. Athanassoula
2005. Bar Diagnostics in Edge-On Spiral Galaxies. III. N-Body Simulations of Disks. *The Astrophysical Journal*, 626(1):159–173.

Burkert, A. and T. Naab
2003. Major Mergers and the Origin of Elliptical Galaxies. In *Galaxies and Chaos*, G. Contopoulos and N. Voglis, eds., volume 626 of *Lecture Notes in Physics, Berlin Springer Verlag*, Pp. 327–339.

Capaccioli, M., G. Piotto, and R. Rampazzo
1988. Photographic and CCD Surface Photometry of Nine Early-Type Galaxies. *Astronomical Journal*, 96:487.

Cappellari, M.
2008. Measuring the inclination and mass-to-light ratio of axisymmetric galaxies via anisotropic Jeans models of stellar kinematics. *Monthly Notices of the Royal Astronomical Society*, 390(1):71–86.

Cappellari, M.
2012. Anisotropic Jeans models of stellar kinematics: second moments including proper motions and radial velocities. *arXiv e-prints*, P. arXiv:1211.7009.

Cappellari, M.
2016. Structure and Kinematics of Early-Type Galaxies from Integral Field Spectroscopy. *Annual review of astronomy and Astrophysics*, 54:597–665.

Cappellari, M. and Y. Copin
2003. Adaptive spatial binning of integral-field spectroscopic data using Voronoi tessellations. *Monthly Notices of the Royal Astronomical Society*, 342:345–354.

Cappellari, M., E. Emsellem, R. Bacon, M. Bureau, R. L. Davies, P. T. de Zeeuw, J. Falcón-Barroso, D. Krajnović, H. Kuntschner, R. M. McDermid, R. F. Peletier, M. Sarzi, R. C. E. van den Bosch, and G. van de Ven
2007. The SAURON project - X. The orbital anisotropy of elliptical and lenticular galaxies: revisiting the (V/σ, ϵ) diagram with integral-field stellar kinematics. *Monthly Notices of the Royal Astronomical Society*, 379:418–444.

Cappellari, M., E. Emsellem, D. Krajnović, R. M. McDermid, N. Scott, G. A. Verdoes Kleijn, L. M. Young, K. Alatalo, R. Bacon, L. Blitz, M. Bois, F. Bournaud, M. Bureau, R. L. Davies, T. A. Davis, P. T. de Zeeuw, P.-A. Duc, S. Khochfar, H. Kuntschner, P.-Y. Lablanche, R. Morganti, T. Naab, T. Oosterloo, M. Sarzi, P. Serra, and A.-M. Weijmans
2011a. The ATLAS^{3D} project - I. A volume-limited sample of 260 nearby early-type galaxies: science goals and selection criteria. *Monthly Notices of the Royal Astronomical Society*, 413:813–836.

Cappellari, M., E. Emsellem, D. Krajnović, R. M. McDermid, P. Serra, K. Alatalo, L. Blitz, M. Bois, F. Bournaud, M. Bureau, R. L. Davies, T. A. Davis, P. T. de Zeeuw, S. Khochfar, H. Kuntschner, P.-Y. Lablanche, R. Morganti, T. Naab, T. Oosterloo, M. Sarzi, N. Scott, A.-M. Weijmans, and L. M. Young
2011b. The ATLAS^{3D} project - VII. A new look at the morphology of nearby galaxies: the kinematic morphology-density relation. *Monthly Notices of the Royal Astronomical Society*, 416(3):1680–1696.

Cappellari, M., R. M. McDermid, K. Alatalo, L. Blitz, M. Bois, F. Bournaud, M. Bureau, A. F. Crocker, R. L. Davies, T. A. Davis, P. T. de Zeeuw, P.-A. Duc, E. Emsellem, S. Khochfar, D. Krajnović, H. Kuntschner, R. Morganti, T. Naab, T. Oosterloo, M. Sarzi, N. Scott, P. Serra, A.-M. Weijmans, and L. M. Young
2013a. The ATLAS^{3D} project - XX. Mass-size and mass-σ distributions of early-type galaxies: bulge fraction drives kinematics, mass-to-light ratio, molecular gas fraction and stellar initial mass function. *Monthly Notices of the Royal Astronomical Society*, 432:1862–1893.

Cappellari, M., N. Scott, K. Alatalo, L. Blitz, M. Bois, F. Bournaud, M. Bureau, A. F. Crocker, R. L. Davies, T. A. Davis, P. T. de Zeeuw, P.-A. Duc, E. Emsellem, S. Khochfar, D. Krajnović, H. Kuntschner, R. M. McDermid, R. Morganti, T. Naab, T. Oosterloo, M. Sarzi, P. Serra, A.-M. Weijmans, and L. M. Young
2013b. The ATLAS^{3D} project - XV. Benchmark for early-type galaxies scaling relations from 260 dynamical models: mass-to-light ratio, dark matter, Fundamental Plane and Mass Plane. *Monthly Notices of the Royal Astronomical Society*, 432:1709–1741.

Chabrier, G.
2003. Galactic Stellar and Substellar Initial Mass Function. *The Publications of the Astronomical Society of the Pacific*, 115(809):763–795.

Chandrasekhar, S.
1943. Dynamical Friction. I. General Considerations: the Coefficient of Dynamical Friction. *The Astrophysical Journal*, 97:255.

Choi, H. and S. Yi
2017a. On the evolution of galaxy spin in a cosmological hydrodynamic simulation of galaxy clusters. *ArXiv e-prints*.

Choi, H. and S. K. Yi
2017b. On the Evolution of Galaxy Spin in a Cosmological Hydrodynamic Simulation of Galaxy Clusters. *The Astrophysical Journal*, 837:68.

Choi, H., S. K. Yi, Y. Dubois, T. Kimm, J. E. G. Devriendt, and C. Pichon
2018. Early-type Galaxy Spin Evolution in the Horizon-AGN Simulation. *The Astrophysical Journal*, 856:114.

Chung, A. and M. Bureau
2004. Stellar Kinematics of Boxy Bulges: Large-Scale Bars and Inner Disks. *Astronomical Journal*, 127(6):3192–3212.

Ciotti, L. and G. Bertin
1999. Analytical properties of the $R^{1/m}$ law. *Astronomy and Astrophysics*, 352:447–451.

Clauwens, B., J. Schaye, M. Franx, and R. G. Bower
2018. The three phases of galaxy formation. *Monthly Notices of the Royal Astronomical Society*, 478(3):3994–4009.

Coccato, L., O. Gerhard, M. Arnaboldi, P. Das, N. G. Douglas, K. Kuijken, M. R. Merrifield, N. R. Napolitano, E. Noordermeer, A. J. Romanowsky, M. Capaccioli, A. Cortesi, F. De

Lorenzi, and K. C. Freeman
2009. Kinematic properties of early-type galaxy haloes using planetary nebulae*. *Monthly Notices of the Royal Astronomical Society*, 394:1249–1283.

Cooper, A. P., S. Cole, C. S. Frenk, S. D. M. White, J. Helly, A. J. Benson, G. De Lucia, A. Helmi, A. Jenkins, J. F. Navarro, V. Springel, and J. Wang
2010. Galactic stellar haloes in the CDM model. *Monthly Notices of the Royal Astronomical Society*, 406(2):744–766.

Cooper, A. P., R. D'Souza, G. Kauffmann, J. Wang, M. Boylan-Kolchin, Q. Guo, C. S. Frenk, and S. D. M. White
2013. Galactic accretion and the outer structure of galaxies in the CDM model. *Monthly Notices of the Royal Astronomical Society*, 434:3348–3367.

Cortese, L., L. M. R. Fogarty, K. Bekki, J. van de Sande, W. Couch, B. Catinella, M. Colless, D. Obreschkow, D. Taranu, E. Tescari, D. Barat, J. Bland-Hawthorn, J. Bloom, J. J. Bryant, M. Cluver, S. M. Croom, M. J. Drinkwater, F. d'Eugenio, I. S. Konstantopoulos, A. Lopez-Sanchez, S. Mahajan, N. Scott, C. Tonini, O. I. Wong, J. T. Allen, S. Brough, M. Goodwin, A. W. Green, I.-T. Ho, L. S. Kelvin, J. S. Lawrence, N. P. F. Lorente, A. M. Medling, M. S. Owers, S. Richards, R. Sharp, and S. M. Sweet
2016. The SAMI Galaxy Survey: the link between angular momentum and optical morphology. *Monthly Notices of the Royal Astronomical Society*, 463:170–184.

Cox, T. J., S. N. Dutta, T. Di Matteo, L. Hernquist, P. F. Hopkins, B. Robertson, and V. Springel
2006. The Kinematic Structure of Merger Remnants. *The Astrophysical Journal*, 650:791–811.

Croom, S. M., J. S. Lawrence, J. Bland-Hawthorn, J. J. Bryant, L. Fogarty, S. Richards, M. Goodwin, T. Farrell, S. Miziarski, R. Heald, D. H. Jones, S. Lee, M. Colless, S. Brough, A. M. Hopkins, A. E. Bauer, M. N. Birchall, S. Ellis, A. Horton, S. Leon-Saval, G. Lewis, Á. R. López-Sánchez, S.-S. Min, C. Trinh, and H. Trowland
2012. The Sydney-AAO Multi-object Integral field spectrograph. *Monthly Notices of the Royal Astronomical Society*, 421:872–893.

Cui, W., A. Knebe, G. Yepes, F. Pearce, C. Power, R. Dave, A. e. Arth, S. Borgani, K. Dolag, P. Elahi, R. Mostoghiu, G. Murante, E. Rasia, D. Stoppacher, J. Vega-Ferrero, Y. Wang, X. Yang, A. Benson, S. A. Cora, D. J. Croton, M. Sinha, A. R. H. Stevens, C. A. Vega-Martínez, J. Arthur, A. S. Baldi, R. Cañas, G. Cialone, D. Cunnama, M. De Petris, G. Durando, S. Ettori, S. Gottlöber, S. E. Nuza, L. J. Old, S. Pilipenko, J. G. Sorce, and C. Welker
2018. The Three Hundred project: a large catalogue of theoretically modelled galaxy clusters for cosmological and astrophysical applications. *Monthly Notices of the Royal Astronomical Society*, 480(3):2898–2915.

Davé, R., R. Thompson, and P. F. Hopkins
2016. MUFASA: galaxy formation simulations with meshless hydrodynamics. *Monthly Notices of the Royal Astronomical Society*, 462(3):3265–3284.

Davies, R. L., H. Kuntschner, E. Emsellem, R. Bacon, M. Bureau, C. M. Carollo, Y. Copin, B. W. Miller, G. Monnet, R. F. Peletier, E. K. Verolme, and P. T. de Zeeuw
2001. Galaxy Mapping with the SAURON Integral-Field Spectrograph: The Star Formation History of NGC 4365. *The Astrophysical Journal*, 548:L33–L36.

Davis, M., G. Efstathiou, C. S. Frenk, and S. D. M. White
1985. The evolution of large-scale structure in a universe dominated by cold dark matter. *The Astrophysical Journal*, 292:371–394.

Davis, T. A., K. Alatalo, M. Sarzi, M. Bureau, L. M. Young, L. Blitz, P. Serra, A. F. Crocker, D. Krajnović, R. M. McDermid, M. Bois, F. Bournaud, M. Cappellari, R. L. Davies, P.-A. Duc, P. T. de Zeeuw, E. Emsellem, S. Khochfar, H. Kuntschner, P.-Y. Lablanche, R. Morganti, T. Naab, T. Oosterloo, N. Scott, and A.-M. Weijmans
2011. The ATLAS^{3D} project - X. On the origin of the molecular and ionized gas in early-type galaxies. *Monthly Notices of the Royal Astronomical Society*, 417(2):882–899.

Davis, T. A., K. Rowlands, J. R. Allison, S. S. Shabala, Y.-S. Ting, C. d. P. Lagos, S. Kaviraj, N. Bourne, L. Dunne, S. Eales, R. J. Ivison, S. Maddox, D. J. B. Smith, M. W. L. Smith, and P. Temi
2015. Molecular and atomic gas in dust lane early-type galaxies - I. Low star formation efficiencies in minor merger remnants. *Monthly Notices of the Royal Astronomical Society*, 449:3503–3516.

Davison, T. A., H. Kuntschner, B. Husemann, M. A. Norris, J. J. Dalcanton, A. De Rosa, P.-A. Duc, S. Bianchi, P. R. Capelo, and C. Vignali
2021. Old and New Major Mergers in the SOSIMPLE galaxy, NGC 7135. *arXiv e-prints*, P. arXiv:2101.07072.

de Bernardis, P., P. A. R. Ade, J. J. Bock, J. R. Bond, J. Borrill, A. Boscaleri, K. Coble, B. P. Crill, G. De Gasperis, P. C. Farese, P. G. Ferreira, K. Ganga, M. Giacometti, E. Hivon, V. V. Hristov, A. Iacoangeli, A. H. Jaffe, A. E. Lange, L. Martinis, S. Masi, P. V. Mason, P. D. Mauskopf, A. Melchiorri, L. Miglio, T. Montroy, C. B. Netterfield, E. Pascale, F. Piacentini, D. Pogosyan, S. Prunet, S. Rao, G. Romeo, J. E. Ruhl, F. Scaramuzzi, D. Sforna, and N. Vittorio
2000. A flat Universe from high-resolution maps of the cosmic microwave background radiation. *Nature*, 404(6781):955–959.

De Lucia, G. and J. Blaizot
2007. The hierarchical formation of the brightest cluster galaxies. *Monthly Notices of the Royal Astronomical Society*, 375(1):2–14.

de Vaucouleurs, G.
1948. Recherches sur les nébuleuses extragalactiques. *Journal des Observateurs*, 31:113.

de Vaucouleurs, G.
1959. General Physical Properties of External Galaxies. *Handbuch der Physik*, 53:311.

de Vaucouleurs, G.
1963. Revised Classification of 1500 Bright Galaxies. *Astrophysical Journal Supplement Series*, 8:31.

de Vaucouleurs, G., A. de Vaucouleurs, H. G. Corwin, Jr., R. J. Buta, G. Paturel, and P. Fouqué
1991. *Third Reference Catalogue of Bright Galaxies. Volume I: Explanations and references. Volume II: Data for galaxies between 0^h and 12^h. Volume III: Data for galaxies between 12^h and 24^h.*

de Vaucouleurs, G., A. de Vaucouleurs, and J. R. Corwin
1976. Second reference catalogue of bright galaxies. In *Second reference catalogue of bright galaxies, Vol. 1976, p. Austin: University of Texas Press.*, volume 1976.

de Zeeuw, P. T., M. Bureau, E. Emsellem, R. Bacon, C. M. Carollo, Y. Copin, R. L. Davies, H. Kuntschner, B. W. Miller, G. Monnet, R. F. Peletier, and E. K. Verolme
2002. The SAURON project - II. Sample and early results. *Monthly Notices of the Royal Astronomical Society*, 329:513–530.

Dehnen, W. and H. Aly
2012. Improving convergence in smoothed particle hydrodynamics simulations without pairing instability. *Monthly Notices of the Royal Astronomical Society*, 425(2):1068–1082.

Dekel, A., Y. Birnboim, G. Engel, J. Freundlich, T. Goerdt, M. Mumcuoglu, E. Neistein, C. Pichon, R. Teyssier, and E. Zinger
2009. Cold streams in early massive hot haloes as the main mode of galaxy formation. *Nature*, 457:451–454.

D'Eugenio, F., R. C. W. Houghton, R. L. Davies, and E. Dalla Bontà
2013. Fast and slow rotators in the densest environments: a FLAMES/GIRAFFE integral field spectroscopy study of galaxies in A1689 at z = 0.183. *Monthly Notices of the Royal Astronomical Society*, 429(2):1258–1266.

Di Matteo, T., V. Springel, and L. Hernquist
2005. Energy input from quasars regulates the growth and activity of black holes and their host galaxies. *Nature*, 433(7026):604–607.

Dicke, R. H. and P. J. E. Peebles
1979. The big bang cosmology - enigmas and nostrums. In *General Relativity: An Einstein centenary survey*, S. W. Hawking and W. Israel, eds., Pp. 504–517.

Dicke, R. H., P. J. E. Peebles, P. G. Roll, and D. T. Wilkinson
1965. Cosmic Black-Body Radiation. *The Astrophysical Journal*, 142:414–419.

Dolag, K., S. Borgani, G. Murante, and V. Springel
2009. Substructures in hydrodynamical cluster simulations. *Monthly Notices of the Royal Astronomical Society*, 399:497–514.

Dolag, K., S. Borgani, S. Schindler, A. Diaferio, and A. M. Bykov
2008. Simulation Techniques for Cosmological Simulations. *Space Science Reviews*, 134(1-4):229–268.

Dolag, K., M. Jubelgas, V. Springel, S. Borgani, and E. Rasia
2004. Thermal Conduction in Simulated Galaxy Clusters. *The Astrophysical Journal*, 606(2):L97–L100.

Dolag, K., E. Komatsu, and R. Sunyaev
2016. SZ effects in the Magneticum Pathfinder simulation: comparison with the Planck, SPT, and ACT results. *Monthly Notices of the Royal Astronomical Society*, 463(2):1797–1811.

Dolag, K., F. Vazza, G. Brunetti, and G. Tormen
2005. Turbulent gas motions in galaxy cluster simulations: the role of smoothed particle hydrodynamics viscosity. *Monthly Notices of the Royal Astronomical Society*, 364:753–772.

Doroshkevich, A. G.
1970. Spatial structure of perturbations and origin of galactic rotation in fluctuation theory. *Astrophysics*, 6(4):320–330.

Dressler, A.
1980. Galaxy morphology in rich clusters: implications for the formation and evolution of galaxies. *The Astrophysical Journal*, 236:351–365.

Drory, N., N. MacDonald, M. A. Bershady, K. Bundy, J. Gunn, D. R. Law, M. Smith, R. Stoll, C. A. Tremonti, D. A. Wake, R. Yan, A. M. Weijmans, N. Byler, B. Cherinka, F. Cope, A. Eigenbrot, P. Harding, D. Holder, J. Huehnerhoff, K. Jaehnig, T. C. Jansen, M. Klaene, A. M. Paat, J. Percival, and C. Sayres
2015. The MaNGA Integral Field Unit Fiber Feed System for the Sloan 2.5 m Telescope. *Astronomical Journal*, 149:77.

D'Souza, R., G. Kauffman, J. Wang, and S. Vegetti
2014. Parametrizing the stellar haloes of galaxies. *Monthly Notices of the Royal Astronomical Society*, 443:1433–1450.

Du, M., V. P. Debattista, J. Shen, and M. Cappellari
2016. Kinematic Properties of Double-barred Galaxies: Simulations versus Integral-field Observations. *The Astrophysical Journal*, 828(1):14.

Dubois, Y., C. Pichon, C. Welker, D. Le Borgne, J. Devriendt, C. Laigle, S. Codis, D. Pogosyan, S. Arnouts, K. Benabed, E. Bertin, J. Blaizot, F. Bouchet, J. F. Cardoso, S. Colombi, V. de Lapparent, V. Desjacques, R. Gavazzi, S. Kassin, T. Kimm, H. McCracken, B. Milliard, S. Peirani, S. Prunet, S. Rouberol, J. Silk, A. Slyz, T. Sousbie, R. Teyssier, L. Tresse, M. Treyer, D. Vibert, and M. Volonteri
2014. Dancing in the dark: galactic properties trace spin swings along the cosmic web. *Monthly Notices of the Royal Astronomical Society*, 444(2):1453–1468.

Ebrová, I. and E. L. Łokas
2015. The Origin of Prolate Rotation in Dwarf Spheroidal Galaxies Formed by Mergers of Disky Dwarfs. *The Astrophysical Journal*, 813:10.

Ebrová, I. and E. L. Łokas
2017. Galaxies with Prolate Rotation in Illustris. *The Astrophysical Journal*, 850:144.

Ebrová, I., E. L. Łokas, and J. Eliášek
2020. Galaxies with kinematically distinct cores in Illustris. *arXiv e-prints*, P. arXiv:2010.02222.

Efstathiou, G., W. J. Sutherland, and S. J. Maddox
1990. The cosmological constant and cold dark matter. *Nature*, 348(6303):705–707.

Einasto, J., E. Saar, A. Kaasik, and A. D. Chernin
1974. Missing mass around galaxies - Morphological evidence. *Nature*, 252:111–113.

Einstein, A.
1915. Zur allgemeinen Relativitätstheorie. *Sitzungsberichte der Königlich Preußischen Akademie der Wissenschaften (Berlin), Seite 778-786.*, Pp. 778–786.

El-Badry, K., A. Wetzel, M. Geha, P. F. Hopkins, D. Kereš, T. K. Chan, and C.-A. Faucher-Giguère
2016. Breathing FIRE: How Stellar Feedback Drives Radial Migration, Rapid Size Fluctuations, and Population Gradients in Low-mass Galaxies. *The Astrophysical Journal*, 820:131.

Emsellem, E., M. Cappellari, D. Krajnović, K. Alatalo, L. Blitz, M. Bois, F. Bournaud, M. Bureau, R. L. Davies, T. A. Davis, P. T. de Zeeuw, S. Khochfar, H. Kuntschner, P.-Y. Lablanche, R. M. McDermid, R. Morganti, T. Naab, T. Oosterloo, M. Sarzi, N. Scott, P. Serra, G. van de Ven, A.-M. Weijmans, and L. M. Young
2011. The ATLAS^{3D} project - III. A census of the stellar angular momentum within the effective radius of early-type galaxies: unveiling the distribution of fast and slow rotators. *Monthly Notices of the Royal Astronomical Society*, 414:888–912.

Emsellem, E., M. Cappellari, D. Krajnović, G. van de Ven, R. Bacon, M. Bureau, R. L. Davies, P. T. de Zeeuw, J. Falcón-Barroso, H. Kuntschner, R. McDermid, R. F. Peletier, and M. Sarzi
2007. The SAURON project - IX. A kinematic classification for early-type galaxies. *Monthly Notices of the Royal Astronomical Society*, 379:401–417.

Emsellem, E., M. Cappellari, R. F. Peletier, R. M. McDermid, R. Bacon, M. Bureau, Y. Copin, R. L. Davies, D. Krajnović, H. Kuntschner, B. W. Miller, and P. T. de Zeeuw
2004. The SAURON project - III. Integral-field absorption-line kinematics of 48 elliptical and lenticular galaxies. *Monthly Notices of the Royal Astronomical Society*, 352:721–743.

Emsellem, E., D. Krajnovic, and M. Sarzi
2014. A kinematically distinct core and minor-axis rotation: the MUSE perspective on M87. *Monthly Notices of the Royal Astronomical Society*, 445:L79–L83.

Faber, S. M. and R. E. Jackson
1976. Velocity dispersions and mass-to-light ratios for elliptical galaxies. *The Astrophysical Journal*, 204:668–683.

Faber, S. M., S. Tremaine, E. A. Ajhar, Y.-I. Byun, A. Dressler, K. Gebhardt, C. Grillmair, J. Kormendy, T. R. Lauer, and D. Richstone
1997. The Centers of Early-Type Galaxies with HST. IV. Central Parameter Relations. *Astronomical Journal*, 114:1771.

Fabjan, D., S. Borgani, L. Tornatore, A. Saro, G. Murante, and K. Dolag
2010. Simulating the effect of active galactic nuclei feedback on the metal enrichment of galaxy clusters. *Monthly Notices of the Royal Astronomical Society*, 401:1670–1690.

Fabricius, M. H., R. P. Saglia, D. B. Fisher, N. Drory, R. Bender, and U. Hopp
2012. Kinematic Signatures of Bulges Correlate with Bulge Morphologies and Sérsic Index. *The Astrophysical Journal*, 754(1):67.

Falcón-Barroso, J., M. Lyubenova, and G. van de Ven
2015. Angular Momentum across the Hubble sequence from the CALIFA survey. In *Galaxy Masses as Constraints of Formation Models*, M. Cappellari and S. Courteau, eds., volume 311 of *IAU Symposium*, Pp. 78–81.

Falcón-Barroso, J., G. van de Ven, M. Lyubenova, J. Méndez-Abreu, J. A. L. Aguerri, B. García-Lorenzo, S. Bekeraité, S. F. Sánchez, B. Husemann, R. García-Benito, R. M. González Delgado, D. Mast, C. J. Walcher, S. Zibetti, L. Zhu, J. K. Barrera-Ballesteros, L. Galbany, P. Sánchez-Blázquez, R. Singh, R. C. E. den van Bosch, V. Wild, J. Bland-Hawthorn, R. Cid Fernandes, A. de Lorenzo-Cáceres, A. Gallazzi, R. A. Marino, I. Márquez, R. F. Peletier, E. Pérez, I. Pérez, M. M. Roth, F. F. Rosales-Ortega, T. Ruiz-Lara, L. Wisotzki, and B. Ziegler
2019a. The CALIFA view on stellar angular momentum across the Hubble sequence. *arXiv e-prints*, P. arXiv:1910.06236.

Falcón-Barroso, J., G. van de Ven, M. Lyubenova, J. Mendez-Abreu, J. A. L. Aguerri, B. García-Lorenzo, S. Bekeraité, S. F. Sánchez, B. Husemann, R. García-Benito, R. M. González Delgado, D. Mast, C. J. Walcher, S. Zibetti, L. Zhu, J. K. Barrera-Ballesteros, L. Galbany, P. Sánchez-Blázquez, R. Singh, R. C. E. van den Bosch, V. Wild, J. Bland-Hawthorn, R. Cid Fernandes, A. de Lorenzo-Cáceres, A. Gallazzi, R. A. Marino, I. Márquez, R. F. Peletier, E. Pérez, I. Pérez, M. M. Roth, F. F. Rosales-Ortega, T. Ruiz-Lara, L. Wisotzki, and B. Ziegler
2019b. The CALIFA view on stellar angular momentum across the Hubble sequence. *Astronomy and Astrophysics*, 632:A59.

Fall, S. M.
1983. Galaxy formation - Some comparisons between theory and observation. In *Internal Kinematics and Dynamics of Galaxies*, E. Athanassoula, ed., volume 100 of *IAU Symposium*, Pp. 391–398.

Fall, S. M. and G. Efstathiou
1980. Formation and rotation of disc galaxies with haloes. *Monthly Notices of the Royal Astronomical Society*, 193:189–206.

Fall, S. M. and A. J. Romanowsky
2013. Angular Momentum and Galaxy Formation Revisited: Effects of Variable Mass-to-light Ratios. *The Astrophysical Journal*, 769(2):L26.

Fall, S. M. and A. J. Romanowsky
2018. Angular Momentum and Galaxy Formation Revisited: Scaling Relations for Disks and Bulges. *The Astrophysical Journal*, 868(2):133.

Feng, S., S.-Y. Shen, F.-T. Yuan, R. A. Riffel, and K. Pan
2020. SDSS-IV MaNGA: Kinematic Asymmetry as an Indicator of Galaxy Interaction in Paired Galaxies. *The Astrophysical Journal*, 892(2):L20.

Ferland, G. J., K. T. Korista, D. A. Verner, J. W. Ferguson, J. B. Kingdon, and E. M. Verner
1998. CLOUDY 90: Numerical Simulation of Plasmas and Their Spectra. *The Publications of the Astronomical Society of the Pacific*, 110(749):761–778.

Ferré-Mateu, A., D. A. Forbes, R. M. McDermid, A. J. Romanowsky, and J. P. Brodie
2019. Spatially Resolved Stellar Populations and Kinematics with KCWI: Probing the Assembly History of the Massive Early-type Galaxy NGC1407. *The Astrophysical Journal*, 878:129.

Fogarty, L. M. R., N. Scott, M. S. Owers, S. Brough, S. M. Croom, M. B. Pracy, R. C. W. Houghton, J. Bland-Hawthorn, M. Colless, R. L. Davies, D. H. Jones, J. T. Allen, J. J. Bryant, M. Goodwin, A. W. Green, I. S. Konstantopoulos, J. S. Lawrence, S. Richards, L. Cortese, and R. Sharp
2014. The SAMI Pilot Survey: the kinematic morphology-density relation in Abell 85, Abell 168 and Abell 2399. *Monthly Notices of the Royal Astronomical Society*, 443(1):485–503.

Fogarty, L. M. R., N. Scott, M. S. Owers, S. M. Croom, K. Bekki, R. C. W. Houghton, J. van de Sande, F. D'Eugenio, G. N. Cecil, M. M. Colless, J. Bland-Hawthorn, S. Brough, L. Cortese, R. L. Davies, D. H. Jones, M. Pracy, J. T. Allen, J. J. Bryant, M. Goodwin, A. W. Green, I. S. Konstantopoulos, J. S. Lawrence, N. P. F. Lorente, S. Richards, and R. G. Sharp
2015. The SAMI Pilot Survey: stellar kinematics of galaxies in Abell 85, 168 and 2399. *Monthly Notices of the Royal Astronomical Society*, 454:2050–2066.

Forbes, D. A. and R.-S. Remus
2018. Metallicity gradients in the globular cluster systems of early-type galaxies: in situ and accreted components? *Monthly Notices of the Royal Astronomical Society*, 479(4):4760–4769.

Forbes, D. A., A. J. Romanowsky, N. Pastorello, C. Foster, J. P. Brodie, J. Strader, C. Usher, and V. Pota
2016. The SLUGGS survey: the assembly histories of individual early-type galaxies. *Monthly Notices of the Royal Astronomical Society*, 457(2):1242–1256.

Forbes, D. A., L. Sinpetru, G. Savorgnan, A. J. Romanowsky, C. Usher, and J. Brodie
2017. The SLUGGS Survey: stellar masses and effective radii of early-type galaxies from Spitzer Space Telescope 3.6 μm imaging. *Monthly Notices of the Royal Astronomical Society*, 464:4611–4623.

Förster Schreiber, N. M., A. Renzini, C. Mancini, R. Genzel, N. Bouché, G. Cresci, E. K. S. Hicks, S. J. Lilly, Y. Peng, A. Burkert, C. M. Carollo, A. Cimatti, E. Daddi, R. I. Davies, S. Genel, J. D. Kurk, P. Lang, D. Lutz, V. Mainieri, H. J. McCracken, M. Mignoli, T. Naab, P. Oesch, L. Pozzetti, M. Scodeggio, K. Shapiro Griffin, A. E. Shapley, A. Sternberg, S. Tacchella, L. J. Tacconi, S. Wuyts, and G. Zamorani
2018. The SINS/zC-SINF Survey of z $\sim$ 2 Galaxy Kinematics: SINFONI Adaptive Optics-assisted Data and Kiloparsec-scale Emission-line Properties. *Astrophysical Journal Supplement Series*, 238(2):21.

Foster, C., J. T. Mendel, C. D. P. Lagos, E. Wisnioski, T. Yuan, F. D'Eugenio, T. M. Barone, K. E. Harborne, S. P. Vaughan, F. Schulze, R. S. Remus, A. Gupta, F. Collacchioni, D. J.

Khim, P. Taylor, R. Bassett, S. M. Croom, R. M. McDermid, A. Poci, A. J. Battisti, J. Bland-Hawthorn, S. Bellstedt, M. Colless, L. J. M. Davies, S. Driver, A. Ferré-Mateu, D. B. Fisher, E. Gjergo, E. J. Johnston, A. Khalid, C. Kobayashi, S. Oh, Y. Peng, A. S. G. Robotham, S. M. Sweet, E. N. Taylor, K. V. H. Tran, J. W. Trayford, J. van de Sande, S. K. Yi, and L. Zanisi
2020. The MAGPI Survey – science goals, design, observing strategy, early results and theoretical framework. *arXiv e-prints*, P. arXiv:2011.13567.

Foster, C., N. Pastorello, J. Roediger, J. P. Brodie, D. A. Forbes, S. S. Kartha, V. Pota, A. J. Romanowsky, L. R. Spitler, J. Strader, C. Usher, and J. A. Arnold
2016. The SLUGGS Survey: stellar kinematics, kinemetry and trends at large radii in 25 early-type galaxies. *Monthly Notices of the Royal Astronomical Society*, 457:147–171.

Foster, C., J. van de Sande, L. Cortese, S. M. Croom, J. Bland-Hawthorn, S. Brough, J. J. Bryant, M. Goodwin, J. S. Lawrence, N. Lorente, A. M. Medling, M. Owers, S. N. Richards, and N. Scott
2018. The SAMI Galaxy Survey: embedded discs and radial trends in outer dynamical support across the Hubble sequence. *Monthly Notices of the Royal Astronomical Society*, 480:3105–3116.

Freeman, K. C.
1970. On the Disks of Spiral and S0 Galaxies. *The Astrophysical Journal*, 160:811.

Friedmann, A.
1922. Über die Krümmung des Raumes. *Zeitschrift fur Physik*, 10:377–386.

Frigo, M., T. Naab, M. Hirschmann, E. Choi, R. S. Somerville, D. Krajnovic, R. Davé, and M. Cappellari
2019. The impact of AGN on stellar kinematics and orbits in simulated massive galaxies. *Monthly Notices of the Royal Astronomical Society*, 489(2):2702–2722.

Gallagher, John S., I. and J. P. Ostriker
1972. A Note on Mass Loss during Collisions between Galaxies and the Formation of Giant Systems. *Astronomical Journal*, 77:288.

Genel, S., S. M. Fall, L. Hernquist, M. Vogelsberger, G. F. Snyder, V. Rodriguez-Gomez, D. Sijacki, and V. Springel
2015. Galactic Angular Momentum in the Illustris Simulation: Feedback and the Hubble Sequence. *The Astrophysical Journal*, 804:L40.

Genzel, R., N. M. Förster Schreiber, H. Übler, P. Lang, T. Naab, R. Bender, L. J. Tacconi, E. Wisnioski, S. Wuyts, T. Alexander, A. Beifiori, S. Belli, G. Brammer, A. Burkert, C. M. Carollo, J. Chan, R. Davies, M. Fossati, A. Galametz, S. Genel, O. Gerhard, D. Lutz, J. T. Mendel, I. Momcheva, E. J. Nelson, A. Renzini, R. Saglia, A. Sternberg, S. Tacchella, K. Tadaki, and D. Wilman
2017. Strongly baryon-dominated disk galaxies at the peak of galaxy formation ten billion years ago. *Nature*, 543(7645):397–401.

Gerhard, O., G. Jeske, R. P. Saglia, and R. Bender
1998. Breaking the degeneracy between anisotropy and mass: the dark halo of the E0 galaxy NGC6703. *Monthly Notices of the Royal Astronomical Society*, 295(1):197–215.

Gerhard, O. E.
1981. N-body simulations of disc-halo galaxies - Isolated systems, tidal interactions and merging. *Monthly Notices of the Royal Astronomical Society*, 197:179–208.

Gerhard, O. E.
1993. Line-of-sight velocity profiles in spherical galaxies: breaking the degeneracy between anisotropy and mass. *Monthly Notices of the Royal Astronomical Society*, 265:213.

Gingold, R. A. and J. J. Monaghan
1977. Smoothed particle hydrodynamics: theory and application to non-spherical stars. *Monthly Notices of the Royal Astronomical Society*, 181:375–389.

Goto, T., C. Yamauchi, Y. Fujita, S. Okamura, M. Sekiguchi, I. Smail, M. Bernardi, and P. L. Gomez
2003. The morphology-density relation in the Sloan Digital Sky Survey. *Monthly Notices of the Royal Astronomical Society*, 346(2):601–614.

Graham, A. W., B. C. Ciambur, and G. A. D. Savorgnan
2016. Disky Elliptical Galaxies and the Allegedly Over-massive Black Hole in the Compact "ES" Galaxy NGC 1271. *The Astrophysical Journal*, 831(2):132.

Greene, J. E., A. Leauthaud, E. Emsellem, J. Ge, A. Aragón-Salamanca, J. Greco, Y.-T. Lin, S. Mao, K. Masters, M. Merrifield, S. More, N. Okabe, D. P. Schneider, D. Thomas, D. A. Wake, K. Pan, D. Bizyaev, D. Oravetz, A. Simmons, R. Yan, and F. van den Bosch
2018. SDSS-IV MaNGA: Uncovering the Angular Momentum Content of Central and Satellite Early-type Galaxies. *The Astrophysical Journal*, 852:36.

Greene, J. E., A. Leauthaud, E. Emsellem, D. Goddard, J. Ge, B. H. Andrews, J. Brinkman, J. R. Brownstein, J. Greco, D. Law, Y. T. Lin, K. L. Masters, M. Merrifield, S. More, N. Okabe, D. P. Schneider, D. Thomas, D. A. Wake, R. Yan, and N. Drory
2017. SDSS-IV MaNGA: Probing the Kinematic Morphology-Density Relation of Early-type Galaxies with MaNGA. *The Astrophysical Journal*, 851(2):L33.

Greene, J. E., M. Veale, C.-P. Ma, J. Thomas, M. E. Quenneville, J. P. Blakeslee, J. L. Walsh, A. Goulding, and J. Ito
2019. The MASSIVE Survey. XII. Connecting Stellar Populations of Early-type Galaxies to Kinematics and Environment. *The Astrophysical Journal*, 874(1):66.

Guérou, A., E. Emsellem, D. Krajnović, R. M. McDermid, T. Contini, and P. M. Weilbacher
2016. Exploring the mass assembly of the early-type disc galaxy NGC 3115 with MUSE. *Astronomy and Astrophysics*, 591:A143.

Gunn, J. E. and I. Gott, J. Richard
1972. On the Infall of Matter Into Clusters of Galaxies and Some Effects on Their Evolution. *The Astrophysical Journal*, 176:1.

Guth, A. H.
1981. Inflationary universe: A possible solution to the horizon and flatness problems. *Physical Review D (Particles and Fields)*, 23(2):347–356.

Halliday, C., R. L. Davies, H. Kuntschner, M. Birkinshaw, R. Bender, R. P. Saglia, and G. Baggley
2001. Line-of-sight velocity distributions of low-luminosity elliptical galaxies. *Monthly Notices of the Royal Astronomical Society*, 326(2):473–489.

Hanany, S., P. Ade, A. Balbi, J. Bock, J. Borrill, A. Boscaleri, P. de Bernardis, P. G. Ferreira, V. V. Hristov, A. H. Jaffe, A. E. Lange, A. T. Lee, P. D. Mauskopf, C. B. Netterfield, S. Oh, E. Pascale, B. Rabii, P. L. Richards, G. F. Smoot, R. Stompor, C. D. Winant, and J. H. P. Wu
2000. MAXIMA-1: A Measurement of the Cosmic Microwave Background Anisotropy on Angular Scales of 10'-5°. *The Astrophysical Journal*, 545(1):L5–L9.

Hawking, S. W.
1982. The development of irregularities in a single bubble inflationary universe. *Physics Letters B*, 115(4):295–297.

Hernquist, L.
1990. An analytical model for spherical galaxies and bulges. *The Astrophysical Journal*, 356:359–364.

Hernquist, L.
1992. Structure of merger remnants. I - Bulgeless progenitors. *The Astrophysical Journal*, 400:460–475.

Hernquist, L. and J. E. Barnes
1991. Origin of kinematic subsystems in elliptical galaxies. *Nature*, 354:210–212.

Hilz, M., T. Naab, J. P. Ostriker, J. Thomas, A. Burkert, and R. Jesseit
2012. Relaxation and stripping - The evolution of sizes, dispersions and dark matter fractions in major and minor mergers of elliptical galaxies. *Monthly Notices of the Royal Astronomical Society*, 425:3119–3136.

Hirschmann, M., K. Dolag, A. Saro, L. Bachmann, S. Borgani, and A. Burkert
2014. Cosmological simulations of black hole growth: AGN luminosities and downsizing. *Monthly Notices of the Royal Astronomical Society*, 442:2304–2324.

Ho, N., M. Geha, R. R. Munoz, P. Guhathakurta, J. Kalirai, K. M. Gilbert, E. Tollerud, J. Bullock, R. L. Beaton, and S. R. Majewski
2012. Stellar Kinematics of the Andromeda II Dwarf Spheroidal Galaxy. *The Astrophysical Journal*, 758:124.

Hoffman, L., T. J. Cox, S. Dutta, and L. Hernquist
2009. The Imprint of Dissipation on the Shapes of Merger Remnant LOSVDs. *The Astrophysical Journal*, 705(1):920–925.

Hoffman, L., T. J. Cox, S. Dutta, and L. Hernquist
2010. Orbital Structure of Merger Remnants. I. Effect of Gas Fraction in Pure Disk Mergers. *The Astrophysical Journal*, 723(1):818–844.

Houghton, R. C. W., R. L. Davies, F. D'Eugenio, N. Scott, N. Thatte, F. Clarke, M. Tecza, G. S. Salter, L. M. R. Fogarty, and T. Goodsall
2013. Fast and slow rotators in the densest environments: a SWIFT IFS study of the Coma cluster. *Monthly Notices of the Royal Astronomical Society*, 436(1):19–33.

Huang, S., L. C. Ho, C. Y. Peng, Z.-Y. Li, and A. J. Barth
2013. Fossil Evidence for the Two-phase Formation of Elliptical Galaxies. *The Astrophysical Journal*, 768:L28.

Hubble, E.
1929. A Relation between Distance and Radial Velocity among Extra-Galactic Nebulae. *Proceedings of the National Academy of Science*, 15(3):168–173.

Hubble, E. P.
1925. NGC 6822, a remote stellar system. *The Astrophysical Journal*, 62:409–433.

Hubble, E. P.
1926. Extragalactic nebulae. *The Astrophysical Journal*, 64:321–369.

Hubble, E. P.
1936. *Realm of the Nebulae*.

Huertas-Company, M., S. Mei, F. Shankar, L. Delaye, A. Raichoor, G. Covone, A. Finoguenov, J. P. Kneib, F. O. Le, and M. Povic
2013. The evolution of the mass-size relation for early-type galaxies from $z \sim 1$ to the present: dependence on environment, mass range and detailed morphology. *Monthly Notices of the Royal Astronomical Society*, 428:1715–1742.

Iannuzzi, F. and E. Athanassoula
2015. 2D kinematic signatures of boxy/peanut bulges. *Monthly Notices of the Royal Astronomical Society*, 450(3):2514–2538.

Jaffé, Y. L., R. Smith, G. N. Candlish, B. M. Poggianti, Y.-K. Sheen, and M. A. W. Verheijen
2015. BUDHIES II: a phase-space view of H I gas stripping and star formation quenching in cluster galaxies. *Monthly Notices of the Royal Astronomical Society*, 448(2):1715–1728.

Jeans, J. H.
1915. On the theory of star-streaming and the structure of the universe. *Monthly Notices of the Royal Astronomical Society*, 76:70–84.

Jesseit, R., M. Cappellari, T. Naab, E. Emsellem, and A. Burkert
2009. Specific angular momentum of disc merger remnants and the λ_R-parameter. *Monthly Notices of the Royal Astronomical Society*, 397:1202–1214.

Jesseit, R., T. Naab, and A. Burkert
2005. Orbital structure of collisionless merger remnants: on the origin of photometric and kinematic properties of elliptical and S0 galaxies. *Monthly Notices of the Royal Astronomical Society*, 360(4):1185–1200.

Jesseit, R., T. Naab, R. F. Peletier, and A. Burkert
2007. 2D kinematics of simulated disc merger remnants. *Monthly Notices of the Royal Astronomical Society*, 376(3):997–1020.

Jimmy, K.-V. Tran, S. Brough, K. Gebhardt, A. von der Linden, W. J. Couch, and R. Sharp
2013. Angular Momenta, Dynamical Masses, and Mergers of Brightest Cluster Galaxies. *The Astrophysical Journal*, 778:171.

Johansson, P. H., A. Burkert, and T. Naab
2009a. The Evolution of Black Hole Scaling Relations in Galaxy Mergers. *The Astrophysical Journal*, 707:L184–L189.

Johansson, P. H., T. Naab, and A. Burkert
2009b. Equal- and Unequal-Mass Mergers of Disk and Elliptical Galaxies with Black Holes. *The Astrophysical Journal*, 690:802–821.

Johnston, E. J., G. K. T. Hau, L. Coccato, and C. Herrera
2018. Mapping the kinematically decoupled core in ngc 1407 with muse. *Monthly Notices of the Royal Astronomical Society*, 480(3):3215–3223.

Karademir, G. S., R.-S. Remus, A. Burkert, K. Dolag, T. L. Hoffmann, B. P. Moster, U. P. Steinwandel, and J. Zhang
2019. The outer stellar halos of galaxies: how radial merger mass deposition, shells, and streams depend on infall-orbit configurations. *Monthly Notices of the Royal Astronomical Society*, 487(1):318–332.

Kauffmann, G., S. D. M. White, T. M. Heckman, B. Ménard, J. Brinchmann, S. Charlot, C. Tremonti, and J. Brinkmann
2004. The environmental dependence of the relations between stellar mass, structure, star formation and nuclear activity in galaxies. *Monthly Notices of the Royal Astronomical Society*, 353(3):713–731.

Kawata, D. and J. S. Mulchaey
2008. Strangulation in Galaxy Groups. *The Astrophysical Journal*, 672(2):L103.

Kelvin, L. S., S. P. Driver, A. S. G. Robotham, D. T. Hill, M. Alpaslan, I. K. Baldry, S. P. Bamford, J. Bland-Hawthorn, S. Brough, A. W. Graham, B. Häussler, A. M. Hopkins, J. Liske, J. Loveday, P. Norberg, S. Phillipps, C. C. Popescu, M. Prescott, E. N. Taylor, and R. J. Tuffs
2012. Galaxy And Mass Assembly (GAMA): Structural Investigation of Galaxies via Model Analysis. *Monthly Notices of the Royal Astronomical Society*, 421:1007–1039.

Khim, D. J., S. K. Yi, C. Pichon, Y. Dubois, J. Devriendt, H. Choi, J. J. Bryant, and S. M. Croom
2020. Star-Gas Misalignment in Galaxies: II. Origins Found from the Horizon-AGN Simulation. *arXiv e-prints*, P. arXiv:2012.04659.

Khoperskov, S., P. Di Matteo, O. Gerhard, D. Katz, M. Haywood, F. Combes, P. Berczik, and A. Gomez
2019. The echo of the bar buckling: Phase-space spirals in Gaia Data Release 2. *Astronomy and Astrophysics*, 622:L6.

Kleiner, D., P. Serra, F. M. Maccagni, A. Venhola, K. Morokuma-Matsui, R. Peletier, E. Iodice, M. A. Raj, W. J. G. de Blok, A. Comrie, G. I. G. Józsa, P. Kamphuis, A. Loni,

S. I. Loubser, D. C. Molnár, M. Ramatsoku, A. Sivitilli, O. Smirnov, K. Thorat, and F. Vitello
2021. A MeerKAT view of pre-processing in the Fornax A group. *arXiv e-prints*, P. arXiv:2101.10347.

Kluge, M., R. Bender, A. Riffeser, C. Goessl, U. Hopp, M. Schmidt, and C. Ries
2020. Photometric dissection of Intracluster Light and its correlations with host cluster properties. *arXiv e-prints*, P. arXiv:2011.12992.

Kluge, M., B. Neureiter, A. Riffeser, R. Bender, C. Goessl, U. Hopp, M. Schmidt, C. Ries, and N. Brosch
2019. Structure of Brightest Cluster Galaxies and Intracluster Light. *arXiv e-prints*, P. arXiv:1908.08544.

Klypin, A. A., S. Trujillo-Gomez, and J. Primack
2011. Dark Matter Halos in the Standard Cosmological Model: Results from the Bolshoi Simulation. *The Astrophysical Journal*, 740(2):102.

Komatsu, E., J. Dunkley, M. R. Nolta, C. L. Bennett, B. Gold, G. Hinshaw, N. Jarosik, D. Larson, M. Limon, L. Page, D. N. Spergel, M. Halpern, R. S. Hill, A. Kogut, S. S. Meyer, G. S. Tucker, J. L. Weiland, E. Wollack, and E. L. Wright
2009. Five-Year Wilkinson Microwave Anisotropy Probe Observations: Cosmological Interpretation. *Astrophysical Journal Supplement Series*, 180(2):330–376.

Komatsu, E., K. M. Smith, J. Dunkley, C. L. Bennett, B. Gold, G. Hinshaw, N. Jarosik, D. Larson, M. R. Nolta, L. Page, D. N. Spergel, M. Halpern, R. S. Hill, A. Kogut, M. Limon, S. S. Meyer, N. Odegard, G. S. Tucker, J. L. Weiland, E. Wollack, and E. L. Wright
2011. Seven-year Wilkinson Microwave Anisotropy Probe (WMAP) Observations: Cosmological Interpretation. *Astrophysical Journal Supplement Series*, 192(2):18.

Kormendy, J.
1977. Brightness distributions in compact and normal galaxies. III. Decomposition of observed profiles in spheroid and disk components. *The Astrophysical Journal*, 217:406–419.

Kormendy, J.
1993. Kinematics of extragalactic bulges: evidence that some bulges are really disks. In *Galactic Bulges*, H. Dejonghe and H. J. Habing, eds., volume 153, P. 209.

Kormendy, J. and R. Bender
1996. A Proposed Revision of the Hubble Sequence for Elliptical Galaxies. *The Astrophysical Journal*, 464:L119.

Kormendy, J. and G. Illingworth
1982. Rotation of the bulge components of disk galaxies. *The Astrophysical Journal*, 256:460.

Kormendy, J. and J. Kennicutt, Robert C.
2004. Secular Evolution and the Formation of Pseudobulges in Disk Galaxies. *Annual review of astronomy and Astrophysics*, 42(1):603–683.

Krajnović, D., K. Alatalo, L. Blitz, M. Bois, F. Bournaud, M. Bureau, M. Cappellari, R. L. Davies, T. A. Davis, P. T. de Zeeuw, P.-A. Duc, E. Emsellem, S. Khochfar, H. Kuntschner, R. M. McDermid, R. Morganti, T. Naab, T. Oosterloo, M. Sarzi, N. Scott, P. Serra, A.-M. Weijmans, and L. M. Young
2013. The ATLAS^{3D} project - XVII. Linking photometric and kinematic signatures of stellar discs in early-type galaxies. *Monthly Notices of the Royal Astronomical Society*, 432:1768–1795.

Krajnović, D., R. Bacon, M. Cappellari, R. L. Davies, P. T. de Zeeuw, E. Emsellem, J. Falcón-Barroso, H. Kuntschner, R. M. McDermid, R. F. Peletier, M. Sarzi, R. C. E. van den Bosch, and G. van de Ven
2008. The SAURON project - XII. Kinematic substructures in early-type galaxies: evidence for discs in fast rotators. *Monthly Notices of the Royal Astronomical Society*, 390(1):93–117.

Krajnović, D., M. Cappellari, P. T. de Zeeuw, and Y. Copin
2006. Kinemetry: a generalization of photometry to the higher moments of the line-of-sight velocity distribution. *Monthly Notices of the Royal Astronomical Society*, 366:787–802.

Krajnović, D., E. Emsellem, M. Cappellari, K. Alatalo, L. Blitz, M. Bois, F. Bournaud, M. Bureau, R. L. Davies, T. A. Davis, P. T. de Zeeuw, S. Khochfar, H. Kuntschner, P.-Y. Lablanche, R. M. McDermid, R. Morganti, T. Naab, T. Oosterloo, M. Sarzi, N. Scott, P. Serra, A.-M. Weijmans, and L. M. Young
2011. The ATLAS^{3D} project - II. Morphologies, kinemetric features and alignment between photometric and kinematic axes of early-type galaxies. *Monthly Notices of the Royal Astronomical Society*, 414:2923–2949.

Krajnović, D., E. Emsellem, M. den Brok, R. A. Marino, K. B. Schmidt, M. Steinmetz, and P. M. Weilbacher
2018. Climbing to the top of the galactic mass ladder: evidence for frequent prolate-like rotation among the most massive galaxies. *Monthly Notices of the Royal Astronomical Society*, 477(4):5327–5337.

Lackner, C. N., R. Cen, J. P. Ostriker, and M. R. Joung
2012. Building galaxies by accretion and in situ star formation. *Monthly Notices of the Royal Astronomical Society*, 425:641–656.

Lagos, C. D. P., C. M. Baugh, M. A. Zwaan, C. G. Lacey, V. Gonzalez-Perez, C. Power, A. M. Swinbank, and E. van Kampen
2014. Which galaxies dominate the neutral gas content of the Universe? *Monthly Notices of the Royal Astronomical Society*, 440(1):920–941.

Lagos, C. d. P., E. Emsellem, J. van de Sande, K. E. Harborne, L. Cortese, T. Davison, C. Foster, and R. J. Wright
2020. The diverse nature and formation paths of slow rotator galaxies in the EAGLE simulations. *arXiv e-prints*, P. arXiv:2012.08060.

Lagos, C. d. P., J. Schaye, Y. Bahé, J. Van de Sande, S. T. Kay, D. Barnes, T. A. Davis, and C. Dalla Vecchia
2018a. The connection between mass, environment, and slow rotation in simulated galaxies. *Monthly Notices of the Royal Astronomical Society*, 476(4):4327–4345.

Lagos, C. d. P., A. R. H. Stevens, R. G. Bower, T. A. Davis, S. Contreras, N. D. Padilla, D. Obreschkow, D. Croton, J. W. Trayford, C. Welker, and T. Theuns
2017a. The catastrophic effect of mergers on the angular momentum and morphology of galaxies in EAGLE. *ArXiv e-prints*.

Lagos, C. d. P., A. R. H. Stevens, R. G. Bower, T. A. Davis, S. Contreras, N. D. Padilla, D. Obreschkow, D. Croton, J. W. Trayford, C. Welker, and T. Theuns
2018b. Quantifying the impact of mergers on the angular momentum of simulated galaxies. *Monthly Notices of the Royal Astronomical Society*, 473:4956–4974.

Lagos, C. d. P., T. Theuns, A. R. H. Stevens, L. Cortese, N. D. Padilla, T. A. Davis, S. Contreras, and D. Croton
2017b. Angular momentum evolution of galaxies in EAGLE. *Monthly Notices of the Royal Astronomical Society*, 464(4):3850–3870.

Lang, P., N. M. Förster Schreiber, R. Genzel, S. Wuyts, E. Wisnioski, A. Beifiori, S. Belli, R. Bender, G. Brammer, A. Burkert, J. Chan, R. Davies, M. Fossati, A. Galametz, S. K. Kulkarni, D. Lutz, J. T. Mendel, I. G. Momcheva, T. Naab, E. J. Nelson, R. P. Saglia, S. Seitz, S. Tacchella, L. J. Tacconi, K.-i. Tadaki, H. Übler, P. G. van Dokkum, and D. J. Wilman
2017. Falling Outer Rotation Curves of Star-forming Galaxies at $0.6 \lesssim z \lesssim 2.6$ Probed with KMOS^{3D} and SINS/zC-SINF. *The Astrophysical Journal*, 840(2):92.

Lange, R., S. P. Driver, A. S. G. Robotham, L. S. Kelvin, A. W. Graham, M. Alpaslan, S. K. Andrews, I. K. Baldry, S. Bamford, J. Bland-Hawthorn, S. Brough, M. E. Cluver, C. J. Conselice, L. J. M. Davies, B. Haeussler, I. S. Konstantopoulos, J. Loveday, A. J. Moffett, P. Norberg, S. Phillipps, E. N. Taylor, Á. R. López-Sánchez, and S. M. Wilkins
2015. Galaxy And Mass Assembly (GAMA): mass-size relations of z¡0.1 galaxies subdivided by Sérsic index, colour and morphology. *Monthly Notices of the Royal Astronomical Society*, 447:2603–2630.

Laporte, C. F. P., I. Minchev, K. V. Johnston, and F. A. Gómez
2019. Footprints of the Sagittarius dwarf galaxy in the Gaia data set. *Monthly Notices of the Royal Astronomical Society*, 485(3):3134–3152.

Larson, R. B., B. M. Tinsley, and C. N. Caldwell
1980. The evolution of disk galaxies and the origin of S0 galaxies. *The Astrophysical Journal*, 237:692–707.

Lemaitre, G. H.
1927. *The Gravitational Field in a Fluid Sphere of Uniform Invariant Density, According to the Theory of Relativity.* PhD thesis, MASSACHUSETTS INSTITUTE OF TECHNOLOGY.

Li, H., S. Mao, E. Emsellem, D. Xu, V. Springel, and D. Krajnović
2018a. The origin and properties of massive prolate galaxies in the Illustris simulation. *Monthly Notices of the Royal Astronomical Society*, 473:1489–1511.

Li, Z.-Y. and J. Shen
2020. Dissecting the Phase Space Snail Shell. *The Astrophysical Journal*, 890(1):85.

Li, Z.-Y., J. Shen, M. Bureau, Y. Zhou, M. Du, and V. P. Debattista
2018b. Shape of LOSVDs in Barred Disks: Implications for Future IFU Surveys. *The Astrophysical Journal*, 854(1):65.

Linde, A. D.
1982. A new inflationary universe scenario: A possible solution of the horizon, flatness, homogeneity, isotropy and primordial monopole problems. *Physics Letters B*, 108(6):389–393.

Lotz, M., K. Dolag, R.-S. Remus, and A. Burkert
2020. Rise and fall of post-starburst galaxies in Magneticum Pathfinder. *arXiv e-prints*, P. arXiv:2011.06602.

Lotz, M., R.-S. Remus, K. Dolag, A. Biviano, and A. Burkert
2019. Gone after one orbit: How cluster environments quench galaxies. *Monthly Notices of the Royal Astronomical Society*, 488(4):5370–5389.

Lucy, L. B.
1977. A numerical approach to the testing of the fission hypothesis. *Astronomical Journal*, 82:1013–1024.

Lynden-Bell, D.
1967. Statistical mechanics of violent relaxation in stellar systems. *Monthly Notices of the Royal Astronomical Society*, 136:101.

Ma, C.-P., J. E. Greene, N. McConnell, R. Janish, J. P. Blakeslee, J. Thomas, and J. D. Murphy
2014. The MASSIVE Survey. I. A Volume-limited Integral-field Spectroscopic Study of the Most Massive Early-type Galaxies within 108 Mpc. *The Astrophysical Journal*, 795:158.

Madau, P. and M. Dickinson
2014. Cosmic Star-Formation History. *Annual review of astronomy and Astrophysics*, 52:415–486.

Maddox, S. J., G. Efstathiou, W. J. Sutherland, and J. Loveday
1990. Galaxy correlations on large scales. *Monthly Notices of the Royal Astronomical Society*, 242:43.

Marsan, Z. C., D. Marchesini, G. B. Brammer, M. Stefanon, A. Muzzin, A. Fernández-Soto, S. Geier, K. N. Hainline, H. Intema, A. Karim, I. Labbé, S. Toft, and P. G. van Dokkum
2015. Spectroscopic Confirmation of an Ultra Massive and Compact Galaxy at z = 3.35: a Detailed Look at an Early Progenitor of Local Giant Ellipticals. *The Astrophysical Journal*, 801(2):133.

McDermid, R. M., R. Bacon, H. Kuntschner, E. Emsellem, K. L. Shapiro, M. Bureau, M. Cappellari, R. L. Davies, J. Falcón-Barroso, D. Krajnović, R. F. Peletier, M. Sarzi, and T. de Zeeuw
2006a. Stellar kinematics and populations of early-type galaxies with the SAURON and OASIS integral-field spectrographs. *New Astron. Rev.*, 49:521–535.

McDermid, R. M., E. Emsellem, K. L. Shapiro, R. Bacon, M. Bureau, M. Cappellari, R. L. Davies, T. de Zeeuw, J. Falcón-Barroso, D. Krajnović, H. Kuntschner, R. F. Peletier, and M. Sarzi
2006b. The SAURON project - VIII. OASIS/CFHT integral-field spectroscopy of elliptical and lenticular galaxy centres. *Monthly Notices of the Royal Astronomical Society*, 373:906–958.

McDonald, M., B. A. Benson, A. Vikhlinin, K. A. Aird, S. W. Allen, M. Bautz, M. Bayliss, L. E. Bleem, S. Bocquet, M. Brodwin, J. E. Carlstrom, C. L. Chang, H. M. Cho, A. Clocchiatti, T. M. Crawford, A. T. Crites, T. de Haan, M. A. Dobbs, R. J. Foley, W. R. Forman, E. M. George, M. D. Gladders, A. H. Gonzalez, N. W. Halverson, J. Hlavacek-Larrondo, G. P. Holder, W. L. Holzapfel, J. D. Hrubes, C. Jones, R. Keisler, L. Knox, A. T. Lee, E. M. Leitch, J. Liu, M. Lueker, D. Luong-Van, A. Mantz, D. P. Marrone, J. J. McMahon, S. S. Meyer, E. D. Miller, L. Mocanu, J. J. Mohr, S. S. Murray, S. Padin, C. Pryke, C. L. Reichardt, A. Rest, J. E. Ruhl, B. R. Saliwanchik, A. Saro, J. T. Sayre, K. K. Schaffer, E. Shirokoff, H. G. Spieler, B. Stalder, S. A. Stanford, Z. Staniszewski, A. A. Stark, K. T. Story, C. W. Stubbs, K. Vanderlinde, J. D. Vieira, R. Williamson, O. Zahn, and A. Zenteno
2014. The Redshift Evolution of the Mean Temperature, Pressure, and Entropy Profiles in 80 SPT-Selected Galaxy Clusters. *The Astrophysical Journal*, 794(1):67.

Méndez, R. H., A. Riffeser, R.-P. Kudritzki, M. Matthias, K. C. Freeman, M. Arnaboldi, M. Capaccioli, and O. E. Gerhard
2001. Detection, Photometry, and Slitless Radial Velocities of 535 Planetary Nebulae in the Flattened Elliptical Galaxy NGC 4697. *The Astrophysical Journal*, 563:135–150.

Méndez, R. H., A. M. Teodorescu, R. P. Kudritzki, and A. Burkert
2009. Kinematics of Planetary Nebulae in the Outskirts of the Elliptical Galaxy NGC 4697. *The Astrophysical Journal*, 691(1):228–240.

Merritt, D.
1983. Relaxation and tidal stripping in rich clusters of galaxies. I. Evolution of the mass distribution. *The Astrophysical Journal*, 264:24–48.

Meza, A., J. F. Navarro, M. Steinmetz, and V. R. Eke
2003. Simulations of Galaxy Formation in a ΛCDM Universe. III. The Dissipative Formation of an Elliptical Galaxy. *The Astrophysical Journal*, 590(2):619–635.

Mihos, J. C. and L. Hernquist
1996. Gasdynamics and Starbursts in Major Mergers. *The Astrophysical Journal*, 464:641.

Miller, T. B., S. C. Chapman, M. Aravena, M. L. N. Ashby, C. C. Hayward, J. D. Vieira, A. Weiß, A. Babul, M. Béthermin, C. M. Bradford, M. Brodwin, J. E. Carlstrom, C.-C. Chen, D. J. M. Cunningham, C. De Breuck, A. H. Gonzalez, T. R. Greve, J. Harnett, Y. Hezaveh, K. Lacaille, K. C. Litke, J. Ma, M. Malkan, D. P. Marrone, W. Morningstar, E. J. Murphy, D. Narayanan, E. Pass, R. Perry, K. A. Phadke, D. Rennehan, K. M. Rotermund, J. Simpson, J. S. Spilker, J. Sreevani, A. A. Stark, M. L. Strandet, and A. L. Strom
2018. A massive core for a cluster of galaxies at a redshift of 4.3. *Nature*, 556(7702):469–472.

Misner, C. W.
1968. The Isotropy of the Universe. *The Astrophysical Journal*, 151:431.

Mo, H., F. C. van den Bosch, and S. White
2010. *Galaxy Formation and Evolution.*

Moody, C. E., A. J. Romanowsky, T. J. Cox, G. S. Novak, and J. R. Primack
2014. Simulating multiple merger pathways to the central kinematics of early-type galaxies. *Monthly Notices of the Royal Astronomical Society*, 444:1475–1485.

Murante, G., M. Arnaboldi, O. Gerhard, S. Borgani, L. M. Cheng, A. Diaferio, K. Dolag, L. Moscardini, G. Tormen, L. Tornatore, and P. Tozzi
2004. The Diffuse Light in Simulations of Galaxy Clusters. *The Astrophysical Journal*, 607(2):L83–L86.

Naab, T. and A. Burkert
2001. The Formation of Disks in Elliptical Galaxies. *The Astrophysical Journal*, 555(2):L91–L94.

Naab, T. and A. Burkert
2003. Statistical Properties of Collisionless Equal- and Unequal-Mass Merger Remnants of Disk Galaxies. *The Astrophysical Journal*, 597:893–906.

Naab, T., R. Jesseit, and A. Burkert
2006. The influence of gas on the structure of merger remnants. *Monthly Notices of the Royal Astronomical Society*, 372(2):839–852.

Naab, T., L. Oser, E. Emsellem, M. Cappellari, D. Krajnović, R. M. McDermid, K. Alatalo, E. Bayet, L. Blitz, M. Bois, F. Bournaud, M. Bureau, A. Crocker, R. L. Davies, T. A. Davis, P. T. de Zeeuw, P.-A. Duc, M. Hirschmann, P. H. Johansson, S. Khochfar, H. Kuntschner, R. Morganti, T. Oosterloo, M. Sarzi, N. Scott, P. Serra, G. v. d. Ven, A. Weijmans, and L. M. Young
2014. The ATLAS^{3D} project - XXV. Two-dimensional kinematic analysis of simulated galaxies and the cosmological origin of fast and slow rotators. *Monthly Notices of the Royal Astronomical Society*, 444:3357–3387.

Naab, T. and J. P. Ostriker
2017. Theoretical Challenges in Galaxy Formation. *Annual review of astronomy and Astrophysics*, 55(1):59–109.

Nilsson, K. K., J. P. U. Fynbo, P. Møller, J. Sommer-Larsen, and C. Ledoux
2006. A Lyman-α blob in the GOODS South field: evidence for cold accretion onto a dark matter halo. *Astronomy and Astrophysics*, 452(3):L23–L26.

Obreschkow, D. and K. Glazebrook
2014. Fundamental Mass-Spin-Morphology Relation Of Spiral Galaxies. *The Astrophysical Journal*, 784(1):26.

Obreschkow, D., K. Glazebrook, R. Bassett, D. B. Fisher, R. G. Abraham, E. Wisnioski, A. W. Green, P. J. McGregor, I. Damjanov, A. Popping, and I. Jørgensen
2015. Low Angular Momentum in Clumpy, Turbulent Disk Galaxies. *The Astrophysical Journal*, 815:97.

Oh, S., S. K. Yi, L. Cortese, J. van de Sande, S. Mahajan, H. Jeong, Y.-K. Sheen, J. T. Allen, K. Bekki, J. Bland-Hawthorn, J. V. Bloom, S. Brough, J. J. Bryant, M. Colless, S. M. Croom, L. M. R. Fogarty, M. Goodwin, A. Green, I. S. Konstantopoulos, J. Lawrence, Á. R. López-Sánchez, N. P. F. Lorente, A. M. Medling, M. S. Owers, S. Richards, N. Scott, R. Sharp, and S. M. Sweet
2016. The SAMI Galaxy Survey: Galaxy Interactions and Kinematic Anomalies in Abell 119. *The Astrophysical Journal*, 832(1):69.

Omori, K. C. and T. T. Takeuchi
2020. Spatially Resolved Properties of Galaxies with a Kinematically Distinct Core. *arXiv e-prints*, P. arXiv:2012.07345.

Oser, L., J. P. Ostriker, T. Naab, P. H. Johansson, and A. Burkert
2010. The Two Phases of Galaxy Formation. *The Astrophysical Journal*, 725(2):2312–2323.

Ostriker, J. P., P. J. E. Peebles, and A. Yahil
1974. The Size and Mass of Galaxies, and the Mass of the Universe. *The Astrophysical Journal*, 193:L1.

Oteo, I., R. J. Ivison, L. Dunne, A. Manilla-Robles, S. Maddox, A. J. R. Lewis, G. de Zotti, M. Bremer, D. L. Clements, A. Cooray, H. Dannerbauer, S. Eales, J. Greenslade, A. Omont, I. Perez–Fournón, D. Riechers, D. Scott, P. van der Werf, A. Weiss, and Z. Y. Zhang
2018. An Extreme Protocluster of Luminous Dusty Starbursts in the Early Universe. *The Astrophysical Journal*, 856(1):72.

Pasquali, A., F. C. van den Bosch, and H.-W. Rix
2007. The Isophotal Structure of Early-Type Galaxies in the SDSS: Dependence on Active Galactic Nucleus Activity and Environment. *The Astrophysical Journal*, 664:738–749.

Pastorello, N., D. A. Forbes, C. Foster, J. P. Brodie, C. Usher, A. J. Romanowsky, J. Strader, and J. A. Arnold
2014. The SLUGGS survey: exploring the metallicity gradients of nearby early-type galaxies to large radii. *Monthly Notices of the Royal Astronomical Society*, 442:1003–1039.

Pastorello, N., D. A. Forbes, C. Usher, J. P. Brodie, A. J. Romanowsky, J. Strader, L. R. Spitler, A. B. Alabi, C. Foster, Z. G. Jennings, S. S. Kartha, and V. Pota
2015. The SLUGGS survey: combining stellar and globular cluster metallicities in the outer regions of early-type galaxies. *Monthly Notices of the Royal Astronomical Society*, 451(3):2625–2639.

Pedrosa, S. E. and P. B. Tissera
2015. Angular momentum evolution for galaxies in a Λ-CDM scenario. *Astronomy and Astrophysics*, 584:A43.

Peebles, P. J. E.
1969. Origin of the Angular Momentum of Galaxies. *The Astrophysical Journal*, 155:393.

Peng, Y., R. Maiolino, and R. Cochrane
2015. Strangulation as the primary mechanism for shutting down star formation in galaxies. *Nature*, 521(7551):192–195.

Peng, Y.-j., S. J. Lilly, K. Kovač, M. Bolzonella, L. Pozzetti, A. Renzini, G. Zamorani, O. Ilbert, C. Knobel, A. Iovino, C. Maier, O. Cucciati, L. Tasca, C. M. Carollo, J. Silverman, P. Kampczyk, L. de Ravel, D. Sanders, N. Scoville, T. Contini, V. Mainieri, M. Scodeggio, J.-P. Kneib, O. Le Fèvre, S. Bardelli, A. Bongiorno, K. Caputi, G. Coppa, S. de la Torre, P. Franzetti, B. Garilli, F. Lamareille, J.-F. Le Borgne, V. Le Brun, M. Mignoli, E. Perez Montero, R. Pello, E. Ricciardelli, M. Tanaka, L. Tresse, D. Vergani, N. Welikala, E. Zucca, P. Oesch, U. Abbas, L. Barnes, R. Bordoloi, D. Bottini, A. Cappi, P. Cassata, A. Cimatti, M. Fumana, G. Hasinger, A. Koekemoer, A. Leauthaud, D. Maccagni, C. Marinoni, H. McCracken, P. Memeo, B. Meneux, P. Nair, C. Porciani, V. Presotto, and R. Scaramella
2010. Mass and Environment as Drivers of Galaxy Evolution in SDSS and zCOSMOS and the Origin of the Schechter Function. *The Astrophysical Journal*, 721(1):193–221.

Peng, Y.-j., S. J. Lilly, A. Renzini, and M. Carollo
2012. Mass and Environment as Drivers of Galaxy Evolution. II. The Quenching of Satellite Galaxies as the Origin of Environmental Effects. *The Astrophysical Journal*, 757(1):4.

Penoyre, Z., B. P. Moster, D. Sijacki, and S. Genel
2017. The origin and evolution of fast and slow rotators in the Illustris simulation. *Monthly Notices of the Royal Astronomical Society*, 468:3883–3906.

Penzias, A. A. and R. W. Wilson
1965. A Measurement of Excess Antenna Temperature at 4080 Mc/s. *The Astrophysical Journal*, 142:419–421.

Perlmutter, S., G. Aldering, G. Goldhaber, R. A. Knop, P. Nugent, P. G. Castro, S. Deustua, S. Fabbro, A. Goobar, D. E. Groom, I. M. Hook, A. G. Kim, M. Y. Kim, J. C. Lee, N. J. Nunes, R. Pain, C. R. Pennypacker, R. Quimby, C. Lidman, R. S. Ellis, M. Irwin, R. G. McMahon, P. Ruiz-Lapuente, N. Walton, B. Schaefer, B. J. Boyle, A. V. Filippenko, T. Matheson, A. S. Fruchter, N. Panagia, H. J. M. Newberg, W. J. Couch, and T. S. C. Project
1999. Measurements of Ω and Λ from 42 High-Redshift Supernovae. *The Astrophysical Journal*, 517(2):565–586.

Pillepich, A., M. Vogelsberger, A. Deason, V. Rodriguez-Gomez, S. Genel, D. Nelson, P. Torrey, L. V. Sales, F. Marinacci, V. Springel, D. Sijacki, and L. Hernquist
2014. Halo mass and assembly history exposed in the faint outskirts: the stellar and dark matter haloes of Illustris galaxies. *Monthly Notices of the Royal Astronomical Society*, 444(1):237–249.

Planck Collaboration, P. A. R. Ade, N. Aghanim, M. Arnaud, M. Ashdown, F. Atrio-Barandela, J. Aumont, C. Baccigalupi, A. Balbi, A. J. Banday, R. B. Barreiro, J. G. Bartlett, E. Battaner, K. Benabed, A. Benoît, J. P. Bernard, M. Bersanelli, R. Bhatia, I. Bikmaev, J. Bobin, H. Böhringer, A. Bonaldi, J. R. Bond, S. Borgani, J. Borrill, F. R. Bouchet, H. Bourdin, M. L. Brown, R. Burenin, C. Burigana, P. Cabella, J. F. Cardoso, P. Carvalho, G. Castex, A. Catalano, L. Cayón, A. Chamballu, L. Y. Chiang, G. Chon, P. R. Christensen, E. Churazov, D. L. Clements, S. Colafrancesco, S. Colombi, L. P. L. Colombo, B. Comis, A. Coulais, B. P. Crill, F. Cuttaia, A. Da Silva, H. Dahle, L. Danese, R. J. Davis, P. de Bernardis, G. de Gasperis, G. de Zotti, J. Delabrouille, J. Démoclès, F. X. Désert, J. M. Diego, K. Dolag, H. Dole, S. Donzelli, O. Doré, U. Dörl, M. Douspis, X. Dupac,

G. Efstathiou, T. A. Enßlin, H. K. Eriksen, F. Finelli, I. Flores-Cacho, O. Forni, P. Fosalba, M. Frailis, E. Franceschi, M. Frommert, S. Galeotta, K. Ganga, R. T. Génova-Santos, M. Giard, Y. Giraud-Héraud, J. González-Nuevo, K. M. Górski, A. Gregorio, A. Gruppuso, F. K. Hansen, D. Harrison, A. Hempel, S. Henrot-Versillé, C. Hernández-Monteagudo, D. Herranz, S. R. Hildebrandt, E. Hivon, M. Hobson, W. A. Holmes, G. Hurier, T. R. Jaffe, A. H. Jaffe, T. Jagemann, W. C. Jones, M. Juvela, E. Keihänen, I. Khamitov, T. S. Kisner, R. Kneissl, J. Knoche, L. Knox, M. Kunz, H. Kurki-Suonio, G. Lagache, A. Lähteenmäki, J. M. Lamarre, A. Lasenby, C. R. Lawrence, M. Le Jeune, R. Leonardi, A. Liddle, P. B. Lilje, M. López-Caniego, G. Luzzi, J. F. Macías-Pérez, D. Maino, N. Mandolesi, M. Maris, F. Marleau, D. J. Marshall, E. Martínez-González, S. Masi, M. Massardi, S. Matarrese, P. Mazzotta, S. Mei, A. Melchiorri, J. B. Melin, L. Mendes, A. Mennella, S. Mitra, M. A. Miville-Deschênes, A. Moneti, L. Montier, G. Morgante, D. Mortlock, D. Munshi, J. A. Murphy, P. Naselsky, F. Nati, P. Natoli, H. U. Nørgaard-Nielsen, F. Noviello, D. Novikov, I. Novikov, S. Osborne, F. Pajot, D. Paoletti, F. Pasian, G. Patanchon, O. Perdereau, L. Perotto, F. Perrotta, F. Piacentini, M. Piat, E. Pierpaoli, R. Piffaretti, S. Plaszczynski, E. Pointecouteau, G. Polenta, N. Ponthieu, L. Popa, T. Poutanen, G. W. Pratt, S. Prunet, J. L. Puget, J. P. Rachen, W. T. Reach, R. Rebolo, M. Reinecke, M. Remazeilles, C. Renault, S. Ricciardi, T. Riller, I. Ristorcelli, G. Rocha, M. Roman, C. Rosset, M. Rossetti, J. A. Rubiño-Martín, B. Rusholme, M. Sandri, G. Savini, D. Scott, G. F. Smoot, J. L. Starck, R. Sudiwala, R. Sunyaev, D. Sutton, A. S. Suur-Uski, J. F. Sygnet, J. A. Tauber, L. Terenzi, L. Toffolatti, M. Tomasi, M. Tristram, J. Tuovinen, L. Valenziano, B. Van Tent, J. Varis, P. Vielva, F. Villa, N. Vittorio, L. A. Wade, B. D. Wandelt, N. Welikala, S. D. M. White, M. White, D. Yvon, A. Zacchei, and A. Zonca
2013. Planck intermediate results. V. Pressure profiles of galaxy clusters from the Sunyaev-Zeldovich effect. *Astronomy and Astrophysics*, 550:A131.

Planck Collaboration, N. Aghanim, Y. Akrami, M. Ashdown, J. Aumont, C. Baccigalupi, M. Ballardini, A. J. Banday, R. B. Barreiro, N. Bartolo, S. Basak, R. Battye, K. Benabed, J. P. Bernard, M. Bersanelli, P. Bielewicz, J. J. Bock, J. R. Bond, J. Borrill, F. R. Bouchet, F. Boulanger, M. Bucher, C. Burigana, R. C. Butler, E. Calabrese, J. F. Cardoso, J. Carron, A. Challinor, H. C. Chiang, J. Chluba, L. P. L. Colombo, C. Combet, D. Contreras, B. P. Crill, F. Cuttaia, P. de Bernardis, G. de Zotti, J. Delabrouille, J. M. Delouis, E. Di Valentino, J. M. Diego, O. Doré, M. Douspis, A. Ducout, X. Dupac, S. Dusini, G. Efstathiou, F. Elsner, T. A. Enßlin, H. K. Eriksen, Y. Fantaye, M. Farhang, J. Fergusson, R. Fernandez-Cobos, F. Finelli, F. Forastieri, M. Frailis, A. A. Fraisse, E. Franceschi, A. Frolov, S. Galeotta, S. Galli, K. Ganga, R. T. Génova-Santos, M. Gerbino, T. Ghosh, J. González-Nuevo, K. M. Górski, S. Gratton, A. Gruppuso, J. E. Gudmundsson, J. Hamann, W. Handley, F. K. Hansen, D. Herranz, S. R. Hildebrandt, E. Hivon, Z. Huang, A. H. Jaffe, W. C. Jones, A. Karakci, E. Keihänen, R. Keskitalo, K. Kiiveri, J. Kim, T. S. Kisner, L. Knox, N. Krachmalnicoff, M. Kunz, H. Kurki-Suonio, G. Lagache, J. M. Lamarre, A. Lasenby, M. Lattanzi, C. R. Lawrence, M. Le Jeune, P. Lemos, J. Lesgourgues, F. Levrier, A. Lewis, M. Liguori, P. B. Lilje, M. Lilley, V. Lindholm, M. López-Caniego, P. M. Lubin, Y. Z. Ma, J. F. Macías-Pérez, G. Maggio, D. Maino, N. Mandolesi, A. Mangilli, A. Marcos-Caballero, M. Maris, P. G. Martin, M. Martinelli, E. Martínez-González, S. Matarrese, N. Mauri, J. D. McEwen, P. R. Meinhold, A. Melchiorri, A. Mennella, M. Migliaccio, M. Millea, S. Mitra, M. A. Miville-Deschênes, D. Molinari, L. Montier, G. Morgante, A. Moss, P. Natoli, H. U. Nørgaard-Nielsen, L. Pagano,

D. Paoletti, B. Partridge, G. Patanchon, H. V. Peiris, F. Perrotta, V. Pettorino, F. Piacentini, L. Polastri, G. Polenta, J. L. Puget, J. P. Rachen, M. Reinecke, M. Remazeilles, A. Renzi, G. Rocha, C. Rosset, G. Roudier, J. A. Rubiño-Martín, B. Ruiz-Granados, L. Salvati, M. Sandri, M. Savelainen, D. Scott, E. P. S. Shellard, C. Sirignano, G. Sirri, L. D. Spencer, R. Sunyaev, A. S. Suur-Uski, J. A. Tauber, D. Tavagnacco, M. Tenti, L. Toffolatti, M. Tomasi, T. Trombetti, L. Valenziano, J. Valiviita, B. Van Tent, L. Vibert, P. Vielva, F. Villa, N. Vittorio, B. D. Wand elt, I. K. Wehus, M. White, S. D. M. White, A. Zacchei, and A. Zonca
2018. Planck 2018 results. VI. Cosmological parameters. *arXiv e-prints*, P. arXiv:1807.06209.

Poci, A., R. M. McDermid, L. Zhu, and G. van de Ven
2019. Combining stellar populations with orbit-superposition dynamical modelling: the formation history of the lenticular galaxy NGC 3115. *Monthly Notices of the Royal Astronomical Society*, 487(3):3776–3796.

Pota, V., D. A. Forbes, A. J. Romanowsky, J. P. Brodie, L. R. Spitler, J. Strader, C. Foster, J. A. Arnold, A. Benson, C. Blom, J. R. Hargis, K. L. Rhode, and C. Usher
2013. The SLUGGS Survey: kinematics for over 2500 globular clusters in 12 early-type galaxies. *Monthly Notices of the Royal Astronomical Society*, 428:389–420.

Pulsoni, C., O. Gerhard, M. Arnaboldi, L. Coccato, A. Longobardi, N. R. Napolitano, E. Moylan, C. Narayan, V. Gupta, A. Burkert, M. Capaccioli, A. L. Chies-Santos, A. Cortesi, K. C. Freeman, K. Kuijken, M. R. Merrifield, A. J. Romanowsky, and C. Tortora
2018. The extended Planetary Nebula Spectrograph (ePN.S) early-type galaxy survey: The kinematic diversity of stellar halos and the relation between halo transition scale and stellar mass. *Astronomy and Astrophysics*, 618:A94.

Pulsoni, C., O. Gerhard, M. Arnaboldi, A. Pillepich, V. Rodriguez-Gomez, D. Nelson, L. Hernquist, and V. Springel
2020. The stellar halos of ETGs in the IllustrisTNG simulations: II. Accretion, merger history, and dark halo connection. *arXiv e-prints*, P. arXiv:2009.01823.

Querejeta, M., M. C. Eliche-Moral, T. Tapia, A. Borlaff, G. van de Ven, M. Lyubenova, M. Martig, J. Falcón-Barroso, and J. Méndez-Abreu
2015. Formation of S0 galaxies through mergers. Explaining angular momentum and concentration change from spirals to S0s. *Astronomy and Astrophysics*, 579:L2.

Raskutti, S., J. E. Greene, and J. D. Murphy
2014. The Stellar Halos of Massive Elliptical Galaxies. III. Kinematics at Large Radius. *The Astrophysical Journal*, 786:23.

Rees, M. J. and J. P. Ostriker
1977. Cooling, dynamics and fragmentation of massive gas clouds: clues to the masses and radii of galaxies and clusters. *Monthly Notices of the Royal Astronomical Society*, 179:541–559.

Reines, F., H. W. Sobel, and E. Pasierb
1980. Evidence for neutrino instability. *Physical Review Letters*, 45(16):1307–1311.

Remus, R.-S., A. Burkert, K. Dolag, P. H. Johansson, T. Naab, L. Oser, and J. Thomas
2013. The Dark Halo – Spheroid Conspiracy and the Origin of Elliptical Galaxies. *The Astrophysical Journal*, 766:71.

Remus, R.-S. and K. Dolag
2016. Connecting Small and Large Scales: The Role of Feedback in Establishing Global Galaxy Properties over Cosmic Times. In *The Interplay between Local and Global Processes in Galaxies,*.

Remus, R.-S., K. Dolag, T. Naab, A. Burkert, M. Hirschmann, T. L. Hoffmann, and P. H. Johansson
2017. The co-evolution of total density profiles and central dark matter fractions in simulated early-type galaxies. *Monthly Notices of the Royal Astronomical Society*, 464:3742–3756.

Remus, R.-S. and D. A. Forbes
2021. Accreted or Not Accreted? The Fraction of Accreted Mass in Galaxies from Simulations and Observations. *arXiv e-prints*, P. arXiv:2101.12216.

Roberts, M. S. and A. H. Rots
1973. Comparison of Rotation Curves of Different Galaxy Types. *Astronomy and Astrophysics*, 26:483–485.

Roberts, P. H.
1962. On the Superpotential and Supermatrix of a Heterogeneous Ellipsoid. *The Astrophysical Journal*, 136:1108.

Romanowsky, A. J. and S. M. Fall
2012. Angular Momentum and Galaxy Formation Revisited. *Astrophysical Journal Supplement Series*, 203:17.

Röttgers, B., T. Naab, and L. Oser
2014. Stellar orbits in cosmological galaxy simulations: the connection to formation history and line-of-sight kinematics. *Monthly Notices of the Royal Astronomical Society*, 445(2):1065–1083.

Rubin, V. C., J. Ford, W. K., and N. Thonnard
1978. Extended rotation curves of high-luminosity spiral galaxies. IV. Systematic dynamical properties, Sa -> Sc. *The Astrophysical Journal*, 225:L107–L111.

Rubin, V. C., J. Ford, W. K., and N. Thonnard
1980. Rotational properties of 21 SC galaxies with a large range of luminosities and radii, from NGC 4605 (R=4kpc) to UGC 2885 (R=122kpc). *The Astrophysical Journal*, 238:471–487.

Sánchez, S. F., R. C. Kennicutt, A. Gil de Paz, G. van de Ven, J. M. Vílchez, L. Wisotzki, C. J. Walcher, D. Mast, J. A. L. Aguerri, S. Albiol-Pérez, A. Alonso-Herrero, J. Alves, J. Bakos, T. Bartáková, J. Bland-Hawthorn, A. Boselli, D. J. Bomans, A. Castillo-Morales, C. Cortijo-Ferrero, A. de Lorenzo-Cáceres, A. Del Olmo, R.-J. Dettmar, A. Díaz, S. Ellis, J. Falcón-Barroso, H. Flores, A. Gallazzi, B. García-Lorenzo, R. González Delgado,

N. Gruel, T. Haines, C. Hao, B. Husemann, J. Iglésias-Páramo, K. Jahnke, B. Johnson, B. Jungwiert, V. Kalinova, C. Kehrig, D. Kupko, Á. R. López-Sánchez, M. Lyubenova, R. A. Marino, E. Mármol-Queraltó, I. Márquez, J. Masegosa, S. Meidt, J. Mendez-Abreu, A. Monreal-Ibero, C. Montijo, A. M. Mourão, G. Palacios-Navarro, P. Papaderos, A. Pasquali, R. Peletier, E. Pérez, I. Pérez, A. Quirrenbach, M. Relaño, F. F. Rosales-Ortega, M. M. Roth, T. Ruiz-Lara, P. Sánchez-Blázquez, C. Sengupta, R. Singh, V. Stanishev, S. C. Trager, A. Vazdekis, K. Viironen, V. Wild, S. Zibetti, and B. Ziegler
2012. CALIFA, the Calar Alto Legacy Integral Field Area survey. I. Survey presentation. *Astronomy and Astrophysics*, 538:A8.

Sánchez-Menguiano, L., S. F. Sánchez, I. Pérez, R. García-Benito, B. Husemann, D. Mast, A. Mendoza, T. Ruiz-Lara, Y. Ascasibar, J. Bland-Hawthorn, O. Cavichia, A. I. Díaz, E. Florido, L. Galbany, R. M. Gónzalez Delgado, C. Kehrig, R. A. Marino, I. Márquez, J. Masegosa, J. Méndez-Abreu, M. Mollá, A. Del Olmo, E. Pérez, P. Sánchez-Blázquez, V. Stanishev, C. J. Walcher, Á. R. López-Sánchez, and Califa Collaboration
2016. Shape of the oxygen abundance profiles in CALIFA face-on spiral galaxies. *Astronomy and Astrophysics*, 587:A70.

Sandage, A.
1961. *The Hubble atlas of galaxies*.

Sandage, A.
1975. *Classification and Stellar Content of Galaxies Obtained from Direct Photography*, P. 1. the University of Chicago Press.

Sarzi, M., J. Falcón-Barroso, R. L. Davies, R. Bacon, M. Bureau, M. Cappellari, P. T. de Zeeuw, E. Emsellem, K. Fathi, D. Krajnović, H. Kuntschner, R. M. McDermid, and R. F. Peletier
2006. The SAURON project - V. Integral-field emission-line kinematics of 48 elliptical and lenticular galaxies. *Monthly Notices of the Royal Astronomical Society*, 366:1151–1200.

Savorgnan, G. A. D. and A. W. Graham
2016a. Explaining the reportedly overmassive black holes in early-type galaxies with intermediate-scale discs. *Monthly Notices of the Royal Astronomical Society*, 457(1):320–327.

Savorgnan, G. A. D. and A. W. Graham
2016b. Supermassive Black Holes and Their Host Spheroids. I. Disassembling Galaxies. *Astrophysical Journal Supplement Series*, 222(1):10.

Schauer, A. T. P., R.-S. Remus, A. Burkert, and P. H. Johansson
2014. The Mystery of the σ-Bump – A New Signature for Major Mergers in Early-type Galaxies? *The Astrophysical Journal*, 783:L32.

Schaye, J., R. A. Crain, R. G. Bower, M. Furlong, M. Schaller, T. Theuns, C. Dalla Vecchia, C. S. Frenk, I. G. McCarthy, J. C. Helly, A. Jenkins, Y. M. Rosas-Guevara, S. D. M. White, M. Baes, C. M. Booth, P. Camps, J. F. Navarro, Y. Qu, A. Rahmati, T. Sawala, P. A. Thomas, and J. Trayford
2015. The EAGLE project: simulating the evolution and assembly of galaxies and their environments. *Monthly Notices of the Royal Astronomical Society*, 446(1):521–554.

Schulze, F., R.-S. Remus, and K. Dolag
2017. On the Kinematics, Stability and Lifetime of Kinematically Distinct Cores: A Case Study. *Galaxies*, 5:41.

Schulze, F., R.-S. Remus, K. Dolag, S. Bellstedt, A. Burkert, and D. A. Forbes
2020. Kinematics of simulated galaxies II: Probing the stellar kinematics of galaxies out to large radii. *Monthly Notices of the Royal Astronomical Society*, 493(3):3778–3799.

Schulze, F., R.-S. Remus, K. Dolag, A. Burkert, E. Emsellem, and G. van de Ven
2018. Kinematics of simulated galaxies - I. Connecting dynamical and morphological properties of early-type galaxies at different redshifts. *Monthly Notices of the Royal Astronomical Society*, 480(4):4636–4658.

Schwarzschild, M.
1979. A numerical model for a triaxial stellar system in dynamical equilibrium. *The Astrophysical Journal*, 232:236–247.

Scott, N., R. L. Davies, R. C. W. Houghton, M. Cappellari, A. W. Graham, and K. A. Pimbblet
2014. Distribution of slow and fast rotators in the Fornax cluster. *Monthly Notices of the Royal Astronomical Society*, 441:274–288.

Serra, P., L. Oser, D. Krajnović, T. Naab, T. Oosterloo, R. Morganti, M. Cappellari, E. Emsellem, L. M. Young, L. Blitz, T. A. Davis, P.-A. Duc, M. Hirschmann, A.-M. Weijmans, K. Alatalo, E. Bayet, M. Bois, F. Bournaud, M. Bureau, A. F. Crocker, R. L. Davies, P. T. de Zeeuw, S. Khochfar, H. Kuntschner, P.-Y. Lablanche, R. M. McDermid, M. Sarzi, and N. Scott
2014. The ATLAS^{3D} project - XXVI. H I discs in real and simulated fast and slow rotators. *Monthly Notices of the Royal Astronomical Society*, 444:3388–3407.

Sérsic, J. L.
1963. Influence of the atmospheric and instrumental dispersion on the brightness distribution in a galaxy. *Boletin de la Asociacion Argentina de Astronomia La Plata Argentina*, 6:41–43.

Sievers, J. L., J. R. Bond, J. K. Cartwright, C. R. Contaldi, B. S. Mason, S. T. Myers, S. Padin, T. J. Pearson, U. L. Pen, D. Pogosyan, S. Prunet, A. C. S. Readhead, M. C. Shepherd, P. S. Udomprasert, L. Bronfman, W. L. Holzapfel, and J. May
2003. Cosmological Parameters from Cosmic Background Imager Observations and Comparisons with BOOMERANG, DASI, and MAXIMA. *The Astrophysical Journal*, 591(2):599–622.

Sillero, E., P. B. Tissera, D. G. Lambas, and L. Michel-Dansac
2017. The evolution of the metallicity gradient and the star formation efficiency in disc galaxies. *Monthly Notices of the Royal Astronomical Society*, 472(4):4404–4413.

Sparre, M. and V. Springel
2017. The unorthodox evolution of major merger remnants into star-forming spiral galaxies. *Monthly Notices of the Royal Astronomical Society*, 470(4):3946–3958.

Spavone, M., M. Capaccioli, N. R. Napolitano, E. Iodice, A. Grado, L. Limatola, A. P. Cooper, M. Cantiello, D. A. Forbes, M. Paolillo, and P. Schipani
2017. VEGAS: A VST Early-type GAlaxy Survey. II. Photometric study of giant ellipticals and their stellar halos. *Astronomy and Astrophysics*, 603:A38.

Spiniello, C., N. R. Napolitano, L. Coccato, V. Pota, A. J. Romanowsky, C. Tortora, G. Covone, and M. Capaccioli
2015. VIMOS mosaic integral-field spectroscopy of the bulge and disc of the early-type galaxy NGC 4697. *Monthly Notices of the Royal Astronomical Society*, 452(1):99–114.

Spitzer, L.
1962. *Physics of Fully Ionized Gases.*

Springel, V.
2005. The cosmological simulation code GADGET-2. *Monthly Notices of the Royal Astronomical Society*, 364:1105–1134.

Springel, V., T. Di Matteo, and L. Hernquist
2005a. Modelling feedback from stars and black holes in galaxy mergers. *Monthly Notices of the Royal Astronomical Society*, 361(3):776–794.

Springel, V. and L. Hernquist
2003. Cosmological smoothed particle hydrodynamics simulations: a hybrid multiphase model for star formation. *Monthly Notices of the Royal Astronomical Society*, 339:289–311.

Springel, V., R. Pakmor, A. Pillepich, R. Weinberger, D. Nelson, L. Hernquist, M. Vogelsberger, S. Genel, P. Torrey, F. Marinacci, and J. Naiman
2018. First results from the IllustrisTNG simulations: matter and galaxy clustering. *Monthly Notices of the Royal Astronomical Society*, 475(1):676–698.

Springel, V., J. Wang, M. Vogelsberger, A. Ludlow, A. Jenkins, A. Helmi, J. F. Navarro, C. S. Frenk, and S. D. M. White
2008. The Aquarius Project: the subhaloes of galactic haloes. *Monthly Notices of the Royal Astronomical Society*, 391(4):1685–1711.

Springel, V., S. D. M. White, A. Jenkins, C. S. Frenk, N. Yoshida, L. Gao, J. Navarro, R. Thacker, D. Croton, J. Helly, J. A. Peacock, S. Cole, P. Thomas, H. Couchman, A. Evrard, J. Colberg, and F. Pearce
2005b. Simulations of the formation, evolution and clustering of galaxies and quasars. *Nature*, 435(7042):629–636.

Springel, V., S. D. M. White, G. Tormen, and G. Kauffmann
2001a. Populating a cluster of galaxies - I. Results at [formmu2]z=0. *Monthly Notices of the Royal Astronomical Society*, 328:726–750.

Springel, V., N. Yoshida, and S. D. M. White
2001b. GADGET: a code for collisionless and gasdynamical cosmological simulations. *New Astron.*, 6:79–117.

Steinborn, L. K., K. Dolag, J. M. Comerford, M. Hirschmann, R.-S. Remus, and A. F. Teklu
2016. Origin and properties of dual and offset active galactic nuclei in a cosmological simulation at z=2. *Monthly Notices of the Royal Astronomical Society*, 458(1):1013–1028.

Steinborn, L. K., K. Dolag, M. Hirschmann, M. A. Prieto, and R.-S. Remus
2015. A refined sub-grid model for black hole accretion and AGN feedback in large cosmological simulations. *Monthly Notices of the Royal Astronomical Society*, 448:1504–1525.

Steinborn, L. K., M. Hirschmann, K. Dolag, F. Shankar, S. Juneau, M. Krumpe, R.-S. Remus, and A. F. Teklu
2018. Cosmological simulations of black hole growth II: how (in)significant are merger events for fuelling nuclear activity? *Monthly Notices of the Royal Astronomical Society*, 481(1):341–360.

Strader, J., A. J. Romanowsky, J. P. Brodie, L. R. Spitler, M. A. Beasley, J. A. Arnold, N. Tamura, R. M. Sharples, and N. Arimoto
2011. Wide-field Precision Kinematics of the M87 Globular Cluster System. *Astrophysical Journal Supplement Series*, 197:33.

Sweet, S. M., D. Fisher, K. Glazebrook, D. Obreschkow, C. Lagos, and L. Wang
2018. Revisiting the Stellar Mass-Angular Momentum-Morphology Relation: Extension to Higher Bulge Fraction and the Effect of Bulge Type. *The Astrophysical Journal*, 860(1):37.

Taylor, P., C. Federrath, and C. Kobayashi
2018. The origin of kinematically distinct cores and misaligned gas discs in galaxies from cosmological simulations. *Monthly Notices of the Royal Astronomical Society*, 479(1):141–152.

Taylor, P. and C. Kobayashi
2015. The effects of AGN feedback on present-day galaxy properties in cosmological simulations. *Monthly Notices of the Royal Astronomical Society*, 448(2):1835–1846.

Taylor, P. and C. Kobayashi
2017. The metallicity and elemental abundance gradients of simulated galaxies and their environmental dependence. *Monthly Notices of the Royal Astronomical Society*, 471(4):3856–3870.

Teklu, A. F., R.-S. Remus, and K. Dolag
2016. Dynamical Properties of Galaxies with Different Morphological Types at z=0 and z=2. In *The Interplay between Local and Global Processes in Galaxies,*.

Teklu, A. F., R.-S. Remus, K. Dolag, A. Arth, A. Burkert, A. Obreja, and F. Schulze
2018. Declining Rotation Curves at z = 2 in ΛCDM Galaxy Formation Simulations. *The Astrophysical Journal*, 854(2):L28.

Teklu, A. F., R.-S. Remus, K. Dolag, A. M. Beck, A. Burkert, A. S. Schmidt, F. Schulze, and L. K. Steinborn
2015. Connecting Angular Momentum and Galactic Dynamics: The Complex Interplay between Spin, Mass, and Morphology. *The Astrophysical Journal*, 812:29.

Teklu, A. F., R.-S. Remus, K. Dolag, and A. Burkert
2017. The morphology-density relation: impact on the satellite fraction. *Monthly Notices of the Royal Astronomical Society*, 472(4):4769–4785.

Teyssier, R., S. Pires, S. Prunet, D. Aubert, C. Pichon, A. Amara, K. Benabed, S. Colombi, A. Refregier, and J. L. Starck
2009. Full-sky weak-lensing simulation with 70 billion particles. *Astronomy and Astrophysics*, 497(2):335–341.

Thomas, J., R. Jesseit, R. P. Saglia, R. Bender, A. Burkert, E. M. Corsini, K. Gebhardt, J. Magorrian, T. Naab, D. Thomas, and G. Wegner
2009. The flattening and the orbital structure of early-type galaxies and collisionless N-body binary disc mergers. *Monthly Notices of the Royal Astronomical Society*, 393:641–652.

Thomas, J., R. P. Saglia, R. Bender, D. Thomas, K. Gebhardt, J. Magorrian, E. M. Corsini, and G. Wegner
2007. Dynamical modelling of luminous and dark matter in 17 Coma early-type galaxies. *Monthly Notices of the Royal Astronomical Society*, 382(2):657–684.

Toomre, A.
1977. Mergers and Some Consequences. In *Evolution of Galaxies and Stellar Populations*, B. M. Tinsley and R. B. G. Larson, D. Campbell, eds., P. 401.

Toomre, A. and J. Toomre
1972. Galactic Bridges and Tails. *The Astrophysical Journal*, 178:623–666.

Tormen, G., F. R. Bouchet, and S. D. M. White
1997. The structure and dynamical evolution of dark matter haloes. *Monthly Notices of the Royal Astronomical Society*, 286(4):865–884.

Tornatore, L., S. Borgani, K. Dolag, and F. Matteucci
2007. Chemical enrichment of galaxy clusters from hydrodynamical simulations. *Monthly Notices of the Royal Astronomical Society*, 382:1050–1072.

Tortora, C., F. La Barbera, N. R. Napolitano, A. J. Romanowsky, I. Ferreras, and R. R. de Carvalho
2014. Systematic variations of central mass density slopes in early-type galaxies. *Monthly Notices of the Royal Astronomical Society*, 445(1):115–127.

Tortora, C., L. Posti, L. V. E. Koopmans, and N. R. Napolitano
2019. The dichotomy of dark matter fraction and total mass density slope of galaxies over five dex in mass. *Monthly Notices of the Royal Astronomical Society*, 489(4):5483–5493.

Tsatsi, A., M. Lyubenova, G. van de Ven, J. Chang, J. A. L. Aguerri, J. Falcón-Barroso, and A. V. Macciò
2017. CALIFA reveals prolate rotation in massive early-type galaxies: A polar galaxy merger origin? *Astronomy and Astrophysics*, 606:A62.

Tsatsi, A., A. V. Macciò, G. van de Ven, and B. P. Moster
2015. A New Channel for the Formation of Kinematically Decoupled Cores in Early-type Galaxies. *The Astrophysical Journal*, 802:L3.

Tully, R. B. and J. R. Fisher
1977. A new method of determining distances to galaxies. *Astronomy and Astrophysics*, 54:661–673.

van de Sande, J., J. Bland-Hawthorn, S. Brough, S. M. Croom, L. Cortese, C. Foster, N. Scott, J. J. Bryant, F. d'Eugenio, C. Tonini, M. Goodwin, I. S. Konstantopoulos, J. S. Lawrence, A. M. Medling, M. S. Owers, S. N. Richards, A. L. Schaefer, and S. K. Yi
2017a. The SAMI Galaxy Survey: revising the fraction of slow rotators in IFS galaxy surveys. *Monthly Notices of the Royal Astronomical Society*, 472(2):1272–1285.

van de Sande, J., J. Bland-Hawthorn, L. M. R. Fogarty, L. Cortese, F. d'Eugenio, S. M. Croom, N. Scott, J. T. Allen, S. Brough, J. J. Bryant, G. Cecil, M. Colless, W. J. Couch, R. Davies, P. J. Elahi, C. Foster, G. Goldstein, M. Goodwin, B. Groves, I.-T. Ho, H. Jeong, D. H. Jones, I. S. Konstantopoulos, J. S. Lawrence, S. K. Leslie, Á. R. López-Sánchez, R. M. McDermid, R. McElroy, A. M. Medling, S. Oh, M. S. Owers, S. N. Richards, A. L. Schaefer, R. Sharp, S. M. Sweet, D. Taranu, C. Tonini, C. J. Walcher, and S. K. Yi
2017b. The SAMI Galaxy Survey: Revisiting Galaxy Classification through High-order Stellar Kinematics. *The Astrophysical Journal*, 835:104.

van de Sande, J., M. Kriek, M. Franx, P. G. van Dokkum, R. Bezanson, R. J. Bouwens, R. F. Quadri, H.-W. Rix, and R. E. Skelton
2013. Stellar Kinematics of z ~2 Galaxies and the Inside-out Growth of Quiescent Galaxies. *The Astrophysical Journal*, 771(2):85.

van de Sande, J., C. D. P. Lagos, C. Welker, J. Bland-Hawthorn, F. Schulze, R.-S. Remus, Y. Bahé, S. Brough, J. J. Bryant, L. Cortese, S. M. Croom, J. Devriendt, Y. Dubois, M. Goodwin, I. S. Konstantopoulos, J. S. Lawrence, A. M. Medling, C. Pichon, S. N. Richards, S. F. Sanchez, N. Scott, and S. M. Sweet
2019. The SAMI Galaxy Survey: comparing 3D spectroscopic observations with galaxies from cosmological hydrodynamical simulations. *Monthly Notices of the Royal Astronomical Society*, 484(1):869–891.

van de Sande, J., S. P. Vaughan, L. Cortese, N. Scott, J. Bland-Hawthorn, S. M. Croom, C. D. P. Lagos, S. Brough, J. J. Bryant, J. Devriendt, Y. Dubois, F. D'Eugenio, C. Foster, A. Fraser-McKelvie, K. E. Harborne, J. S. Lawrence, S. Oh, M. S. Owers, A. Poci, R.-S. Remus, S. N. Richards, F. Schulze, S. M. Sweet, M. R. Varidel, and C. Welker
2020. The SAMI Galaxy Survey: Towards an Optimal Classification of Galaxy Stellar Kinematics. *arXiv e-prints*, P. arXiv:2011.08199.

van de Ven, G., C. Hunter, E. K. Verolme, and P. T. de Zeeuw
2003. General solution of the Jeans equations for triaxial galaxies with separable potentials. *Monthly Notices of the Royal Astronomical Society*, 342(4):1056–1082.

van de Voort, F., T. A. Davis, D. Kereš, E. Quataert, C.-A. Faucher-Giguère, and P. F. Hopkins
2015. The creation and persistence of a misaligned gas disc in a simulated early-type galaxy. *Monthly Notices of the Royal Astronomical Society*, 451(3):3269–3277.

van den Bergh, S.
1976. A new classification system for galaxies. *The Astrophysical Journal*, 206:883–887.

van den Bosch, F. C., T. Abel, R. A. C. Croft, L. Hernquist, and S. D. M. White
2002. The Angular Momentum of Gas in Protogalaxies. I. Implications for the Formation of Disk Galaxies. *The Astrophysical Journal*, 576(1):21–35.

van den Bosch, R. C. E., G. van de Ven, E. K. Verolme, M. Cappellari, and P. T. de Zeeuw
2008. Triaxial orbit based galaxy models with an application to the (apparent) decoupled core galaxy NGC 4365. *Monthly Notices of the Royal Astronomical Society*, 385:647–666.

van der Marel, R. P. and M. Franx
1993. A new method for the identification of non-Gaussian line profiles in elliptical galaxies. *The Astrophysical Journal*, 407:525–539.

van Dokkum, P., A. Wasserman, S. Danieli, R. Abraham, J. Brodie, C. Conroy, D. A. Forbes, C. Martin, M. Matuszewski, A. J. Romanowsky, and A. Villaume
2019. Spatially Resolved Stellar Kinematics of the Ultra-diffuse Galaxy Dragonfly 44. I. Observations, Kinematics, and Cold Dark Matter Halo Fits. *The Astrophysical Journal*, 880(2):91.

Veale, M., C.-P. Ma, J. E. Greene, J. Thomas, J. P. Blakeslee, N. McConnell, J. L. Walsh, and J. Ito
2017a. The MASSIVE Survey - VII. The relationship of angular momentum, stellar mass and environment of early-type galaxies. *Monthly Notices of the Royal Astronomical Society*, 471:1428–1445.

Veale, M., C.-P. Ma, J. Thomas, J. E. Greene, N. J. McConnell, J. Walsh, J. Ito, J. P. Blakeslee, and R. Janish
2017b. The MASSIVE Survey - V. Spatially resolved stellar angular momentum, velocity dispersion, and higher moments of the 41 most massive local early-type galaxies. *Monthly Notices of the Royal Astronomical Society*, 464(1):356–384.

Vogelsberger, M., S. Genel, V. Springel, P. Torrey, D. Sijacki, D. Xu, G. Snyder, D. Nelson, and L. Hernquist
2014. Introducing the Illustris Project: simulating the coevolution of dark and visible matter in the Universe. *Monthly Notices of the Royal Astronomical Society*, 444(2):1518–1547.

Vudragović, A., S. Samurović, and M. Jovanović
2016. Full stellar kinematical profiles of central parts of nearby galaxies. *Astronomy and Astrophysics*, 593:A40.

Weinmann, S. M., F. C. van den Bosch, X. Yang, and H. J. Mo
2006. Properties of galaxy groups in the Sloan Digital Sky Survey - I. The dependence of colour, star formation and morphology on halo mass. *Monthly Notices of the Royal Astronomical Society*, 366(1):2–28.

White, S. D. M.
1984. Angular momentum growth in protogalaxies. *The Astrophysical Journal*, 286:38–41.

White, S. D. M., C. S. Frenk, and M. Davis
1983. Clustering in a neutrino-dominated universe. *The Astrophysical Journal*, 274:L1–L5.

White, S. D. M. and M. J. Rees
1978. Core condensation in heavy halos: a two-stage theory for galaxy formation and clustering. *Monthly Notices of the Royal Astronomical Society*, 183:341–358.

Wilkinson, A., R. M. Sharples, R. A. E. Fosbury, and P. T. Wallace
1986. Stellar dynamics of CEN A. *Monthly Notices of the Royal Astronomical Society*, 218:297–329.

Wisnioski, E., N. M. Förster Schreiber, S. Wuyts, E. Wuyts, K. Bandara, D. Wilman, R. Genzel, R. Bender, R. Davies, M. Fossati, P. Lang, J. T. Mendel, A. Beifiori, G. Brammer, J. Chan, M. Fabricius, Y. Fudamoto, S. Kulkarni, J. Kurk, D. Lutz, E. J. Nelson, I. Momcheva, D. Rosario, R. Saglia, S. Seitz, L. J. Tacconi, and P. G. van Dokkum
2015. The KMOS^{3D} Survey: Design, First Results, and the Evolution of Galaxy Kinematics from 0.7 ¡= z ¡= 2.7. *The Astrophysical Journal*, 799(2):209.

Wright, E. L., S. S. Meyer, C. L. Bennett, N. W. Boggess, E. S. Cheng, M. G. Hauser, A. Kogut, C. Lineweaver, J. C. Mather, G. F. Smoot, R. Weiss, S. Gulkis, G. Hinshaw, M. Janssen, T. Kelsall, P. M. Lubin, J. Moseley, S. H., T. L. Murdock, R. A. Shafer, R. F. Silverberg, and D. T. Wilkinson
1992. Interpretation of the Cosmic Microwave Background Radiation Anisotropy Detected by the COBE Differential Microwave Radiometer. *The Astrophysical Journal*, 396:L13.

Wu, X., O. Gerhard, T. Naab, L. Oser, I. Martinez-Valpuesta, M. Hilz, E. Churazov, and N. Lyskova
2014. The mass and angular momentum distribution of simulated massive early-type galaxies to large radii. *Monthly Notices of the Royal Astronomical Society*, 438:2701–2715.

Xu, G.
1995. A New Parallel N-Body Gravity Solver: TPM. *Astrophysical Journal Supplement Series*, 98:355.

Zavala, J., C. S. Frenk, R. Bower, J. Schaye, T. Theuns, R. A. Crain, J. W. Trayford, M. Schaller, and M. Furlong
2016. The link between the assembly of the inner dark matter halo and the angular momentum evolution of galaxies in the EAGLE simulation. *Monthly Notices of the Royal Astronomical Society*, 460(4):4466–4482.

Zhu, L., G. van de Ven, R. Leaman, R. J. J. Grand, J. Falcón-Barroso, P. Jethwa, L. L. Watkins, S. Mao, A. Poci, R. M. McDermid, and D. Nelson
2020. Disentangling the formation history of galaxies via population-orbit superposition: method validation. *Monthly Notices of the Royal Astronomical Society*, 496(2):1579–1597.

Zwicky, F.
1933. Die Rotverschiebung von extragalaktischen Nebeln. *Helvetica Physica Acta*, 6:110–127.

Zwicky, F.
1937. On the Masses of Nebulae and of Clusters of Nebulae. *The Astrophysical Journal*, 86:217.

List of Figures

List of Tables

Acknowledgements

First and foremost, I'd like to thank Prof. Andreas Burkert for giving me the chance to write my PhD thesis as part of the CAST group. I spent most of my scientific career in this group and never regretted this decision. I'm deeply grateful that you enabled me to work in this scientifically diverse group of amazing people and that you let me travel all over the world.

Second, I thank Dr. Rhea-Silvia Remus for many things. For the almost endless amount of ideas and the great scientific guidance that led to amazing results. Apart from that it was so much fun to travel all over the world with you, bringing me to places I never believed I would visit. In the same way I'd like to thank PD Klaus Dolag for always taking the time for discussions and support on any scientific matter and for letting me be part of the Magneticum team. Furthermore, thanks for the coffee meetings which are the the social glue of the CAST group.

Third, I want to thank many people at the USM that contributed to the success of my PHD, scientifically as well as morally. My long-time office-mate Adelheid for great scientific and non-scientific discussions. My later office-mates Joe, Uli, Marcel and Kristina for making open-space office life as good as it gets. Another thanks to Ludwig and Stefan for always having an open ear and a positive attitude. Furthermore, I'd like to thank everyone in the CAST group, including former members, for the scientific input and the great atmosphere within the group. Special thanks are due to Tadziu for all matters concerning failing computers. Thanks to Nicola, Gudrun and Sabine for making life at the USM and communication with the MPE so much easier.

Finally, I want to thank my family and friends for always being there and sometimes knowing me better than I know myself. Without you my PHD would not have been possible. Your contribution to my PHD and also personal happiness in life cannot be emphasised enough.